

Mechanical response of the porcine cervical spine to acute and repetitive anterior-posterior shear

by

Samuel J. Howarth

A thesis  
presented to the University of Waterloo  
in fulfillment of the  
thesis requirement for the degree of  
Doctor of Philosophy  
in  
Kinesiology

Waterloo, Ontario, Canada, 2011

© Samuel J. Howarth 2011

## **AUTHOR'S DECLARATION**

I hereby declare that I am the sole author of this thesis. This is a true copy of the thesis, including any required final revisions, as accepted by my examiners.

I understand that my thesis may be made electronically available to the public.

## ABSTRACT

Approximately 80% of the population will experience low-back pain within their lifetime. Significant research efforts have focused on compressive loading as an injury mechanism that could lead to low-back pain and injury. However, the influence of shear loading, and its relationship to vertebral tissue tolerances as well as modulating factors for these tolerances have not been studied as extensively. The primary objective of this thesis was to produce a series of investigations that begin to determine the roles of different modulating factors such as posture, compression, bone density, bone morphology, and repetitive load magnitude on measured vertebral joint shear failure tolerances.

The thesis comprises four independent studies using *in vitro* mechanical testing, imaging modalities, and finite element modeling. Each of the *in vitro* studies within this thesis used a validated porcine cervical model as a surrogate for the human lumbar spine. The first study employed *in vitro* mechanical testing to investigate the combined roles of flexion/extension postural deviation and compressive load on the measured ultimate shear failure tolerances. Peripheral quantitative computed tomography scans of the pars interarticularis and measurements of vertebral bone morphology were used in the second investigation along with *in vitro* mechanical testing to identify the morphological characteristics that can be used to predict ultimate shear failure tolerances. The influence of sub-maximal shear load magnitude on the cumulative shear load and number of loading cycles sustained prior to failure were investigated with *in vitro* mechanical testing in the third study. Finally, a finite element model of the porcine C3-C4 functional spinal unit was used to investigate the plausibility of hypotheses, developed from previous

research and the findings of the first investigation for this thesis, surrounding alterations in measured ultimate shear failure tolerances as a function of changes in facet interaction.

Results from the first investigation showed that there was no statistically significant interaction between postural deviation and compressive force on ultimate shear failure tolerance. However, ultimate shear failure tolerance was reduced (compared to neutral) by 13.2% with flexed postures, and increased (compared to neutral) by 12.8% with extended postures. Each 15% increment (up to a maximum of 60% of predicted compressive failure tolerance) in compressive force was met with an average 11.1% increase in ultimate shear failure tolerance. It was hypothesized that alterations in flexion/extension posture and/or compressive force altered the location for the force centroid of facet contact. These changes in the location of facet contact were hypothesized to produce subsequent changes in the bending moment at the pars interarticularis that altered the measured ultimate shear failure tolerance.

The three leading factors for calculating of measured ultimate shear failure tolerance were the pars interarticularis length for the cranial vertebra, the average facet angle measured in the transverse plane, and cortical bone area through the pars interarticularis. A bi-variate linear regression model that used the cranial vertebra's pars interarticularis length and average facet angle as inputs was developed to non-destructively calculate ultimate shear failure tolerances of the porcine cervical spine. Longer pars interarticularis lengths and facets oriented closer to the sagittal plane were associated with higher measured ultimate shear failure tolerances. Fractures observed in this investigation were similar to those reported for studies performed with human specimens and also similar to reported spondylolitic fractures associated with shear



loading in humans. This provided additional evidence that the porcine cervical spine is a suitable surrogate *in vitro* model for studying human lumbar spine mechanics.

Altered sub-maximal shear load magnitude create a non-linear decrease in both the number of cycles and the cumulative shear load sustained prior to failure. These findings suggested that estimates of cumulative shear load should assign greater importance to higher instantaneous shear loads. This was due to an increased injury potential at higher instantaneous shear loads. Cumulative load sustained prior to failure was used to develop a tissue-based weighting factor equation that would apply non-linearly increased weight to higher shear load magnitudes in estimates of cumulative shear load.

A finite element model of the porcine C3-C4 functional spinal unit was created, and simulations were performed using similar boundary conditions as the comparable *in vitro* tests, to assess the plausibility of the moment arm hypothesis offered within the first investigation of this thesis. Moment arm length between the force centroid of facet contact and the location of peak stress within the pars interarticularis was increased for flexed postures and decreased for extended postures. Alterations in moment arm length were larger for postural deviation than compressive force, suggesting a secondary mechanism to explain the observed increase in shear failure tolerance with higher compressive loads from the first investigation. One such possibility was the increase in the number of contacting nodes with higher compressive forces. Alterations in moment arm length were able to explain 50% of the variance in measured ultimate shear failure tolerances from the first study. Thus, the finite element model was successful in demonstrating the plausibility of moment arm length between the force centroid of facet

contact and the pars interarticularis as a modulator of measured ultimate shear failure tolerance.

This thesis has developed the basis for understanding how failure of the vertebral joint exposed to shear loading can be modulated. In particular, this thesis has developed novel equations to predict the ultimate shear failure tolerance measured during *in vitro* testing, and to determine appropriate weighting factors for sub-maximal shear forces in calculations of cumulative shear load. Evidence presented within this thesis also provides support for the long-standing moment arm hypothesis for modulation of shear injury potential.

## ACKNOWLEDGEMENTS

First, I would like to acknowledge the endless support of my supervisor Dr. Jack Callaghan. Your mentorship has provided me with every opportunity to succeed. I began my doctoral studies as one of nine PhD students within your lab. Nonetheless, you somehow always found time to always be available to answer my questions or provide your critical insights.

I would also like to recognize Drs. Stuart McGill, Duane Cronin, Clark Dickerson, and Jennifer Durkin for serving as valuable members of my thesis committee. Furthermore, I would like to thank Dr. Peter Crompton for serving as the external examiner for my doctoral thesis defence. Your questions, comments, and suggestions have greatly improved the contributions of this work.

I have been very fortunate to have met and become friends with so many great people after having spent over a decade as a student at the University of Waterloo. My interactions with everyone have certainly shaped the person I have become. In particular, I could always rely on Tyson Beach or Steven Fischer for lighthearted discussions on anything from sports to digital signal processing methods. I would also like to recognize Tom Karakolis' help with constructing the finite element model presented in this thesis.

My family must also be thanked for supporting my endeavors whether it was playing competitive golf, or pursuing a doctorate. My mother and father should be credited with instilling the principles of a strong work ethic within myself. It has also been a pleasure to watch my brothers and sisters grow to be hardworking and honest individuals which keeps me humble and honest.

Lastly, I would like to thank Katie Bonsall who has been with me throughout the completion of my doctorate. Your love has propelled me through many difficult times, and also brought me happiness that I had never previously experienced. I am also grateful to you for having introduced me to such a wonderful family as yours. Their positive outlook and understanding have been extraordinary. I know that the completion of my PhD has been a difficult process for you as well, and I cannot thank-you enough for repeatedly picking me up when I was down, and for telling me to suck it up when I needed it. You have far surpassed anything I could have ever expected as a partner!

## TABLE OF CONTENTS

AUTHOR’S DECLARATION .....	ii
ABSTRACT .....	iii
ACKNOWLEDGEMENTS .....	vii
TABLE OF CONTENTS .....	vii
LIST OF FIGURES .....	xii
LIST OF TABLES .....	xviii
 CHAPTER 1 - INTRODUCTION .....	 1
1.1 General introduction .....	2
1.2 Thesis questions and objectives .....	6
1.3 Thesis hypotheses .....	7
 CHAPTER 2 - REVIEW OF LITERATURE .....	 9
2.1 Basic anatomy of the human lumbar vertebral joint .....	10
2.2 Use of the porcine cervical spine as a surrogate for the human lumbar spine .....	12
2.3 Components of the functional spinal unit that resist shear .....	15
2.3.1 Intervertebral disc .....	15
2.3.1.1 Structure and composition of the intervertebral disc .....	15
2.3.1.2 Innervation and sensory function of the intervertebral disc .....	18
2.3.1.3 Mechanical properties of the intervertebral disc under external shear loading .....	18
2.3.2 Facet joints .....	19
2.3.2.1 Structure of facets and facet joints .....	19
2.3.2.2 Innervation of the facet capsule .....	22
2.3.2.3 Mechanical resistance of the facet joints to shear loading .....	23
2.3.3 Ligaments .....	24
2.3.3.1 Structure and composition of ligaments .....	24
2.3.3.2 Innervation and sensory function of ligaments .....	24
2.3.3.3 Mechanical properties of ligaments under shear loading .....	25
2.4 Mechanical properties of the spine under external shear load .....	27
2.4.1 Effect of load and or displacement rate on mechanical properties of biological tissues and FSU’s .....	28
2.4.2 Effect of compression on mechanical properties of FSU’s .....	29
2.4.3 Effect of posture on mechanical properties of FSU’s .....	31
2.5 Effect of freezing on the mechanical properties of FSU’s .....	33
2.6 Use of quantitative computed tomography and bone mineral density measures for estimation and prediction of failure tolerances .....	35
2.7 Overview of the finite element method .....	38
2.7.1 General overview .....	38
2.7.2 Utility of the finite element method for spine modeling .....	40
2.7.3 Geometry modeling .....	42
2.7.3.1 Mesh density, element size and convergence .....	44
2.7.3.2 Element type and mesh generation .....	46
2.7.4 Material property modeling .....	48

2.7.5 Boundary condition definition .....	51
CHAPTER 3 - COMBINED INFLUENCE OF COMPRESSION AND POSTURE ON SHEAR FAILURE MECHANISMS FOR THE PORCINE CERVICAL SPINE .....	
3.1 Introduction.....	54
3.2 Methods.....	56
3.2.1 Specimen preparation and assessment.....	56
3.2.2 Instrumentation .....	58
3.2.3 Loading protocol.....	60
3.2.4 Post-failure analysis .....	64
3.2.5 Data processing and analysis .....	65
3.2.6 Statistical analysis.....	67
3.3 Results.....	68
3.3.1 Specimen randomization.....	68
3.3.2 Vertebral level.....	71
3.3.3 Compression .....	71
3.3.4 Posture.....	74
3.3.5 Post-failure analysis .....	80
3.4 Discussion .....	83
CHAPTER 4 - INFLUENCE OF VERTEBRAL MORPHOLOGY AND PARS INTERARTICULARIS BONE DENSITY AS FACTORS FOR CALCULATING ANTERIOR SHEAR FAILURE TOLERANCE FOR THE PORCINE CERVICAL SPINE: DEVELOPMENT OF A MATHEMATICAL MODEL .....	
4.1 Introduction.....	91
4.2 Methods.....	93
4.2.1 Specimen preparation and assessment.....	93
4.2.1.1 Specimen assessment .....	93
4.2.1.2 Imaging of the pars interarticularis .....	95
4.2.3 Specimen fixation .....	99
4.2.4 Instrumentation .....	100
4.2.5 Loading protocol.....	102
4.2.6 Post-failure analysis .....	105
4.2.7 Data processing and analysis .....	105
4.2.7.1 Force versus displacement data .....	105
4.2.7.2 pQCT image processing.....	106
4.2.8 Development and testing of a mathematical model for non-destructively calculating ultimate shear force .....	108
4.3 Results.....	110
4.3.1 Specimen randomization.....	110
4.3.2 Vertebral level.....	111
4.3.3 Post-failure analysis .....	114
4.3.4 Regression model development .....	116
4.3.5 Regression model error testing .....	118
4.4 Discussion .....	119

CHAPTER 5 - INVESTIGATING THE NON-LINEAR RELATIONSHIP BETWEEN SUB-MAXIMAL SHEAR LOAD AND CUMULATIVE SHEAR LOAD SUSTAINED PRIOR TO FIALURE: DEVELOPMENT OF A TISSUE-BASED WEIGHTING ALGORITHM FOR DETERMINING CUMULATIVE SHEAR LOAD .....	125
5.1 Introduction.....	126
5.2 Methods.....	128
5.2.1 Specimen preparation and assessment.....	128
5.2.2 Loading protocol.....	131
5.2.3 Post-failure analysis .....	138
5.2.4 Data processing and analysis .....	139
5.2.5 Statistical analysis and weighting factor generation.....	139
5.2.5.1 Statistical analysis.....	139
5.2.5.2 Weighting factor generation .....	140
5.3 Results.....	141
5.3.1 Specimen randomization and vertebral level.....	141
5.3.2 Post-failure analysis.....	143
5.3.3 Cumulative load and cycles sustained prior to failure.....	145
5.3.4 Weighting factor generation .....	146
5.4 Discussion.....	148
CHAPTER 6 - USE OF FINITE ELEMENT ANALYSIS FOR QUANTITATIVELY INVESTIGATING THE MOMENT ARM HYPOTHESIS FOR ALTERED SHEAR FAILURE TOLERANCES UNDER COMBINED COMPRESSIVE LOADING AND FLEION/EXTENSION POSTURES.....	156
6.1 Introduction.....	157
6.2 Methods.....	160
6.2.1 Geometry generation.....	160
6.2.1.1 Individual vertebrae .....	160
6.2.1.2 Functional spinal unit (FSU).....	164
6.2.2 Element type, material properties and mesh refinement.....	165
6.2.2.1 Components .....	166
6.2.2.1.1 Cortical bone.....	166
6.2.2.1.2 Trabecular bone .....	166
6.2.2.1.3 Endplates.....	166
6.2.2.1.4 Intervertebral disc .....	167
6.2.2.2 Determining appropriate mesh size .....	169
6.2.3 Simulation conditions .....	171
6.2.3.1 Loads.....	171
6.2.3.2 Boundary conditions .....	171
6.2.3.3 Contact formulation .....	172
6.2.4 Post-processing .....	173
6.2.5 Model verification and validation.....	174
6.3 Results.....	176
6.3.1 Convergence study.....	176
6.3.2 Model verification and validation.....	176
6.3.3 Simulation results following 3 mm of shear displacement.....	178

6.3.3.1 Compression .....	178
6.3.3.2 Posture.....	183
6.3.4 Simulation results at consistent strain.....	184
6.3.5 Relationship of moment arm length changes with ultimate failure from <i>in vitro</i> testing.....	188
6.4 Discussion .....	190
CHAPTER 7 - THESIS SUMMARY AND CONTRIBUTIONS.....	201
7.1 Thesis summary .....	202
7.2 Hypotheses revisited .....	206
7.3 Conceptual model for modulation of anterior joint shear failure .....	209
7.4 Global limitation .....	213
7.5 Future research directions .....	216
7.6 Contributions of the thesis .....	218
REFERENCES .....	221
APPENDICES .....	237
A. GALIL code .....	238
A.1 Shear precondition .....	238
A.2 Acute shear failure .....	239
A.3 Repetitive shear failure .....	240
B. Data processing cutoff determination .....	242
B.1 Digital filter cutoffs for Chapters 3-5.....	242
B.2 Inter-rater reliability of measurements made from peripheral quantitative computed tomography .....	243
B.3 Half maximum height (HMH) cutoff determination and inter-rater reliability .....	244
C. Control algorithm performance.....	245
C.1 Repetitive shear control algorithm performance.....	245
D. Calculations.....	246
D.1 Analytical solution for a cantilevered beam .....	246

## LIST OF FIGURES

Figure 1.1 – A hypothetical scenario of a person whose trunk is partially flexed (A). The gravitational force from the mass of the trunk (above the L4-L5 point), arms and head is the only external force ( $F_g$ ) acting on the body above L4-L5 (B). This force creates a flexion moment that must be counteracted by an equal and oppositely directed extensor moment generated by muscular force that imposes additional vertebral joint compression (C). The labels C and S (C.) respectively refer to the L4-L5 vertebral joint compressive and shear axes. ....	4
Figure 1.2 – Flowchart outlining the logical connections and titles of the studies for this thesis. ....	7
Figure 2.1 – Bony landmarks of a human lumbar vertebra. (Image taken from McGill, 2007). ....	10
Figure 2.2 – Ligaments of the lumbar spine. SSL = Supraspinous ligament, ISL = Interspinous ligament, LF = Ligamentum flavum, PLL = Posterior longitudinal ligament, ALL = Anterior longitudinal ligament. (Image taken from Adams et al., 2002) .....	12
Figure 2.3 – Sagittal section showing the nucleus pulposus (NP), anterior and posterior portions of the annulus fibrosus (AF) and the superior and inferior endplates (EP). (Image taken from Adams et al., 2002).....	15
Figure 2.4 - Annular fiber angles for the anterior (A) and posterior (B) portions of the annulus fibrosus from the porcine cervical spine as well as the angle between adjacent lamellar layers (C). Angles for individual lamellar layers (A and B) are measured with respect to the vertical axis. (Images taken from Tampier, 2006).....	17
Figure 2.5 – Transverse MRI slice through the L4 vertebra of the human lumbar spine. The image on the left shows the lateral and anterior facing orientation of the inferior facets from L3 and the medial and posterior facing orientation of the superior facets from L4. (Image taken from Kalichman and Hunter, 2007).....	20
Figure 2.6 – Transverse image of a facet joint illustrating the two articulating facets being distracted by forceps to reveal the meniscus (m). (Image taken from Bogduk and Engel, 1984) .....	21
Figure 2.7 – Hypothetical load-elongation (a) and stress-strain (b) curves with characteristic features. The curves are derived from tensile loading of ligaments, the definition of the structural properties attained from each of these curves is consistent with all <i>in vitro</i> material and structural testing. (Image taken from Woo et al., 2000).....	27



Figure 2.8 – Bone density exhibits minimal change from cranial vertebrae (T10 in this example) to caudal vertebrae (L5 in this case). However, endplate area does increase in more caudal vertebrae. Increased endplate area of more caudal vertebrae has been associated with increased ultimate compressive load of vertebral bodies. (Image taken from Brinckmann et al., 1989).....	37
Figure 2.9 – Definition of a generic element to be used in a finite element model. Nodes are sequentially numbered and the edges are defined by the connectivity between specifically numbered nodes. (Image taken from Brown, 2004).....	43
Figure 2.10 – Increasing the number of elements improves the model’s geometrical resolution and can improve the resolution of the finite element model’s solution. A coarse model is depicted on the left while a fine model is depicted on the right. (Image taken from Crawford et al., 2003) .....	44
Figure 2.11 – Regional definition of element densities can improve the model’s resolution in areas that are of primary interest while also enhancing computational efficiency by minimizing the total number of elements in the model. In this example, the element density of the intervertebral disc is modeled with a larger number of elements because the disc was the structure of primary importance for this study. (Image taken from Belytschko et al., 1974).....	46
Figure 2.12 – Examples of a brick (shown on the left) and a tetrahedral element (shown on the right). (Image taken from Brown, 2004).....	47
Figure 2.13 – Images depicting a pixel representation from a section of MRI scanned geometry (a) and three mesh generators (b-d) with various levels of geometrical smoothing to reduce volume distortion of the final finite element model geometry. (Image taken from Kaminsky et al., 2005) .....	48
Figure 3.1 – X-ray of a specimen taken in the transverse plane. Left and right facet angles ( $\theta_L$ and $\theta_R$ ) were measured as the angle between a line parallel to the posterior aspect of the vertebral body and a line parallel to the gap between the facets.....	57
Figure 3.2 – Experimental setup for all shear testing protocols. IREDs = infrared light emitting diodes.....	59
Figure 3.3 – Schematic drawing of the <i>in vitro</i> testing setups for the unconstrained (A.) flexion/extension tests, and the constrained (B.) shear tests.....	61
Figure 3.4 – Sample shear displacement versus force curve obtained from an ultimate shear failure tests (C3-C4). The calculated linear stiffness (k), elastic limit (A), initial failure point (B) and ultimate failure point (C) are illustrated.....	66

Figure 3.5 – Linear shear stiffness increases with static compressive load. Error bars represent the standard error of the mean. Means with different letters are statistically different from one another. ....	73
Figure 3.6 – Energy stored until the initial failure point with increased static compressive load. Error bars represent the standard error of the mean. Means with different letters are statistically different from one another. ....	74
Figure 3.7 – Ultimate shear force sustained in each of the extended, neutral and flexed postures. Error bars represent the standard error of the mean. Means with different letters are statistically different from one another. ....	75
Figure 3.8 – Linear shear stiffness in each of the extended, neutral and flexed postures. Error bars represent the standard error of the mean. Means with different letters are statistically different from one another. ....	76
Figure 3.9 – Energy stored until ultimate shear failure in each of the extended, neutral and flexed postures. Error bars represent the standard error of the mean. Means with different letters are statistically different from one another. ....	76
Figure 3.10 – Displacement (A.), energy stored (B.) and force (C.) at initial failure for both C3-C4 and C5-C6 specimens tested in each of the extended, neutral and flexed postures. Error bars represent the standard error of the mean. Means with different letters are statistically different from one another. ....	78
Figure 3.11 – Energy stored (A.) and force (B.) at the elastic limit for both C3-C4 and C5-C6 specimens tested in each of the extended, neutral and flexed postures. Error bars represent the standard error of the mean. Means with different letters are statistically different from one another. ....	79
Figure 3.12 – Transverse image of a C3 vertebra following acute shear failure. The black arrows indicate the bilateral pars interarticularis fracture that was the predominant injury present in shear failure. ....	80
Figure 3.13 – Images of a bilateral pars interarticularis fracture of the caudal vertebra (A), unilateral pars interarticularis fracture (B), and a unilateral facet fracture (C). ....	81
Figure 3.14 – Illustration of how posture and compressive force may alter the moment arm length between the centroid of facet contact force and the pars interarticularis between the neutral (A), flexed (B), extended (C), and compressed (D) conditions. Flexion may produce an increase in moment arm length while extension and compression may decrease the moment arm length, which would respectively require decreased and increased measured shear failure forces. ....	86

Figure 4.1 – X-ray of a specimen taken in the transverse plane. Left and right facet angles ( $\theta_L$ and $\theta_R$ ) were measured as the angle between a line parallel to the posterior aspect of the vertebral body and a line parallel to the gap between the facets.....	95
Figure 4.2 – (A.) Sagittal plane x-ray of a vertebral specimen that illustrates digitized locations (B.) for determining the pars interarticularis length (l), angle ( $\alpha$ ) and reference distance (d) for computed tomography scanning of the pars interarticularis.....	97
Figure 4.3 – Experimental setup for the computed tomography imaging protocol. ....	98
Figure 4.4 – Scout scan of a specimen. The reference location for the nail is illustrated as the intersection of the two red lines. This reference location was used to define the gantry position for computed tomography scanning of the pars interarticularis. ....	99
Figure 4.5 – Experimental setup for all shear protocols. IREDs = infrared light emitting diodes. ....	100
Figure 4.6 – Computed tomography scan illustrating the region of interest defined as the pars interarticularis. Density and area measures were made on the selected region of interest.....	107
Figure 4.7 – Transverse image of a C3 vertebra following acute shear failure. The black arrows indicate the bilateral pars interarticularis fracture that was the predominant injury caused by shear failure.....	114
Figure 4.8 – Absolute (A.) and relative (B.) errors in calculated ultimate shear failure tolerance produced by each mathematical model generated by first three iterations of the stepwise regression analysis. Error bars indicate the standard error of the mean calculation error. ....	119
Figure 5.1 – X-ray of a specimen taken in the transverse plane. Left and right facet angles ( $\theta_L$ and $\theta_R$ ) were measured as the angle between a line parallel to the posterior aspect of the vertebral body and a line parallel to the gap between the facets.....	129
Figure 5.2 – Sagittal plane x-ray of the specimen used to digitize locations for the pars interarticularis of the cranial vertebra as well as the calibration frame. ....	130
Figure 5.3 – Experimental setup for all shear loading protocols. ....	134
Figure 5.4 – Example of cycle-by-cycle average stiffness, shear displacement and hysteresis indicating the point of shear fatigue failure shown by the vertical dashed line. ....	136
Figure 5.5 – Outline of the control algorithm for the repetitive shear loading protocol. Dashed lines represent feedback from the load cells that measure shear force, and is used to continuously update linear actuator displacement rates. ....	137

Figure 5.6 – Filtered shear force versus time profile (for the first 10 cycles) demonstrating the triangular loading/unloading waveform used for this investigation. The dashed black line shows the target shear load. Vertical lines indicate half-second intervals that were the targeted loading and unloading durations. The shear force versus time profile stabilized during the repetitive shear loading protocol. ....	137
Figure 5.7 – Cumulative shear sustained by specimens that survived (black) and failed during (gray) the repetitive shear failure protocol. Different letters illustrates cumulative shear for specimens that failed during the repetitive shear failure protocol with statistically different means. The number above each bar (N) represents the number of specimens that either failed or survived at each loading magnitude. Error bars represent the standard error of the mean. ....	145
Figure 5.8 – The number of shear loading cycles sustained prior to failure for specimens in the 40%, 60% and 80% loading magnitude groups. The vertical axis is logarithmic. Statistical differences between means are given with different letters. The number above each bar (N) denotes the number of specimens that were injured during the repetitive shear loading protocol. Error bars represent the standard error of the mean. ....	146
Figure 5.9 – Power law relationship between sub-maximal load magnitude and cumulative shear. Circles indicate cumulative shear sustained by individual specimens assigned to each loading magnitude. Crosses indicate cumulative shear values used for obtaining the power law relationship. ....	147
Figure 5.10 – Piecewise continuous weighting factor function of shear loading magnitude. ....	148
Figure 6.1 – Flowchart illustrating the step-by-step process of generating the vertebral geometry, meshing the functional spinal unit, defining simulation boundary conditions and analyzing results from the simulations. ....	162
Figure 6.2 – Comparison of the stacked vertebrae (left) used to define the geometry of the modeled functional spinal unit (right). ....	164
Figure 6.3 – The defined location for the pars interarticularis (A.), stress distribution following 3 mm of C4 backward shear displacement illustrating the location of peak stress within the pars interarticularis (B.), and the contacting node locations as well as the moment arm length between the force centroid of facet contact and the location of peak stress within the pars interarticularis (C.) for the C3 vertebra. ....	174
Figure 6.4 – Magnitude of stress at the location of peak stress within the C3 left and right pars interarticularis at the end of the 3 mm shear displacement phase for each simulation. ....	179
Figure 6.5 – Strain at the locations of peak stress within the C3 left and right pars interarticularis at the end of the 3 mm shear displacement phase for each simulation. ...	180

Figure 6.6 – The number of C3 cortical shell nodes, divided into left and right sides, in contact with the C4 cortical shell at the end of the 3 mm shear displacement phase for each simulation. .... 180

Figure 6.7 – Moment arm length between the center of facet contact force location on the left and right C3 facets and the locations of peak stress within the left and right pars interarticularis after the 3 mm shear displacement phase for each simulation. .... 183

Figure 6.8 – Alterations in stress distribution and the number of facet nodes in contact with extended, neutral and flexed postures with 15% of compressive force applied to the superior surface of the C3 vertebra for identical strain. Note that the color of stress near the marked location of peak stress within the pars interarticularis changes from green to yellow to orange with extended, flexed, and neutral postures respectively. This indicates that stress within the pars interarticularis increases from an extended posture to a flexed posture for a given strain..... 186

Figure 6.9 – The change in moment arm length, relative to the simulation with 15% compression and in the neutral posture, for each simulation versus the quantified ultimate shear failure tolerances for the identical test conditions in Chapter 3. Black, white, and gray symbols represent simulations/*in vitro* tests conducted in extended, neutral, and flexed postures respectively. Diamonds, circles, squares, and triangles represent simulations/*in vitro* tests conducted under 15%, 30%, 45%, and 60% compressive force respectively. Error bars represent the standard error of the mean ultimate shear failure tolerance calculated in Chapter 3. .... 189

Figure 7.1 – Conceptual model for modulation of vertebral injury potential as a result of shear loading. The model consists of four primary factors that were addressed by the respectively shown chapters. Each of the primary factors has the potential to interact with any or all of the other three primary factors. The possibilities for some of these interactions were investigated within this thesis and are shown here. The dashed arrow indicates that Chapter 6 addressed the interaction between physical characteristics of the vertebra and the influence of compressive force on facet interaction. .... 210

## LIST OF TABLES

Table 2.1 – Comparison of morphology and structural properties between human lumbar and porcine cervical specimens. The asterisk indicates that all ranges of motion are based on pure moment loading with $\pm 2 - 2.5$ Nm applied to the specimen. ....	14
Table 2.2 - Strain in ligaments surrounding the L4-L5 human lumbar joint as a function of flexion/extension posture with 0 mm of shear (S), 25 mm of shear (E) and the change ( $C = E - S$ ) in strain from 0 mm shear to 25 mm of shear. Elongation is presented as positive strain while shortening is presented as negative strain. Positive values indicating elongation from the ligament lengths determined with 0 mm shear and in neutral posture are highlighted in grey. ALL = Anterior Longitudinal Ligament; PLL = Posterior Longitudinal Ligament; LF = Ligamentum Flavum; IT = Inter-transverse Ligament; ISP1-3 = Interspinous Ligament Sections 1-3; LC = Lateral Capsular Ligament; MC = Medial Capsular Ligament; SS = Supraspinous Ligament. ....	26
Table 2.3 – Changes in rotational motion accompanied by changes in the modulus of elasticity for the intervertebral disc and ligaments of a cervical FE model. (Data from this table are taken from Kumaresan et al., 1999) .....	49
Table 2.4 – Changes in the elastic modulus for bone altered the finite element model stiffness while subsequent changes in the yield strength led to changes in finite element model strength. Alterations to the Poisson ratio had a minimal effect on each of the stiffness and strength of the finite element model. (Data from this table are taken from Jones and Wilcox, 2007) .....	50
Table 3.1 – Characteristics of specimens assigned to each compressive load group for acute shear failure. Standard error of each mean is presented in parentheses. Asterisks indicate measures that contain statistically significant differences between the compressive load magnitudes. Means within a single measure and with the same letter are statistically similar. ....	69
Table 3.2 – Characteristics of specimens assigned to each posture group for acute shear failure. Standard error of each mean is presented in parentheses. Asterisks indicate measures that contain statistically significant differences between the compressive load magnitudes. Means within a single measure and with the same letter are statistically similar. ....	70
Table 3.3 – Ultimate force, displacement and energy stored during acute shear failure for specimens from each vertebral level. Standard error of each mean is presented in parentheses. Asterisks indicate a statistical difference between means for a single measure. ....	71

Table 3.4 – Measures of the elastic limit, initial and ultimate acute shear failure loads for each compressive load group. Standard error of each mean is presented in parentheses. Means within a single measure and with the same letter are statistically similar.....	72
Table 3.5 – Post-failure observations of tissue damage arranged within vertebral level, compressive load, posture and overall. Values are reported as a percentage of all specimens in each group. ....	82
Table 4.1 – Morphological measurements, and the respective measurement device/source, for each specimen. ....	94
Table 4.2 – Ultimate failure tolerance, bone density and morphological measurements made for specimens assigned to each of the model generation and testing groups. Standard error of the mean is presented in parentheses. ....	110
Table 4.3 – Measured height and width of the pedicle and lamina, as well as the pars interarticularis length for specimens assigned to each of the model generation and testing groups. Standard error of the mean is presented in parentheses. ....	111
Table 4.4 – Ultimate failure tolerance, bone density and morphological measurements made for specimens from each vertebral level. Standard error of the mean is presented in parentheses. Measurements that achieved statistical significance between vertebral levels have their <i>p</i> -values reported in a bold font. ....	112
Table 4.5 – Measured height and width of the pedicle and lamina, as well as the pars interarticularis length for individual (C3, C4, C5, and C6) vertebrae. Standard error of the mean is presented in parentheses. Statistically significant differences between vertebral levels are shown below each measure in a bold font. Statistically significant differences between caudal and cranial vertebrae are shown to the right in a bold font. The asterisk indicates that a significant interaction between individual vertebrae occurred for the lamina width. Means with the same letter (for lamina width) are statistically similar. ..	113
Table 4.6 – Post-failure observations of tissue damage arranged within vertebral level, model group and overall. Values are reported as a percentage of all specimens in each group. Percentages within a single block of vertebral level or model group since a specimen may have multiple injuries following acute shear failure testing. ....	115
Table 4.7 – Factors, coefficient estimates and explained variance for each model developed by the stepwise linear regression analysis. The final equation for calculating ultimate shear failure tolerance has the form $F = aX_1 + bX_2 + cX_3 + I$ . The standardized estimate illustrates the relative importance of each variable in each mathematical model (i.e. a higher standardized estimate indicates that changing the value of the parameter's corresponding variable creates a larger change in calculated ultimate shear failure tolerance).....	117

Table 5.1 – Morphological measurements and the resulting calculated ultimate shear failure tolerance for specimens from each vertebral level. An asterisk indicates a statistically significant difference between vertebral levels. ....	142
Table 5.2 – Morphological measurements and the resulting calculated ultimate shear failure tolerance for specimens assigned to each shear loading magnitude. An asterisk indicates a statistically significant effect of loading magnitudes. Means with the same letter are statistically similar. ....	143
Table 5.3 – Observed tissue damage for specimens that did not survive the entire repetitive shear loading duration of 21,600 cycles. ....	144
Table 6.1 – Estimates of the elastic modulus for the entire intervertebral disc using compressive forces, disc area, disc height changes from Chapter 3 (shown with a superscript ‘a’), and an average height for the unloaded porcine cervical intervertebral disc reported by Yates (2009) (shown with a superscript ‘b’). ....	168
Table 6.2 – The number of nodes, elements, the magnitude of stress at the location of peak stress within the pars interarticularis and the percent change in stress between each of the three meshes constructed to identify convergence. ....	170
Table 6.3 – Comparison of simulated reaction forces and the 95% confidence interval of measured shear forces, from comparable <i>in vitro</i> tests conducted in Chapter 3, following 3 mm of posterior shear displacement of an FSUs caudal vertebra. ....	177
Table 6.4 – Shear displacement applied prior to initial facet contact for the left and right facets and for each simulation condition. ....	179
Table 6.5 – Center of facet contact force location at the end of each simulation for both left and right facets. The center of force location for the 0% compression and neutral posture served as the reference location for all other simulations. Values reported in this table are derived from the non-deformed nodal coordinates of nodes that were in contact at the end of each simulation. This ensures that the location for the center of facet contact force shown in this table is presented in the same context for each simulation. Anterior, upward, and medial migrations are given by positive values while posterior, downward and lateral migrations are given by negative values. ....	182
Table 6.6 – Magnitude of stress, moment arm length, and the number of contacting nodes for the identical strain of each posture within a single compressive load. ....	187
Table 7.1 – Comparison of morphology and structural properties between human lumbar and porcine cervical specimens from previous studies as well as this thesis. The asterisk indicates that all ranges of motion are based on pure moment loading with $\pm 2 - 2.5$ Nm applied to the specimen. ....	214



# **CHAPTER 1**

## **INTRODUCTION**

## 1.1 GENERAL INTRODUCTION

Typically, the risk of injury for an individual while performing a job is defined by examining three criteria: force, repetition and posture. Guidelines for risk of low back injury have been well established for both compressive as well as shear loading. The influence of compressive loading has been studied extensively, and the *in vitro* relationship between compressive loading and low back injury has been well documented under a variety of acute (Oxland et al., 1991; Gunning et al., 2001) and repetitive loading scenarios (Smeathers and Joanes, 1988; Parkinson and Callaghan 2007b; Parkinson and Callaghan 2008) as well as loading and posture combinations (Gunning et al., 2001).

The effects that shear loading and individual modifying factors such as flexion/extension posture or compressive load have on the incidence of tissue failure from shear loading have been studied independently (Dunlop et al., 1994; Cripton et al., 1995; Yingling and McGill, 1999; van Dieën et al. 2006). However, a series of investigations on the factors that may modulate shear failure tolerances of functional spinal unit (FSU) *in vitro* under acute and repetitive loading protocols has not been undertaken.

Peak shear loading was identified as one of four primary risk factors correlated with the likelihood of reporting low back pain in automobile assembly workers (Norman et al., 1998). Furthermore, it has been suggested that shear stress is an important variable in mechanical failure of the lumbar spine (Gracovetsky et al., 1981).

Agreement exists that osteoligamentous resistance to anteriorly directed shear applied to the cranial vertebra of a vertebral joint in the neutral posture is primarily provided by the interaction between the inferior facets of the cephalad vertebra and the

superior of the caudal vertebra and the intervertebral disc. Debate still exists regarding the relative importance of each tissue towards resisting shear loading. Yingling and McGill (1999) claimed that the intervertebral disc resisted upwards of 77% of the externally applied shear load. Meanwhile, Lu and colleagues (2005) demonstrated that removal of the posterior elements (i.e. leaving the disc as the only structure to resist shear loads) resulted in a 78% decrease in FSU stiffness while transection of the intervertebral disc led to a 23% decrease in FSU stiffness. Based upon these results, the authors concluded that the posterior elements were more efficient for resisting shear. Force applied in a posterior direction perpendicular to the superior facet's surface of an isolated human lumbar vertebra leads to fractures of the pars interarticularis or the pedicle (Cyron et al., 1976). Furthermore, repetitive loading in the same manner as Cyron and colleagues (1976) also leads to fracture of the pars interarticularis of the isolated human lumbar vertebra (Cyron and Hutton, 1978) and human FSUs (Beadon et al., 2008).

The response of the FSU to externally applied loads is influenced by the load rate, postural orientation and morphological characteristics of the vertebrae comprising the FSU. Examples of such modulating factors in the case of externally applied shear loading are applied compressive loads as well as alterations in the FSU's flexion/extension posture. Applied compressive load decreases the height of the intervertebral disc, which will subsequently alter the contact area between the articulating facets of the FSU during applied shear loading (Dunlop et al., 1984). Applied compressive load has also been shown to increase the FSU stiffness in all six of the rotational and translational degrees of freedom for a single joint (Gardner-Morse and Stokes, 2003). Furthermore, facet

articulation area decreases from an extended posture to flexed postures that alter the role of the facet joints for bearing loads (Dunlop et al., 1984).

Adams and colleagues (Adams et al., 2002) provide an example of the interdependence between shear loading and the modulating factors of compression and posture. Consider a person whose trunk is partially flexed (Figure 1.1A).

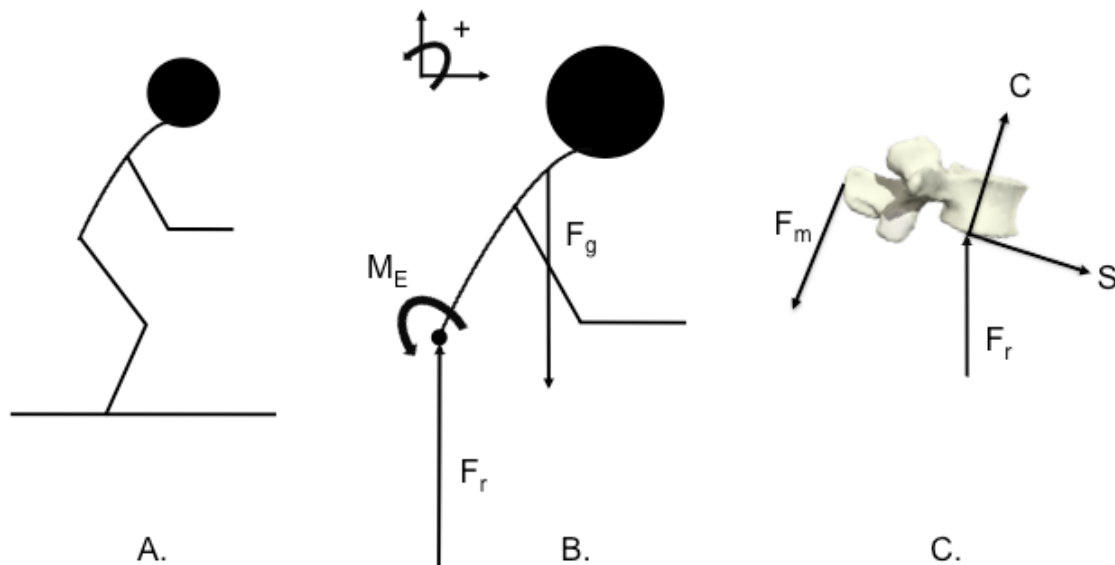


Figure 1.1 – A hypothetical scenario of a person whose trunk is partially flexed (A). The gravitational force from the mass of the trunk (above the L4-L5 point), arms and head is the only external force ( $F_g$ ) acting on the body above L4-L5 (B). This force creates a flexion moment that must be counteracted by an equal and oppositely directed extensor moment generated by muscular force that imposes additional vertebral joint compression (C). The labels C and S (C.) respectively refer to the L4-L5 vertebral joint compressive and shear axes.

The gravitational force acting downwards on the upper body's center of mass requires an upward reaction force and an extensor moment at the L4-L5 joint to maintain static equilibrium (Figure 1.1B). The extensor moment is generated by muscle forces within the low-back extensor musculature (Figure 1.1C). In a neutral posture, the low-back extensor muscles have a line of action that would counteract shear forces. Spine

flexion causes the low-back extensor muscle line of action to become more aligned with the compressive axis (McGill et al., 2000). Therefore, extensor muscular force required to counteract the moment generated by the gravitational force acting on the mass of the upper body also increases the L4-L5 joint compression. This example illustrates how shear force, vertebral joint compression, and vertebral flexion/extension posture can be related.

Studying flexion/extension posture and applied compression, independent of one another, is not the most desirable means for determining the influence that each of these factors has on the mechanical response of the FSU under applied shear loading. Instead flexion/extension posture and applied compressive load must be considered together in order to elucidate their combined effects on failure tolerances and load distributions within the vertebral joint under externally applied shear loading. Once the macroscopic mechanical response of the FSU to externally applied shear loading has been thoroughly investigated and injuries resulting from destructive testing have been documented, it is important to determine the internal tissue stress and strain, through appropriate models, that occurs during the *in vitro* tests. Linking the documented damage of the FSU during *in vitro* testing to internal tissue stress and strain may assist in describing injury mechanisms for tissues of the low back.

## 1.2 THESIS QUESTIONS AND OBJECTIVES

The global purpose of the thesis is to develop a framework for understanding how failure properties of the porcine FSU under acute and repetitive shear loading are modulated. Specifically, the thesis will investigate 5 questions:

1. How does the combination of compressive load and flexion/extension posture influence the ability of the porcine FSU to resist external acute shear loads?
2. How does bone density through the pars interarticularis and vertebral morphology affect ultimate shear failure of the porcine FSU and can these factors be used to determine ultimate shear failure tolerances without loading?
3. How does the magnitude of repeatedly applied external shear load influence failure of the porcine FSU and the cumulative load sustained prior to failure?
4. How do altered flexion/extension postures and compressive force modulate stress within the pars interarticularis?
5. How do the model results help explain results and hypotheses derived from the comparable *in vitro* work in Question #1?

A series of four focused studies will be performed in an attempt to answer the questions that are listed above (Figure 1.2).

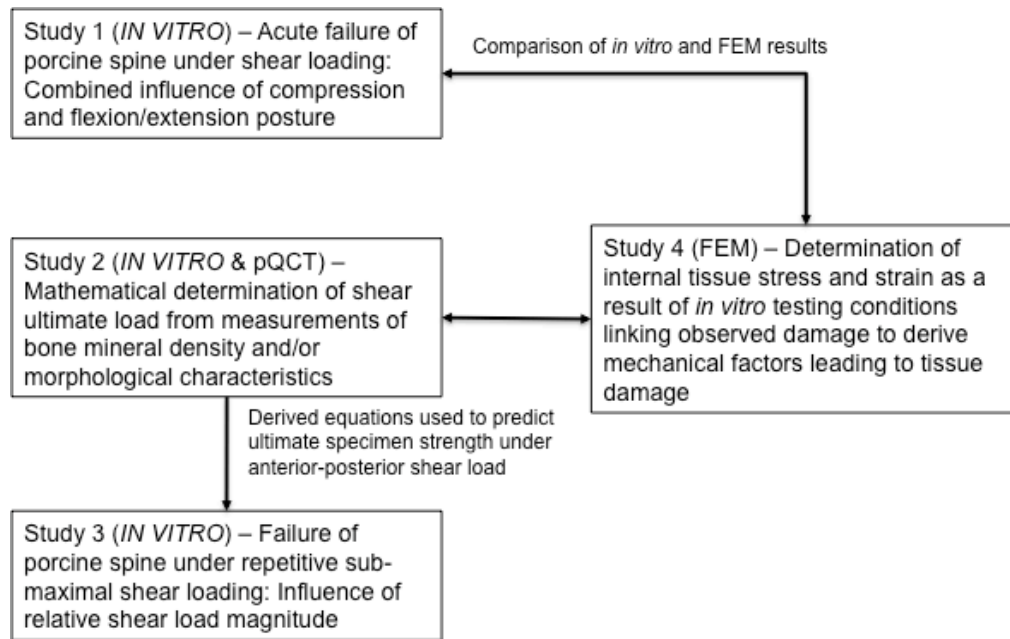


Figure 1.2 – Flowchart outlining the logical connections and titles of the studies for this thesis.

### 1.3 THESIS HYPOTHESES

The general hypothesis for this thesis is that the mechanical response of the FSU under shear loading will be influenced by a combination of flexion/extension postures, compressive loads, bone density, vertebral morphology, and the submaximal loading magnitude (for repetitive loading scenarios). The following are the null hypotheses for the questions listed in Section 1.1.

1. Ultimate failure load and displacement of the porcine FSU as well as shear stiffness and energy stored until failure under acute external shear load will not be influenced by varying compressive loads or flexion/extension postures.

2. Combinations of bone mineral density and morphological factors of the posterior elements will not provide appropriate estimates of the ultimate failure load under shear loading.
3. The magnitude of external shear loading will not influence the cumulative shear load experienced by the porcine cervical FSU prior to failure.
4. Flexion/extension postures as well as compressive loads will not influence the internal stress developed at the pars interarticularis under shear loading.
5. Model results will not be related to any hypotheses derived from the comparable *in vitro* work performed in Study 1.



# **CHAPTER 2**

## **REVIEW OF LITERATURE**

## 2.1 BASIC ANATOMY OF THE HUMAN LUMBAR VERTEBRAL JOINT

A human, osteoligamentous, vertebral joint is comprised of two adjacent vertebrae, the intervertebral disc between them and a series of ligaments. Within the literature, an isolated vertebral joint has been called a functional spinal unit (FSU) (Oxland et al., 1991; Cripton et al. 1995; Parkinson et al., 2005). The defining bony features of a single human vertebra are the vertebral body, spinous process, transverse process, lamina, pedicle, accessory process as well as the superior and inferior facets (Figure 2.1).

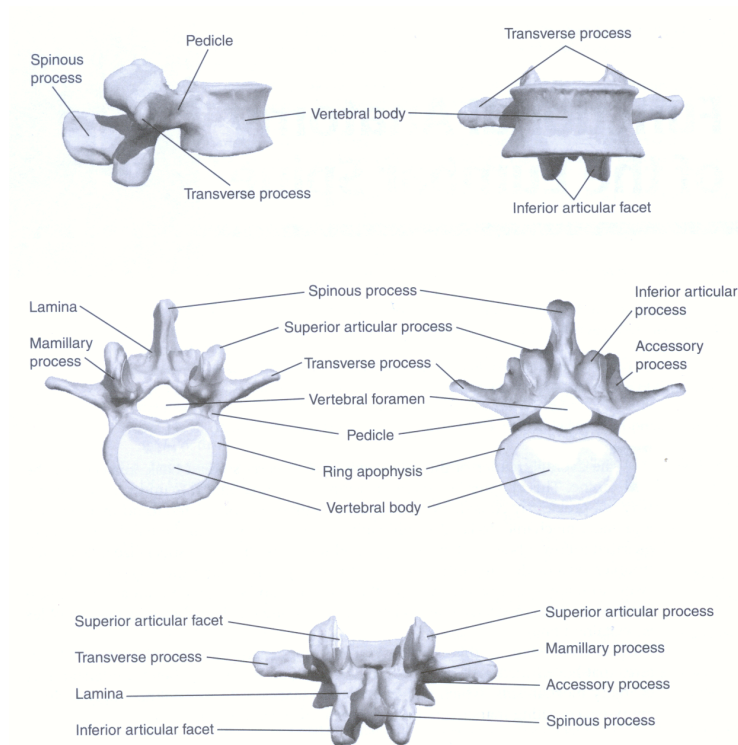


Figure 2.1 – Bony landmarks of a human lumbar vertebra. (Image taken from McGill, 2007).

Vertebrae are primarily composed from cancellous bone that is organized into a network of vertical and horizontal trabeculae. This cancellous bone is surrounded by a thin shell of cortical bone that bears between 34% of applied compressive load at the level of the endplate and 63% at the midtransverse plane of the vertebral body (Cao et al., 2001).

Junctions between adjacent vertebrae occur at the superior and inferior surfaces of the vertebral bodies as well as the surfaces of the superior and inferior facets. The superior and inferior surfaces of the vertebral body are covered with hyaline cartilage called the endplate (Adams et al., 2002). Endplates are the attachment location between the vertebral body and the intervertebral disc. The superior and inferior facet surfaces are also covered with articular cartilage (Adams et al., 2002). Junctions between the superior facets of the caudal vertebra and the inferior facets of the cephalad vertebra (facet joints) of an FSU are also surrounded by viscoelastic tissue creating a synovial joint capsule (Hukins and Meakin, 2000; Kalichman and Hunter 2007).

Ligaments also provide connections between adjacent vertebrae in the osteoligamentous FSU. The complete set of ligaments for an FSU are the anterior longitudinal ligament, posterior longitudinal ligament, ligamentum flavum, interspinous ligament, supraspinous ligament and the intertransverse ligament (Figure 2.2).

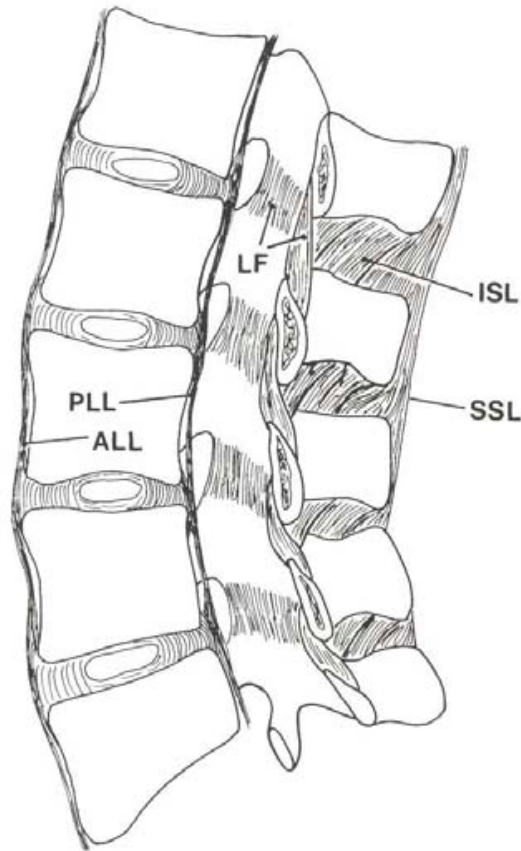


Figure 2.2 – Ligaments of the lumbar spine. SSL = Supraspinous ligament, ISL = Interspinous ligament, LF = Ligamentum flavum, PLL = Posterior longitudinal ligament, ALL = Anterior longitudinal ligament. (Image taken from Adams et al., 2002)

The composition for each of these structures (intervertebral disc, facets and ligaments) is discussed in sections 2.3.1, 2.3.2 and 2.3.3 along with the innervation (sensory) of these structures and their specific roles in resisting shear loads applied to the osteoligamentous FSU.

## **2.2 USE OF THE PORCINE CERVICAL SPINE AS A SURROGATE FOR THE HUMAN LUMBAR SPINE**

Human FSU's used for *in vitro* structural testing are typically acquired from older cadavers with variable specimen age, lifetime exposure to load, modes of death and

degrees of tissue degradation (Yingling et al., 1999). Controlling potential confounding factors such as FSU age and load exposure prior to death as well as the means by which death occurs may help improve inter-specimen homogeneity for *in vitro* testing (Smit, 2002; Schmidt et al., 2005). Animal FSU models have been used as a surrogate for human FSU's in an attempt to control some of these confounding factors (Yingling et al., 1999). Selection of a feasible animal model that properly mimics the response of human specimens is necessary to enhance the link between results derived from *in vitro* testing using an animal model and human tissue properties and further linking these results to potential injury mechanisms (Alini et al., 2008).

The porcine cervical spine is morphologically similar to the human lumbar spine. Endplate width and depth of the porcine cervical spine are smaller than the human lumbar spine specimens (Yingling et al., 1999) (Table 2.1). These differences in endplate dimensions have been shown to produce a discrepancy of approximately 500 mm<sup>2</sup> in endplate area between porcine cervical and human lumbar specimens (Yingling et al., 1999). Porcine cervical specimens have also been shown to have a smaller pars interarticularis (Yingling et al., 1999). The facet orientation of the porcine cervical spine has been qualitatively documented to be similar to the human lumbar spine (Oxland et al., 1991) (Table 2.1).

Smit (2002) stated that trabecular architecture of the porcine vertebral bodies is predominantly vertically oriented which is similar to the trabecular architecture of human vertebral bodies. It has been suggested that the similarity in cancellous bone structure and the bone mineral density of the porcine specimens is a function of the rooting behaviour

and compressive loads imposed upon the cervical spine for supporting the cantilevered head of a quadruped (Yingling et al., 1999; Smit, 2002).

Table 2.1 – Comparison of morphology and structural properties between human lumbar and porcine cervical specimens. The asterisk indicates that all ranges of motion are based on pure moment loading with  $\pm 2 - 2.5$  Nm applied to the specimen.

Measurement	Human Lumbar	Porcine Cervical
Upper Endplate Depth (mm)	32.7 – 34.7 <sup>1</sup>	22.28 <sup>1</sup>
Lower Endplate Depth (mm)	33.9 – 34.9 <sup>1</sup>	22.53 <sup>1</sup>
Pedicle Width (mm)	6.9 – 16.2 <sup>1-3</sup>	8.67 – 8.91 <sup>1</sup>
Pars Interarticularis Height (mm)	44.8 – 49.1 <sup>1</sup>	28.81 – 29.34 <sup>1</sup>
Pars Interarticularis Width (mm)	N/A	8.35 – 8.48 <sup>1</sup>
Sagittal Facet Angle (degrees)	40.88 – 62.3 <sup>1,4,5</sup>	44.5 – 48.5 <sup>1,11</sup>
Transverse Facet Angle (degrees)	87.2 – 90 <sup>1</sup>	81.2 – 81.7 <sup>1</sup>
Spinal Canal Depth (mm)	12.1 – 18.1 <sup>1,2</sup>	9.78 <sup>1</sup>
Spinal Canal Width (mm)	16.1 – 17.1 <sup>1,2</sup>	17.92 <sup>1</sup>
Flexion/Extension Range of Motion* (degrees)	3 – 8 <sup>6-9</sup>	22.4 – 23.9 <sup>12,13</sup>
Lateral Bend Range of Motion* (degrees)	4.5 – 6.9 <sup>6-9</sup>	27 – 35.2 <sup>12,13</sup>
Axial Rotation Range of Motion* (degrees)	1 – 2 <sup>6-9</sup>	4.5 – 8.5 <sup>12,13</sup>
Anterior Shear Stiffness (N/mm)	155 <sup>10</sup>	139 – 212 <sup>1,11</sup>
Ultimate Anterior Shear Force (N)	1710 – 2894 <sup>10</sup>	1980 – 3538 <sup>1,11</sup>
Ultimate Anterior Shear Displacement (mm)	13 <sup>10</sup>	10 – 18 <sup>11,14</sup>

1. Yingling et al., 1999.

2. Zhou et al., 2000.

3. McLain et al., 2004.

4. Masharawi et al., 2004.

5. Panjabi et al., 1993

6. Kettler et al., 2007.

7. Oxland and Panjabi, 1992.

8. Panjabi et al., 1994.

9. Busscher et al., 2010.

10. Cripton et al., 1995.

11. Gallagher et al., 2010.

12. Schmidt et al., 2005.

13. Goertzen et al., 2004.

14. Yingling and McGill, 1999.

The porcine cervical spine can withstand similar dynamic compressive load as the human lumbar spine (Yingling et al., 1997; Yingling et al., 1999). Likewise, Yingling and colleagues (1999) found close agreement between the acute failure loads of porcine cervical and human lumbar specimens under applied shear loading (Table 2.1).

## **2.3 COMPONENTS OF THE FUNCTIONAL SPINAL UNIT THAT RESIST SHEAR**

### **2.3.1 Intervertebral disc**

#### *2.3.1.1 Structure and composition of the intervertebral disc*

Each intervertebral disc of the human lumbar spine is approximately 10 mm thick (Adams et al., 2002). The intervertebral disc is a structure of three components; annulus fibrosus, nucleus pulposus and the endplates. The nucleus pulposus is contained within the innermost layer of the annulus fibrosus while the endplates provide the superior and inferior boundaries of the intervertebral disc (Figure 2.3).

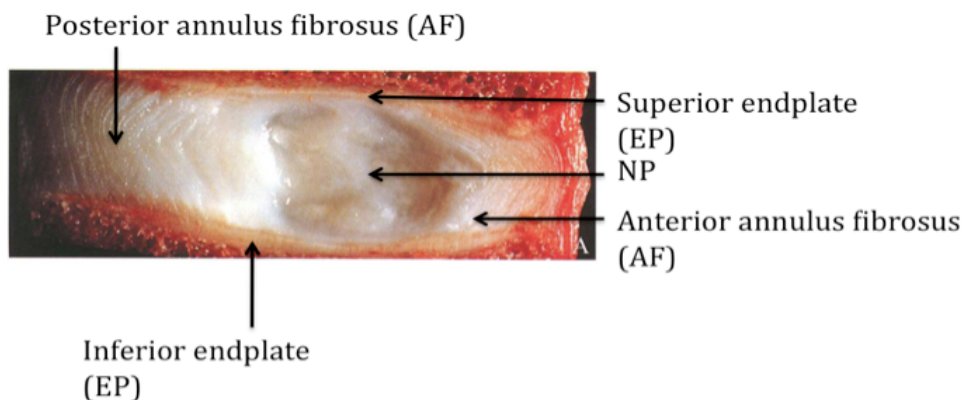
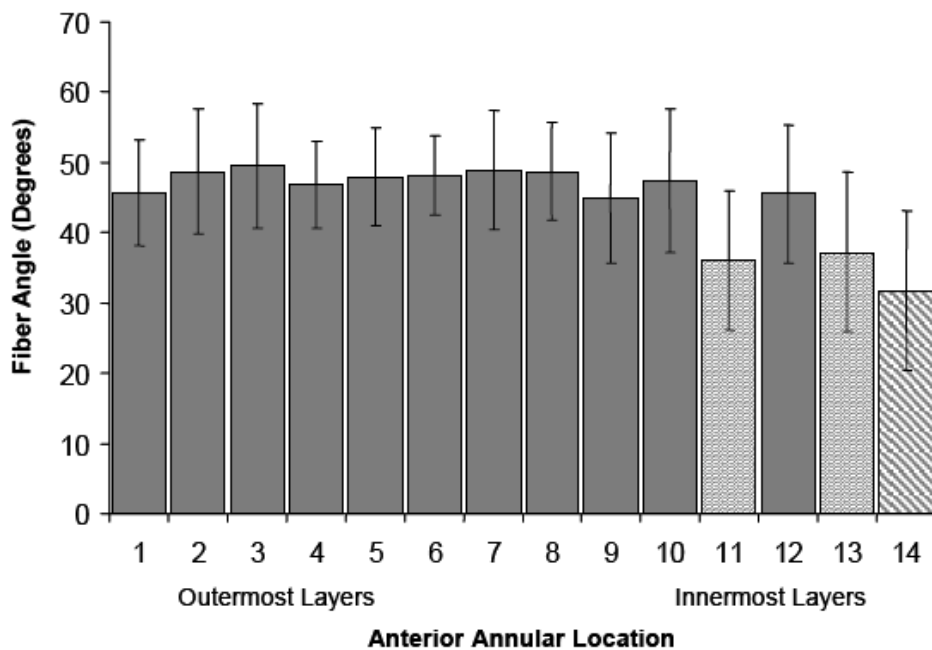


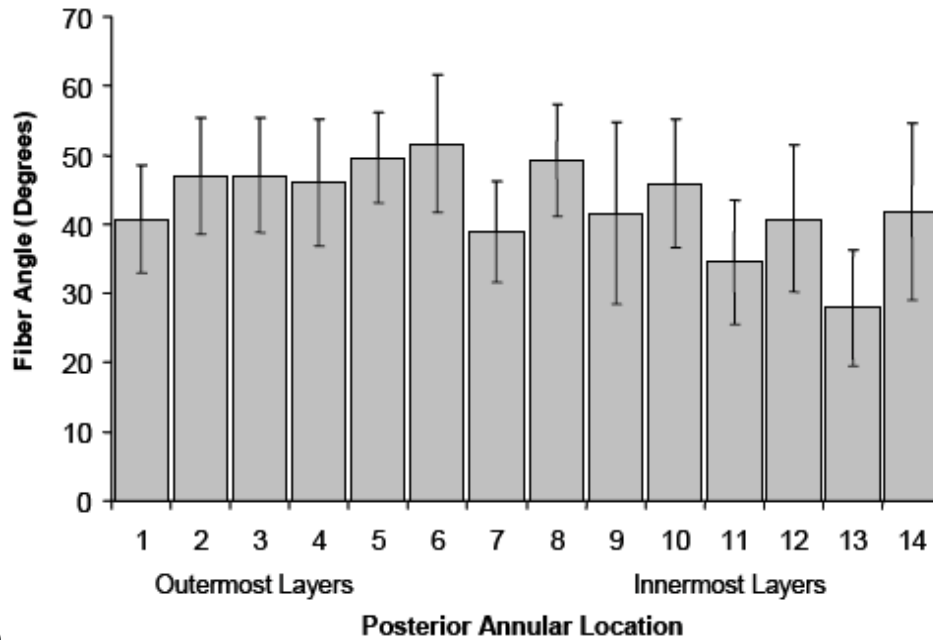
Figure 2.3 – Sagittal section showing the nucleus pulposus (NP), anterior and posterior portions of the annulus fibrosus (AF) and the superior and inferior endplates (EP). (Image taken from Adams et al., 2002)

The annulus of the human and porcine intervertebral disc is arranged into a series of 15-25 lamellar layers (Tampier, 2006). The inner layers of the annulus are composed primarily from type I collagen and proteoglycans while the outer layers of the annulus are composed primarily of type II collagen. Water constitutes 60-70% of the annulus weight in the human intervertebral disc which is due to the presence of proteoglycans within the inner lamellar layers (Bogduk & Twomey, 1991). The collagenous fibers of each lamellar layer for both porcine cervical and human lumbar intervertebral discs are oriented approximately 45-65 degrees from vertical (Figure 2.4 A-B) and the fibers between adjacent layers are oriented approximately 130 degrees relative to each other (Figure 2.4 C) (Cramer and Darby, 1995; Tampier, 2006).

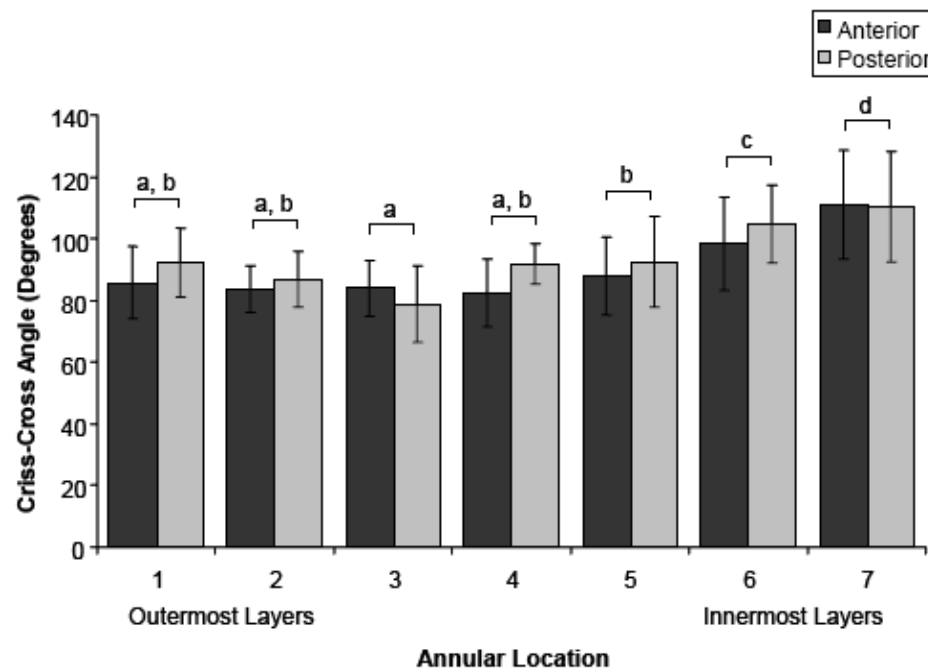


A.)





B.)



C.)

Figure 2.4 - Annular fiber angles for the anterior (A) and posterior (B) portions of the annulus fibrosus from the porcine cervical spine as well as the angle between adjacent lamellar layers (C). Angles for individual lamellar layers (A and B) are measured with respect to the vertical axis. (Images taken from Tampier, 2006)

For the porcine cervical intervertebral disc, the angle of the lamellar fibers has been shown to decrease from the outer layers to the inner layers and the angle between adjacent layers increases (Tampier, 2006).

The second structure that makes up the intervertebral disc is the nucleus pulposus. The nucleus has been modeled primarily as either an inviscid fluid or poroelastic solid (Belytschko et al., 1974; Argoubi and Shirazi-Adl, 1996). This is a function of the nucleus' composition which is primarily proteoglycans, which again contributes to the nucleus' high water content (70-90%) (Bogduk and Twomey, 1991).

Human vertebral endplates are approximately 1-3 mm thick (Cramer and Darby, 1995) and are composed of hyaline cartilage (Adams et al., 2002). The endplates contain channels that allow for fluid flow in and out of the disc (van der Veen et al., 2007).

#### *2.3.1.2 Innervation and sensory function of the intervertebral disc*

The human intervertebral disc has been cited as a potential source of low back pain (Adams et al., 2002). Nerve fibers are present in the outer third of the annulus that provide pain sensation as well as proprioceptive output (Bodguk et al., 1981).

#### *2.3.1.3 Mechanical properties of the intervertebral disc under external shear loading*

Markolf (1972) was one of the first researchers to investigate the mechanical properties of the isolated human intervertebral disc under applied shear loading. In this work, he demonstrated that the force-displacement relationship, under applied shear loading, of the middle vertebra from a human thoracolumbar specimen of three vertebrae and the two intervening intervertebral discs was approximately linear. Recent literature is

divided on the relative importance of the intervertebral disc for resisting shear loads. Yingling and McGill (1999) showed that the intervertebral disc of the porcine cervical FSU carried 62.5% of the ultimate failure shear load. Conversely, transsection of the intervertebral disc in human lumbar FSUs produced a 22% reduction in FSU stiffness while sectioning of the posterior elements through the pedicles, independent of disc transection, resulted in a 78% reduction in FSU stiffness (Lu et al., 2005). Removal of the posterior elements has been shown to reduce the time to failure by approximately 87% compared to intact porcine thoracolumbar specimens under repeated external shear loading of the porcine lumbar FSU (van Dieën et al., 2006). However, no comparison of the time to failure was made between intact specimens, specimens that had their posterior elements removed, and specimens that had their disc transected with posterior elements left intact. These authors also concluded that flexed postures did not alter the time to failure of porcine thoracolumbar specimens under repeated external shear loading with a single static compressive load of 1600 N. This investigation did not test the role of shear load magnitude on the time to failure of their porcine specimens, nor did they investigate the effects of varying the compressive load as well as flexion/extension posture on the acute anterior-posterior ultimate shear load.

### **2.3.2 Facet joints**

#### *2.3.2.1 Structure of facets and facet joints*

The superior facets of the caudal vertebra and the inferior facets of the cephalad vertebra provides surfaces of interaction between vertebrae of an FSU. The joint between

these facets is called a facet joint, apophyseal joint or zygapophyseal joint. Facet joints will be the terminology used for the remainder of this document. For the purposes of this review and the remainder of this document, the distinction will be made between the facets and the facet joints.

The facets of the human lumbar spine are oriented vertically while the inferior facets maintain a medial facing direction and the superior facets have a lateral facing direction (Figure 2.5) (Taylor and Twomey, 1986).

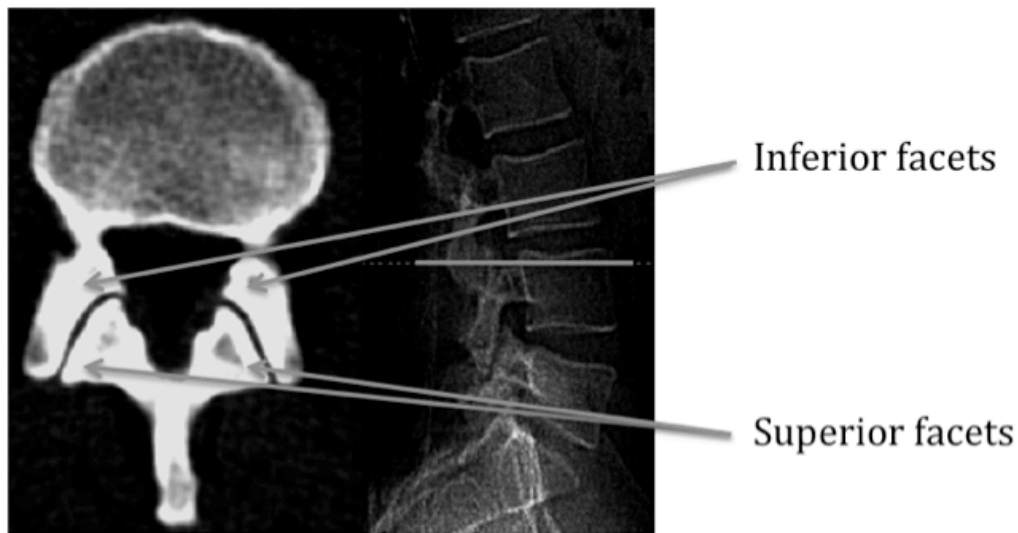


Figure 2.5 – Transverse MRI slice through the L4 vertebra of the human lumbar spine. The image on the left shows the lateral and anterior facing orientation of the inferior facets from L3 and the medial and posterior facing orientation of the superior facets from L4. (Image taken from Kalichman and Hunter, 2007)

The facets of the human lumbar spine become more aligned with the sagittal plane from cephalad (L1) to caudal (L5) (Panjabi et al., 1993). Likewise, the estimated facet surface area for human lumbar vertebrae increases in the same direction with the superior and inferior facets that make up a single facet joint (for example, the superior facets of L4 and the inferior facets of L3) having a similar estimated surface area (Panjabi

et al., 1993). Human lumbar superior facets are comprised of cancellous bone whose trabecular orientation has been shown to be similar to a plate-like structure (i.e. in the transverse plane) that has been associated, according to Wolff's Law, with the primary loading direction of the facet joints (Drews et al., 2008). The trabecular density of the human L2 superior facets has also been shown to be smaller than the trabecular density of the human S1 superior facets and has been attributed to higher axial strain of the superior facets for the S1 vertebra than the L2 vertebra (Drews et al., 2008).

A thin layer of hyaline articular cartilage covers the surface of each facet (Bogduk and Twomey, 1991; Cramer and Darby, 1995). The facet joint has been described as a true synovial joint containing menisci, synovial fluid and an articular capsule (Bogduk and Engel, 1984; Hukins and Meakin, 2000; Kalichman and Hunter, 2007). The articular capsule is bounded laterally by the ligamentum flavum and medially by an extension of the articular cartilage (Cramer and Darby, 1995). The primary function of the menisci is to create a space between the articulating facets of the facet joint and they have been implicated in the production of low back pain (Figure 2.6) (Bogduk and Engel, 1984).

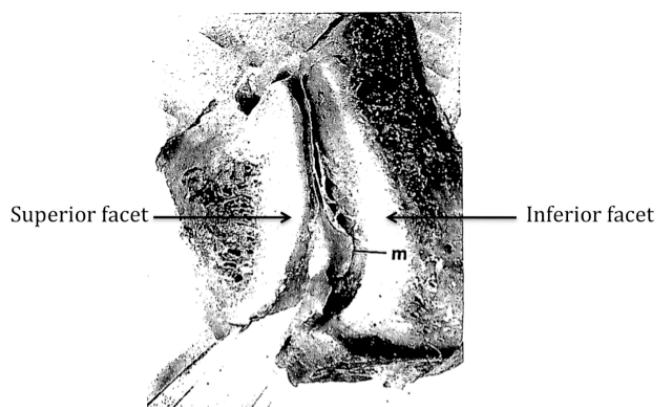


Figure 2.6 – Transverse image of a facet joint illustrating the two articulating facets being distracted by forceps to reveal the meniscus (m). (Image taken from Bogduk and Engel, 1984)

#### *2.3.2.2 Innervation of the facet capsule*

Facet joints have been cited as a potential source for low-back pain (Mooney and Robertson, 1976; Yang and King, 1984; Cavanaugh et al., 2006). Each facet joint of the human lumbar spine is innervated by the posterior rami at the joint's level (Cramer and Darby, 1995; Cohen and Raja, 2007). Histological analysis has shown that the human facet joint capsule contains Pacinian corpuscles, Ruffini and free nerve endings that suggests both nociceptive and proprioceptive functions of the facet innervations (Cavanaugh et al., 1996). Referred pain patterns have also been generated in humans by injection of hypertonic saline into the facet joint capsule (Mooney and Robertson, 1976). These pain patterns were observed to be indistinguishable from pain complaints that are often associated with discogenic pain (Mooney and Robertson, 1976).

Mechanical theories and data have been presented for how pain signals are generated from the facet joint capsule. Yang and King (1984) theorized that compression of the facet joint capsule causes contact between the tip of the inferior facet from the cephalad vertebra and the pars interarticularis of the caudal vertebra, in a lumbar vertebral joint. This causes backward rotation leading to stretching of the facet joint capsule that may be a mechanical basis for the generation of low back pain from the facets. Cavanaugh and colleagues (2006) demonstrated that the nociceptive neural discharge from the facets of anesthetized female goats indeed increases upon facet capsule stretching that partially confirms the hypothesis of Yang and King (1984).

### *2.3.2.3 Mechanical resistance of the facet joints to shear loading*

The orientation of the facets of the lumbar spine as well as the small distance between articulating facets enables the facets to resist anterior shear displacement of the cephalad vertebra relative to the caudal vertebra (Tencer and Mayer, 1983; Adams, 2002). The average ultimate failure loads of superior facets from human lumbar vertebrae under load applied perpendicularly to the facet surface and directed posteriorly, for slow (0.05 cm/s) and fast (5 cm/s) rates of displacement were 1860 N and 1480 N respectively (Cyron et al., 1976). This is similar to documented acute shear failure loads of human lumbar FSU's (Cripton et al., 1995), porcine cervical (Yingling and McGill, 1999) and porcine thoracolumbar osteoligamentous FSU's in a neutral posture (van Dieën et al., 2006). Loading of the superior facet, perpendicularly to the facet surface and directed posteriorly leads to spondylitic fracture of the pars interarticularis in isolated human lumbar vertebrae (Cyron et al., 1976; Cyron, 1978).

Markolf (1972) studied the force-displacement characteristics of multisegmental human lumbar specimens with three vertebrae and two intervening discs under shear loading with the posterior elements removed. Their rationale for removing the posterior elements was that a previous investigation (Hirsch and Nachemson, 1954) had deemed them to be unimportant for resisting applied compressive load. Recently, Lu and colleagues (2005) showed that human lumbar FSU stiffness under shear loading decreased by 78% when the posterior elements were removed compared to a 22% reduction in stiffness when the intervertebral disc had been transected. Likewise, van Dieën et al. (2006) have shown that porcine thoracolumbar specimens failed approximately 87% sooner with repeated shear loading when the posterior elements had

been removed. Due to the contact that occurs between the facets in shear loading, disc strain using a finite element model of the human lumbar vertebral joint was found to be approximately 50% relative to the disc strain under posterior-shear loading (Tencer and Mayer, 1983). The results from this finite element model also showed that anterior displacement of the cephalad vertebra under the same 90 N of shear load increased the displacement, which suggests that the facets act as a mechanical stop for the vertebrae under shear loading.

### **2.3.3 Ligaments**

#### *2.3.3.1 Structure and composition of ligaments*

The majority of ligaments in the human lumbar spine are composed of collagen fibers (Hukins and Meakin, 2000). Microscopic investigation of collagen fiber arrangements in the interspinous and supraspinous ligaments demonstrate a crimped pattern that is consistent with ligaments of other joints such as the anterior cruciate ligament of the knee (Yahia et al., 1990). Typically, ligaments surrounding the lumbar spine (the specific ligaments are listed in section 2.1) are able to resist motion only when elongated from their resting length. The sole exception to the previous statement is the ligamentum flavum that contains primarily elastin fibers (Yahia et al., 1990).

#### *2.3.3.2 Innervation and sensory function of ligaments*

Investigators have documented the presence of free nerve endings in the human anterior and posterior longitudinal ligaments along with a lack of nerve endings in the



interspinous and supraspinous ligaments as well as the ligamentum flavum (Jackson et al., 1966). However, these investigators were unable to document the specific role of these free nerve endings within the ligaments. More recently, Cavanaugh and colleagues (1997) have suggested that the nociceptive nerve endings of the ligaments in New Zealand white rabbits are mechanosensitive or chemosensitive which signal for low-back pain.

#### *2.3.3.3 Mechanical properties of ligaments under shear loading*

Due to their crimped structural nature, ligaments will only resist motion of the bones to which they attach after having been elongated outside their toe region (Mycklebust et al., 1988). In vivo, elongation of ligaments occurs by changing the relative orientation and/or position of vertebrae. Modeled attachment locations for the ligaments surrounding the human L4-L5 vertebral joint (Cholewicki and McGill, 1996) indicate that elongation of the ligaments rarely occur when L4 is displaced anteriorly relative to L5, in the model's initial and neutral (zero degrees of flexion/extension, lateral bend and axial twist) configuration, along the L4-L5 joint shear axis (Table 2.2).

Table 2.2 - Strain in ligaments surrounding the L4-L5 human lumbar joint as a function of flexion/extension posture with 0 mm of shear (S), 25 mm of shear (E) and the change (C = E - S) in strain from 0 mm shear to 25 mm of shear. Elongation is presented as positive strain while shortening is presented as negative strain. Positive values indicating elongation from the ligament lengths determined with 0 mm shear and in neutral posture are highlighted in grey. ALL = Anterior Longitudinal Ligament; PLL = Posterior Longitudinal Ligament; LF = Ligamentum Flavum; IT = Inter-transverse Ligament; ISP1-3 = Interspinous Ligament Sections 1-3; LC = Lateral Capsular Ligament; MC = Medial Capsular Ligament; SS = Supraspinous Ligament.

	NEUTRAL			FLEXED			EXTENDED		
	S	E	C	S	E	C	S	E	C
<b>ALL</b>	0	-0.17	-0.17	-10.59	-10.61	-0.02	4.76	4.77	0.01
<b>PLL</b>	0	-0.91	-0.91	14.12	14.07	-0.06	-8.69	-8.69	0.00
<b>LF</b>	0	-0.86	-0.86	25.66	25.62	-0.04	-14.40	-14.39	0.01
<b>IT</b>	0	-1.49	-1.49	15.69	15.63	-0.06	-10.21	-10.26	-0.05
<b>ISP1</b>	0	-9.55	-9.55	53.58	53.29	-0.29	-34.03	-34.48	-0.45
<b>ISP2</b>	0	-11.65	-11.65	25.92	25.54	-0.38	-21.06	-21.55	-0.49
<b>ISP3</b>	0	-9.53	-9.53	7.38	7.03	-0.35	-11.50	-11.88	-0.38
<b>LC</b>	0	-15.72	-15.72	19.44	18.97	-0.47	-26.46	-27.15	-0.69
<b>MC</b>	0	3.08	3.08	27.97	28.15	0.18	8.82	9.01	0.19
<b>SS</b>	0	-1.46	-1.46	61.51	61.42	-0.08	-33.13	-33.14	0.00

This evidence, suggests that the spinal ligaments may not provide much resistance to shear loading while the vertebral joint is in a neutral posture. Moreover, serial transection of the ligaments surrounding the human FSU does not significantly influence the force-displacement relationship of the FSU under shear loading (Lee and Evans, 2000).

Nonetheless, ligaments have been shown to improve stability of the human lumbar spine and resist motion in flexed postures (Sharma et al., 1995). Sharma and colleagues (1995) also demonstrated, using a finite element model of the human L3-L4 vertebral joint that the presence of ligaments may alter the shear force-displacement relationship in a flexed posture.

## 2.4 MECHANICAL PROPERTIES OF THE SPINE UNDER EXTERNAL SHEAR LOAD

The typical mechanical variables of interest during *in vitro* testing of FSU's and isolated biological tissues are stiffness, ultimate failure load, ultimate failure displacement, stress, strain, energy to failure, strength, toughness and modulus of elasticity (Woo et al., 2000). Figure 2.7 demonstrates the hypothetical force-displacement relationship for a structure (a.) as well as stress-strain (b.) relationship of a hypothetical material. The figures illustrate each of the structural and/or material properties that have been previously listed.

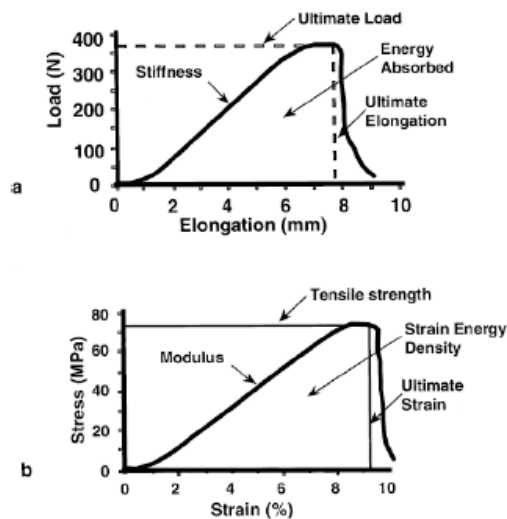


Figure 2.7 – Hypothetical load-elongation (a) and stress-strain (b) curves with characteristic features. The curves are derived from tensile loading of ligaments, the definition of the structural properties attained from each of these curves is consistent with all *in vitro* material and structural testing. (Image taken from Woo et al., 2000)

The following sections describe, and outline the specific consequences that three factors (rates of load and/or displacement, compressive loads and flexion/extension postures) have on altering the mechanical response of biological tissues and FSUs *in vitro*.

#### **2.4.1 Effect of load and or displacement rate on mechanical properties of biological tissues and FSU's**

The dependence of a material or structure on loading or displacement rate is defined as viscoelasticity. Given the description from section 2.1, the osteoligamentous FSU contains bone, ligaments, cartilage and a collagenous intervertebral disc that each has their own specific responses to different loading and displacement or stress and strain rates. Human cancellous bone has demonstrated higher modulus of elasticity, ultimate stress and less plastic deformation with increasing compressive load rates (McElhaney, 1966). A viscoelastic model of the anterior longitudinal ligament of the porcine spine has been applied to determine the effects of temperature on ligament compliance (Bass et al., 2007). The compressive stiffness of the human lumbar intervertebral disc also increases linearly with increasing compressive load rate (Kemper et al., 2007). Ultimate compressive failure load of human and porcine cervical FSU's increased (Hutton et al., 1979; Yingling et al., 1997) while ultimate vertical displacement decreased in porcine cervical FSU's with increases in compressive load rate (Yingling et al., 1997). Ochia and colleagues (2003) have demonstrated that the ultimate compressive failure load of both the human lumbar vertebral body and the vertebral endplates increases together with compressive load rate.

It has been suggested that the mode of tissue failure under higher loading rates may not be a consequence of tissue tolerances and instead could be due to altered load sharing at the higher loading rates (Ochia et al., 2003). The failure pattern of bone varies according to the compressive load rate (Nordin and Frankel, 2001). Shear loading at a rate of 10 810 N/s has been shown to cause fractures of the pars interarticularis as well as

avulsion of the endplate whereas slower shear loading rates have been shown to only create fractures of the pars interarticularis in porcine cervical specimens (Yingling and McGill, 1999). Recently, Drake and Callaghan (in press), using porcine cervical specimens, have shown that axial rotation at a rate of 10 degrees/s caused both facet and endplate fractures compared to only fractures of the facets under axial rotation at a rate of 2 degrees/s. Similarly, increasing compressive load rate between 100 N/s and 16 000 N/s has been shown to alter the mode of failure in porcine cervical FSU's from endplate fractures at low (100 N/s) loading rates to failure of the vertebral body higher (> 1000 N/s) loading rates (Yingling et al., 1997).

#### **2.4.2 Effect of compression on mechanical properties of FSU's**

*In vivo*, compressive loads are applied to the vertebral joints through loads applied externally to the body, loads due to the body mass above the vertebral joint of interest, the combined force resulting from muscle activation and elongation of passive tissues and inertial effects of the movement. Large compressive loads (2200 N and 4400 N) have been shown to increase the stiffness about each of the three rotational and in the three translational degrees of freedom of human lumbar FSU's (Janevic et al., 1991). Stokes and colleagues (2003) demonstrated that human lumbar FSU stiffness increases in a non-linear asymptotic manner, about each of the three rotational and in the three translational degrees of freedom with smaller compressive preloads (0 N, 200 N and 400 N). Likewise, Lin and colleagues (1978) showed that human lumbar FSU anterior-posterior displacement decreased under a maximum of 150 N of shear force with subsequent increases in compressive load (0-440 N). These authors suggested two mechanisms by

which anterior-posterior stiffness was increased with added compressive load. The first proposed mechanism is increased pressurization of the nucleus pulposus that causes bulging of the annular fibers and changes their orientation to resist shear loading while the second mechanism is that compressive load removes the space separating the articulating facets of the vertebral joint (Lin et al., 1978).

*In vitro* testing has shown that 60% of the increase, associated with applied compressive loading, in human lumbar FSU anterior-posterior stiffness is attributed to the disc while the remaining 40% of the increase in FSU stiffness is attributed to the posterior elements (Gardner-Morse et al., 2003). The same investigators also demonstrated that linearity of the anterior-posterior force-displacement relationship increased with 400 N of compressive load with intact human lumbar FSU's as well as FSU's that had their posterior elements removed (Gardner-Morse et al., 2003).

Vibration resulting in repetitive compressive loads applied *in vivo* to humans in a seated posture leads to a reduction in spine height (Sullivan and McGill, 1990). The reduction in spine height as a result of compressive loading has been attributed to the expulsion of fluid from the intervertebral disc in caprine lumbar spines (van der Veen et al., 2007). Increased disc height within the human lumbar spine (5 mm) has reduced facet joint articulation overlap by 30% at L4-L5 (Liu et al., 2006). Dunlop and colleagues (1984) determined the peak facet contact pressure in human lumbar FSUs with 1000 N of applied compressive load with 400 N of shear load. The specimens for this investigation were separated into groups that had their specimen height reduced by 0 mm, 1 mm, and 4 mm. The results showed that reducing specimen height by 1 mm and 4mm respectively led to a 36% and 61% increase in peak facet contact pressure under the combined

compressive and shear loads relative to specimens that had not undergone disc height reduction. Increasing compressive load has shown to increase the contact area between articulating facets of the human lumbar spine (Lorenz et al., 1983). Thus, increased facet articulation overlap and interaction of the inferior facet of the cephalad vertebra with the pars interarticularis of the caudal vertebra in a vertebral joint (Yang and King, 1984) with additional compressive load are feasible mechanisms by which shear stiffness of an FSU is increased.

#### **2.4.3 Effect of posture on mechanical properties of FSU's**

Maximum flexed postures have been shown to reduce the passive stiffness of the lumbar spine in axial twist while maximum extended postures have been shown to increase *in vivo* passive resistance of the lumbar spine to axial twist moments (Drake and Callaghan, 2008). Altering the flexion/extension angle of the vertebral joint will cause changes to the orientation of the passive tissues. Flexion of a lumbar vertebral joint results in elongation of the ligaments and reorientation of the intervertebral disc's annular fibers (Adams et al., 2002). Furthermore, flexion of the vertebral joint is achieved by reorientation of the vertebrae that comprise the vertebral joint. Vertebral flexion increases the gap between the inferior facets of the cephalad vertebra and the superior facets of the caudal vertebra in the porcine FSU (Drake et al., 2008). Increased distance between the articulating facet surfaces of a lumbar vertebral joint allows for a larger range of axial twist motion (Drake et al., 2008) and will also likely influence the passive response of an isolated FSU to shear loading.

Adams and Hutton (1980) attempted to determine the percentage of compressive load that was borne by the facets in extended, neutral and flexed postures of human lumbar FSU's. These authors found that the facets provided no resistance to compressive load when the specimens were flexed 2 degrees while the facets resisted 4% of the compressive load when the specimens were extended 2 degrees. Reducing specimen disc height following sustained compressive loading increased the percentages of compressive load resisted by the facets to 1% in the 2 degree flexed posture and 16% in the 2 degree extended posture (Adams and Hutton, 1980). In extended postures, it has been hypothesized that the articulating facets of the FSU come into contact with each other (i.e. 'kiss') that provides an avenue for resisting or transferring compressive load across the joint (Dunlop et al., 1984).

Shear loading of flexed (10 degrees) porcine cervical specimens demonstrated an increase in the ultimate failure load, but does not increase the FSU stiffness (Yingling and McGill, 1999). These authors suggested that the ultimate shear failure load increased due to an increase in the moment arm length of the pars interarticularis that was the location of fracture following destructive shear loading. Modeling of the human L4-L5 facet surface orientation showed that the gap between articulating facet surfaces would increase by 0.4 mm with 10 degrees of flexion at L4-L5 (Yingling and McGill, 1999). Van Dieën and colleagues (2006) on porcine thoracolumbar FSUs showed that flexing porcine lumbar FSU's by 10 degrees when compared to FSU's in a neutral posture did not influence the time to failure, under repeated shear loading. The lack of change in specimen anterior-posterior stiffness observed by Yingling and McGill (1999) in flexed porcine cervical FSUs may be a reason why the time to failure did not increase in the



study performed by van Dieën and colleagues (2006). Drake and colleagues (2008) showed that the gap between articulating facets of the porcine cervical FSU increases with flexion which suggests that anterior translation of the cephalad vertebra may increase as a result of applied shear loading. However, van Dieën and colleagues (2006) did not show an increase in initial shear amplitude between the neutral and flexed porcine thoracolumbar specimens. Drake and colleagues (2008) compared the facet gaps of a single MRI slice at the same depth for each of their porcine cervical specimens. It is possible that the facet gap does not change appreciably at the nearest point of contact between the articulating facets in the neutral and flexed postures which would assist in explaining the lack of differences observed during repeated shear testing in neutral as well as flexed postures.

Lastly, porcine cervical specimens that underwent shear loading in a neutral posture fractured the pars interarticularis whereas specimens that were tested in a flexed posture (10 degrees) fractured the pars interarticularis and had their endplates avulsed (Yingling and McGill, 1999).

## **2.5 EFFECTS OF FREEZING ON THE MECHANICAL PROPERTIES OF FSU'S**

Conflicting evidence has been presented regarding the effects of freezing and subsequent thawing on the mechanical properties of biological tissues. Freezing and subsequent thawing of human lumbar FSU's has been shown to not significantly alter the creep response of the intervertebral disc under 20 minutes of static compressive load followed by a 40 minute recovery period in a saline bath (Dhillon et al., 2001). Freezing does not affect the tensile properties of the human annulus fibrosus (Hirsch and Galante,

1967), or the mechanical properties of human femoral cortical bone (Sedlin and Hirsch, 1966). Panjabi and colleagues (1985) showed that anterior displacement of the human thoracic FSU cephalad vertebra and rotation (axial rotation and lateral bending) did not change significantly for each of the 14 testing days following thawing. The compressive stiffness and hysteresis of human FSU's have been shown to be altered by less than 1% between fresh and thawed specimens under repetitive sub-acute failure compressive loads (Smeathers and Joanes, 1988). However, the compressive loads tested in this investigation ( $750 \pm 250$  N) were much smaller than published ultimate compressive loads of porcine cervical FSU's (Gunning et al., 2001). Callaghan and McGill (1995) showed that the ultimate compressive load of thawed porcine cervical FSUs increased by 24% relative to the ultimate compressive load of fresh FSUs. Freezing human lumbar FSUs has been shown to increase intervertebral disc height, but that disc height recovers to pre-frozen values upon thawing (Dhillon et al., 2001). The permeability and swelling pressures are also lower in frozen immature porcine specimens (Bass et al., 1997). Differences in the compressive creep response of the intervertebral disc were more pronounced during the 5<sup>th</sup> creep cycle than the 1<sup>st</sup> creep cycle (Bass et al., 1997). These authors suggested that freezing biological tissue may cause tissue microdamage that leads to differences in the mechanical response to compressive loading.

Specimens thawed from a frozen state are predominantly used for *in vitro* biomechanical testing despite the continuing controversy regarding the adequacy of these specimens for biomechanical *in vitro* testing. The evidence suggests that mechanical properties of frozen human specimens are not affected under sub-acute failure loads (Panjabi et al., 1985; Smeathers and Joanes, 1988). Conversely, acute failure tolerances

of porcine cervical FSUs may be significantly affected by the freezing process (Callaghan and McGill, 1995). Acknowledgement of this limitation and the potential affects that freezing tissue for *in vitro* testing may have on the mechanical response of FSUs is necessary. The only study to investigate the effects of freezing on human FSU response to shear loading did not find any difference in anterior displacement of frozen and thawed specimens (Panjabi et al., 1985).

## **2.6 USE OF QUANTITATIVE COMPUTED TOMOGRAPHY AND BONE MINERAL DENSITY MEASURES FOR ESTIMATION AND PREDICTION OF FAILURE TOLERANCES**

Quantitative computed tomography (QCT) is a non-invasive method for estimating the trabecular bone content and density (Reinbold et al., 1986; Eriksson et al., 1989; Edmondston et al., 1994). Previous investigations have attempted to relate trabecular (from QCT) and total bone density (from dual energy x-ray absorptiometry (DXA)) to the ultimate compressive load/stress in human (Hansson et al., 1980; Biggemann et al., 1988; Brinckmann et al., 1989; Eriksson et al., 1989; Edmondston et al., 1994; Edmondston et al., 1997; Ebbesen et al., 1999), monkey (Dickerson et al., 2008) as well as porcine vertebrae (Parkinson et al., 2005). Each of the previously cited studies used a linear regression to estimate ultimate compressive load/stress from measures of trabecular or total bone density with the exception of Ebbesen and colleagues (1999) who used both linear and power law curve fits and found little difference in the regression coefficient between the two curve fitting approaches. Ebbesen and colleagues (1999) also concluded that trabecular bone density of the human lumbar vertebral body is better correlated with ultimate compressive stress than with

ultimate compressive load. Other investigations have shown that bone mineral content or bone mineral density of the human lumbar vertebral body were good ( $0.62 \leq r^2 \leq 0.68$ , standard error = 1.4 kN) predictors of compressive strength (Biggemann et al., 1988; Brinckmann et al., 1989). Predictive equations of ultimate compressive load/stress for the human lumbar spine, based on bone mineral content have been developed and can be used for scaling load magnitudes for in vitro analyses. Average errors in predicted ultimate compressive load have been reported as high as 1.4 kN (Biggemann et al., 1988).

Inclusion of morphometric parameters in the predictive equations for determining ultimate compressive load/stress may improve the estimate accuracy (Biggemann et al., 1988; Eriksson et al., 1989; Dickerson et al., 2008). In particular, Biggemann and colleagues (1988) showed that correlating the product of vertebral body bone mineral density and endplate cross-sectional area with ultimate compressive load reduced the standard error of the estimated ultimate compressive load by 44% in human lumbar vertebrae. Furthermore, the relationship between the ultimate compressive load and the product of endplate area and bone mineral density improved to  $r^2 = 0.91$  from  $r^2 = 0.68$  when the relationship was determined between ultimate compressive load and bone mineral density. Bone mineral density within the human lumbar spine changes very little in the cephalad to caudal direction of the spine while endplate area increases in the same direction (Figure 2.8) (Brinckmann et al., 1989).

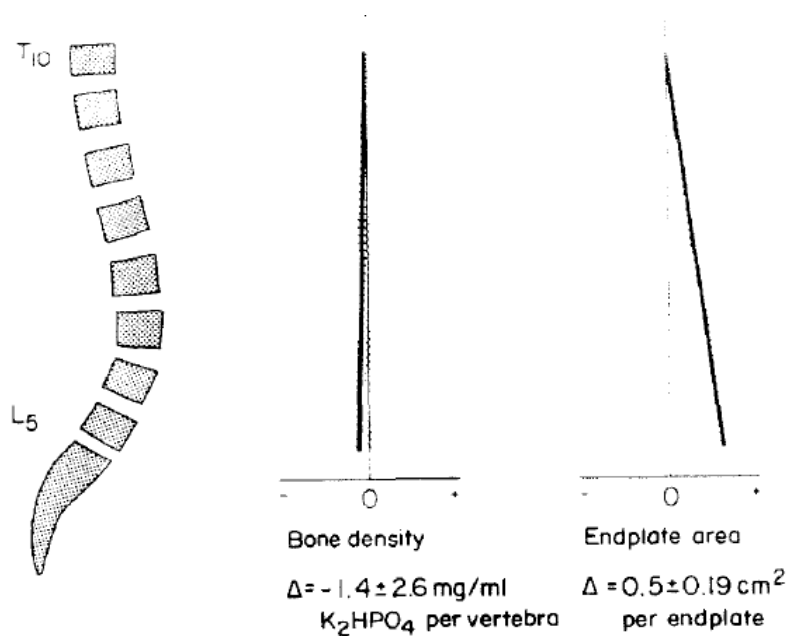


Figure 2.8 – Bone density exhibits minimal change from cranial vertebrae (T10 in this example) to caudal vertebrae (L5 in this case). However, endplate area does increase in more caudal vertebrae. Increased endplate area of more caudal vertebrae has been associated with increased ultimate compressive load of vertebral bodies. (Image taken from Brinckmann et al., 1989)

These authors suggested that the increase in ultimate compressive load at more caudal vertebral levels is a function of the increased endplate area. Edmondston and colleagues (1997) showed that morphological characteristics of the human lumbar vertebral body such as anterior/middle/posterior vertebral body heights, vertebral wedging and concavity added very little to explained variance in ultimate compressive load. Error in predicting compressive strength of an independent sample of porcine cervical specimens was 11% when using endplate area versus 13% when using the combination of bone density and endplate area (Parkinson et al., 2005). However, these authors suggested that the anterior processes of the porcine cervical spine may have influenced bone mineral density measures which could have altered the reliability of the results. Although inclusion of morphometric parameters in the predictive equations may improve the accuracy of

predicted ultimate compressive load, consideration must be given to the specific type of parameters that are included (Dickerson et al., 2008).

The utility of these predictive models is in their ability to provide estimates of *in vivo* compressive tolerances (Biggemann et al., 1988; Brinckmann et al., 1989) as well as their utility for normalizing loads applied *in vitro* to allow for comparisons between specimens and between species for submaximal repeated testing (Parkinson et al., 2005).

## **2.7 OVERVIEW OF THE FINITE ELEMENT METHOD**

### **2.7.1 General overview**

The finite element (FE) method divides a structure or material into a particular finite number of smaller constituent elements that are defined to interact at their adjoining points called nodes (Goel and Gilbertson, 1995; Brown, 2004). Initially the FE method was developed for testing aircraft designs (Fagan et al., 2002a). The mathematical formulations for the FE method have been well established throughout the years and can be used to examine nearly a limitless number of mechanical problems (Gallagher et al., 1982).

The FE method allows for approximation of stress and strain distributions throughout a structure by simultaneously solving a system of equations governing a structure's behavior using numerical methods (Brown, 2004). Individual nodal displacements resulting from forces applied to each node that comprises a single element are dependent upon the defined element stiffness. This generates the global formulation

of the FE problem, which involves solving for the undefined nodal forces and displacements (Equation 2.1).

$$\{F\} = [K]\{U\} \quad (2.1)$$

This is where  $\{F\}$  is the global set of nodal forces,  $[K]$  is the global stiffness matrix for the structure and  $\{U\}$  is the global set of nodal displacements (Brown, 2004).

Finite element analyses require the definition of:

1. Structural geometry
2. Individual material/elemental properties
3. Boundary conditions

Structural geometry incorporates defining the number of elements that make up the structure, the element type as well as the interpolation functions used to derive continuous mechanical variables throughout the structure. Properties defined for each material in the structure are the modulus of elasticity as well as the Poisson ratio.

Elements belonging to different materials must have the appropriate material properties applied to them. The modulus of elasticity may include properties that define the anisotropic behavior a material. Boundary conditions involve the definition of external loads (magnitude and direction of point and/or distributed loads) as well as particular nodal constraints (for example, displacement or velocity constraints on nodes located at an edge of the structure). Each of these components is discussed in the following sections with specific relevance to spine biomechanics.

### 2.7.2 Utility of the finite element method for spine modeling

The utility of the FE method in biomechanics for calculating the distribution of stress and strain throughout a structure under almost an unlimited number of external load, postural and damage scenarios has been widely acknowledged (Simon et al., 1985; Lu et al., 1996; Fagan et al., 2002a; Pitzen et al., 2002). Detailed FE models of the spine/FSU will include the proper geometry and relevant material properties for the individual materials that make up structures such as ligaments, vertebrae and intervertebral disc (Goel and Gilbertson, 1995). Fagan and colleagues (2002a) in a review paper stated four uses of the FE method for spine biomechanics:

1. Assessment of spine health
2. Assessment of the degenerated or damaged spine
3. Assessment of mechanical changes following insertion of spinal instrumentation.
4. Development of spinal instrumentation.

Provided that appropriate boundary conditions have been implemented and the geometry and material properties of the structure's constituent materials have been properly modeled, the FE method can be useful for predicting failure loads as well as failure patterns leading to mechanical explanations for the process of damage and tissue injury (Silva et al., 1998). Finite element models of the lumbar spine have been used to compliment *in vitro* work by mimicking the experimental testing conditions to determine internal tissue stress and strain distributions and predict the biomechanical behavior of the spine as well as the potential implications from implantation of spinal instrumentation (Graham et al., 2000; Pitzen et al., 2002). Validation of the FE results may be performed by comparison with *in vitro* results (Pitzen et al., 2002). Comparison between *in vitro*



work and FE results is relevant provided the geometry, testing conditions and material properties of the model match the *in vitro* specimen geometry, testing conditions and material properties (Sharma et al., 1998).

Spine biomechanics has made extensive use of the FE method. Models have been developed to study fluid flow within the intervertebral disc under static compressive loading as it is related to the creep response of the FSU (Simon et al., 1985). Lu and colleagues (1996) developed a viscoelastic finite element model of a lumbar FSU for studying the effects that bending, twisting and changing the fluid content of the nucleus pulposus would have on the annular fiber stress as it pertained to generation of intervertebral disc prolapse by movement of nuclear material. Finite element analyses have also been applied to study the stress distribution throughout the neural arch under point forces applied in a posterior direction to the inferior facet surfaces (Inoue et al., 1998).

The FE method can also be used to obtain estimates of structural loading and stress/strain distributions throughout a structure that may not be easily or possibly accessible by *in vitro* or *in vivo* methods without damaging either the specimen or participant. The problem of determining facet contact areas and stresses are two such examples. Sharma and colleagues (1998) have modeled the contact between facets of vertebral joints as a non-linear moving contact problem to show that the facet contact area in the modeled FSU is dependent upon both the orientation and gap between articulating facets of the vertebral joint. Likewise, the loads imposed upon the facets have been determined using FE models under many different combinations of external load and vertebral joint posture (Shirazi-Adl, 1991).

Finite element models are also useful for determining the consequences from removal (i.e. transection) or addition of structures. For example, Sharma and colleagues (1995) modeled the changes in the force-displacement relationship of the FE model of the human L3-L4 FSU by iteratively removing the facets and ligaments from their FE model of the L3-L4 FSU. Eberlein and colleagues (2001) have also developed a detailed model of the intervertebral disc and implemented it with a model of the human L2-L3 vertebral body. Their intention was to use this model for predicting the redistribution of loads within the vertebral joint upon artificial disc implantation. Knowledge of the load sharing between implants and biological structures and changes in the stress distribution throughout a structure following implantation is important and can be done with a FE model that appropriately models the geometry and individual material properties of the intact FSU.

### **2.7.3 Geometry modeling**

As previously stated in section 2.7.1, proper modeling of the structure's geometry is a preliminary requirement for enhancing accuracy of the FE model outputs and for allowing comparison of the FE results to in vitro and in vivo studies (Sharma et al., 1998). Narrowing the gap between articulating facets in a FE model of the human L3/L4 FSU increased load transmission to 2%, 17.5% and 71.2% (from 0%, 3.5% and 32.3%) through the facets under 400 N of compressive load, 6 Nm of applied extension moment and 6 Nm of applied axial twist moment respectively (Sharma et al., 1998). Meanwhile altering facet orientation in either the sagittal or transverse planes did not produce equivalent changes in load transmission through the facets.

The structure's geometry is modeled using a series of connected nodes to define a mesh (Brown, 2004). Each element in the mesh is defined by a subset of nodes and the connectivity between the nodes in each subset (Figure 2.9).

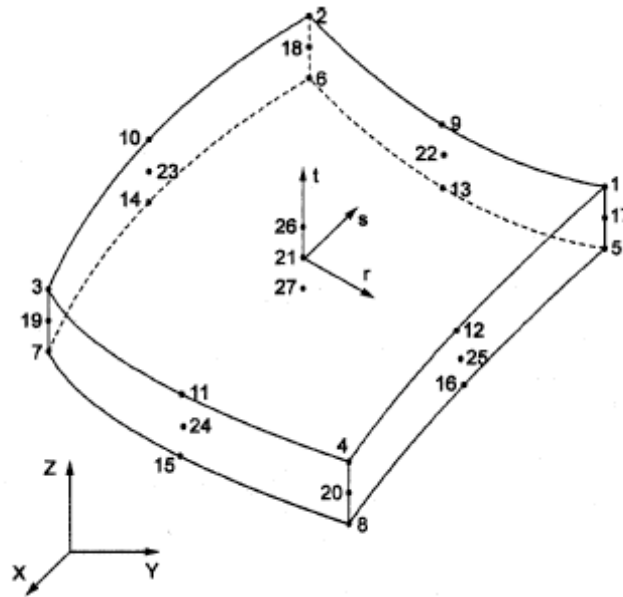


Figure 2.9 – Definition of a generic element to be used in a finite element model. Nodes are sequentially numbered and the edges are defined by the connectivity between specifically numbered nodes. (Image taken from Brown, 2004)

The mesh density (number of elements in a given area/volume), element size, element shape and the method of mesh generation can greatly influence the results from FE models. Each of these factors is covered in the following sections. Computational efficiency can be enhanced by assuming some geometrical symmetries in the FE model at the expense of FE solution accuracy (Belytschko et al., 1974; Shirazi-Adl, 1989; Suwito et al., 1992).

### 2.7.3.1 Mesh density, element size and convergence

Increasing the number of elements in a FE model will improve the resolution of the model's solution (Figure 2.10) (Brown, 2004).

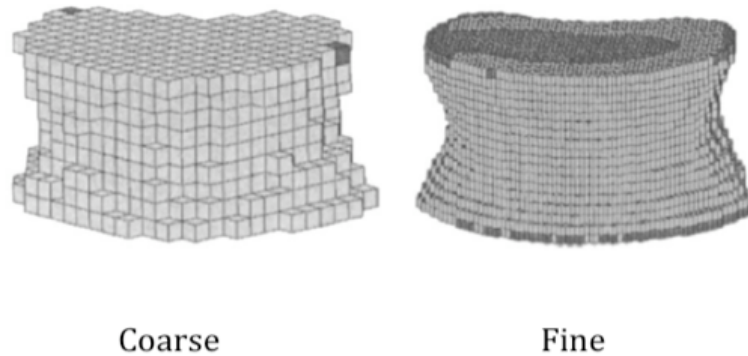


Figure 2.10 – Increasing the number of elements improves the model's geometrical resolution and can improve the resolution of the finite element model's solution. A coarse model is depicted on the left while a fine model is depicted on the right. (Image taken from Crawford et al., 2003)

However, increasing the number of elements also increases the computational time required to generate a solution. Thus, studies, called convergence studies, are required to determine the minimum number of elements required for properly modeling the structure's geometry. Convergence is achieved when a particular FE output changes by less than a predefined tolerance upon refining the FE mesh by adding elements. For example, Liebschner and colleagues (2003) considered their model of the vertebral body to have converged when stiffness changed by less than 2% with the addition of a higher number of elements.

Element size is directly related to the number of elements for a given volume. Stiffness and strength of the vertebral body calculated from a FE model showed that reducing the element size from  $64 \text{ mm}^3$  to  $8 \text{ mm}^3$  (subsequently increasing the number of

elements) changed the stiffness and strength predictions by 23% and 18% respectively (Jones and Wilcox, 2007). Further reduction of element size from 8 mm<sup>3</sup> to 1 mm<sup>3</sup> produced changes in stiffness and strength of only 6.1% and 1.6% respectively (Jones and Wilcox, 2007). Linearity of the relationship between FE model stiffness and fracture strength of the vertebral body was not improved ( $r^2 = 0.94$  small elements,  $r^2 = 0.92$  large elements) by reducing element size from 27 mm<sup>3</sup> to 1.5 mm<sup>3</sup> (Crawford et al., 2003). Jones and Wilcox (2007) suggest that an element size of 8 mm<sup>3</sup> (2 x 2 x 2 mm) is sufficient for modeling the human lumbar vertebral body (Jones and Wilcox, 2007). Similarly, differences between a coarse (3690 elements) and fine (8018 elements) mesh of a human L2/L3 FSU have shown no real difference in the flexion/extension moment versus angle relationship or modeled intradiscal pressure (Eberlein et al., 2004). Likewise, coarse (24 elements) and fine (48 elements) meshes of the intervertebral disc have shown little difference in FE model stress and strain outputs (Eberlein et al., 2001).

Another method whereby FE solutions can be improved in areas of interest is by regional definition of element densities. Most commercial FE software will allow the investigator to specify the element density for the whole structure or by region. Regional definition of element density is particularly useful for analyses with known areas of stress concentrations and where better resolution is desired. This will reduce the total number of elements in the FE model, which will also reduce the solution time. Beltyschko and colleagues (1974) developed a FE model of the vertebral body and intervertebral disc with the intent of performing a stress analysis of the intervertebral disc. Since the disc was of primary importance to their investigation, higher element density was used to model the disc geometry than the vertebral body (Figure 2.11).

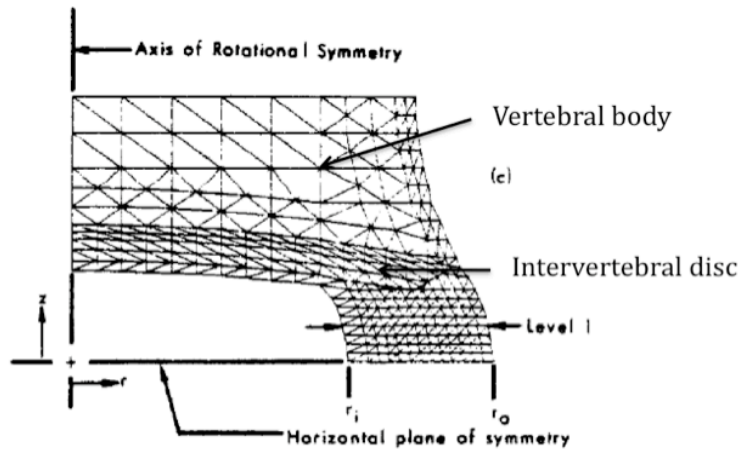
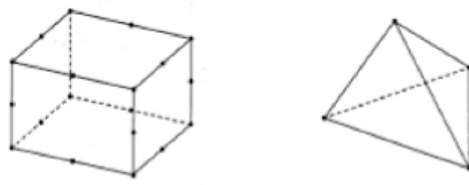


Figure 2.11 – Regional definition of element densities can improve the model’s resolution in areas that are of primary interest while also enhancing computational efficiency by minimizing the total number of elements in the model. In this example, the element density of the intervertebral disc is modeled with a larger number of elements because the disc was the structure of primary importance for this study. (Image taken from Belytschko et al., 1974)

However, regional definition of element densities is not typically used in biomechanical FE models.

### 2.7.3.2 Element type and mesh generation

Mesh generation for FE models requires selection of the element type for each of the structure’s components. Three examples of element types used for modeling bone in biomechanics are brick, tetrahedral and shell elements while ligaments are generally modeled as elastic beam elements (Breau et al., 1991). Brick and tetrahedral elements are typically used for modeling the vertebral cancellous core (Figure 2.12) (Breau et al., 1991; Crawford et al., 2003; Wong et al., 2003; Jones and Wilcox, 2007) while the shell elements can be used to model the cortical shell surrounding the cancellous bone (Kumaresan et al., 1999).



**Brick**

**Tetrahedral**

Figure 2.12 – Examples of a brick (shown on the left) and a tetrahedral element (shown on the right). (Image taken from Brown, 2004)

Complex geometries, such as that of an FSU, can be generated by reconstructive methods using a series of computed tomography (CT) scans (Breau et al., 1991). Computer routines have been implemented to generate specimen specific finite element meshes from CT scans in a ‘semi-automatic’ manner that greatly reduces the time for generating a mesh for individual specimens (Kaminsky et al., 2005). However, specimen/subject specific meshing is still computationally intensive and requires some investigator intervention (Wilcox, 2007). It has been suggested that automated meshing, without separately meshing individual components of the vertebra, may only be performed using tetrahedral elements due to its non-isoparametric nature (Eberlein et al., 2004). Generation of specimen specific meshes can be important for effectively estimating the effects that disc implants or posterior instrumentation would have on an individual (Eberlein et al., 2001). The selected element type and element size for the model may not identically fit the contours of the complex vertebral geometry causing volume distortion (Kaminsky et al., 2005). Improper modeling of the vertebral volume by selection of different element types or element sizes may be a source of discrepancy between FE outputs of the same structure (Jones and Wilcox, 2007). Recent literature has focused on reducing volume distortion caused by semi-automatic mesh generation

methods with smoothing routines (Kaminsky et al., 2005). Some smoothing routines may cause elements within the mesh to deform prior to applying the boundary conditions that may create errors in the final FE stress and strain distribution (Figure 2.13).

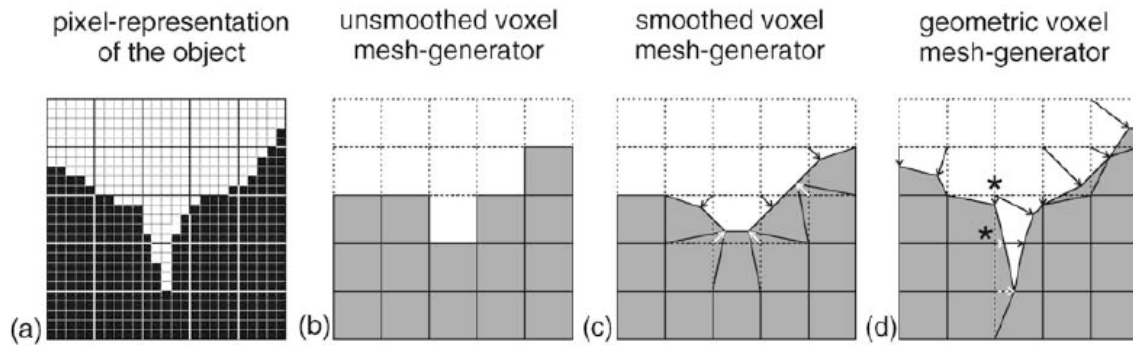


Figure 2.13 – Images depicting a pixel representation from a section of MRI scanned geometry (a) and three mesh generators (b-d) with various levels of geometrical smoothing to reduce volume distortion of the final finite element model geometry. (Image taken from Kaminsky et al., 2005)

#### 2.7.4 Material property modeling

Material properties have been identified as one of the most sensitive parameters for FE models (Suwito et al., 1992). For a linear isotropic material, the Young's modulus and Poisson's ratio are the required material properties for FE models. Anisotropic materials require explicit definition of moduli pertaining to the response of the material to different directions of loading (Crawford et al., 2003; Liebschner et al., 2003). Biological tissues are anisotropic, but FE models have differed on whether or not material anisotropy is modeled (Belytschko et al., 1974; Kumaresan et al., 1999). Alterations in the anisotropic ratio (compressive modulus to modulus along a horizontal axis of loading) of cancellous bone (from 3 to 1 with 3 being the typical anisotropic ratio) have been shown to increase the shell force fraction by 100% under modeled compressive loading



(Silva et al., 1997). Finite element models of structures containing many different materials require definition of the properties for each material in the structure.

Many studies have been performed to test the sensitivity of biomechanical FE models of FSUs, intervertebral discs and vertebral bodies to changes in material properties (Suwito et al., 1992; Shirazi-Adl, 1994; Silva et al., 1997; Kumaresan et al., 1999; Fagan et al., 2002b; Liebschner et al., 2003; Jones and Wilcox, 2007; Wilcox, 2007). Kumaresan and colleagues (1999) showed that increased and decreased moduli for the intervertebral disc and ligaments respectively had the largest increase and decrease in rotational motion in a FE model of the cervical spine (Table 2.3).

Table 2.3 – Changes in rotational motion accompanied by changes in the modulus of elasticity for the intervertebral disc and ligaments of a cervical FE model. (Data from this table are taken from Kumaresan et al., 1999)

	<b>Intervertebral disc</b>		<b>Ligament</b>	
<b>Change in modulus</b>	29% ↓	294% ↑	50% ↓	200% ↑
<b>Change in rotational motion with change in modulus</b>	93% ↑	46% ↓	41% ↑	32% ↓

The same authors also demonstrated that changes in the endplate and cancellous bone moduli resulted in the largest changes in vertebral body centrum stress. Increased vertebral body modulus and yield strength in a FE model of the vertebral body have been shown to result in increased model compressive stiffness and strength outputs while changes to the Poisson ratio had little effect (Table 2.4) (Jones and Wilcox, 2007).

Table 2.4 – Changes in the elastic modulus for bone altered the finite element model stiffness while subsequent changes in the yield strength led to changes in finite element model strength. Alterations to the Poisson ratio had a minimal effect on each of the stiffness and strength of the finite element model. (Data from this table are taken from Jones and Wilcox, 2007)

<b>Elastic modulus</b>	<b>Increase</b>			<b>Constant</b>				
	<b>10</b>	<b>20</b>	<b>50</b>					
<b>Yield strength</b>	<b>Constant</b>			<b>Increase</b>			<b>Constant</b>	
				<b>10</b>	<b>20</b>	<b>50</b>		
<b>Poisson ratio</b>	<b>0.3</b>	<b>0.3</b>	<b>0.3</b>	<b>0.3</b>	<b>0.3</b>	<b>0.3</b>	<b>0.2</b>	<b>0.4</b>
<b>Increase in stiffness</b>	10.1	19.2	49.6	0.0	0.0	0.0	-0.7	0.4
<b>Increase in strength</b>	0.6	5.0	5.1	9.8	26.0	56.5	-0.4	5.2

However, Suwito and colleagues (1992) have identified the endplate and annulus Poisson ratios as input parameters that are among the most sensitive for FE solutions of the FSU under compressive load. Comparison between the results of these two studies is likely difficult due to differences in the moduli used for the cancellous bone as well as the differences in models (vertebral body versus whole FSU). Silva and colleagues (1997) have also shown that the load sharing relationship between the modeled cortical shell and cancellous centrum increased by 130% simply by changing the cancellous Poisson ratio from 0.3 to 0.1. Cancellous as well as cortical bone is typically modeled using Poisson ratios near 0.3 (Suwito et al., 1992; Silva et al., 1997; Jones and Wilcox, 2007).

Differences in cancellous bone compliance have shown differences in rotation of a FE model of a human FSU (Shirazi-Adl, 1994).

A goal of some FE investigations is to provide a specimen/subject specific model for predicting tissue failure. Prediction of failure properties is limited by the multidirectional nature of failure for bone (Silva et al., 1998). Since FE model outputs are sensitive to material property inputs, accuracy of specimen specific FE model outputs is dependent on the agreement between specimen material properties and the modeled properties of individual materials within the FE model (Fagan et al., 2002b). Eberlein and colleagues (2001) also state that ‘state-of-the-art’ material properties need to be used for enhancing the accuracy of FE models.

#### **2.7.5 Boundary condition definition**

Boundary conditions are considered to be constraints placed upon nodal displacements and/or velocities as well as the external loading parameters. For example, Inoue and colleagues (1998) defined the boundary conditions for their FE model by constraining displacements of the superior and inferior surfaces of the vertebral body in all directions and applying a static 285 N force in the posterior direction to the inferior facets of the L4 vertebra. Jones and Wilcox (2007) also stated that predictions of vertebral body compressive strength are highly sensitive to the representation of boundary conditions and in particular application of load to the FE model of the vertebral body. For their FE model, a rigid plate was attached to the top of their model that was allowed to rotate in the sagittal and frontal planes to maintain consistency with the *in vitro* testing conditions. Displacement was applied to the model according to displacements that were observed during *in vitro* testing. The inferior surface of the manually generated FE models was constrained from moving in all degrees of freedom to

match the in vitro testing conditions. The FE models generated with semi-automatic meshing had a second rigid plate affixed to flatten the bottom surface of the model and this rigid plate was constrained from moving in all degrees of freedom. Finally, it has been suggested that differences between studies using FE models is likely due to differences in boundary condition definition (Overaker et al., 1999).

## **CHAPTER 3**

# **COMBINED INFLUENCE OF COMPRESSION AND POSTURE ON SHEAR FAILURE MECHANISMS FOR THE PORCINE CERVICAL SPINE**

### 3.1 INTRODUCTION

Reporting of occupational low-back pain has been significantly correlated to peak anterior shear load (Norman et al., 1998). Despite this finding, limited attention has been given towards studying *in vitro* shear loading as a mechanism for low-back injury (Potvin, 2008). Interaction between articulating facet surfaces, that governs shear failure tolerance, changes as a result of applied compression and postural deviation (Adams and Hutton, 1980; Lorenz et al., 1983; Dunlop et al., 1984; Drake et al., 2008). Independent researchers have quantified shear failure tolerance of the vertebral joint under different levels of constant compressive load (Cripton et al., 1995) as well as postural deviations (Yingling and McGill, 1999). However, there have been no investigations on the combined effect that altering compressive load and posture may have on anterior shear failure tolerances of the vertebral joint. The current investigation studies the combined roles of compressive load and postural deviation in altering the vertebral joint's shear failure tolerance.

*In vitro* tests have demonstrated that the most common fracture location for vertebral functional spinal units (FSUs) exposed to anterior shear loading is the cranial vertebra's pars interarticularis (Yingling and McGill, 1999; Beadon et al., 2008). This fracture is a consequence of interaction between the superior and inferior facets of adjacent vertebrae that is thought to generate a moment about the cranial vertebra's pars interarticularis (Cyron et al., 1976; Yingling and McGill, 1999). Linking changes in facet articulation to alterations in shear failure tolerance could enhance our understanding of shear failure mechanisms.

Previous literature has shown that FSU stiffness increases about each of the three rotational and in the three translational degrees of freedom by increasing compressive loads (Janevic et al., 1991; Gardner-Morse and Stokes, 2003). Increased stiffness as a result of increased compressive load has been attributed to changes in facet interaction as well as pressurization of the nucleus pulposus causing increased disc and overall FSU stiffness (Lin et al., 1978; Dunlop et al., 1984; Yang and King, 1984). Higher compressive loads as a secondary mode of loading, when combined with a primary mode of loading, have been shown to alter the primary loading mode's failure tolerance for the vertebral joint (Callaghan and McGill, 2001).

Flexed postures have been shown to reduce the ultimate compressive load sustained by a porcine cervical FSU (Gunning et al., 2001). Altering flexion/extension (F/E) posture has been shown to bilaterally alter the contact area between the superior and inferior facets of an FSU (Dunlop et al., 1984). Specifically, extension brings the facets closer into contact (Adams and Hutton, 1980) while flexion causes stretching of the facet joint capsule and increases the gap between the articulating facet surfaces (Yingling and McGill, 1999; Drake et al., 2008). Furthermore, flexed postures have been postulated to increase the moment arm length of facet contact forces relative to the pars interarticularis by lengthening the distance from the center of pressure occurring on the facet surface to the location of the pars interarticularis (Yingling and McGill, 1999). This hypothesis suggests that postural deviation may also alter the vertebral joint's anterior shear failure tolerance. Conflicting evidence has shown that repetitively applied anterior shear loads did not cause differences in the time to failure of porcine specimens that had been flexed 10 degrees when compared to specimens tested in a neutral posture (van

Dieën et al., 2006). These contradictory statements demonstrate that the role of deviated flexion/extension postures in modulating shear failure tolerance of the vertebral joint is not yet well understood.

The purpose of the current investigation was to quantify acute shear failure loads, stiffness, displacement and energy stored prior to failure for vertebral joints that were simultaneously exposed to different magnitudes of compressive load in extended, neutral and flexed postures. It was hypothesized that higher compressive forces would cause increased shear failure tolerance, stiffness, energy stored until failure and would decrease shear displacement at failure. Flexed postures were hypothesized to decrease shear failure tolerance, stiffness and energy stored until failure while increasing shear displacement at failure.

## **3.2 METHODS**

### **3.2.1 Specimen preparation and assessment**

Ninety-six FSUs (48 C3-C4 and 48 C5-C6) were excised from forty-eight frozen porcine cervical spines obtained from a local abattoir. Specimens were thawed overnight prior to removal of muscle and fat leaving an osteoligamentous FSU comprised of two vertebrae, the intervertebral disc and ligaments. Following dissection, quality of the exposed superior and inferior intervertebral disc was assessed using the grading scale outlined by Galante (1967). Only specimens with disc quality of Grade 1 were used for this investigation. Measurements of endplate anterior-posterior depth (D) and mediolateral width (W) were obtained using digital calipers for both exposed endplates.



Area of each exposed endplate was calculated using the equation for area of an ellipse ( $\pi WD/4$ ) (Callaghan and McGill, 1995). The area of the FSUs intervertebral disc was estimated as the average area between the two exposed endplates (Parkinson et al., 2005). Bilateral facet angles and tropism between left and right facet joints were also quantified (Boden et al., 1996) using ImageJ (National Institutes of Health, USA) from an x-ray taken in the transverse plane (Figure 3.1).

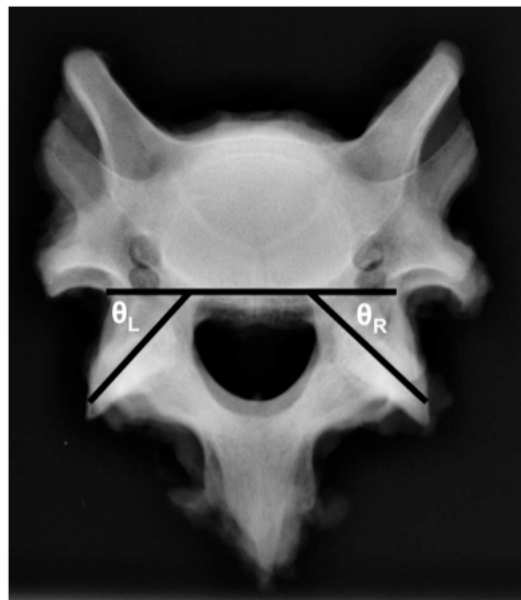


Figure 3.1 – X-ray of a specimen taken in the transverse plane. Left and right facet angles ( $\theta_L$  and  $\theta_R$ ) were measured as the angle between a line parallel to the posterior aspect of the vertebral body and a line parallel to the gap between the facets.

Specimens were mounted between a set of two custom aluminum cups using a combination of steel wire, screws and dental plaster. Two screws were partially inserted so that they protruded from the anterior aspect of the cranial vertebral body. One screw was inserted through the bottom of each cup so that each screw pierced the center of the exposed superior and inferior endplates. An additional six screws (three for each vertebra) were inserted through threaded holes in the aluminum cups so that they were

sunk approximately 5 mm into the anterior and lateral aspects of the vertebral bodies. A single length of 18 gauge galvanized steel wire was looped around the caudal vertebra's spinous process, threaded through two holes in the bottom of the aluminum cup and tightened by twisting the two ends together. Lastly, non-exothermic dental plaster (Denstone, Miles, IN, USA) was poured into the cups, and allowed to harden, so that the exposed screws were completely immersed and that any space between the specimen and the aluminum cup was filled.

### **3.2.2 Instrumentation**

Complete three-dimensional kinematics of the vertebrae as well as the aluminum cups were measured during all tests with a single optoelectronic camera (Optotrak Certus, Northern Digital Inc., Waterloo, ON, Canada) and a series of infrared light emitting diodes (IREDs) affixed to rigid metal plates. Four IREDs were mounted to each rigid plate with a quick drying adhesive. The geometrical configuration for the markers affixed to a single rigid plate was characterized and used to define the three-dimensional position and orientation of the rigid plate within the camera's predefined coordinate system. Each rigid plate measured the three-dimensional kinematics for either a single aluminum cup or a single vertebra through a rigid coupling (Figure 3.2).

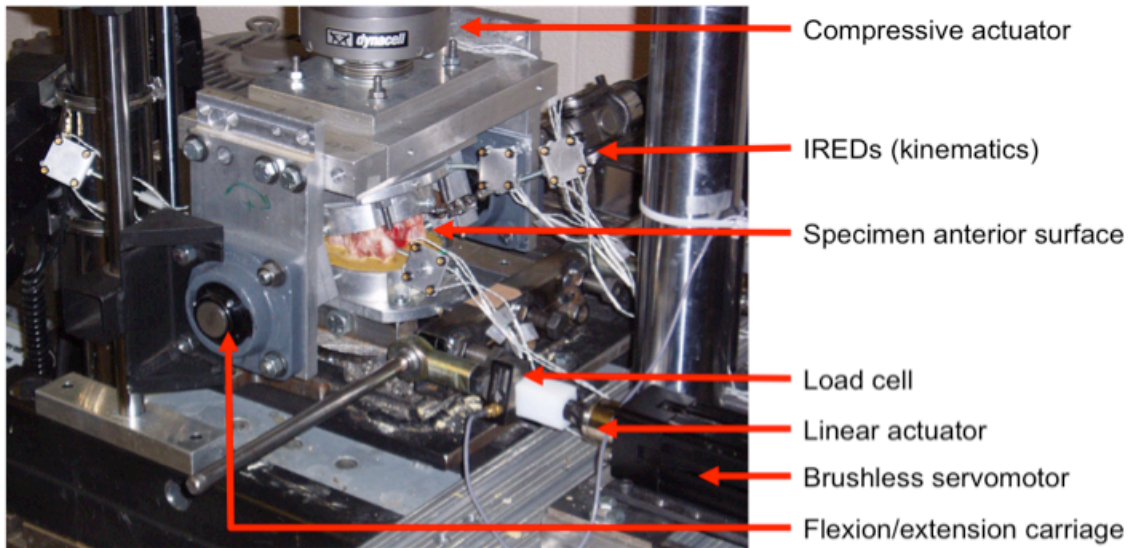


Figure 3.2 – Experimental setup for all shear testing protocols. IREDs = infrared light emitting diodes.

Prior to loading, three specific locations within the camera's global coordinate system for each vertebra and cup were digitized with a manufactured probe that had a predefined geometrical relationship between the probe's tip and a series of four IREDs arranged in a known geometrical configuration. Global coordinates for each digitized location were continuously measured as a virtual marker during all tests using a fixed geometrical relationship between the reference rigid body's orientation and position and the location of the probe's tip within the camera's global coordinate system. The digitized locations for each component (vertebra or cup) were selected to determine a local coordinate system representing their anatomical position and orientation. For each component, the first two digitized positions defined a mediolateral anatomical axis (i.e. flexion/extension) while the third digitized point was used in conjunction with the first two points to define a plane that was subsequently used to calculate the structure's anteroposterior (lateral bend) and vertical (axial twist) axes. Three additional locations on

the linear actuator were also digitized and expressed within the camera's coordinate system using the same probe. These locations were used to construct a coordinate system whose anteroposterior axis was coincident with the direction of applied displacement (and force) during all shear tests. Kinematics for all markers and digitized locations were continuously sampled at a rate of 128 Hz.

Analog data from two load cells (MLP-500, Transducer Technologies, Temecula, CA, USA) that measured applied force during all shear tests, and a torque cell (T120-106-1K, SensorData Technologies Inc., Sterling Heights, MI, USA) that measured applied flexion/extension moment during all tests were temporally synchronized with the kinematic data and digitally sampled at a rate of 1024 Hz using a 16-bit analog to digital conversion (Optotrak Data Acquisition Unit II, Northern Digital Inc., Waterloo, ON, Canada).

### **3.2.3 Loading protocol**

Following fixation, the cup containing the FSUs cranial vertebra was secured to a servohydraulic material testing system (Instron 8872, Instron Canada, Burlington, ON, Canada) that had been coupled to a brushless servomotor (AKM23D; Kollmorgen/Danaher Motion, Radford, VA, USA) capable of simultaneously applying flexion/extension moments to the specimen (Figure 3.2). First, a compressive preload of 300 N was applied under load control for a 15-minute duration to counter the effects of post-mortem swelling (Callaghan and McGill, 2001). The flexion/extension posture was continuously adjusted by monitoring the torque cell feedback loop and driving the servomotor in position control to reduce the joint moment throughout the 15-minute

duration in order to determine the position where zero or the smallest moment possible was recorded by the torque cell.

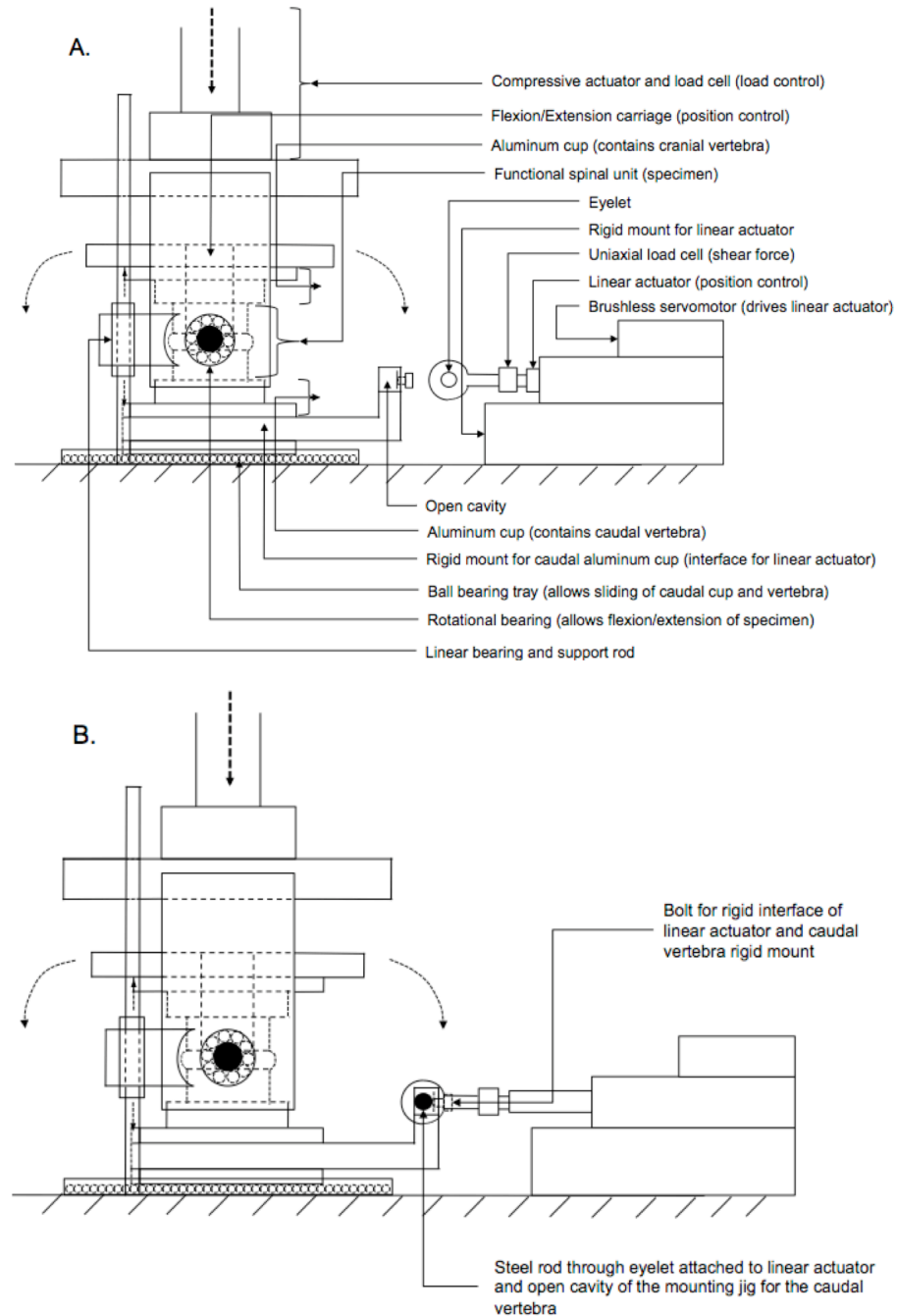


Figure 3.3 – Schematic drawing of the *in vitro* testing setups for the unconstrained (A.) flexion/extension tests, and the constrained (B.) shear tests.

Following the preload, five continuous repeats of position controlled passive flexion/extension were performed at a rate of 0.5 degrees/second, and under a constant load controlled compressive force of 300 N (Callaghan and McGill, 2001) to determine the specimen's neutral zone for rotational loading about the flexion/extension axis. The cup containing the FSU's caudal vertebra was allowed to translate freely in the horizontal plane during the preload and passive flexion/extension tests on metallic ball bearings that provided a near-frictionless surface (Figure 3.3A). Flexion and extension angles where the moment versus angle relationship deviated from linear for the last three repeats were defined as endpoints of a linear region similar to the neutral zone (Panjabi, 1992; Callaghan and McGill, 2001).

The neutral position defined at the end of the 15-minute preload identified a position within the specimen's neutral zone that satisfies a zero flexion/extension moment. However, there are many flexion/extension angles within the neutral zone that simultaneously satisfy the zero moment condition. The first position that satisfies the zero flexion/extension moment condition is defined as the first approximation of the neutral posture. Using data provided under similar load and testing conditions (Callaghan and McGill, 2001), the neutral posture was set to be 36% of the neutral zone length from the selected extension limit (Equation 3.1).

$$\theta_{neutral} = \theta_{ext} + 0.36(\theta_{flex} - \theta_{ext}) \quad (3.1)$$

This was performed so that each specimen received the same approach for determining the neutral posture. The flexion and extension limits determined from the

passive test were redefined in reference to the calculated neutral posture.

For shear testing, the cup containing the specimen's caudal vertebra (either C4 or C6) was rigidly interfaced with two linear actuators (RSA24, Tolomatic Inc., Hamel, MN, USA) driven by a pair of brushless servomotors (AKM22E, Danaher Motion Inc., Radford, VA, USA) (Figure 3.2). This constrained sliding of the caudal vertebra to allow only the imposed anterior/posterior displacements applied by the linear actuators during all shear tests (Figure 3.3B). The linear actuators were equidistant from the specimen's mid-sagittal plane in order to prevent application of an axial twisting moment and were controlled in parallel to insure equal movement profiles. A uniaxial load cell (MLP-500, Transducer Technologies, Temecula, CA, USA) mounted in series to each linear actuator was used to measure applied shear force during all tests.

In addition to the flexion/extension passive tests, specimens were also preconditioned in anterior/posterior shear under position control prior to the acute failure protocol. Displacement during anterior/posterior shear preconditioning was applied at a constant rate of 0.05 mm/second using a continuous motion control algorithm (Appendix A.1). The targets were  $\pm 400$  N (positive force being anterior shear and negative force being posterior shear) of applied shear force for preconditioning. This target was approximately 14% of the ultimate anterior shear failure load (van Dieën et al., 2006; Gallagher et al., 2010).

Following the conditioning test, each specimen was randomly assigned to one of twelve different combinations of predicted compressive failure tolerance (15% ( $1446.8 \pm 25.1$  N), 30% ( $2932.0 \pm 52.8$  N), 45% ( $4498.1 \pm 94.2$  N) or 60% ( $5964.8 \pm 110.1$  N)) and flexion/extension posture (extended ( $-4.39 \pm 0.13$  degrees), neutral (0 degrees) or flexed

( $7.89 \pm 0.23$  degrees)) to be applied during the acute shear failure protocol. Compressive failure tolerance for each specimen was determined using average endplate area as the input to a previously determined linear regression equation (Parkinson et al., 2005). Flexion and extension limits were used as test flexion or extension angles for acute failure tests performed in either flexed or extended postures. The reference posture determined from the flexion/extension passive test was used for acute failure tests performed in the neutral posture. Shear failure was induced for each specimen by applying shear displacement under position control at a constant rate of 0.15 mm/second (Appendix A.2). This displacement rate was consistent with a previous acute shear failure protocol (van Dieën et al., 2006) and was targeted to apply shear load at a rate that was consistent with shear loading rates while lifting a load deemed safe for 99% of the population from the floor to waist height (Howarth et al., 2009).

Following the shear failure protocol, the specimen was returned to the neutral position and uncoupled from the linear actuators. A second flexion/extension passive test was performed using the same load and displacement conditions as the test performed prior to the acute failure protocol.

### **3.2.4 Post-failure analysis**

Specimens were removed from their fixation upon completion of the loading protocol. A sagittal plane x-ray was taken of the specimen to identify possible locations of bone failure. Due to irregular geometry of the vertebral joint, specimen positioning for the x-ray was controlled to the unloaded and neutral posture by placing the specimen's right side onto a formed impression created in a 25.4 mm thick block of extruded



polystyrene foam. Each specimen was carefully sectioned into individual vertebrae and photographed. An investigator also visually documented bone failure.

### **3.2.5 Data processing and analysis**

Three-dimensional orientation and position of the coordinate system for each vertebra and cup were transformed from the camera's global coordinate system into the local actuator-based coordinate system for the complete duration of the shear failure test. Vertebral shear displacement was calculated at each instant as the difference in position between the origins of each vertebra-based coordinate system with respect to the orientation of the actuator-based coordinate system.

Digitally sampled voltages from each load cell on the shear actuators were calibrated to force and filtered using a second order dual-pass Butterworth digital filter with a cutoff frequency of 3.5 Hz. Filtered forces were also downsampled to 128 Hz in order to match the kinematic sampling rate. Measured shear forces and kinematics were transformed into the specimen's local joint coordinate system for all acute failure tests. Total applied shear force was calculated as the sum of the forces recorded from the two load cells. Kinematic data from the virtual markers were also filtered using a second order dual-pass Butterworth digital filter with a cutoff frequency of 2.5 Hz. Filter cutoff frequencies were determined from residual analyses conducted on data collected during shear failure tests using the conditions for acute failure testing outlined in Chapter 4 (Appendix B.1).

Shear stiffness for each specimen was calculated using the maximum slope on the force versus displacement relationship, over a 0.5 mm region, that satisfied a 95%

linearity criterion (Figure 3.4). Ultimate shear force was defined as the maximum shear force achieved throughout the failure test and ultimate displacement was the shear displacement that coincided with the ultimate shear force (Figure 3.4). Two additional definitions of failure (elastic limit and initial failure) were also determined (Figure 3.4). Initial failure force was defined as the instant where a 3.25% decrease in total applied shear force occurred over a 0.5 second window (Gunning et al., 2001). The initial failure point was set to be equivalent to the ultimate failure point in the event that no points on the force versus displacement relationship satisfied the defined initial failure criterion. The elastic limit was calculated using a 2% deviation of linearity in the shear displacement versus force relationship from the calculated stiffness.

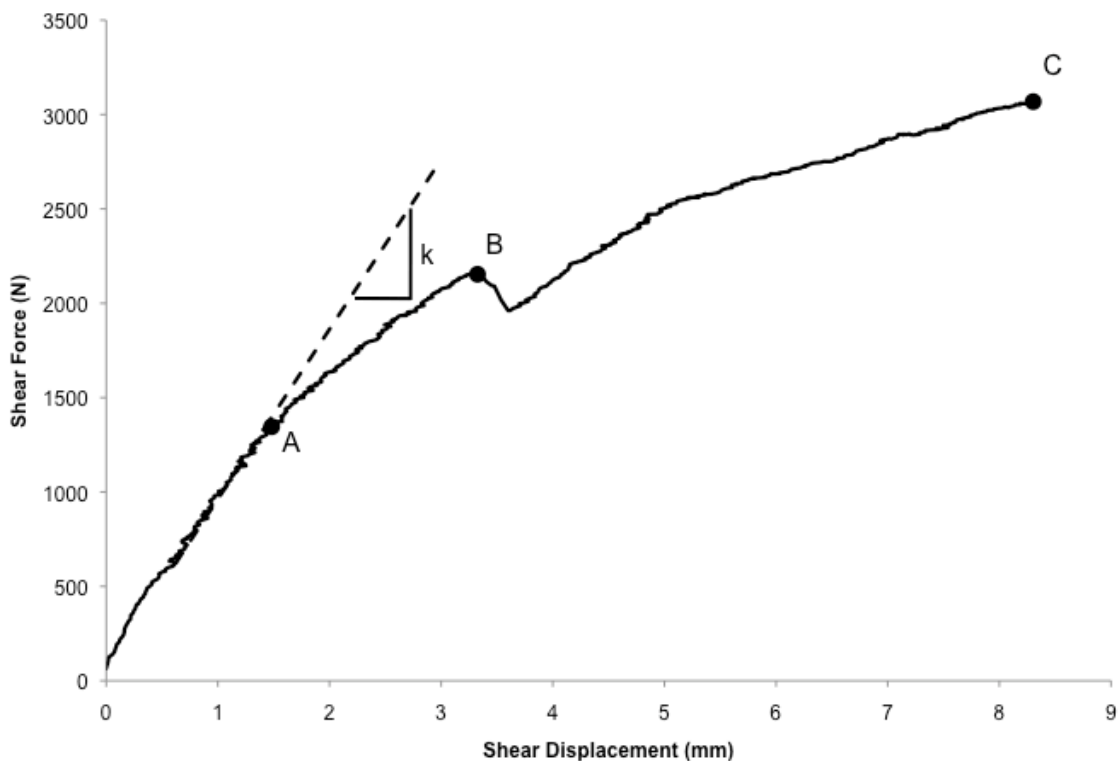


Figure 3.4 – Sample shear displacement versus force curve obtained from an ultimate shear failure tests (C3-C4). The calculated linear stiffness ( $k$ ), elastic limit (A), initial failure point (B) and ultimate failure point (C) are illustrated.

Shear displacements at initial failure and the elastic limit were also determined. Energy stored in the passive tissues during the acute failure test was also calculated by integrating the force versus displacement relationship between the starting location (zero shear displacement) and the displacements at each of the three determined failure points.

### **3.2.6 Statistical analysis**

Randomization of the specimens into each of the twelve different acute shear failure testing conditions was assessed using a three factor (LEVEL, COMPRESSION and POSTURE) analysis of variance (ANOVA) for measurements of endplate area, average facet angle and facet tropism (SAS 9.1, SAS Institute Inc., Cary, NC, USA). Similarly, a three factor ANOVA was used to test for statistically significant differences in each of the three shear failure tolerances, their corresponding displacements and stored energy values as well as the linear stiffness. Tukey's post-hoc analyses were performed for any significant main effects or interactions. The level of statistical significance was set to  $p < 0.05$  for all tests. Effect sizes for all statistically significant differences between pairs of means were evaluated using Cohen's  $d$ .

### **3.3 RESULTS**

#### **3.3.1 Specimen randomization**

Facet surfaces for specimens assigned to the 45% compressive load had smaller angles relative to the frontal plane than either of the 30% and 60% groups by  $2.5^\circ$  ( $p = 0.0234$ ,  $d = 0.82$ ) and  $2.2^\circ$  ( $p = 0.0459$ ,  $d = 0.69$ ) respectively (Table 3.1). There were no other statistically significant differences in any of the specimen specific measurements or characteristics across the different compressive loads and postures ( $p \geq 0.0526$ ) (Table 3.2).

Table 3.1 – Characteristics of specimens assigned to each compressive load group for acute shear failure. Standard error of each mean is presented in parentheses. Asterisks indicate measures that contain statistically significant differences between the compressive load magnitudes. Means within a single measure and with the same letter are statistically similar.

Compression	Extension Limit (degrees)	Flexion Limit (degrees)	Endplate Area (mm <sup>2</sup> )	Average Facet Angle (degrees)	Facet Tropism (degrees)	Specimen Height Loss (mm)
<b>15%</b>	-4.5 (0.1)	8.0 (0.2)	657.7 (12.1)	45.4 (0.5) A,B	3.1 (0.4)	0.85 (0.05) A
<b>30%</b>	-4.4 (0.2)	7.9 (0.3)	667.2 (12.8)	47.0 (0.6) A	4.3 (0.5)	1.85 (0.07) B
<b>45%</b>	-4.4 (0.1)	8.0 (0.2)	683.1 (15.4)	44.5 (0.7) B	3.8 (0.4)	2.74 (0.07) C
<b>60%</b>	-4.5 (0.1)	8.0 (0.2)	678.8 (13.1)	46.7 (0.7) A	3.3 (0.5)	3.88 (0.17) D
<b><i>p</i></b>	0.9383	0.9898	0.5498	0.014*	0.0526	< 0.0001*

Table 3.2 – Characteristics of specimens assigned to each posture group for acute shear failure. Standard error of each mean is presented in parentheses. Asterisks indicate measures that contain statistically significant differences between the compressive load magnitudes. Means within a single measure and with the same letter are statistically similar.

<b>Posture</b>	<b>Extension Limit (degrees)</b>	<b>Flexion Limit (degrees)</b>	<b>Endplate Area (mm<sup>2</sup>)</b>	<b>Average Facet Angle (degrees)</b>	<b>Facet Tropism (degrees)</b>	<b>Specimen Height Loss (mm)</b>
<b>Extended</b>	-4.4 (0.1)	7.8 (0.2)	665.8 (11.3)	46.3 (0.6)	4.2 (0.4)	2.19 (0.19) A
<b>Neutral</b>	-4.5 (0.1)	8.2 (0.2)	658.9 (12.2)	45.8 (0.5)	3.2 (0.4)	2.49 (0.22) B
<b>Flexed</b>	-4.4 (0.1)	7.9 (0.2)	690.4 (10.7)	45.5 (0.5)	3.4 (0.4)	2.31 (0.24) A,B
<b><i>p</i></b>	0.7682	0.489	0.1495	0.5713	0.3527	0.0467*

### 3.3.2 Vertebral level

All three measurements obtained at ultimate failure were smaller (22% decrease in ultimate force, 21% decreased in ultimate displacement and 36% decrease in energy stored until ultimate failure) for the C3-C4 specimens than the C5-C6 specimens ( $p \leq 0.001$ ,  $0.71 \leq d \leq 1.00$ ) (Table 3.3).

Table 3.3 – Ultimate force, displacement and energy stored during acute shear failure for specimens from each vertebral level. Standard error of each mean is presented in parentheses. Asterisks indicate a statistical difference between means for a single measure.

Vertebral Level	Ultimate Force (N)	Ultimate Displacement (mm)	Ultimate Energy (J)
C3-C4	2095.2 (75.3)	5.3 (0.4)	8.2 (0.8)
C5-C6	2648.6 (86.0)	6.8 (0.3)	12.8 (0.7)
<i>p</i>	0.0001*	< 0.0001*	< 0.0001*

Displacement at the elastic limit for C3-C4 specimens was  $0.38 \pm 0.09$  mm smaller than C5-C6 specimens ( $p < 0.0001$ ,  $d = 1.79$ ).

### 3.3.3 Compression

Each level of compressive load produced greater reductions in specimen height ( $p < 0.0001$ ,  $1.84 \leq d \leq 6.72$ ) (Table 3.1). Ultimate force and initial failure force at the 15% compressive load were smaller than failure loads at either the 45% (ultimate force  $p =$

0.0055, **d** = 0.78; initial failure force  $p = 0.0032$ , **d** = 0.79) or 60% (ultimate force  $p < 0.0001$ , **d** = 1.44; initial failure force  $p < 0.0001$ , **d** = 1.73) compressive loads (Table 3.4).

Table 3.4 – Measures of the elastic limit, initial and ultimate acute shear failure loads for each compressive load group. Standard error of each mean is presented in parentheses. Means within a single measure and with the same letter are statistically similar.

Compression	Elastic Limit (N)	Initial Failure Force (N)	Ultimate Failure Force (N)
<b>15%</b>	935.7 (62.1) A	1711.3 (103.7) A	2003.3 (79.5) A
<b>30%</b>	1235.6 (90.9) B	2006.3 (116.6) A,B	2310.8 (108.9) B
<b>45%</b>	1335.4 (72.4) B	2169.9 (135.4) B	2431.7 (140.3) B,C
<b>60%</b>	1549.0 (59.0) C	2582.6 (144.5) C	2741.9 (129.1) C

Likewise, ultimate failure force and initial failure force at the 30% compressive load were smaller than at the 60% compressive load (ultimate force  $p = 0.0051$ , **d** = 0.75; initial failure force  $p = 0.0001$ , **d** = 0.92) (Table 3.4). Initial failure force was also smaller at the 45% compressive level when compared to the 60% compressive level ( $p = 0.0095$ , **d** = 0.61) (Table 3.4). Force at the elastic limit was smaller at the 15% compressive load than all other compressive loads ( $p \leq 0.0017$ ,  $0.80 \leq \mathbf{d} \leq 2.11$ ) (Table 3.4). Force at the elastic limit was also higher at the 60% compressive load than all other compressive loads ( $p \leq 0.042$ ,  $0.67 \leq \mathbf{d} \leq 2.11$ ) (Table 3.4). Force at the elastic limit at the 15% compressive load was smaller than at the 30% compressive load ( $p = 0.0027$ , **d** = 0.77) (Table 3.4).



Displacement at the elastic limit was  $0.34 \pm 0.15$  mm smaller for specimens under 45% compressive force than the 30% compressive force ( $p = 0.0326$ ,  $d = 0.68$ ). Linear shear stiffness of the specimens under 15% compressive load were smaller than linear stiffness at all three other compressive loads ( $p \leq 0.0136$ ,  $0.89 \leq d \leq 1.81$ ) while linear stiffness of specimens exposed to the 30% compressive load were also smaller than stiffness of specimens at the 60% compressive load ( $p = 0.0004$ ,  $d = 1.08$ ) (Figure 3.5). Lastly, energy stored until initial failure for the 60% compressive load was higher than energy stored at all other compressive loads ( $p \leq 0.0025$ ,  $0.56 \leq d \leq 0.77$ ) (Figure 3.6).

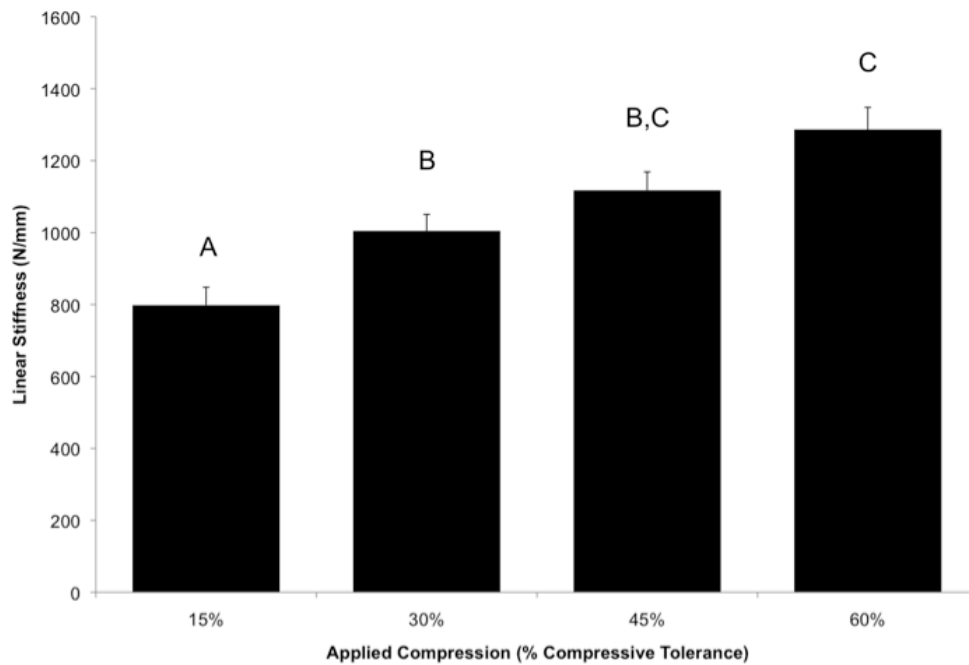


Figure 3.5 – Linear shear stiffness increases with static compressive load. Error bars represent the standard error of the mean. Means with different letters are statistically different from one another.

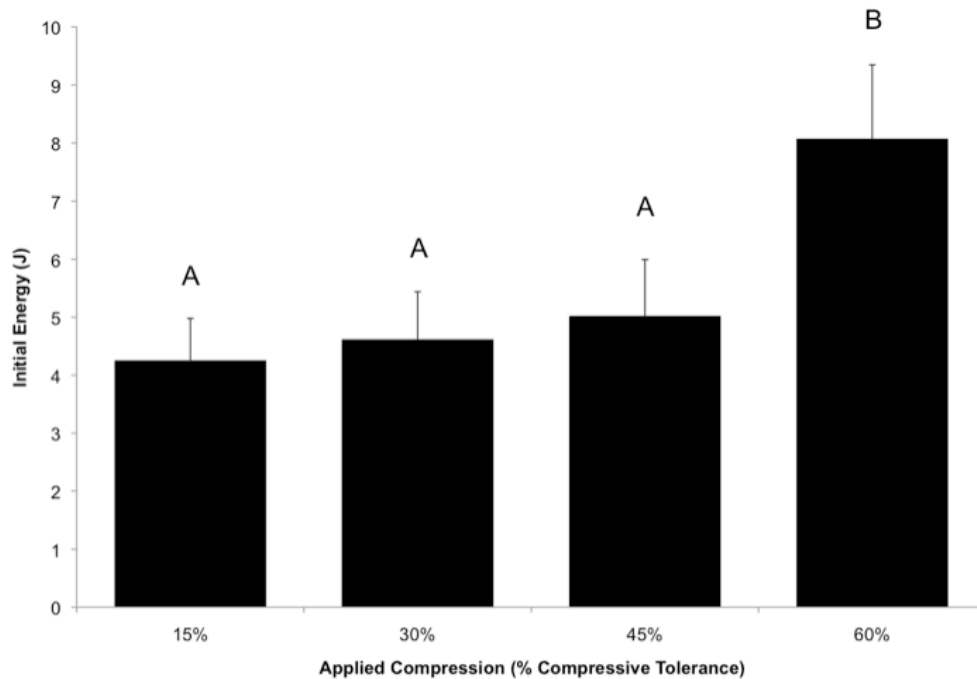


Figure 3.6 – Energy stored until the initial failure point with increased static compressive load. Error bars represent the standard error of the mean. Means with different letters are statistically different from one another.

### 3.3.4 Posture

Specimens tested in flexed postures had greater height loss than those tested in extended postures ( $p = 0.0374$ ,  $d = 0.27$ ) (Table 3.2). Ultimate force decreased for each posture condition with the highest ultimate force being sustained in the extended posture ( $p \leq 0.0176$ ,  $0.51 \leq d \leq 1.08$ ) (Figure 3.7).

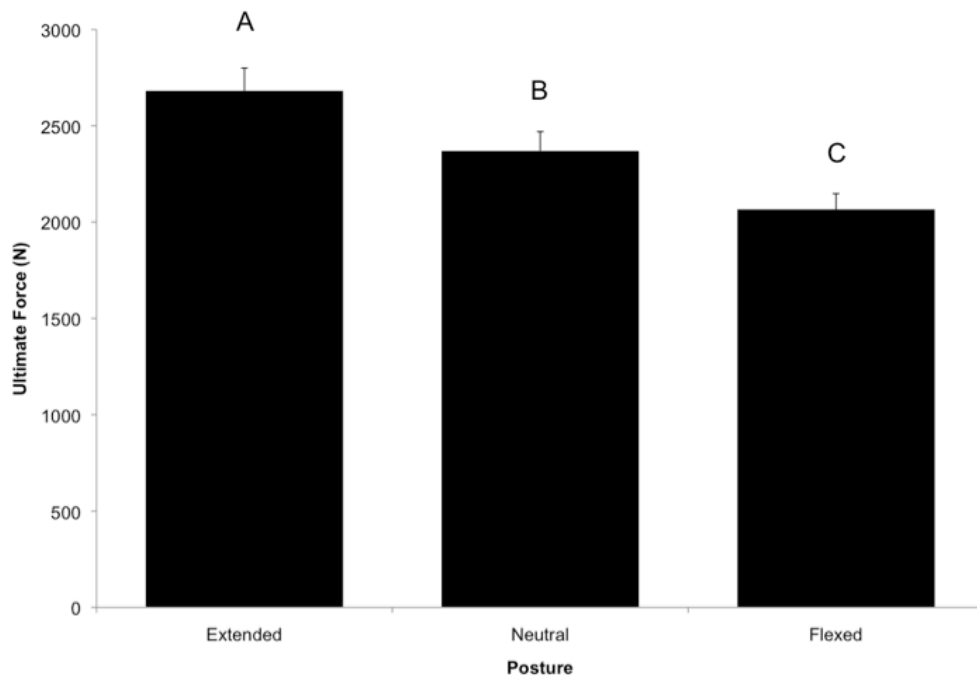


Figure 3.7 – Ultimate shear force sustained in each of the extended, neutral and flexed postures. Error bars represent the standard error of the mean. Means with different letters are statistically different from one another.

The flexed posture had lower shear stiffness than either the extended ( $p = 0.0012$ ,  $d = 0.71$ ) or neutral ( $p = 0.0009$ ,  $d = 0.82$ ) postures (Figure 3.8). Flexed postures also had reductions in energy stored until ultimate failure ( $p = 0.0205$ ,  $d = 0.65$ ) when compared to the extended postures (Figure 3.9).

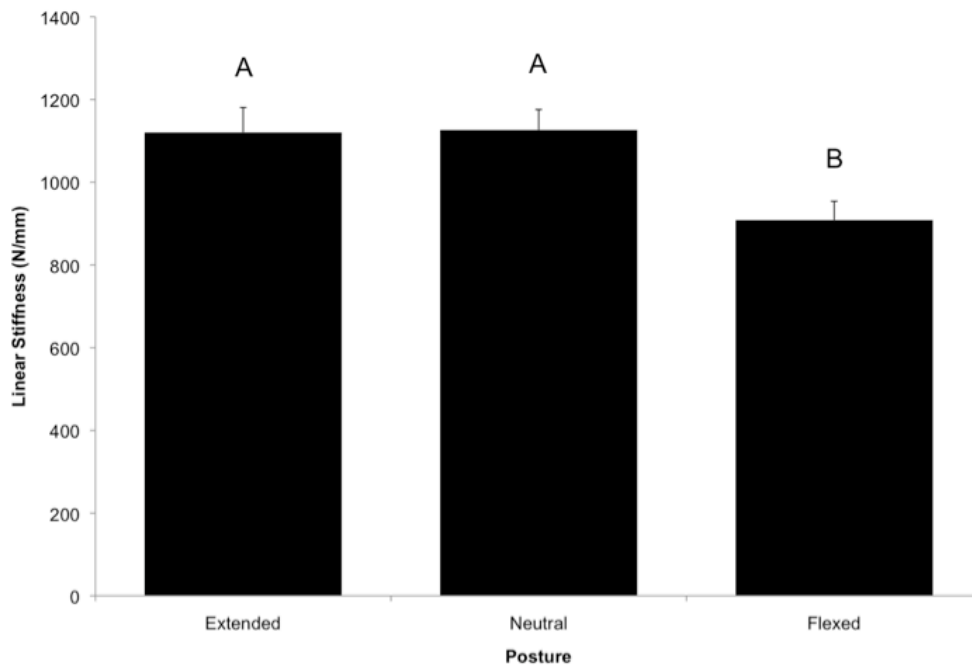


Figure 3.8 – Linear shear stiffness in each of the extended, neutral and flexed postures. Error bars represent the standard error of the mean. Means with different letters are statistically different from one another.

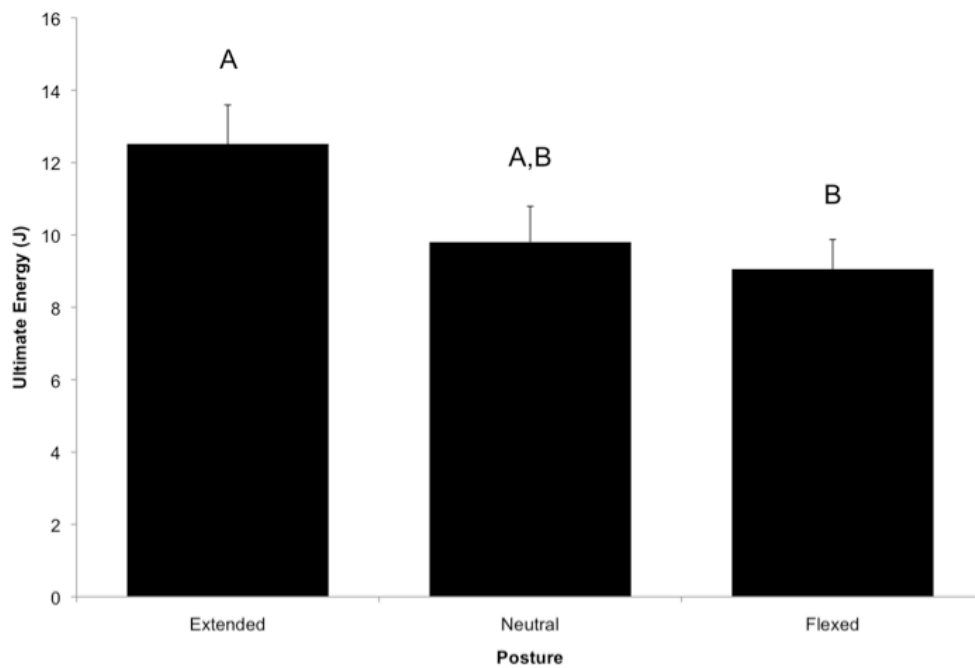
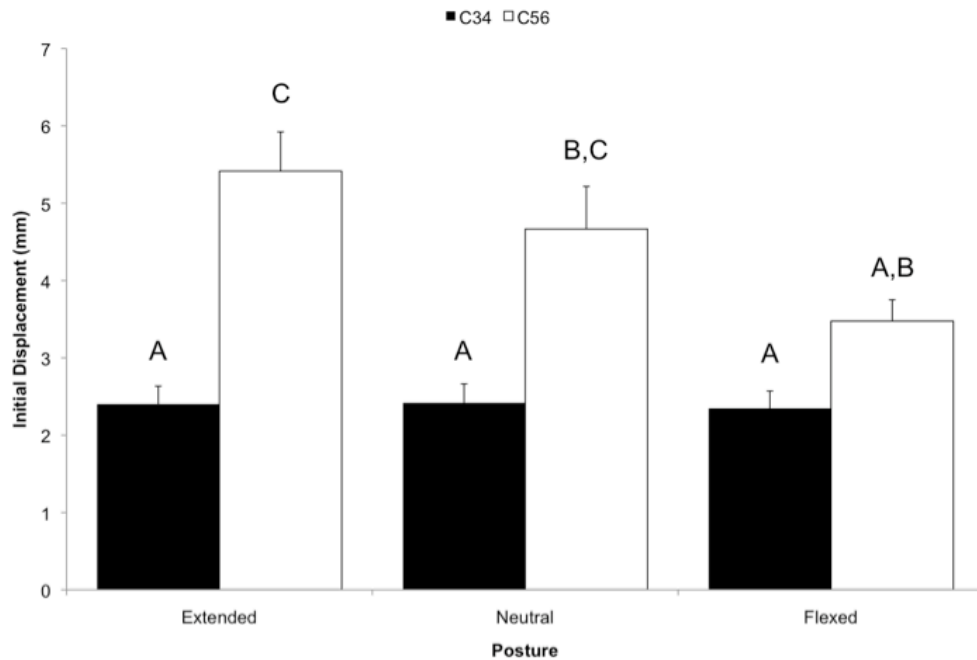
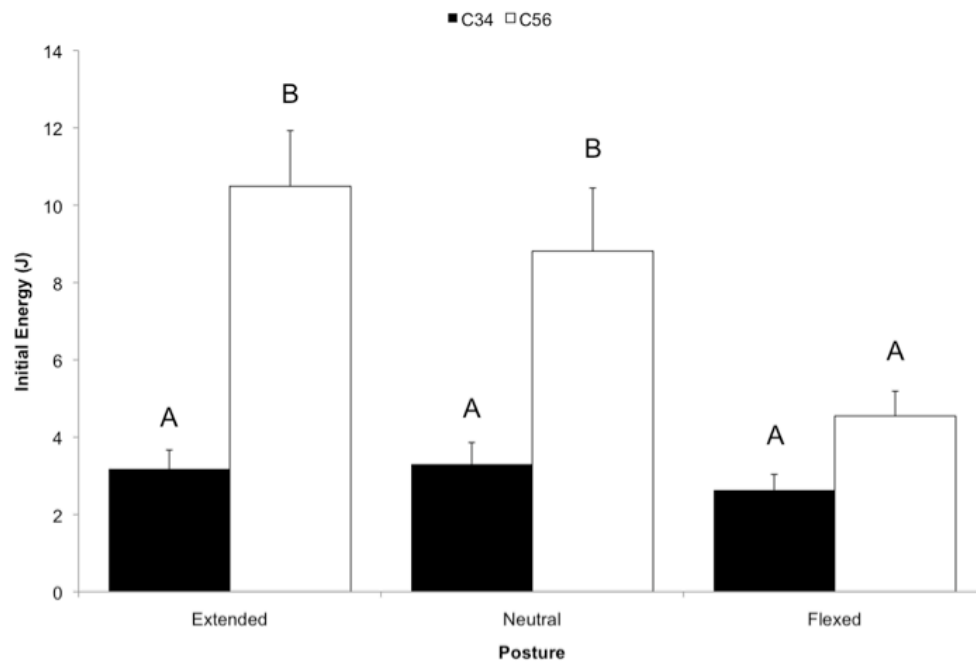


Figure 3.9 – Energy stored until ultimate shear failure in each of the extended, neutral and flexed postures. Error bars represent the standard error of the mean. Means with different letters are statistically different from one another.

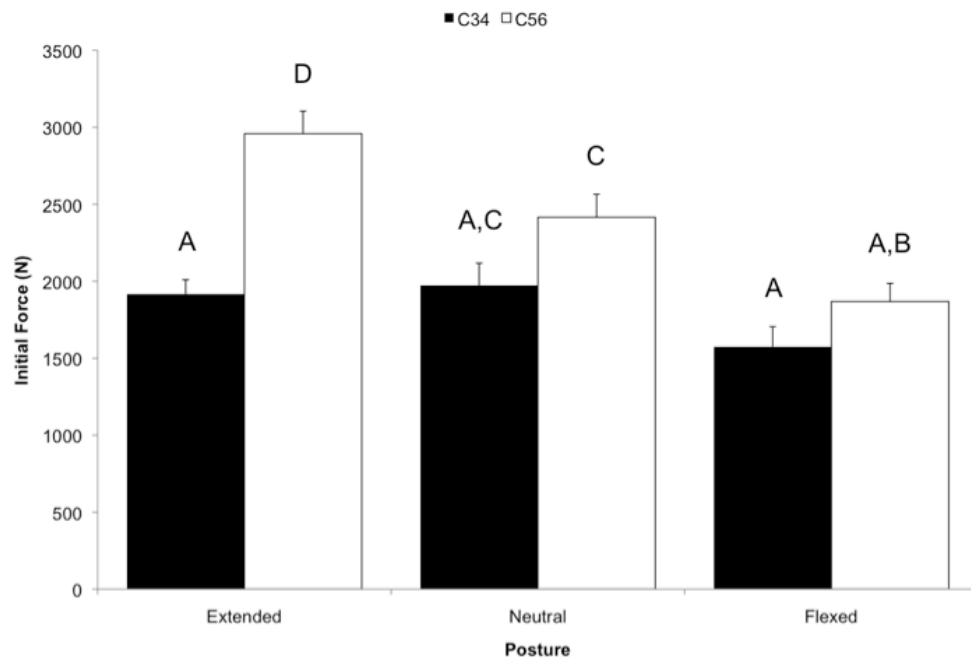
Displacement at the elastic limit was  $0.36 \pm 0.13$  mm smaller for specimens tested in flexed versus extended postures ( $p = 0.0026$ ,  $d = 0.69$ ). Force and energy stored demonstrated statistically significant interactions between vertebral level and posture for both the elastic limit and initial failure point ( $p \leq 0.0171$ ). Initial failure displacement also demonstrated a statistically significant interaction between vertebral level and posture ( $p = 0.0484$ ). Initial failure displacement and energy stored until initial failure were smaller for the C3-C4 than C5-C6 specimens in both the extended ( $p < 0.0001$ ,  $1.76 \leq d \leq 1.97$ ) and neutral ( $p \leq 0.0012$ ,  $1.16 \leq d \leq 1.36$ ) postures (Figure 3.10A-B).



A.)



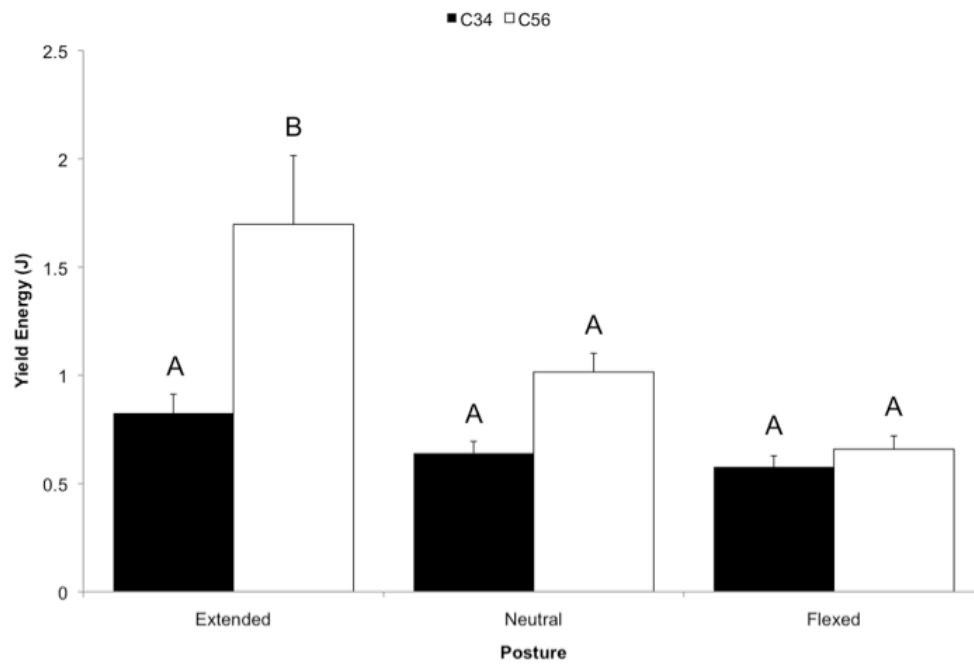
B.)



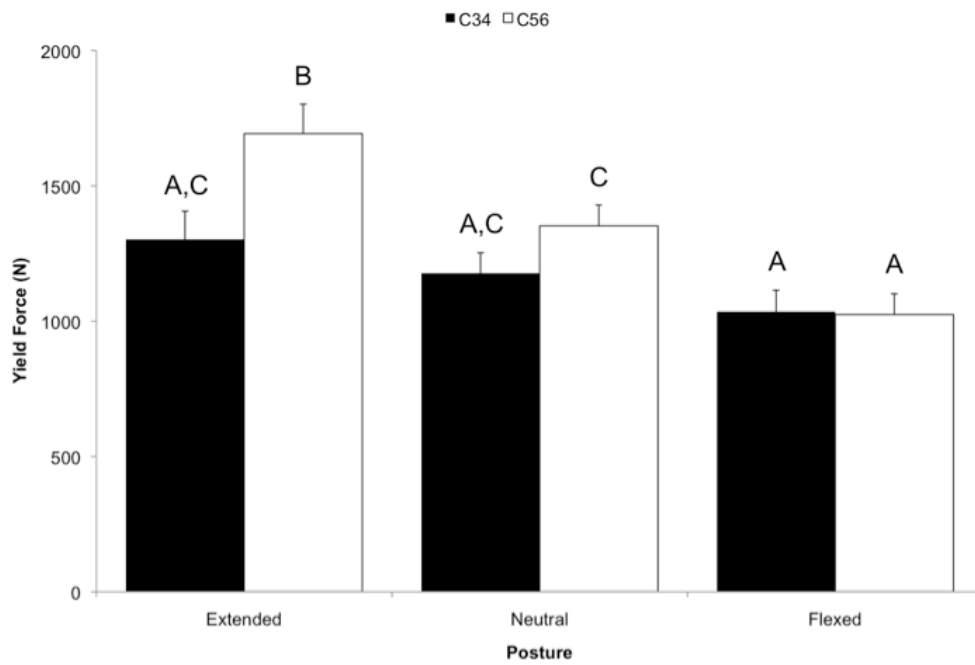
C.)

Figure 3.10 – Displacement (A.), energy stored (B.) and force (C.) at initial failure for both C3-C4 and C5-C6 specimens tested in each of the extended, neutral and flexed postures. Error bars represent the standard error of the mean. Means with different letters are statistically different from one another.

Energy stored until the elastic limit ( $p < 0.0001$ ,  $d = 1.23$ ) was smaller for the C3-C4 than C5-C6 specimens in the extended posture (Figure 3.11A).



A.)



B.)

Figure 3.11 – Energy stored (A.) and force (B.) at the elastic limit for both C3-C4 and C5-C6 specimens tested in each of the extended, neutral and flexed postures. Error bars represent the standard error of the mean. Means with different letters are statistically different from one another.

Initial failure force and force at the elastic limit decreased at each posture condition for the C5-C6 specimens with the highest forces being sustained in the extended posture ( $p \leq 0.0347$ ,  $0.95 \leq \mathbf{d} \leq 2.27$ ) (Figures 3.10C, 3.11B). C5-C6 specimens tested in the flexed posture also had smaller initial failure displacements than C5-C6 specimens tested in extended postures ( $p = 0.0066$ ,  $\mathbf{d} = 1.22$ ) (Figure 3.10A). Furthermore, C5-C6 specimens tested in the flexed posture also stored less energy until initial failure than either the extended ( $p = 0.0004$ ,  $\mathbf{d} = 1.38$ ) or neutral ( $p < 0.0225$ ,  $\mathbf{d} = 0.89$ ) postures (Figure 3.10B).

### 3.3.5 Post-failure analysis

The predominant posterior element injury (65% of all specimens) was a bilateral fracture of the cranial vertebra's pars interarticularis (Table 3.5, Figure 3.12). Other common injuries that occurred were bilateral and unilateral fractures of the caudal vertebra's pars interarticularis (18% bilateral; 21% unilateral) and/or unilateral facet fractures (Table 3.5, Figure 3.13).

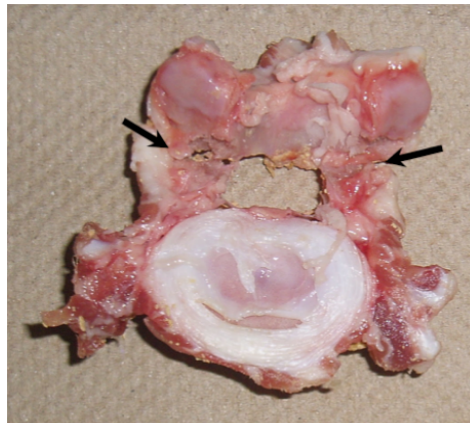


Figure 3.12 – Transverse image of a C3 vertebra following acute shear failure. The black arrows indicate the bilateral pars interarticularis fracture that was the predominant injury present in shear failure.



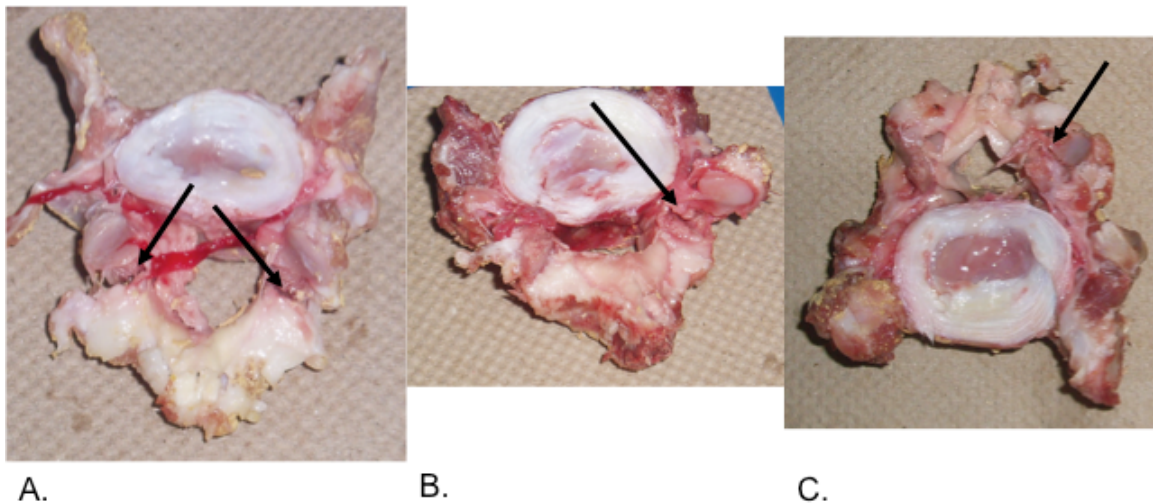


Figure 3.13 – Images of a bilateral pars interarticularis fracture of the caudal vertebra (A), unilateral pars interarticularis fracture (B), and a unilateral facet fracture (C). Incidence rate of bilateral cranial pars interarticularis fracture was much higher for C3-C4 specimens than C5-C6 specimens (41.6% difference) (Table 3.5). Increasing compression also increased the incidence of bilateral fracture of the cranial pars interarticularis with 88% of specimens demonstrating this failure pattern at the 60% compressive load magnitude (Table 3.5). Flexed postures had lower incidence rates of bilateral fracture of the cranial pars interarticularis than either the extended (28.1% difference) or neutral (25% difference) postures (Table 3.5). Instead, flexed postures exhibited higher incidence of caudal bilateral pars interarticularis fractures than either the extended or neutral postures (Table 3.5, Figure 3.13A).

Table 3.5 – Post-failure observations of tissue damage arranged within vertebral level, compressive load, posture and overall. Values are reported as a percentage of all specimens in each group.

	<b>Pars Interarticularis</b>				<b>Facet</b>				<b>Endplate</b>	
	Cranial		Caudal		Superior		Inferior		Superior	Inferior
	Bilateral	Unilateral	Bilateral	Unilateral	Bilateral	Unilateral	Bilateral	Unilateral		
<b>C3-C4</b>	85.4	0.0	8.3	6.3	0.0	0.0	0.0	0.0	0.0	4.2
<b>C5-C6</b>	43.8	6.3	27.1	35.4	4.2	22.9	0.0	0.0	2.1	0.0
<b>15%</b>	37.5	4.2	25.0	37.5	0.0	16.7	0.0	0.0	0.0	0.0
<b>30%</b>	58.3	8.3	16.7	20.8	0.0	20.8	0.0	0.0	0.0	4.2
<b>45%</b>	75.0	0.0	12.5	12.5	8.3	4.2	0.0	0.0	0.0	4.2
<b>60%</b>	87.5	0.0	16.7	12.5	0.0	4.2	0.0	0.0	4.2	0.0
<b>Extended</b>	75.0	6.3	6.3	21.9	0.0	15.6	0.0	0.0	0.0	3.1
<b>Neutral</b>	71.9	0.0	15.6	15.6	6.3	3.1	0.0	0.0	0.0	0.0
<b>Flexed</b>	46.9	3.1	31.3	25.0	0.0	15.6	0.0	0.0	3.1	3.1
<b>Overall</b>	<b>64.6</b>	<b>3.1</b>	<b>17.7</b>	<b>20.8</b>	<b>2.1</b>	<b>11.5</b>	<b>0.0</b>	<b>0.0</b>	<b>1.0</b>	<b>2.1</b>

### 3.4 DISCUSSION

Results from this investigation demonstrate that facet interaction modulates shear failure tolerance for the vertebral joint. Interaction between articulating facets is altered by both compressive force and postural deviation and will influence shear injury potential during activities such as manual materials handling. Increasing compression enhanced shear failure tolerance and stiffness while vertebral joint flexion reduced these measures. There was no statistical interaction between compression and posture as they related to shear failure tolerance. Extension produced an average increase of 12.8% while flexion produced an average decrease of 13.2% in ultimate shear failure tolerance. Meanwhile, ultimate shear failure tolerance increased by an average of 11.1% with each 15% increment in compressive force. Based on these results, compression and postural deviations have a similar magnitude of influence on ultimate shear failure tolerance. However, posture must carefully be considered since flexion can diminish the vertebral joint's capacity to withstand shear loads.

Similar to the current investigation, previous studies have shown that linear shear stiffness increases with larger compressive forces (Janevic et al., 1991; Gardner-Morse and Stokes, 2003). In contrast to the findings of this investigation, Cripton and colleagues (1995) found that increasing compression generated very small changes in ultimate shear failure tolerance. These investigators applied a maximum compressive force of 2200 N, which is smaller than average compressive loads used for specimens assigned to the 30%, 45% and 60% of compressive failure tolerance groups in our investigation. It is possible that the difference between compressive loads used by Cripton and colleagues (1995) was not large enough to generate a difference in shear failure tolerance.

Compression causes reductions in overall specimen height (van der Veen et al., 2007) and has been hypothesized to decrease the space between articulating facets (Lin et al., 1978). The intervertebral disc provides increases in linear shear stiffness with higher compressive forces (Gardner-Morse and Stokes, 2003). Meanwhile, contact area between articulating facets changes with alterations in specimen height (Lorenz et al., 1983; Liu et al., 2006). Specifically, facet contact area increases by as much as 36% and 61% with 1mm and 4 mm reductions in disc height respectively (Dunlop et al., 1984). Reducing specimen height alters facet contact area and may also change the center of facet contact pressure, which may directly lead to increases in linear shear stiffness and shear failure tolerance. The moment arm between the center of facet contact pressure and the location of the pars interarticularis has been implicated as a modulator of anterior shear failure tolerance (Cyron et al., 1976; Yingling and McGill, 1999). A theory for modulation of ultimate shear failure tolerance that has been supported by the results of this investigation is that reducing vertebral joint height and increasing facet contact area with higher compressive forces may also reduce the moment arm of facet contact force relative to the pars interarticularis. This theory implies that larger applied shear forces would be required to generate a critical bending moment for fracturing the pars.

Flexed postures increase the gap between articulating facets while extended postures have been found to decrease the gap (Drake et al., 2008). Results from this investigation showed that vertebral joint shear failure tolerance and linear shear stiffness is reduced for flexed postures while extended postures did not significantly influence failure loads. Investigators had previously found an increase in shear failure tolerance and no significant change in linear stiffness between specimens tested in flexed and neutral

postures (Yingling and McGill, 1999). These authors attributed their findings to increases in the moment arm length of the facet contact force relative to the pars interarticularis (the primary site of failure). However, for two identical specimens, increasing the moment arm length of the facet contact force relative to the pars interarticularis by flexing one specimen should in theory reduce the force required to generate the same bending moment at the pars interarticularis. Thus, if the bending moment at the pars interarticularis is the primary factor governing shear failure, a larger moment arm (created by flexed postures) will require less shear force to produce failure. This theory is more congruent with the findings of the current study. Thus, it is our hypothesis that decreases in measured shear failure tolerance with flexed postures may be directly related to an increased moment arm length between the centroid of facet contact force and the pars interarticularis (Figure 3.14B). Conversely, increases in measured shear failure tolerance may be a direct result of decreases in the moment arm length (Figure 3.14C-D). It is possible that differences in loading protocols and experimental setup as well as failure criteria between the current investigation and the work of Yingling and McGill (1999) could account for the differences in results.

*In vivo* loading of the lumbar spine involves a complex combination of forces in all three rotational and translational degrees of freedom. Furthermore, tissue damage can occur due to excessive loading in any of these six degrees of freedom. Similar to the results of this study that found decreased shear failure tolerance with flexion, Gunning and colleagues (2001) have also shown that a flexed posture reduced the vertebral joint's compressive failure tolerance. While in a flexed posture, any possible increase in shear failure tolerance resulting from higher compressive loads also increases the risk of injury

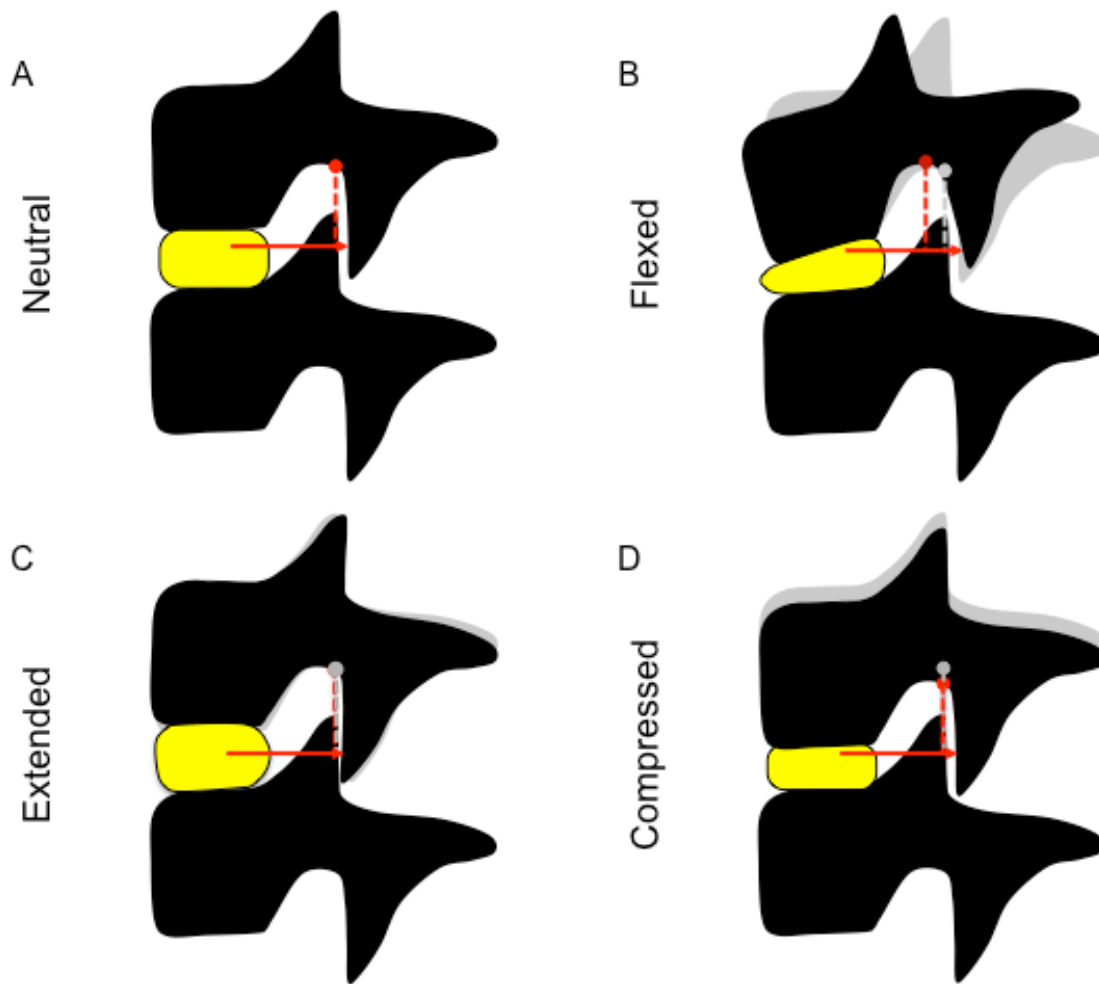


Figure 3.14 – Illustration of how posture and compressive force may alter the moment arm length between the centroid of facet contact force and the pars interarticularis between the neutral (A), flexed (B), extended (C), and compressed (D) conditions. Flexion may produce an increase in moment arm length while extension and compression may decrease the moment arm length, which would respectively require decreased and increased measured shear failure forces.

due to excessive compressive loading. Flexed postures have more influence on injury thresholds for the lumbar spine since these postures decrease the failure tolerance of the vertebral joint in multiple degrees of freedom.

Ascribed compressive load for each specimen was based on an estimate of the specimen's compressive failure tolerance in the neutral posture (Parkinson et al., 2005). In a flexed posture, the compressive failure tolerance of the porcine vertebral joint is

approximately 68% of the failure tolerance in the neutral posture (Gunning et al., 2001). Thus, compressive load magnitudes for the 60% group in the flexed posture approached the flexed compressive failure tolerance. Despite this limitation, only 4% of specimens exposed to the 60% compressive load and 3% of the flexed specimens had endplate fractures that are consistent with compressive failure. Furthermore, examination of the compressive force versus time profiles did not indicate signs of compressive failure prior to shear load application.

The shear displacement versus force relationship illustrated in Figure 3.4 demonstrates three points at which structural damage is occurring to the FSU. These three points corresponded to the elastic limit, initial failure, and ultimate failure points calculated in this study. Acute failure under shear was imposed to a porcine cervical vertebral joint by applying a backward displacement to the caudal vertebra at a constant rate. At the start of the acute shear failure test, there is a gap between the articulating inferior and superior facets of the cranial and caudal vertebrae respectively. Also at the start of the acute failure test, a ligamentous facet capsule connects the medial and lateral sides of each articulating facet to complete the facet joint capsule. Articulating facet surfaces are also covered by a layer of cartilage. The space between these articulating surfaces is also filled with synovial fluid. As shear displacement is applied, the articulating facet surfaces attempt to interact with each other, building up pressure within the facet joint capsule. The elastic limit, calculated in this study, is possibly linked to excessive stretching of the facet joint capsular ligaments. It is hypothesized that the initial failure point occurs when the ligaments surrounding the facet joint capsule rupture as a result of this pressure build-up. Following the initial failure point, the cartilaginous facet

surfaces continue to become engaged, leading to bone deformation, and subsequent fracture, of the vertebral posterior elements and ultimate vertebral joint failure under shear loading.

Typically reaction shear forces computed from linked segment models are directly related to flexed postures (McGill et al., 1998; Gregory et al., 2006; Howarth et al., 2009). McGill and colleagues (1998) defined action limits and maximum permissible limits of 500 N and 1000 N respectively for shear which is approximately 25-50% of the shear failure tolerance for specimens collected in a flexed posture from this investigation and is much lower than shear failure tolerances for specimens tested in the neutral posture. These limits are very conservative and likely are also applicable to reduced shear failure tolerance in a flexed posture. For example, lifting in a flexed posture requires extensor muscle activity to generate an internal extensor moment for returning the spine to an upright position. In a neutral posture, vertebral joint shear is modulated by a component of the extensor muscular arrangement in direct opposition to reaction shear forces (Potvin et al., 1991). Flexed postures cause the extensor muscle line of action to become more aligned with the vertebral joint's compressive axis, thus negating the direct muscular contributions to resisting shear loads (McGill et al., 2000). However, this realignment likely maintains shear failure tolerance while lifting in a flexed posture by increasing the vertebral joint compression. Thus, the hypothesis that previously defined shear action and maximum permissible limits are applicable for postural deviations is supported by findings in the current investigation demonstrating that shear failure tolerance of flexed specimens is increased with higher compressive loads.



However, flexed postures, typically associated with larger calculated reaction shear forces, reduce the vertebral joint's compressive tolerance by approximately 33% (Gunning et al., 2001). Thus, protection from shear-related injuries provided by muscular compressive force would increase vertebral joint compression that may increase the change for a vertebral joint compressive injury. This demonstrates how a scenario where protective mechanisms for shear injuries alters low-back injury potential in other modes of loading.

This study has comprehensively shown that both compressive force and postural deviation modulate shear failure tolerance of the vertebral joint. In particular, increasing compression and flexed postures respectively lead to increased and reduced vertebral joint shear failure tolerance. The hypothesized mechanism for modulation of vertebral shear failure tolerance is alteration in the moment arm length between the center of facet contact pressure and the pars interarticularis location. Due to the relationship between peak shear and low-back pain reporting, both compression and postural deviation should be considered while assessing the shear injury potential of an occupational task.

## **CHAPTER 4**

# **INFLUENCE OF VERTEBRAL MORPHOLOGY AND PARS INTERARTICULARIS BONE DENSITY AS FACTORS FOR CALCULATING ANTERIOR SHEAR FAILURE TOLERANCE FOR THE PORCINE CERVICAL SPINE: DEVELOPMENT OF A MATHEMATICAL MODEL**

## 4.1 INTRODUCTION

Normalization of sub-maximal loads relative to estimated failure limits during *in vitro* testing enhances comparison of results between animal and human specimens and can also reduce the effects of biological variability. The normalization process is particularly useful during *in vitro* studies using a cyclical loading paradigm whereby each specimen can be loaded to a percentage of its estimated tolerance in a specific mode of loading. The current investigation develops and tests errors associated with a mathematical model for predicting ultimate anterior shear failure tolerances of the porcine cervical spine.

Regression equations have been developed, tested and validated for predicting the ultimate compressive load of human (Hansson et al., 1980; Biggemann et al., 1988; Brinckmann et al., 1989) and porcine FSUs (Parkinson et al., 2005). Typically these regression equations provide a prediction of ultimate compressive load from bone mineral density and/or morphological characteristics such as endplate area. Bone mineral density can be measured using non-destructive imaging techniques such as quantitative computed tomography (QCT) (Biggemann et al., 1988; Brinckmann et al., 1989; Ebbesen et al., 1999) or dual energy x-ray absorptiometry (DXA) (Edmondston et al., 1994; Edmondston et al., 1997; Ebbesen et al., 1999; Parkinson et al., 2005). Inclusion of morphological characteristics with bone mineral density has traditionally improved the estimate of predicted ultimate compressive loads in human vertebral bodies and monkey FSUs (Biggemann et al., 1988; Dickerson et al., 2008).

The regression equations for predicting ultimate compressive load primarily use the bone mineral density from a section of the vertebral body. Since the primary bony

structures that resist anterior shear loads are the facets (Lu et al., 2005) and the pars interarticularis (Cyron et al., 1976; Yingling and McGill, 1999; Beadon et al., 2008; Gallagher et al., 2010), measures of the vertebral body bone mineral density are not appropriate for estimating vertebral ultimate shear load. Thus, new equations and methods are required to estimate anterior shear failure tolerances for the vertebral joint. As outlined by Parkinson and colleagues (2005), the method for obtaining any measures that predict failure tolerances must be non-destructive and provide accurate predictions. Destructive measurements would alter the specimen's mechanical response, failure tolerances and negates further testing. Accuracy of predicted shear failure tolerance is necessary for enhancing comparison of results obtained between human and animal models and for improving homogeneity of load exposure during sub-maximal *in vitro* repetitive loading protocols (Parkinson et al., 2005). In this regard, measurements of posterior element morphology and/or bone density are likely to be more appropriate for predicting anterior shear failure tolerances.

The purpose of this investigation was to identify specimen-specific parameters that can be measured using non-destructive methods for calculating anterior shear failure tolerances of the porcine cervical spine without loading. Accuracy of the mathematical models developed from this investigation will also be determined from an independent sample. It is hypothesized that combining measurements of bone mineral density from the posterior vertebral elements with morphological measures will produce the most feasible mathematical model for determining anterior shear failure tolerance. A secondary purpose of this investigation will be to identify critical morphological parameters that are linked to fracture risk from shear loading.

## 4.2 METHODS

### 4.2.1 Specimen preparation and assessment

#### 4.2.1.1 Specimen assessment

Forty FSUs (20 C3-C4 and 20 C5-C6) were excised from twenty frozen porcine cervical spines obtained from a local abattoir. Specimens were thawed overnight prior to removal of muscle and fat leaving an osteoligamentous FSU comprised of two vertebrae, the intervertebral disc and ligaments. Following dissection, quality of the exposed superior and inferior intervertebral disc was assessed using the grading scale outlined by Galante (1967). All specimens met the disc quality criterion of Grade 1 and were included in this investigation. Measurements of endplate anterior-posterior depth (D) and mediolateral width (W) were obtained using digital calipers for both exposed endplates. Area of each exposed endplate was calculated using the equation for area of an ellipse ( $\pi WD/4$ ) (Callaghan and McGill, 1995) (Table 4.1). The area of the FSUs intervertebral disc was estimated as the average area between the two exposed endplates (Parkinson et al., 2005). Bilateral morphological measurements of the vertebral posterior elements were also made using digital calipers (Table 4.1). Bilateral facet angles and tropism between left and right facet joints were also quantified (Boden et al., 1996) using ImageJ (National Institutes of Health, USA) from a transverse plane x-ray (Table 4.1)(Figure 4.1).

Table 4.1 – Morphological measurements, and the respective measurement device/source, for each specimen.

Meaurement	Source
Endplate Area (mm <sup>2</sup> )	Equation of ellipse Major diameter = endplate width Minor diameter = endplate depth
Facet Area (mm <sup>2</sup> )	Equation of ellipse Major diameter = facet width Minor diameter = facet height
Average Facet Angle (degrees)	Transverse plane x-ray
Facet Tropism (degrees)	Transverse plane x-ray
Superior Facet Height (mm)	Digital calipers
Superior Facet Width (mm)	Digital calipers
Superior Inside Interfacet Width (mm)	Digital calipers
Superior Outside Interfacet Width (mm)	Digital calipers
Inferior Facet Height (mm)	Digital calipers
Inferior Facet Width (mm)	Digital calipers
Inferior Inside Interfacet Width (mm)	Digital calipers
Inferior Outside Interfacet Width (mm)	Digital calipers
Cranial Pedicle Height (mm)	Digital calipers
Caudal Pedicle Height (mm)	Digital calipers
Cranial Pedicle Width (mm)	Digital calipers
Caudal Pedicle Width (mm)	Digital calipers
Cranial Lamina Height (mm)	Digital calipers
Caudal Lamina Height (mm)	Digital calipers
Cranial Lamina Width (mm)	Digital calipers
Caudal Lamina Width (mm)	Digital calipers
Cranial Pars Interarticularis Length (mm)	Digitized locations from sagittal plane x-ray
Caudal Pars Interarticularis Length (mm)	Digitized locations from sagittal plane x-ray

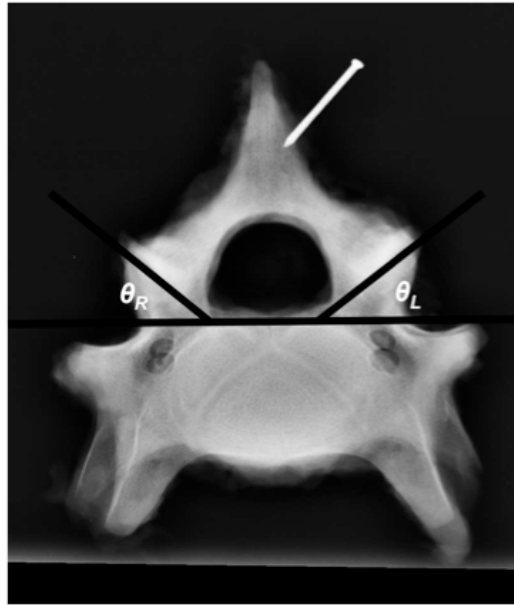


Figure 4.1 – X-ray of a specimen taken in the transverse plane. Left and right facet angles ( $\theta_L$  and  $\theta_R$ ) were measured as the angle between a line parallel to the posterior aspect of the vertebral body and a line parallel to the gap between the facets.

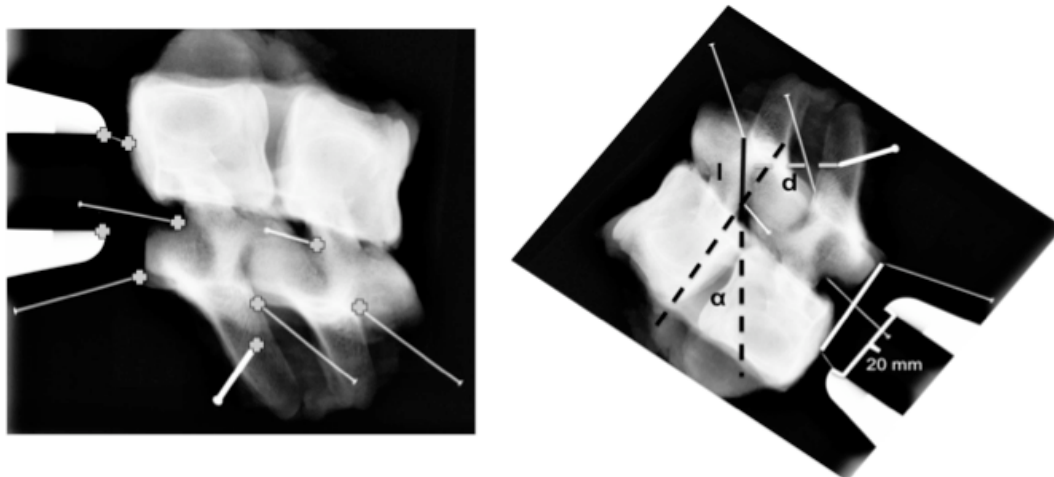
#### 4.2.1.2 Imaging of the pars interarticularis

Four metal pins (diameter = 0.5 mm) were inserted to mark the inferior and superior borders of the pars interarticularis for each of the cranial and caudal vertebrae on the specimen's left side. The superior border was defined as the lateral junction between the superior facet and the lamina while the inferior border was defined as the medial junction between the inferior facet and the pedicle. The pars interarticularis (and subsequent fracture plane after acute shear failure) for each respective vertebra was assumed to lie in the cutting plane created by connecting each pair of pins defining the superior and inferior borders. This line is also consistent with previously identified fracture lines in specimens following exposure to direct facet loading (Cyron et al., 1976) and acute shear failure (Yingling and McGill, 1999; Gallagher et al., 2010; Chapter 3). Two additional pins were inserted to the most inferior points on the exposed endplate and

left inferior facet of the caudal vertebra. One metal nail (diameter = 1.25 mm) was also inserted to the spinous process of the cranial vertebra.

A sagittal plane x-ray was taken that included the specimen with the metal pins and nail as well as a 20 mm calibration frame. Calibration between pixels and distance was identical for both the width and length of the x-ray image. Due to irregular geometry of the vertebral joint, specimen positioning for the x-ray was controlled to the unloaded and neutral posture by placing the specimen's right side onto a formed impression created in a 25.4 mm thick block of extruded polystyrene foam. The sagittal plane x-ray was digitally developed (Kodak DirectView CR500, Carestream, Toronto, ON, Canada) and planar coordinates on the image corresponding to each pinhead, nail and calibration frame endpoint were manually digitized (ImageJ, National Institutes of Health, USA) (Figure 4.2 A). Angles for the plane of the pars interarticularis (of both the cranial and caudal vertebrae) were calculated relative to the line connecting the digitized pinhead locations on the exposed inferior endplate and facet (Figure 4.2 B). Distances from the nail tip inserted into the spinous process of the cranial vertebra to the superior border for each of the cranial and caudal pars interarticularis were also determined from the digitized locations (Figure 4.2 B). Pars interarticularis lengths for the cranial and caudal vertebrae were calculated as the distance between digitized locations for the respective superior and inferior borders of the pars interarticularis.





A.)

B.)

Figure 4.2 – (A.) Sagittal plane x-ray of a vertebral specimen that illustrates digitized locations (B.) for determining the pars interarticularis length ( $l$ ), angle ( $\alpha$ ) and reference distance ( $d$ ) for computed tomography scanning of the pars interarticularis.

Metal pins were removed from the specimen following the sagittal plane x-ray, but the nail remained as a reference point for subsequent peripheral computed tomography scanning (pQCT) (XCT200L, Stratec Medizintechnik GmbH, Pforzheim, Germany). The specimen was wrapped in saline soaked gauze and then wrapped with cellophane in order to prevent specimen drying during pQCT imaging. Prior to specimen scanning a cone phantom containing material of known density was scanned in order to calibrate individual voxel intensities to measurements of tissue density. Plastic zip ties were used to rigidly mount the specimen to a custom-built plastic jig that could have the angle between two rectangular plastic plates adjusted and fixed (Figure 4.3).

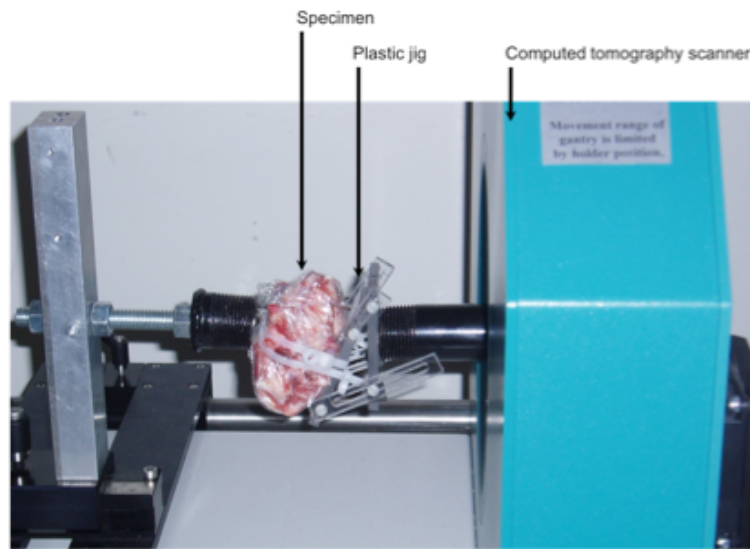


Figure 4.3 – Experimental setup for the computed tomography imaging protocol.

The specimen was positioned on the jig's surface so that the dihedral angle between the specimen's mid-sagittal plane and the plane of the jig's surface was 90 degrees. In order to align the plane of the pars interarticularis with the pQCT scan plane, the jig's angle was set to the measured pars interarticularis angle from the sagittal plane x-ray. The specimen and jig were affixed between two posts on either side of the pQCT's gantry so that the pars interarticularis plane and the jig's plastic surface, not in contact with the specimen, were both parallel to the scan plane. This mounting protocol was performed once for scanning the pars interarticularis for each of the cranial and caudal vertebrae.

Both the cranial and caudal pars interarticularis for each specimen were scanned with 5 contiguous slices consisting of 15 scans per slice (i.e. rendering 12 degrees of each slice per scan) at a scan speed of 10 mm/second, slice thickness of 1.1 mm and a voxel size of 0.2 mm. First, the reference location (nail) for scanning the pars interarticularis was determined from a scout scan (40 mm/sec) of the specimen (Figure 4.4). The gantry position of the third slice (corresponding to the location of the pars interarticularis) was

determined by adding the distance calculated between the nail and the superior border of the pars interarticularis from the sagittal plane x-ray to the reference location. This distance was greater than twice the slice thickness in order to ensure that the nail was not present in any of the slices to prevent beam-hardening artifact caused by the metal.

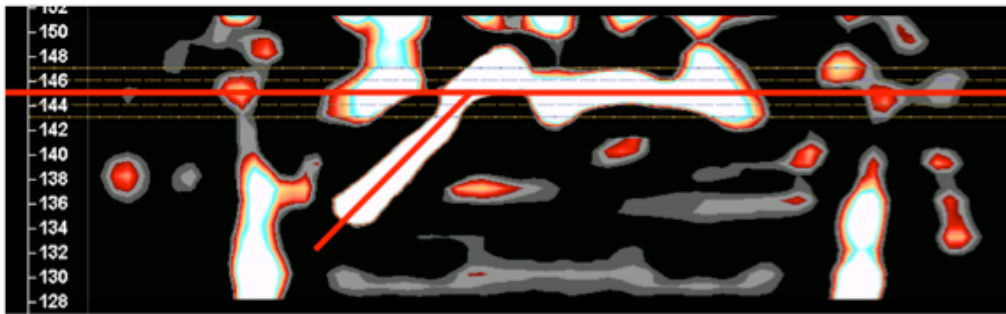


Figure 4.4 – Scout scan of a specimen. The reference location for the nail is illustrated as the intersection of the two red lines. This reference location was used to define the gantry position for computed tomography scanning of the pars interarticularis.

#### 4.2.3 Specimen fixation

For the failure testing specimens were mounted between a set of two custom aluminum cups using a combination of steel wire, screws and dental plaster. Two screws were partially inserted so that they protruded from the anterior aspect of the superior vertebral body. One screw was inserted through the bottom of each cup so that each screw pierced the center of the exposed superior and inferior endplates. An additional six screws (three for each vertebra) were inserted through threaded holes in the aluminum cups so that they were sunk approximately 5 mm into the anterior and lateral aspects of the vertebral bodies. A single length of 18 gauge galvanized steel wire was looped around the caudal vertebra's spinous process, threaded through two holes in the bottom of the aluminum cup and tightened by twisting the two ends together. Lastly, non-exothermic

dental plaster (Denstone, Miles, IN, USA) was poured into the cups, and allowed to harden, so that the exposed screws were completely immersed and that any space between the specimen and the aluminum cup was filled.

#### 4.2.4 Instrumentation

Complete three-dimensional kinematics of the vertebrae as well as the aluminum cups were measured during all tests with a single optoelectronic camera (Optotrak Certus, Northern Digital Inc., Waterloo, ON, Canada) and a series of infrared light emitting diodes (IREDs) affixed to rigid metal plates. Four IREDs were mounted to each rigid plate with a quick drying adhesive (Figure 4.5).

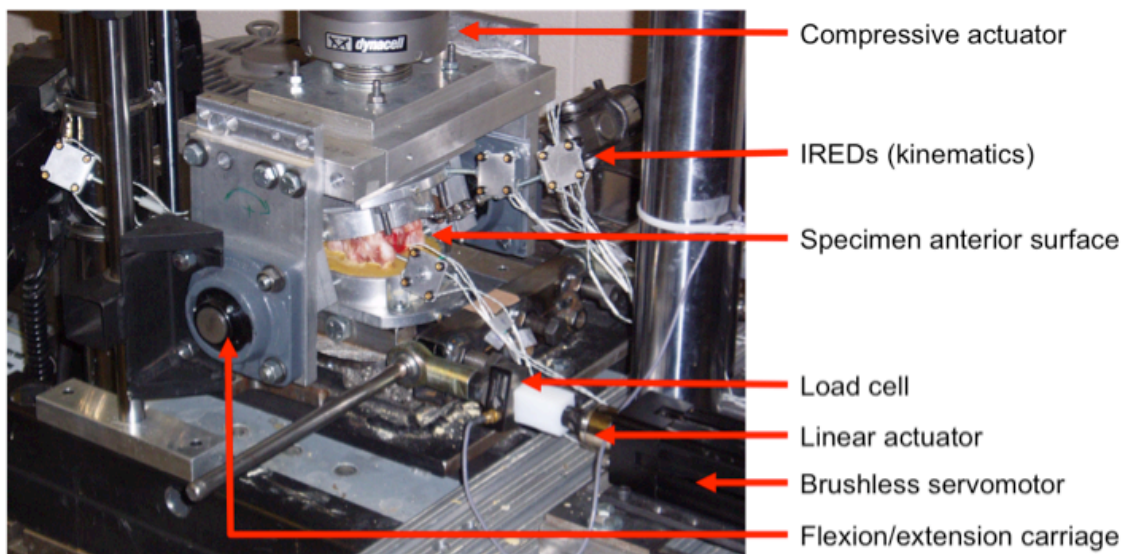


Figure 4.5 – Experimental setup for all shear protocols. IREDs = infrared light emitting diodes.

The geometrical configuration for the markers affixed to a single rigid plate was characterized and used to define the three-dimensional position and orientation of the rigid plate within the camera's predefined coordinate system. Each rigid plate measured

the three-dimensional kinematics for either a single aluminum cup or a single vertebra through a rigid coupling. Prior to loading, three specific locations within the camera's global coordinate system for each vertebra and cup were digitized with a manufactured probe that had a predefined geometrical relationship between the probe's tip and a series of four IREDs arranged in a known geometrical configuration. Global coordinates for each digitized location were continuously measured as a virtual marker during all tests using a fixed geometrical relationship between the reference rigid body's orientation and position and the location of the probe's tip within the camera's global coordinate system. The digitized locations for each component (vertebra or cup) were selected to determine a local coordinate system representing their anatomical position and orientation. For each component, the first two digitized positions defined a mediolateral anatomical axis (i.e. flexion/extension) while the third digitized point was used in conjunction with the first two points to define a plane that was subsequently used to calculate the structure's anteroposterior (lateral bend) and vertical (axial twist) axes. Three additional locations on the linear actuator were also digitized and expressed within the camera's coordinate system using the same probe. These locations were used to construct a coordinate system whose anteroposterior axis was coincident with the direction of applied displacement (and force) during all shear tests. Kinematics for all markers and digitized locations were continuously sampled at a rate of 128 Hz.

Analog data from two load cells (MLP-500, Transducer Technologies, Temecula, CA, USA) that measured applied force during all shear tests, and a torque cell (T120-106-1K, SensorData Technologies Inc., Sterling Heights, MI, USA) that measured applied flexion/extension moment during all tests were temporally synchronized with the

kinematic data and digitally sampled at a rate of 1024 Hz using a 16-bit analog to digital conversion (Optotrak Data Acquisition Unit II, Northern Digital Inc., Waterloo, ON, Canada).

#### **4.2.5 Loading protocol**

Following fixation, the cup containing the FSUs cranial vertebra was secured to a servohydraulic material testing system (Instron 8872, Instron Canada, Burlington, ON, Canada) that had been coupled to a brushless servomotor (AKM23D; Kollmorgen/Danaher Motion, Radford, VA, USA) capable of simultaneously applying flexion/extension moments to the specimen (Figure 4.5). First, a compressive preload of 300 N was applied under load control for a 15-minute duration to counter the effects of post-mortem swelling (Callaghan and McGill, 2001). The flexion/extension posture was continuously adjusted by monitoring the torque cell feedback loop and driving the servomotor in position control to reduce the joint moment throughout the 15-minute duration in order to determine the position where zero or the smallest moment possible was recorded by the torque cell.

Following the preload, five continuous repeats of position controlled passive flexion/extension were performed at a rate of 0.5 degrees/second, and under a constant load controlled compressive force of 300 N (Callaghan and McGill, 2001) to determine the specimen's neutral zone for rotational loading about the flexion/extension axis. The cup containing the FSU's caudal vertebra was allowed to translate freely in the horizontal plane during the preload and passive flexion/extension tests on metallic ball bearings that provided a near-frictionless surface (See Figure 3.3A). Flexion and extension angles

where the moment versus angle relationship deviated from linear for the last three repeats were defined as endpoints of a linear region similar to the neutral zone (Panjabi, 1992; Callaghan and McGill, 2001).

The neutral position defined at the end of the 15-minute preload identified a position within the specimen's neutral zone that satisfies a zero flexion/extension moment. However, there are many flexion/extension angles within the neutral zone that simultaneously satisfy the zero moment condition. The first position that satisfies the zero flexion/extension moment condition is defined as the first approximation of the neutral posture. Using data provided under similar load and testing conditions (Callaghan and McGill, 2001), the neutral posture was set to be 36% of the neutral zone length from the selected extension limit (Equation 4.1).

$$\theta_{neutral} = \theta_{ext} + 0.36(\theta_{flex} - \theta_{ext}) \quad (4.1)$$

This was performed so that each specimen received the same approach for determining the neutral posture. The flexion and extension limits determined from the passive test were redefined in reference to the calculated neutral posture.

For shear testing, the cup containing the specimen's caudal vertebra (either C4 or C6) was rigidly interfaced with two linear actuators (RSA24, Tolomatic Inc., Hamel, MN, USA) driven by a pair of brushless servomotors (AKM22E, Danaher Motion Inc., Radford, VA, USA) (Figure 4.5). This constrained sliding of the caudal vertebra to allow only the imposed anterior/posterior displacements applied by the linear actuators during all shear tests (See Figure 3.3B). The linear actuators were equidistant from the

specimen's mid-sagittal plane in order to prevent application of an axial twisting moment and were controlled in parallel to insure equal movement profiles. A uniaxial load cell (MLP-500, Transducer Technologies, Temecula, CA, USA) mounted in series to each linear actuator was used to measure applied shear force during all tests.

In addition to the flexion/extension passive tests, specimens were also preconditioned in anterior/posterior shear under position control prior to the acute failure protocol. Displacement during anterior/posterior shear preconditioning was applied at a constant rate of 0.05 mm/second using a continuous motion control algorithm (Appendix A.1). The targets were  $\pm 400$  N (positive force being anterior shear and negative force being posterior shear) of applied shear force for preconditioning. This target was approximately 14% of the ultimate anterior shear failure load (van Dieën et al., 2006; Gallagher et al., 2010).

A load controlled compressive force equal to 15% ( $1546.8 \pm 22.7$  N) of each specimen's predicted compressive failure tolerance was applied during the acute failure test. Compressive failure tolerance for each specimen was determined using average endplate area as the input to a previously determined linear regression equation (Parkinson et al., 2005). The chosen compressive load for this study was similar to prior investigations of acute shear failure tolerances (van Dieën et al., 2006; Gallagher et al., 2010). The reference posture determined from the flexion/extension passive test was used as the neutral posture for acute shear failure tests. Shear failure was induced for each specimen by applying shear displacement under position control at a constant rate of 0.15 mm/second (Appendix A.2). This displacement rate was consistent with a previous acute shear failure protocol (van Dieën et al., 2006) and was targeted to apply shear load at a



rate that was consistent with shear loading rates while lifting a load deemed safe for 99% of the population from the floor to waist height (Howarth et al., 2009).

Following the shear failure protocol, the specimen was returned to the neutral position and uncoupled from the linear actuators. A second flexion/extension passive test was performed using the same load and displacement conditions as the test performed prior to the acute failure protocol.

#### **4.2.6 Post-failure analysis**

Specimens were carefully removed from their fixation upon completion of the loading protocol. A sagittal plane x-ray was taken of the specimen to identify possible locations of bone failure. Sinking the specimen into a 25.4 mm thick block of extruded polystyrene foam controlled positioning of the specimen within the x-ray suite. Each specimen was carefully sectioned into individual vertebrae and photographed. Bone failure was re-assessed both manually and visually by an investigator.

#### **4.2.7 Data processing and analysis**

##### *4.2.7.1 Force versus displacement data*

Digitally sampled voltages from each load cell were calibrated to shear force and filtered using a second order dual-pass Butterworth digital filter with a cutoff frequency of 3.5 Hz. Filtered forces were also downsampled to 128 Hz in order to match the kinematic sampling rate. Total applied shear force was calculated as the sum of the forces recorded from the two load cells. Kinematic data from the virtual markers were also

filtered using a second order dual-pass Butterworth digital filter with a cutoff frequency of 2.5 Hz. Filter cutoff frequencies were determined from residual analyses conducted on data collected during each shear failure test (Appendix B.1).

Three-dimensional orientation and position of the coordinate system for each vertebra and cup were transformed from the camera's global coordinate system into the local actuator-based coordinate system for the complete duration of the shear failure test. Vertebral shear displacement was calculated at each instant as the difference in position between the origins of each vertebra-based coordinate system with respect to the orientation of the actuator-based coordinate system. Ultimate shear force was defined as the maximum shear force achieved throughout the failure test and ultimate displacement was the shear displacement that coincided with the ultimate shear force.

#### *4.2.7.2 pQCT image processing*

The third slice from each series of 5 contiguous slices was chosen for analysis of pars interarticularis bone density and area. The following was performed for both the cranial and caudal vertebrae of each specimen so that a total of 80 pQCT images (40 specimens x 2 slices per specimen (1 cranial and 1 caudal)) were analyzed for this investigation. The third slice contained the pars interarticularis by definition of the previously described specimen mounting procedures and pQCT scanning parameters. Two raters independently analyzed each of the selected slices using the Stratec Medizintechnik software (Stratec Medizintechnik v. 6.0B, Stratec Medizintechnik GmbH, Pforzheim, Germany).

Each rater manually selected regions of interest corresponding to the left and right pars interarticularis (Total area  $r^2 = 0.686$  and Difference =  $8.8 \text{ mm}^2$ , Total density  $r^2 = 0.984$  and Difference =  $0.7 \text{ mg/cm}^3$ , Appendix B.2) (Figure 4.6).

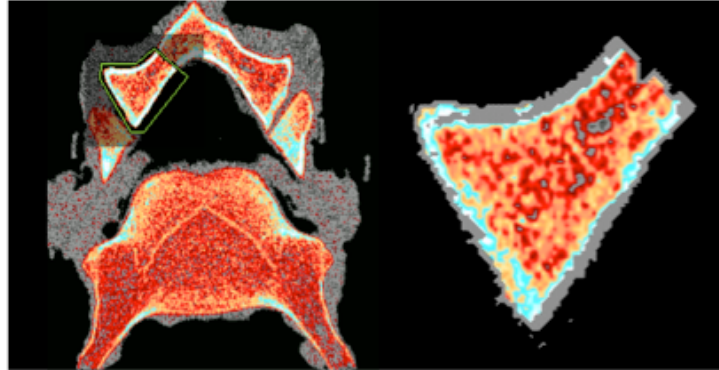


Figure 4.6 – Computed tomography scan illustrating the region of interest defined as the pars interarticularis. Density and area measures were made on the selected region of interest.

A threshold-based algorithm built into the analysis software (Contour Mode = 1, Peel Mode = 2) was used to separate soft tissue, trabecular bone and cortical bone using two user defined threshold values (Ashe et al., 2006). The defined threshold between soft tissue and trabecular bone was set to  $260 \text{ mg/cm}^3$  and the threshold between trabecular bone and cortical bone was  $754 \text{ mg/cm}^3$ . These threshold values were determined by each rater using Half Maximum Height (HMH) values (Spoor et al., 1993) on a subset of 20 randomly selected pQCT slices of the pars interarticularis ( $r^2 = 0.233$  and  $0.483$ , Threshold difference =  $7.3$  and  $10.6 \text{ mg/cm}^3$  respectively for threshold between soft tissue and trabecular bone and threshold between trabecular bone and cortical bone, Appendix B.3). Briefly, the HMH method determines maximum voxel density individually for cortical bone, trabecular bone and soft tissue. The cutoff is determined as the midpoint between the maximum densities for successive tissue types.

Analysis of each region of interest selected from the pQCT images provided measures of total bone density, trabecular bone density, cortical bone density, pars interarticularis cross-sectional area (total bone area), trabecular bone area and cortical bone area. Values obtained for these measures were averaged between the two raters due to moderate high inter-rater reliability ( $r^2 \geq 0.686$ , Appendix B.2). Furthermore, the measures were also averaged between left and right sides since the primary mode of shear failure is a bilateral fracture of the pars interarticularis (Yingling and McGill, 1999; Beadon et al., 2008; Gallagher et al., 2010; Chapter 3).

#### **4.2.8 Development and testing of a mathematical model for non-destructively calculating ultimate shear force**

Following mechanical testing, data (ultimate failure loads, morphological measurements and measures obtained from pQCT scanning) for 20 specimens (10 C3-C4 and 10 C5-C6) were randomly assigned to a group used to develop linear regression models that calculated ultimate anterior shear force of the porcine cervical spine. Data for the remaining 20 specimens (10 C3-C4 and 10 C5-C6) were assigned to a group used to test the accuracy of these mathematical models.

Stepwise linear regression was performed using the data from the mathematical model generation group to develop equations that attempted to determine ultimate shear failure of the porcine cervical spine from combinations of the morphological measurements and measures obtained from the pQCT slices of the pars interarticularis. A maximum of three iterations in the stepwise regression model was used since a small sample size of 20 specimens was used to develop these equations. Ultimate shear failure

loads were computed for all specimens in the model testing group and for each iteration of the stepwise linear regression. Absolute and relative discrepancies (Equation 4.2) between measured and calculated ultimate anterior shear failure tolerances were determined for each specimen in the model testing group.

$$\begin{aligned} E_{absolute} &= |F_{calculated} - F_{measured}| \\ E_{relative} &= \frac{E_{absolute}}{F_{measured}} \times 100 \end{aligned} \quad (4.2)$$

A two factor (LEVEL, MODEL GROUP) analysis of variance (ANOVA) was used to analyze the data, with the exception of the width and height for the pedicle and lamina as well as the pars interarticularis length, entered into the stepwise regression for differences between vertebral levels and also to assess the random assignment of specimens to either the prediction generation or testing groups (SAS 9.1, SAS Institute Inc., Cary, NC, USA). A separate three factor (LEVEL, MODEL GROUP, VERTEBRA) ANOVA was used to analyze statistical differences for pedicle, lamina and the pars interarticularis measurements. A single factor (REGRESSION MODEL) ANOVA was used to analyze differences in absolute and relative error for each mathematical model generated by the stepwise regression. Tukey's post-hoc tests were performed for any significant main effects or interactions. The level of statistical significance for the ANOVA and post-hoc tests was set to  $p < 0.05$ . All statistical techniques were approved by a statistical consultant at the University of Waterloo.

## 4.3 RESULTS

### 4.3.1 Specimen randomization

There were no statistically significant differences between the mathematical model generation and testing groups for ultimate force, pQCT measurements or morphological measurements ( $p \geq 0.1319$ ) (Tables 4.2 & 4.3).

Table 4.2 – Ultimate failure tolerance, bone density and morphological measurements made for specimens assigned to each of the model generation and testing groups. Standard error of the mean is presented in parentheses.

	Generation		Testing		<i>p</i>
N	20		20		
Ultimate Force (N)	2262.0	(91.5)	2144.7	(103.1)	0.8209
Total Density (mg/cm <sup>3</sup> )	560.4	(20.0)	546.0	(18.8)	0.3613
Total Area (mm <sup>2</sup> )	117.2	(4.5)	115.9	(6.1)	0.4829
Trabecular Density (mg/cm <sup>3</sup> )	472.8	(16.6)	452.4	(13.5)	0.1177
Trabecular Area (mm <sup>2</sup> )	77.4	(3.6)	78.7	(5.3)	0.7981
Cortical Density (mg/cm <sup>3</sup> )	733.6	(15.4)	733.2	(17.4)	0.8471
Cortical Area (mm <sup>2</sup> )	39.8	(3.4)	37.2	(2.7)	0.3942
Endplate Area (mm <sup>2</sup> )	713.6	(16.8)	705.6	(14.9)	0.5189
Facet Area (mm <sup>2</sup> )	124.9	(4.2)	130.3	(5.0)	0.7888
Average Facet Angle (degrees)	45.4	(1.1)	45.8	(0.9)	0.4198
Facet Tropism (degrees)	2.9	(0.5)	3.1	(0.5)	0.8133
Superior Facet Height (mm)	13.7	(0.3)	13.5	(0.3)	0.2154
Superior Facet Width (mm)	13.2	(0.3)	12.7	(0.3)	0.1805
Superior Inside Interfacet Width (mm)	23.3	(0.6)	24.0	(0.7)	0.4096
Superior Outside Interfacet Width (mm)	43.8	(0.6)	43.2	(0.9)	0.1403
Inferior Facet Height (mm)	11.9	(0.2)	12.1	(0.3)	0.1599
Inferior Facet Width (mm)	12.5	(0.3)	12.2	(0.2)	0.0592
Inferior Inside Interfacet Width (mm)	23.1	(0.3)	23.8	(0.4)	0.1562
Inferior Outside Interfacet Width (mm)	41.3	(0.6)	41.4	(0.7)	0.8295

Table 4.3 – Measured height and width of the pedicle and lamina, as well as the pars interarticularis length for specimens assigned to each of the model generation and testing groups. Standard error of the mean is presented in parentheses.

	Generation		Testing		<i>p</i>
N	40		40		
Pedicle Height (mm)	12.3	(0.2)	12.2	(0.2)	0.7771
Pedicle Width (mm)	9.5	(0.2)	9.5	(0.2)	0.7945
Lamina Height (mm)	12.5	(0.2)	12.2	(0.2)	0.4245
Lamina Width (mm)	7.1	(0.2)	6.8	(0.2)	0.1482
Pars Length (mm)	14.8	(0.4)	15.2	(0.5)	0.4784

#### 4.3.2 Vertebral level

Morphologically, the C5-C6 specimens had longer pars interarticularis', facets that were oriented closer to the sagittal plane, larger distances between facets and thinner pedicles. These morphological differences likely contributed to higher ultimate shear forces observed for the C5-C6 specimens than the C3-C4 specimens. Ultimate force was 27.6% higher for C5-C6 specimens than C3-C4 specimens ( $p < 0.0001$ ,  $d = 1.60$ ) (Table 4.4). Total and trabecular bone densities measured from the pQCT were smaller by 9.3% and 9.9% respectively for C5-C6 specimens (total density  $p = 0.0474$ ,  $d = 0.67$ ; trabecular density  $p = 0.0198$ ,  $d = 0.77$ ) (Table 4.4). Facet surfaces were 9.6% smaller ( $p = 0.0498$ ,  $d = 0.67$ ) for C5-C6 specimens, oriented 3.1 degrees closer to the sagittal plane ( $p = 0.0283$ ,  $d = 0.75$ ) and had larger distances between left and right facets by 17.9% and 5.2% respectively (superior inside facet width  $p < 0.0001$ ,  $d = 2.05$ ; inferior inside facet width  $p = 0.0141$ ,  $d = 0.81$ ) (Table 4.4).

Table 4.4 – Ultimate failure tolerance, bone density and morphological measurements made for specimens from each vertebral level. Standard error of the mean is presented in parentheses. Measurements that achieved statistical significance between vertebral levels have their *p*-values reported in a bold font.

	C3-C4		C5-C6		<i>p</i>
N	20		20		
Ultimate Force (N)	1935.8	(72.9)	2470.9	(80.6)	< <b>0.0001</b>
Total Density (mg/cm <sup>3</sup> )	580.3	(18.9)	526.1	(18.0)	<b>0.0474</b>
Total Area (mm <sup>2</sup> )	112.3	(5.8)	120.9	(4.7)	0.2666
Trabecular Density (mg/cm <sup>3</sup> )	486.7	(15.4)	438.5	(13.0)	<b>0.0198</b>
Trabecular Area (mm <sup>2</sup> )	72.1	(4.8)	84.0	(3.9)	0.0662
Cortical Density (mg/cm <sup>3</sup> )	748.7	(13.6)	718.1	(18.1)	0.1984
Cortical Area (mm <sup>2</sup> )	40.2	(3.2)	36.8	(2.9)	0.451
Endplate Area (mm <sup>2</sup> )	694.9	(13.3)	724.3	(17.5)	0.1977
Facet Area (mm <sup>2</sup> )	134.1	(4.4)	121.1	(4.4)	<b>0.0498</b>
Average Facet Angle (degrees)	44.0	(1.0)	47.1	(0.9)	<b>0.0283</b>
Facet Tropism (degrees)	2.8	(0.4)	3.2	(0.5)	0.5725
Superior Facet Height (mm)	13.9	(0.3)	13.2	(0.3)	0.0756
Superior Facet Width (mm)	13.3	(0.3)	12.6	(0.3)	0.101
Superior Inside Interfacet Width (mm)	21.7	(0.4)	25.6	(0.5)	< <b>0.0001</b>
Superior Outside Interfacet Width (mm)	42.0	(0.7)	45.0	(0.7)	<b>0.0065</b>
Inferior Facet Height (mm)	12.3	(0.2)	11.8	(0.3)	0.1826
Inferior Facet Width (mm)	12.6	(0.3)	12.1	(0.3)	0.1593
Inferior Inside Interfacet Width (mm)	22.8	(0.4)	24.0	(0.3)	<b>0.0141</b>
Inferior Outside Interfacet Width (mm)	42.2	(0.6)	40.5	(0.5)	0.0573

Pedicle width was larger by 8.8% ( $p = 0.0004$ ,  $d = 0.86$ ) and pars interarticularis length was shorter by 21.2% ( $p < 0.0001$ ,  $d = 1.14$ ) for C3-C4 specimens (Table 4.5). Caudal vertebrae (C4 and C6) had a 6.8% increase in pedicle height ( $p = 0.0005$ ,  $d = 0.81$ ), a 5.9% decrease in lamina height ( $p = 0.0211$ ,  $d = 0.54$ ), and a 16.7% increase in pars interarticularis length ( $p < 0.0001$ ,  $d = 1.07$ ) compared to the cranial vertebrae (C3 and C5) (Table 4.5). Lamina width demonstrated a significant interaction between



individual vertebrae of the two vertebral levels ( $p < 0.0001$ ). Specifically, the lamina width of C6 was larger than each of C3 ( $p = 0.0004$ ,  $d = 1.37$ ), C4 ( $p < 0.0001$ ,  $d = 1.95$ ), and C5 ( $p < 0.0001$ ,  $d = 1.94$ ) by 21.7%, 34.7%, and 25.3% respectively (Table 4.5).

Table 4.5 – Measured height and width of the pedicle and lamina, as well as the pars interarticularis length for individual (C3, C4, C5, and C6) vertebrae. Standard error of the mean is presented in parentheses. Statistically significant differences between vertebral levels are shown below each measure in a bold font. Statistically significant differences between caudal and cranial vertebrae are shown to the right in a bold font. The asterisk indicates that a significant interaction between individual vertebrae occurred for the lamina width. Means with the same letter (for lamina width) are statistically similar.

			C3-C4		C5-C6		<i>p</i>
		N	20		20		
Pedicle Height (mm)	Caudal	20	12.3	(0.2)	13.0	(0.3)	0.0005
	Cranial		11.7	(0.2)	11.9	(0.2)	
	<i>p</i>		0.0576				
Pedicle Width (mm)	Caudal	20	9.7	(0.2)	8.9	(0.2)	0.1397
	Cranial		10.1	(0.2)	9.2	(0.3)	
	<i>p</i>		0.0004				
Lamina Height (mm)	Caudal	20	12.1	(0.3)	11.9	(0.3)	0.0211
	Cranial		13.0	(0.3)	12.4	(0.3)	
	<i>p</i>		0.1669				
*Lamina Width (mm)	Caudal	20	6.2 A	(0.3)	8.4 B	(0.3)	
	Cranial		6.9 A	(0.2)	6.3 A	(0.2)	
	<i>p</i>						
Pars Interarticularis Length (mm)	Caudal	20	14.8	(0.5)	17.9	(0.6)	< 0.0001
	Cranial		12.3	(0.3)	15.0	(0.4)	
	<i>p</i>		< 0.0001				

### 4.3.3 Post-failure analysis

The predominant posterior element injury (68% of all specimens) was a bilateral fracture of the cranial vertebra's pars interarticularis (Table 4.6, Figure 4.7). Other common injuries that occurred were bilateral and unilateral fractures of the caudal vertebra's pars interarticularis (10% bilateral; 25% unilateral) (Table 4.6). Incidence rate of bilateral cranial pars interarticularis fracture was higher for C3-C4 specimens than C5-C6 specimens (35% difference) (Table 4.6). Failure patterns were consistent between specimens assigned to the mathematical model generation and testing groups (Table 4.6).



Figure 4.7 – Transverse image of a C3 vertebra following acute shear failure. The black arrows indicate the bilateral pars interarticularis fracture that was the predominant injury caused by shear failure.

Table 4.6 – Post-failure observations of tissue damage arranged within vertebral level, model group and overall. Values are reported as a percentage of all specimens in each group. Percentages within a single block of vertebral level or model group since a specimen may have multiple injuries following acute shear failure testing.

	<b>Pars Interarticularis</b>				<b>Facet</b>				<b>Endplate</b>	
	Cranial		Caudal		Superior		Inferior		Superior	Inferior
	Bilateral	Unilateral	Bilateral	Unilateral	Bilateral	Unilateral	Bilateral	Unilateral		
<b>C3-C4</b>	85	0	0	15	5	5	0	0	0	0
<b>C5-C6</b>	50	10	20	35	0	20	0	10	0	0
<b>Generation</b>	70	10	10	30	0	10	0	5	0	0
<b>Testing</b>	65	0	10	20	5	15	0	5	0	0
<b>Overall</b>	<b>67.5</b>	<b>5</b>	<b>10</b>	<b>25</b>	<b>2.5</b>	<b>12.5</b>	<b>0</b>	<b>5</b>	<b>0</b>	<b>0</b>

#### 4.3.4 Regression model development

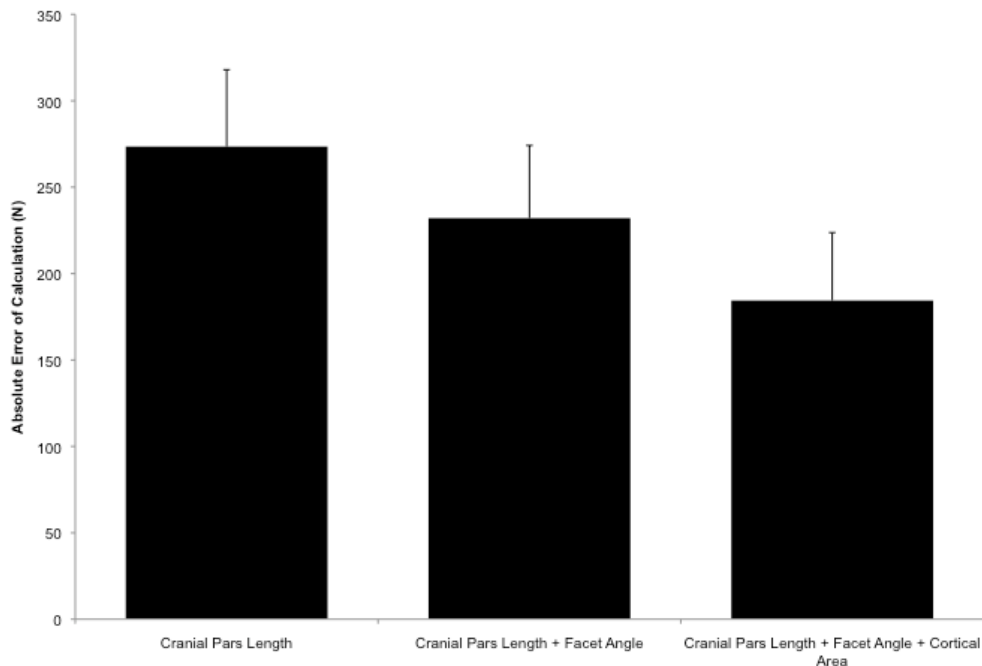
Stepwise linear regression identified the cranial pars interarticularis length measured from the sagittal plane x-ray as the dominant measurement ( $p = 0.0014$ , 44.3% explained variance) for mathematically calculating ultimate shear failure (Table 4.7). Longer cranial pars interarticularis lengths generated higher calculated ultimate shear failure tolerances. The second and third predictive factors respectively were the average facet angle relative to the coronal plane ( $p = 0.0418$ , 12.3% explained variance) measured from the transverse plane x-ray and the cortical bone area ( $p = 0.0254$ , 11.9% explained variance) measured from the pQCT (Table 4.7). Increasing average facet angles and cortical bone density generated larger calculated ultimate shear failure tolerances. An average facet angle of 0 degrees was equivalent to the facets being coincident with the coronal plane while an average facet angle of 90 degrees meant that the facets were coincident with the sagittal plane. Standardized regression coefficient estimates showed that changes in superior pars interarticularis length was consistently the largest determinant of changes in calculated ultimate shear failure tolerance (Table 4.7). None of the morphological measurements made using the digital calipers were identified as significant factors for mathematically determining ultimate shear failure tolerance.

Table 4.7 – Factors, coefficient estimates and explained variance for each model developed by the stepwise linear regression analysis. The final equation for calculating ultimate shear failure tolerance has the form  $F = aX_1 + bX_2 + cX_3 + I$ . The standardized estimate illustrates the relative importance of each variable in each mathematical model (i.e. a higher standardized estimate indicates that changing the value of the parameter's corresponding variable creates a larger change in calculated ultimate shear failure tolerance).

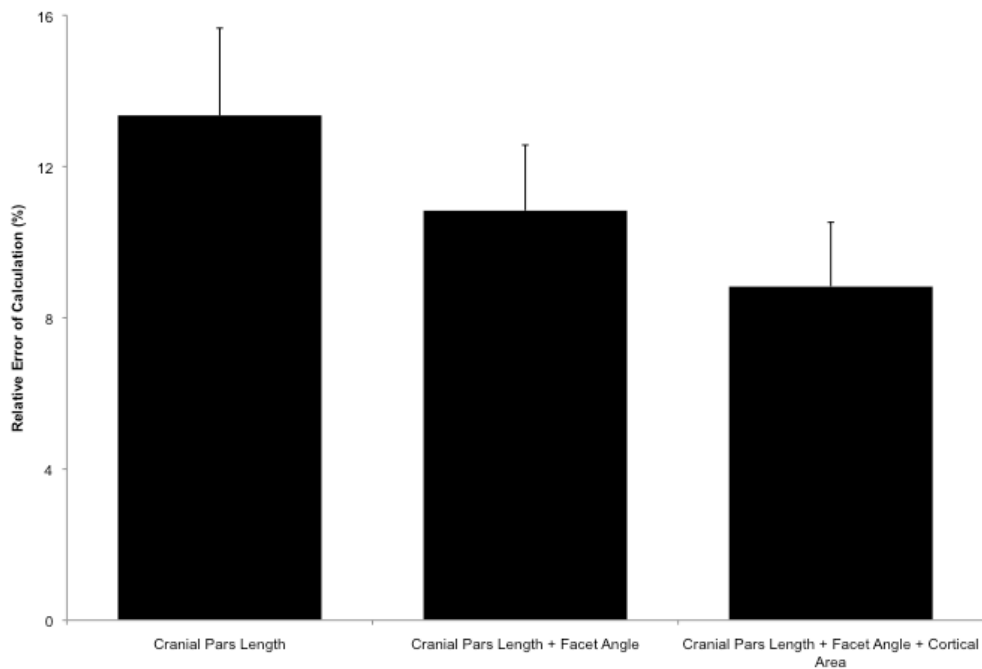
	STEP 1		STEP 2		STEP 3	
	Parameter Estimate	Standardized Estimate	Parameter Estimate	Standardized Estimate	Parameter Estimate	Standardized Estimate
<b>Intercept (I)</b>	181.12171	0	-1566.61338	0	-1981.47622	0
<b>Cranial Pars Length (X<sub>1</sub>) (mm)</b>	144.29936	0.666	140.84439	0.650	137.88987	0.636
<b>Facet Angle (X<sub>2</sub>) (degrees)</b>			39.19734	0.352	38.57859	0.346
<b>Cortical Area (X<sub>3</sub>) (mm<sup>2</sup>)</b>					12.97971	0.346
<b>Partial R<sup>2</sup></b>	0.4432		0.1234		0.1194	
<b>Model R<sup>2</sup></b>	0.4432		0.5666		0.686	
<b>p</b>	0.0014		≤ 0.0418		≤ 0.0254	

#### 4.3.5 Regression model error testing

Despite a trend towards decreasing error with increasing mathematical model complexity, neither absolute nor relative errors were statistically different for any of the three linear regression models developed from this investigation (Absolute error –  $p = 0.3313$ , Figure 4.8 A; Relative error –  $p = 0.2608$ , Figure 4.8 B). Calculating ultimate shear failure from only the cranial pars interarticularis length had an average absolute error of  $273.5 \pm 44.5$  N (equivalent to  $13.4 \pm 2.3\%$  of the measured shear failure tolerance). However, including measurements of the average facet angle and the cortical bone area respectively reduced the absolute error of calculating ultimate failure tolerance to  $232.1 \pm 42.1$  N and  $184.4 \pm 39.3$  N (equivalent to  $10.8 \pm 1.7\%$  and  $8.8 \pm 1.7\%$ ) (Figure 4.8).



A.)



B.)

Figure 4.8 – Absolute (A.) and relative (B.) errors in calculated ultimate shear failure tolerance produced by each mathematical model generated by first three iterations of the stepwise regression analysis. Error bars indicate the standard error of the mean calculation error.

#### 4.4 DISCUSSION

This investigation was the first to develop and test a mathematical model for calculating ultimate shear failure tolerance of the porcine cervical spine and also identified critical morphological parameters that influence the risk of vertebral injury from shear loading. Cranial pars interarticularis length, average facet angle and cortical bone area were identified using stepwise linear regression as the three most prominent factors for calculating ultimate anterior shear failure tolerance. Calculated ultimate shear failure tolerances, for each regression model, increased with longer cranial pars interarticularis lengths, average facet angles that were oriented closer to the sagittal plane

(i.e. an angle of 0 degrees = frontal plane; an angle of 90 degrees = sagittal plane), and higher cortical bone area. Increasing the number of variables in the regressive model produced successive reductions in relative calculated shear tolerance errors but without statistical significance.

Results from this investigation show that the shorter length of the cranial vertebra's pars interarticularis make this structure the most likely site of failure under shear loading. Bilateral fractures of the cranial pars interarticularis that was observed following acute shear failure in this investigation were similar to documented shear-related injuries for isolated human lumbar vertebrae (Cyron et al., 1976) and were also consistent with *in vivo* shear-related injuries in humans (Farfan et al., 1976). The use of the porcine cervical spine as a surrogate animal model for the human lumbar spine is further validated since failure patterns observed in this study are congruent with observations of shear-related injuries in humans. Thus, the deterministic morphological characteristics that modulate shear injury tolerances for the porcine cervical spine are also likely to be modulators of shear injury tolerances in the human lumbar spine. Furthermore, hypotheses developed regarding modulation of failure tolerance from *in vitro* studies conducted using the porcine cervical spine are likely to be relevant to the human lumbar spine.

Acute and repetitive shear loading of the vertebral joint has been demonstrated to result in fracture of primarily the pars interarticularis of the most cranial vertebra in an FSU pairing (Yingling and McGill, 1999; Beadon et al., 2008; Gallagher et al., 2010; Chapter 3). This primary mode of vertebral bony fracture, following acute shear failure, was corroborated by the current investigation. Direct application of force to the inferior



facets of a single vertebra has been shown to cause fractures across the narrowest section of the pars interarticularis (Cyron et al., 1976). Furthermore, notching of the cranial vertebra's pars interarticularis leads to bilateral fracture of the pars interarticularis following exposure to repetitive shear loading (Beadon et al., 2008). These findings support the inclusion, as found in this investigation, of the cranial vertebra's pars interarticularis length as the primary factor in any mathematical model for calculating vertebral ultimate shear failure tolerance.

Backward shearing of the caudal vertebra (effectively producing anterior shear of the cranial vertebra) in a vertebral joint also causes direct interaction between the inferior and superior facets of the cranial and caudal vertebrae respectively. The amount of shear force from linear actuator displacement that is transmitted through the facet contact to the pars interarticularis is likely influenced by the facet orientation in the transverse plane. Transverse orientation of facets closer to the sagittal plane are more likely to provide direct resistance for axial twisting while frontal plane orientation provides more direct resistance to shear loading (Serhan et al., 2007). Previous investigations have also demonstrated that isthmic spondylolysis is more prevalent when facet orientation is closer to the frontal plane (Masharawi et al., 2007; Don and Robertson, 2008). Orientation of the facets closer to the frontal plane has also been linked to increased resistance of anterior shear that may increase force concentration at the pars interarticularis (Don and Robertson, 2008). These findings coincide with results from the stepwise regression that found increasing ultimate shear failure tolerance with increasing facet angles (i.e. more sagittally oriented facets) and also support the inclusion of average facet angle as a factor for calculating ultimate shear failure tolerance.

Lastly, cortical bone is stronger than trabecular bone. Thus, larger cortical bone area through the pars interarticularis may also be associated with increased ultimate shear failure tolerances. Dickerson and colleagues (2008) identified a positive correlation of 0.84 between cortical bone area and ultimate load for acute compressive failure of vertebral bodies. This supports our finding from the stepwise regression identifying cortical bone area through the pars interarticularis as the third most predominant factor for calculating ultimate shear failure tolerance.

Contrary to our hypothesis, bone density through the pars interarticularis was not identified by stepwise linear regression as a factor for calculating ultimate shear failure tolerance. This indicates that bone density through the pars interarticularis has diminished utility towards calculating ultimate shear failure tolerance. The range in total density for all specimens in this investigation through the pars interarticularis spanned  $350 \text{ mg/cm}^3$  despite the fact that the porcine specimens were obtained from a common source that controlled for diet, age, weight and activity level. This is larger than the range of density values reported for predictions of compressive failure tolerance for human vertebral bodies (Ebbesen et al., 1999). Therefore, the authors believe that density measures used for this investigation spanned a sufficient range to be entered into the stepwise regression analysis. Furthermore, the range of trabecular ( $314.8\text{-}605.1 \text{ mg/cm}^3$ ) and cortical ( $500.2\text{-}868.4 \text{ mg/cm}^3$ ) densities from this investigation spanned comparable values to previous studies using a porcine model (Inui et al., 2004). Bone density measures from this investigation were also larger than previously reported values for human specimens (Mosekilde and Danielsen, 1987; Ebbesen et al., 1999; Schmidt et al., 2005). Low to moderate inter-rater reliability in developing the HMH thresholds as well as measuring

bone density and cross-sectional area from the pQCT scans may have also limited these measurements from being stronger factors for calculating ultimate shear failure strength.

Previous research has developed similar mathematical models for compressive failure tolerance. These investigations have used different combinations of vertebral body trabecular bone density and/or measurements of endplate area to calculate compressive failure tolerance (Hansson et al., 1980; Biggemann et al., 1988; Brinckmann et al., 1989; Parkinson et al., 2005; Dickerson et al., 2008). Parkinson and colleagues (2005) tested errors for their mathematical model using an independent sample of specimens and obtained a mean error of 11% in compressive failure tolerance. Results from this investigation demonstrate that at minimum a bivariate regressive model is required in order to achieve a similar magnitude of relative error in calculated shear failure tolerance. Both bivariate and trivariate models developed in this investigation reflect the higher ultimate shear failure tolerance found in the C5-C6 specimens since these specimens had greater pars interarticularis length and the facet surfaces were oriented closer to the sagittal plane. Greater pars interarticularis length and facets oriented closer to the sagittal plane resulted in larger calculated ultimate shear failure tolerances.

Based on methodological considerations, the authors propose that the bivariate model is most suitable for future *in vitro* research that requires non-destructive calculation of ultimate shear failure tolerance (Equation 4.3).

$$F_{ultimate} = -1566.61338 + 140.84439x_1 + 39.19734x_2 \quad (4.3)$$

This is where  $x_1$ , and  $x_2$  respectively correspond to the pars interarticularis length (in millimeters) of the cranial vertebra, and the average facet angle (in degrees) measured in the horizontal plane. The trivariate regression model uses cortical bone area as the third factor for calculating ultimate shear failure tolerance. Non-destructive quantification of cortical bone density and area requires access to an imaging modality (e.g. pQCT, DXA, magnetic resonance imaging) that may not be possible for all researchers and would require additional specimen preparation time prior to loading. However, quantification of average facet angle and superior pars interarticularis length (the two required variables for the bivariate model) uses standard x-ray technology or may even be possible by using digital photography and/or digital caliper measurements. Furthermore, calculation errors between the bivariate and trivariate regression models were not statistically different which means that neither model would necessarily provide a better calculation of ultimate shear failure tolerance. Therefore, the combination of improved calculation error (compared to calculation errors from similar regression models calculating ultimate compressive load) and facilitated implementation makes the bivariate regression model most suitable (absolute error =  $232.1 \pm 42.1$  N; relative error =  $10.8 \pm 1.7\%$  of the ultimate shear failure tolerance) for calculating ultimate shear failure tolerance of the healthy and intact vertebral joint.

## **CHAPTER 5**

### **INVESTIGATING THE NON-LINEAR RELATIONSHIP BETWEEN SUB-MAXIMAL SHEAR LOAD AND CUMULATIVE SHEAR LOAD SUSTAINED PRIOR TO FAILURE: DEVELOPMENT OF A TISSUE-BASED WEIGHTING ALGORITHM FOR DETERMINING CUMULATIVE SHEAR LOAD**

## 5.1 INTRODUCTION

Evidence exists that cumulative compressive load exposure is linked to *in vivo* tissue damage (Seidler et al., 2001; Seidler et al., 2003). Moreover, sub-maximal compressive load magnitude is non-linearly related to incidence of tissue damage accumulated from cyclic compressive loading (Hansson et al., 1987; Brinckmann et al., 1988; Parkinson and Callaghan, 2007b). Findings from studies on repetitive compressive loading support the idea that correspondence between cumulative load and vertebral tissue injury is enhanced with non-linearly weighted estimates of cumulative exposure (Seidler et al., 2001; Seidler et al., 2003; Parkinson and Callaghan 2007a). This has led to development of a tissue-based non-linear weighting method for sub-maximal loads while determining cumulative compressive load (Parkinson and Callaghan, 2007a).

Potvin (2008) recently identified quantifying the cumulative tolerance of the vertebral joint to shear as one of the next areas for understanding occupational low-back injury. The current investigation determined the relationship between shear load magnitude and the fatigue life of the vertebral joint exposed to repetitive shear loading. A novel tissue-based weighting method for shear load was also developed for application while calculating cumulative shear load and enhancing injury prediction.

Vertebral tissue injury and failure tolerances resulting from shear loading have been primarily studied using an acute loading paradigm. These studies have identified the pars interarticularis as the primary site of failure and that acute ultimate shear failure tolerance is approximately 2000 N (Cyron et al., 1976; Cripton et al., 1995; Yingling and McGill, 1999; van Dieën et al., 2006; Gallagher et al., 2010; Chapters 3-4). The first study of this thesis also demonstrated that acute ultimate shear failure tolerance of the

vertebral joint is modulated by the presence of compressive load and joint or functional spinal unit (FSU) posture. Fewer *in vitro* research efforts have been directed towards understanding vertebral injury thresholds and mechanisms resulting from cyclically applied sub-maximal shear loads. Cyron and Hutton (1978) first identified the pars interarticularis as the primary structure being damaged from cyclically applied load directly to the inferior facets of isolated single vertebra. More recently, van Dieën and colleagues (2006) demonstrated that time to failure under repetitive shear loading decreased when the posterior elements were removed from porcine lumbar FSUs compared to intact specimens, indicating the facet joints were a key component in resisting shear loading. Beadon and colleagues (2008) found that cyclic shear loading to a maximum of 600 N (equivalent to approximately 27% of ultimate shear failure tolerance) for a minimum of 7200 loading cycles did not cause significant forward displacement but that impulse loading to 1500 N produced significant forward slip and fracture of the pars interarticularis after only 4 cycles. This provides evidence that, similar to compressive loading, the magnitude of repetitively applied sub-maximal shear load may also be related to the incidence of shear failure.

The purpose of this investigation was to determine if the magnitude of sub-maximal shear load influences cumulative shear load sustained prior to failure of porcine cervical FSUs. Based on work presented by Parkinson and Callaghan (2007a; 2007b) as well as prior results from Beadon and colleagues (2008), it is hypothesized that cumulative shear failure tolerance will be non-linearly related to repetitive shear load magnitude. This investigation also presents a weighting scheme for sub-maximal shear

loads when calculating cumulative shear load exposures to correct for the corresponding non-linear injury risk associated with load magnitude.

## **5.2 METHODS**

### **5.2.1 Specimen preparation and assessment**

Thirty-two FSUs (16 C3-C4 and 16 C5-C6) were excised from sixteen frozen porcine cervical spines obtained from a local abattoir. Specimens were thawed overnight prior to removal of muscle and fat leaving an osteoligamentous FSU comprised of two vertebrae, the intervertebral disc and ligaments. Following dissection, quality of the exposed cranial and caudal intervertebral disc was assessed using the grading scale outlined by Galante (1967). Only specimens with disc quality of Grade 1 were used for this investigation. Measurements of endplate anterior-posterior depth (D) and mediolateral width (W) were obtained using digital calipers for both exposed endplates. Area of each exposed endplate was calculated using the equation for area of an ellipse ( $\pi WD/4$ ) (Callaghan and McGill, 1995). The area of the FSUs intervertebral disc was estimated as the average area between the two exposed endplates (Parkinson et al., 2005). Bilateral facet angles and tropism between left and right facet joints were also quantified (Boden et al., 1996) using ImageJ (National Institutes of Health, USA) from an x-ray taken in the transverse plane (Figure 5.1).



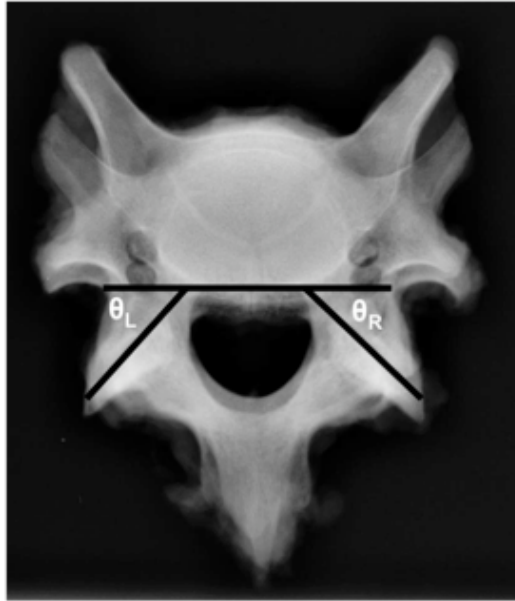


Figure 5.1 – X-ray of a specimen taken in the transverse plane. Left and right facet angles ( $\theta_L$  and  $\theta_R$ ) were measured as the angle between a line parallel to the posterior aspect of the vertebral body and a line parallel to the gap between the facets.

Pars interarticularis length for the cranial vertebra was also quantified since the linear regression equation developed in Chapter 4 requires this input as well as the average facet angle. Cranial pars interarticularis length was determined from an x-ray taken in the specimen's sagittal plane. Prior to x-raying, two metal pins (diameter = 0.5 mm) were inserted to mark the inferior and superior borders of the pars interarticularis for the cranial vertebra on the specimen's left side. The superior border was defined as the lateral junction between the superior facet and the lamina while the inferior border was defined as the medial junction between the inferior facet and the pedicle. The pars interarticularis (and subsequent fracture plane after acute shear failure) for each respective vertebra was assumed to lie in the cutting plane created by connecting each pair of pins defining the superior and inferior borders. This line is also consistent with previously identified fracture lines in specimens following exposure to direct facet loading (Cyron et al., 1976) and acute shear failure (Yingling and McGill, 1999;

Gallagher et al., 2010; Chapters 3-4).

The sagittal plane x-ray produced an image of the specimen with the metal pins as well as a 20 mm calibration frame. Calibration between pixels and distance was identical for both the width and length of the x-ray image. Due to irregular geometry of the vertebral joint, specimen positioning for the x-ray was controlled to the unloaded and neutral posture by placing the specimen's right side onto a formed impression created in a 25.4 mm thick block of extruded polystyrene foam. The sagittal plane x-ray was digitally developed (Kodak DirectView CR500, Carestream, Toronto, ON, Canada) and planar coordinates on the image corresponding to each pinhead and calibration frame endpoint were manually digitized (ImageJ, National Institutes of Health, USA) (Figure 5.2). Pars interarticularis length for the cranial vertebra was calculated as the distance between digitized locations for the superior and inferior borders of the pars interarticularis.

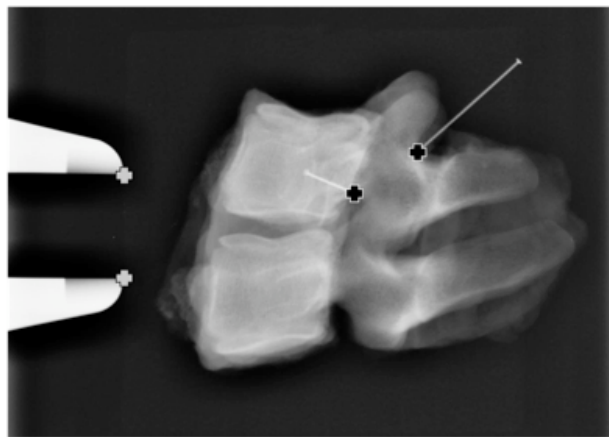


Figure 5.2 – Sagittal plane x-ray of the specimen used to digitize locations for the pars interarticularis of the cranial vertebra as well as the calibration frame.

Specimens were then mounted between a set of two custom aluminum cups using a combination of steel wire, screws and dental plaster. Two screws were partially inserted so that they protruded from the anterior aspect of the cranial vertebral body. One screw

was inserted through the bottom of each cup so that each screw pierced the center of the exposed superior and inferior endplates. An additional six screws (three for each vertebra) were inserted through threaded holes in the aluminum cups so that they were sunk approximately 5 mm into the anterior and lateral aspects of the vertebral bodies. A single length of 18 gauge galvanized steel wire was looped around the caudal vertebra's spinous process, threaded through two holes in the bottom of the aluminum cup and tightened by twisting the two ends together. Lastly, non-exothermic dental plaster (Denstone, Miles, IN, USA) was poured into the cups, and allowed to harden, so that the exposed screws were completely immersed and that any space between the specimen and the aluminum cup was filled.

### **5.2.2 Loading protocol**

Following fixation, the cup containing the FSUs cranial vertebra was secured to a servohydraulic material testing system (Instron 8872, Instron Canada, Burlington, ON, Canada) that had been coupled to a brushless servomotor (AKM23D; Kollmorgen/Danaher Motion, Radford, VA, USA) capable of simultaneously applying flexion/extension moments to the specimen (Figure 5.3). First, a compressive preload of 300 N was applied under load control for a 15-minute duration to counter the effects of post-mortem swelling (Callaghan and McGill, 2001). The flexion/extension posture was continuously adjusted by monitoring the torque cell feedback loop and driving the servomotor in position control to reduce the joint moment throughout the 15-minute duration in order to determine the position where zero or the smallest moment possible was recorded by the torque cell.

Following the preload, five continuous repeats of position controlled passive flexion/extension were performed at a rate of 0.5 degrees/second, and under a constant load controlled compressive force of 300 N (Callaghan and McGill, 2001) to determine the specimen's neutral zone for rotational loading about the flexion/extension axis. The cup containing the FSU's caudal vertebra was allowed to translate freely in the horizontal plane during the preload and passive flexion/extension tests on metallic ball bearings that provided a near-frictionless surface (See Figure 3.3A). Flexion and extension angles where the moment versus angle relationship deviated from linear for the last three repeats were defined as endpoints of a linear region similar to the neutral zone (Panjabi, 1992; Callaghan and McGill, 2001).

The neutral position defined at the end of the 15-minute preload identified a position within the specimen's neutral zone that satisfies a zero flexion/extension moment. However, there are many flexion/extension angles within the neutral zone that simultaneously satisfy the zero moment condition. The first position that satisfies the zero flexion/extension moment condition is defined as the first approximation of the neutral posture. Using data provided under similar load and testing conditions (Callaghan and McGill, 2001), the neutral posture was set to be 36% of the neutral zone length from the selected extension limit (Equation 5.1).

$$\theta_{neutral} = \theta_{ext} + 0.36(\theta_{flex} - \theta_{ext}) \quad (5.1)$$

This was performed so that each specimen received the same approach for determining the neutral posture. The flexion and extension limits determined from the

passive test were redefined in reference to the calculated neutral posture.

For shear testing, the cup containing the specimen's caudal vertebra (either C4 or C6) was rigidly interfaced with two linear actuators (RSA24, Tolomatic Inc., Hamel, MN, USA) driven by a pair of brushless servomotors (AKM22E, Danaher Motion Inc., Radford, VA, USA) (Figure 5.3). This constrained sliding of the caudal vertebra to allow only the imposed anterior/posterior displacements applied by the linear actuators during all shear tests (See Figure 3.3B). The linear actuators were equidistant from the specimen's mid-sagittal plane in order to prevent application of an axial twisting moment and were controlled in parallel to insure equal movement profiles. A uniaxial load cell (MLP-500, Transducer Technologies, Temecula, CA, USA) mounted in series to each linear actuator was used to measure applied shear force during all tests. Shear displacement was measured using a linear potentiometer with a 50 mm stroke that was mounted in parallel with the linear actuators (TS50, Novotechnik U.S. Inc., Southborough, MA, USA). Voltages from the load cells and linear potentiometer were digitally sampled at a rate of 64 Hz using a 16-bit analog to digital conversion board for all shear loading protocols (PCI 6034E, National Instruments Inc., Austin, TX, USA).

In addition to the flexion/extension passive tests, specimens were also preconditioned in anterior/posterior shear under position control prior to the acute failure protocol. Displacement during anterior/posterior shear preconditioning was applied at a constant rate of 0.05 mm/second using a continuous motion control algorithm (Appendix A.1). The targets were  $\pm 400$  N (positive force being anterior shear and negative force being posterior shear) of applied shear force for preconditioning. This target was approximately 14% of the ultimate anterior shear failure load (van Dieën et al., 2006;

Gallagher et al., 2010).

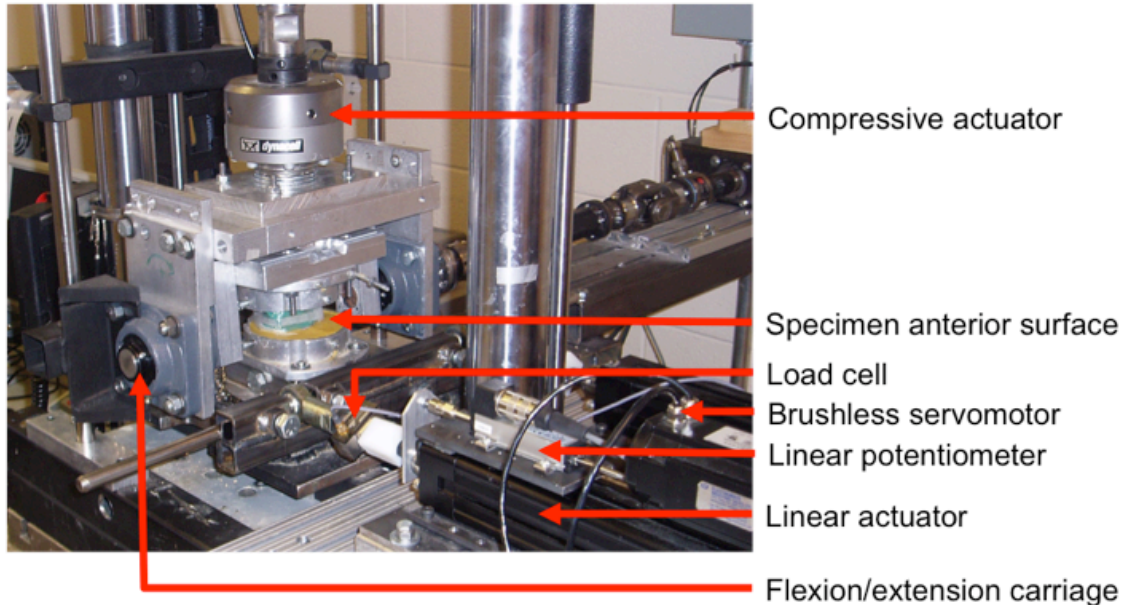


Figure 5.3 – Experimental setup for all shear loading protocols.

A constant load controlled compressive force equal to 15% ( $1454.1 \pm 23.1$  N) of each specimen's predicted compressive failure tolerance was applied during the repetitive failure test. Compressive failure tolerance for each specimen was determined using average endplate area as the input to a previously determined linear regression equation (Parkinson et al., 2005). The chosen compressive load for this study was similar to prior investigations of acute shear failure tolerances (van Dieën et al., 2006; Gallagher et al., 2010). The reference posture determined from the flexion/extension passive test was used as the neutral posture for repetitive shear failure tests.

Specimens were randomly assigned to be repetitively loaded to one of four percentages of calculated ultimate shear failure tolerance (20%, 40%, 60% or 80% of predicted ultimate shear load). Ultimate shear failure force for each specimen was *a priori* calculated by entering the length of the cranial pars interarticularis ( $x_1$ , given in

millimeters) and the average facet angle ( $x_2$ , given in degrees) into the linear regression equation developed in Chapter 4 (Equation 5.2).

$$F_{ultimate} = -1566.61338 + 140.84439x_1 + 39.19734x_2 \quad (5.2)$$

Specimens were repetitively loaded and unloaded to their targeted percentage of ultimate shear failure force at a targeted rate of 1 Hz until failure occurred or until the specimen had undergone 21600 loading cycles (equivalent to 6 hours of loading). The maximum number of loading cycles is equivalent to the maximum number of cycles for a similar investigation with compressive loading (Parkinson and Callaghan, 2007b). The selected loading frequency is identical to one other protocol that has studied failure of the vertebral joint exposed to repetitive submaximal shear loading (van Dieën et al., 2006) and studies of disc herniation resulting from repetitive flexion/extension (Callaghan and McGill, 2001; Drake et al., 2005). Failure was identified as a step change in the cycle-by-cycle shear displacement, average shear and hysteresis (Figure 5.4). A custom algorithm written in the GALIL motion control language (DMC-1800, Galil Motion Control Inc., Rocklin, CA, USA) controlled repetitive loading for each specimen (Appendix A.3) (Figure 5.5). The algorithm used shear force feedback from the load cells to adjust the controlled displacement rate in an attempt to generate a triangular force versus time waveform that loaded the specimen at a constant rate (Equation 5.3) whereby the ascribed submaximal shear load was achieved in a period of 0.5 seconds and returning to a position where zero shear force was recorded in another 0.5 seconds (Figure 5.6).

$$R = \frac{p(2F_{ultimate})}{100} \quad (5.3)$$

Where  $R$  is the targeted constant loading rate (N/s),  $p$  is the percentage of shear failure given as a value between 0 and 100, and  $F_{ultimate}$  is the *a priori* calculated ultimate force (N).

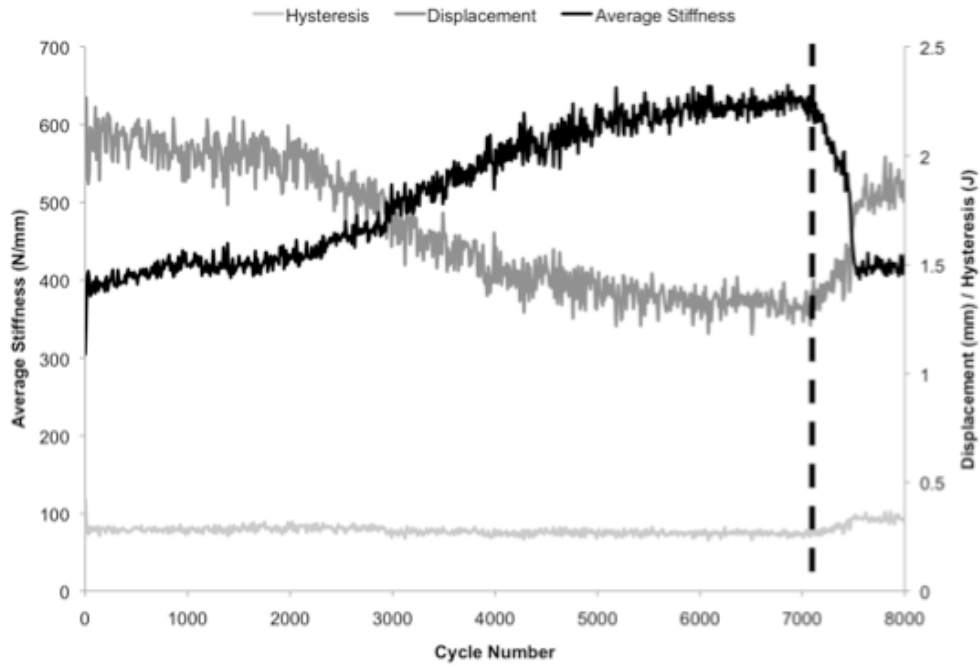


Figure 5.4 – Example of cycle-by-cycle average stiffness, shear displacement and hysteresis indicating the point of shear fatigue failure shown by the vertical dashed line.



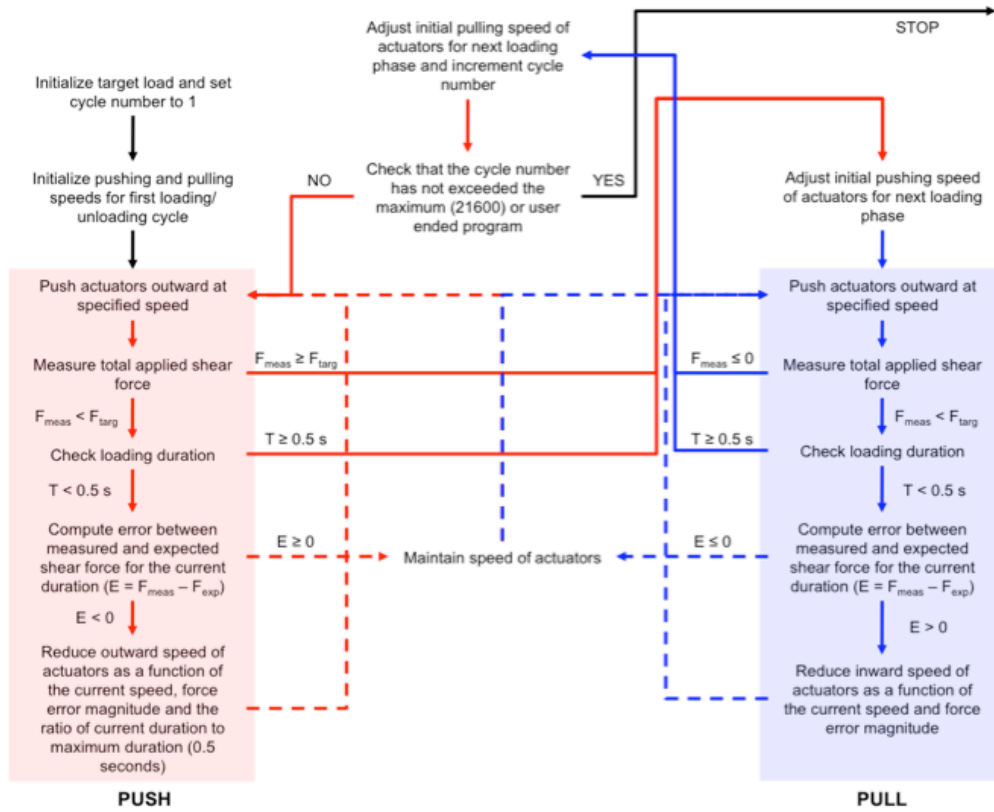


Figure 5.5 – Outline of the control algorithm for the repetitive shear loading protocol. Dashed lines represent feedback from the load cells that measure shear force, and is used to continuously update linear actuator displacement rates.

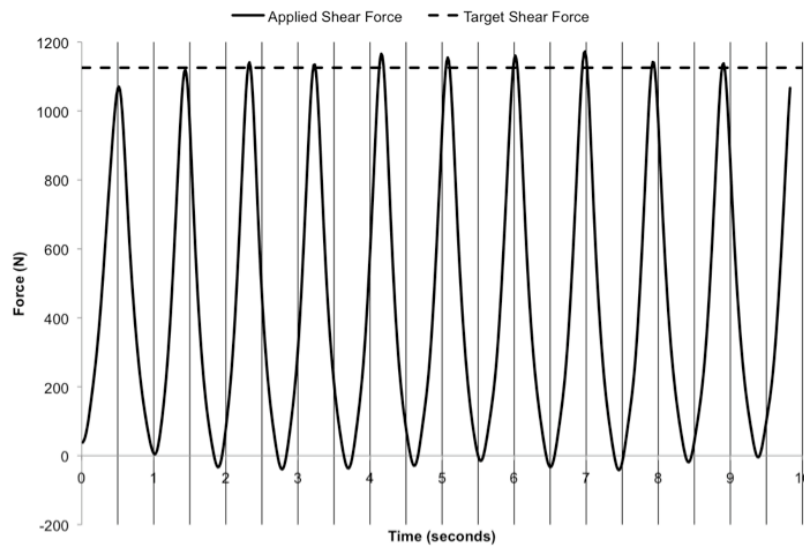


Figure 5.6 – Filtered shear force versus time profile (for the first 10 cycles) demonstrating the triangular loading/unloading waveform used for this investigation. The dashed black line shows the target shear load. Vertical lines indicate half-second intervals that were the targeted loading and unloading durations. The shear force versus time profile stabilized during the repetitive shear loading protocol.

The targeted force versus time profile was achieved by symmetrically adjusting the displacement rate (at an approximate rate of 140 updates per second) for both linear actuators throughout the loading and unloading phases. Displacement rate adjustment was based on the error between the expected and measured loading/unloading rates. Algorithm performance for all specimens tested in this study is summarized in Appendix C.1.

Following the shear failure protocol, the specimen was returned to the neutral position and uncoupled from the linear actuators. A second flexion/extension passive test was performed using the same load and displacement conditions as the test performed prior to the acute failure protocol.

### **5.2.3 Post-failure analysis**

Specimens were carefully removed from their fixation upon completion of the loading protocol. Due to irregular geometry of the vertebral joint, specimen positioning for the x-ray was controlled to the unloaded and neutral posture by placing the specimen's right side onto a formed impression created in a 25.4 mm thick block of extruded polystyrene foam. Each specimen was carefully sectioned into individual vertebrae and photographed. Bone failure was re-assessed both manually and visually by an investigator.

#### **5.2.4 Data processing and analysis**

Digitally sampled voltages from each load cell and the linear actuator were calibrated to shear force and displacement and filtered using a second order dual-pass Butterworth digital filter with respective cutoff frequencies of 3.5 and 4.25 Hz (Appendix B.1). Total applied shear force was calculated as the sum of the forces recorded from the two load cells. Cycle by cycle displacement, average loading stiffness and hysteresis were calculated from the calibrated force and displacement signals in order to assess the occurrence of failure. Measures of cumulative shear were obtained by integrating the force versus time profile from the start of the repetitive loading protocol until the end of the failure cycle or until the maximum number of cycles in the event that failure did not occur.

#### **5.2.5 Statistical analysis and weighting factor generation**

##### *5.2.5.1 Statistical analysis*

Randomization of specimens into loading magnitude groups was assessed using a two-factor (LEVEL and LOADING MAGNITUDE) analysis of variance (ANOVA) on the measured endplate area, cranial pars interarticularis length, average facet angle, facet tropism and calculated ultimate shear force (SAS 9.1, SAS Institute Inc., Cary, NC, USA). A single factor (LOADING MAGNITUDE) ANOVA was used to test for difference in cumulative load sustained for all failed specimens. Tukey's post-hoc tests were performed for all significant main effects and interactions. The level of significance was set to  $p < 0.05$  for all statistical analyses.

#### *5.2.5.2 Weighting factor generation*

Weighting factors were generated using a similar protocol described by Parkinson and Callaghan (2007a). Cumulative shear loads for specimens that failed prior to the maximum cycle limit were used for weighting factor generation. Data from specimens in the 20% shear load magnitude group were not used for determining weighting factors since all of the specimens in this group survived for the entire 21600 cycles. The number of data points (cumulative shear loads) at the 60% and 80% shear load magnitudes were reduced to match the number of failed specimens (three) at the 40% shear load magnitude in order to ensure equal weighting of data between all load magnitudes during curve fitting. Cumulative shear loads sustained prior to failure for each of the eight specimens in both the 60% and 80% groups were randomly assigned to one of three smaller groups at each load magnitude (i.e. two groups of three specimens and one group of two specimens at each load magnitude). Average cumulative shear load was calculated within each of the six smaller groups yielding three data points for each of the 60% and 80% load magnitudes. A continuous relationship between shear load magnitude (expressed as a percentage of ultimate shear failure tolerance) and cumulative shear load sustained prior to failure was obtained by fitting a power law function to the nine remaining cumulative shear load values.

The minimum weighting factor was set to a value of 1. Applying this weighting factor would neither enhance nor denigrate the importance of submaximal shear loads receiving this weighting factor when determining cumulative shear loads in subsequent investigations. Average cumulative shear load for the five survivor specimens exposed to the 40% shear load magnitude was used to define a threshold shear load magnitude for

assigning weighting factors above the minimum weighting factor. Shear load magnitudes at and below this threshold were assigned the minimum weighting factor. The threshold was determined by substituting the average cumulative shear load sustained by the survivors at the 40% shear load magnitude into the derived power law function relating submaximal shear load to sustained cumulative shear load and solving for the corresponding submaximal shear load magnitude. Weighting factors for each shear load magnitude from 1-100% were determined using a piecewise function (Equation 5.4).

$$w = \begin{cases} 1 & i \in R \mid [0, T] \\ \frac{1}{\alpha i^\beta} + 1 & i \in R \mid (T, 100] \end{cases} \quad (5.4)$$

Where  $w$  is the derived weighting factor function for a given shear load magnitude  $i$  (expressed as a percentage of ultimate shear failure),  $T$  is the defined threshold (expressed as a percentage of calculated shear failure tolerance), and  $\alpha$  and  $\beta$  are coefficients from the derived power law function relating submaximal shear load magnitude to the cumulative load sustained prior to failure.

## 5.3 RESULTS

### 5.3.1 Specimen randomization and vertebral level

The cranial pars interarticularis length for the C5-C6 specimens was 14% larger for C5-C6 than C3-C4 specimens ( $p = 0.0002$ ,  $d = 1.49$ ) (Table 5.1). This was reflected by 18.0% higher calculated ultimate shear tolerance for the C5-C6 specimens than the

C3-C4 specimens ( $p = 0.0003$ ,  $d = 1.55$ ) (Table 5.1). Facet tropism of specimens assigned to the 20% and 40% sub-maximal load magnitudes were smaller than the specimens assigned to the 80% load magnitude group by 2.8 ( $p = 0.0192$ ,  $d = 1.54$ ) and 2.5 ( $p = 0.0408$ ,  $d = 1.29$ ) degrees respectively (Table 5.2). There were no other statistically significant differences between sub-maximal load magnitudes for any of the other morphological measures ( $p \geq 0.3073$ ) (Table 5.2).

Table 5.1 – Morphological measurements and the resulting calculated ultimate shear failure tolerance for specimens from each vertebral level. An asterisk indicates a statistically significant difference between vertebral levels.

Level	Endplate Area (mm <sup>2</sup> )	Cranial Pars Length (mm)	Average Facet Angle (degrees)	Facet Tropism (degrees)	Calculated Ultimate Shear Failure Tolerance (N)
C3-C4	669.4 (16.8)	12.56 (0.30)	44.0 (0.9)	3.7 (0.5)	1925.2 (60.3)
C5-C6	658.9 (15.6)	14.32 (0.32)	46.5 (1.0)	3.1 (0.5)	2271.7 (55.4)
<i>P</i>	0.6688	0.0002*	0.0882	0.3117	0.0003*

Table 5.2 – Morphological measurements and the resulting calculated ultimate shear failure tolerance for specimens assigned to each shear loading magnitude. An asterisk indicates a statistically significant effect of loading magnitudes. Means with the same letter are statistically similar.

<b>Loading Magnitude</b>	<b>Endplate Area (mm<sup>2</sup>)</b>	<b>Cranial Pars Length (mm)</b>	<b>Average Facet Angle (degrees)</b>	<b>Facet Tropism (degrees)</b>	<b>Calculated Ultimate Shear Failure Tolerance (N)</b>
<b>20%</b>	652.3 (17.3)	13.91 (0.75)	44.7 (2.0)	2.3 (0.4) A	2145.9 (145.9)
<b>40%</b>	656.2 (24.3)	13.06 (0.36)	44.7 (1.0)	2.6 (0.5) A	2023.5 (67.5)
<b>60%</b>	688.3 (24.6)	13.04 (0.55)	45.3 (0.7)	3.6 (0.7) A,B	2043.9 (88.4)
<b>80%</b>	659.9 (25.7)	13.75 (0.41)	46.2 (1.5)	5.1 (0.9) B	2180.5 (98.7)
<b><i>p</i></b>	0.7154	0.3073	0.8625	0.017*	0.4709

### 5.3.2 Post-failure analysis

There were no specimens that had bone failure at the 20% load magnitude (Table 5.3). Bilateral fracture of the cranial pars interarticularis was the predominant injury, occurring in 78.9% of all failed specimens (Table 5.3). This injury was particularly consistent (10/11 = 90.9% of specimens) amongst specimens that failed at the 40% and 60% loading magnitudes (Table 5.3). Specimens loaded to 80% of their calculated ultimate shear failure tolerance demonstrated bilateral fracture of the cranial pars interarticularis in a less consistent manner (5/8 = 62.5% of specimens). Instead, specimens exposed to the 80% loading magnitude demonstrated a higher likelihood of

injury to a combination of structures such as unilateral fractures of either the cranial or caudal pars interarticularis, bilateral fracture of the caudal pars interarticularis, and endplate avulsion. Qualitatively, injury patterns at the 80% loading magnitude were also less consistent than either of the 40% or 60% loading magnitudes (Table 5.3).

Table 5.3 – Observed tissue damage for specimens that did not survive the entire repetitive shear loading duration of 21,600 cycles.

<b>Loading Magnitude</b>	<b>Vertebral Level</b>	<b>Fracture/Damage Location</b>
40%	C3-C4	Bilateral cranial pars interarticularis fracture
40%	C5-C6	Bilateral cranial pars interarticularis fracture
40%	C5-C6	Bilateral cranial pars interarticularis fracture
60%	C3-C4	Bilateral cranial pars interarticularis fracture
60%	C3-C4	Bilateral cranial pars interarticularis fracture
60%	C3-C4	Bilateral cranial pars interarticularis fracture
60%	C3-C4	Bilateral cranial pars interarticularis fracture
60%	C5-C6	Bilateral caudal pars interarticularis fracture
60%	C5-C6	Bilateral cranial pars interarticularis fracture
60%	C5-C6	Bilateral cranial pars interarticularis fracture
60%	C5-C6	Bilateral cranial pars interarticularis fracture, left caudal pars interarticularis fracture
80%	C3-C4	Bilateral cranial pars interarticularis fracture
80%	C3-C4	Bilateral cranial pars interarticularis fracture
80%	C3-C4	Bilateral cranial pars interarticularis fracture, inferior endplate avulsion
80%	C3-C4	Bilateral cranial pars interarticularis fracture
80%	C5-C6	Right caudal pars interarticularis fracture, left superior facet fracture
80%	C5-C6	Right cranial pars interarticularis fracture, left caudal pars interarticularis fracture
80%	C5-C6	Right caudal pars interarticularis fracture
80%	C5-C6	Bilateral cranial and caudal pars interarticularis fracture, inferior endplate avulsion



### 5.3.3 Cumulative load and cycles sustained prior to failure

The relationships between sub-maximal shear loading magnitude and cumulative shear as well as the number of loading cycles sustained prior to failure was non-linear. Cumulative shear sustained by the failed specimens at the 40% was higher than cumulative shear sustained at either the 60% (difference = 2.52 MN\*s,  $p < 0.0001$ ,  $d = 12.0$ ) or 80% (difference = 2.63 MN\*s,  $p < 0.0001$ ,  $d = 15.90$ ) levels (Figure 5.7). There was no statistical difference between cumulative shear sustained by failed specimens at the 60% and 80% load magnitudes ( $p = 0.297$ ) (Figure 5.7). However, the number of shear loading cycles sustained by specimens at each shear loading magnitude was statistically different from one another ( $p < 0.0001$ ,  $d > 2.0$ , Figure 5.8)

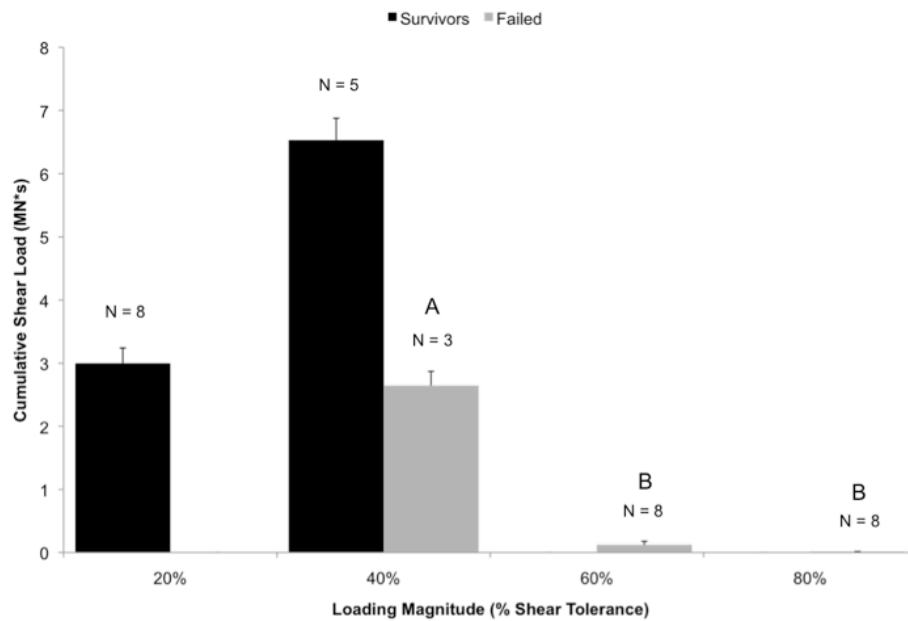


Figure 5.7 – Cumulative shear sustained by specimens that survived (black) and failed during (gray) the repetitive shear failure protocol. Different letters illustrates cumulative shear for specimens that failed during the repetitive shear failure protocol with statistically different means. The number above each bar (N) represents the number of specimens that either failed or survived at each loading magnitude. Error bars represent the standard error of the mean.

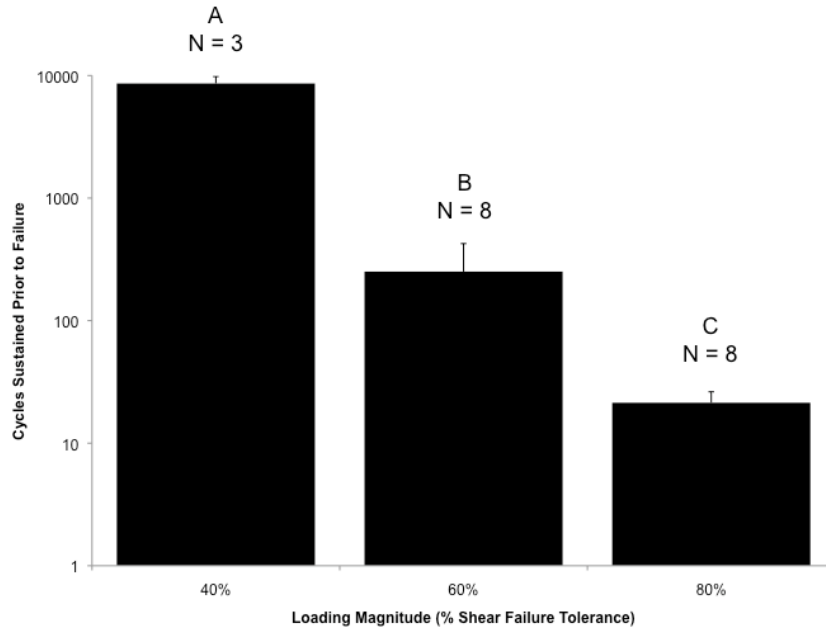


Figure 5.8 – The number of shear loading cycles sustained prior to failure for specimens in the 40%, 60% and 80% loading magnitude groups. The vertical axis is logarithmic. Statistical differences between means are given with different letters. The number above each bar (N) denotes the number of specimens that were injured during the repetitive shear loading protocol. Error bars represent the standard error of the mean.

### 5.3.4 Weighting factor generation

Data from the failed specimens at the 40%, 60% and 80% load magnitudes were used for generating weighting factors. The power law relationship between sub-maximal load magnitude and cumulative shear (Equation 5.5) explained 98.2% of the variance for the reduced dataset (Figure 5.9).

$$C_{shear} = (4 \times 10^{12})x^{-7.595} \quad (5.5)$$

Where  $C_{shear}$  is the cumulative shear (Ns) sustained prior to failure and  $x$  is a sub-maximal shear load expressed as a percentage (0-100%) of the calculated acute shear failure tolerance. The submaximal load threshold of 35.6% for applying the minimum

weighting was determined by substituting the cumulative shear sustained by specimens that survived the entire 21,600 loading cycles at the 40% sub-maximal load magnitude ( $6.53 \pm 0.35 \text{ MN}\cdot\text{s}$ ) into the power law relationship and then solving for the corresponding sub-maximal shear load magnitude.

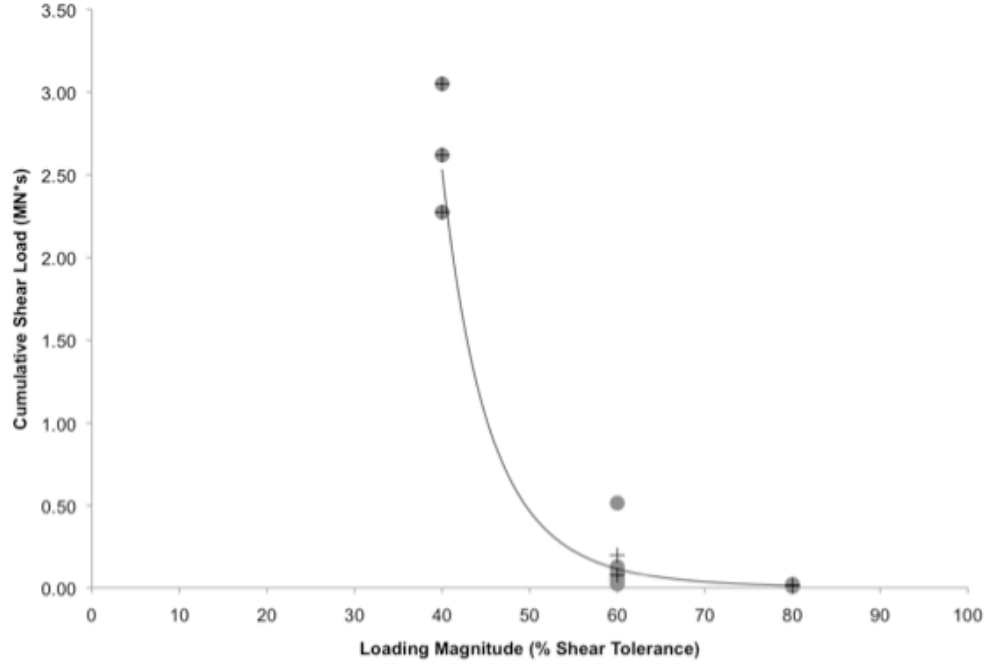


Figure 5.9 – Power law relationship between sub-maximal load magnitude and cumulative shear. Circles indicate cumulative shear sustained by individual specimens assigned to each loading magnitude. Crosses indicate cumulative shear values used for obtaining the power law relationship.

The final piecewise continuous weighting factor function is given by equation 5.6, and illustrated by figure 5.10.

$$w = \begin{cases} 1 & i \in R \setminus [0, 35.6] \\ \frac{1}{(4 \times 10^{12})i^{-7.595}} & i \in R \setminus (35.6, 100] \end{cases} \quad (5.6)$$

This is where  $i$  is a percentage of the calculated shear failure tolerance given as a real number between 0 and 100.

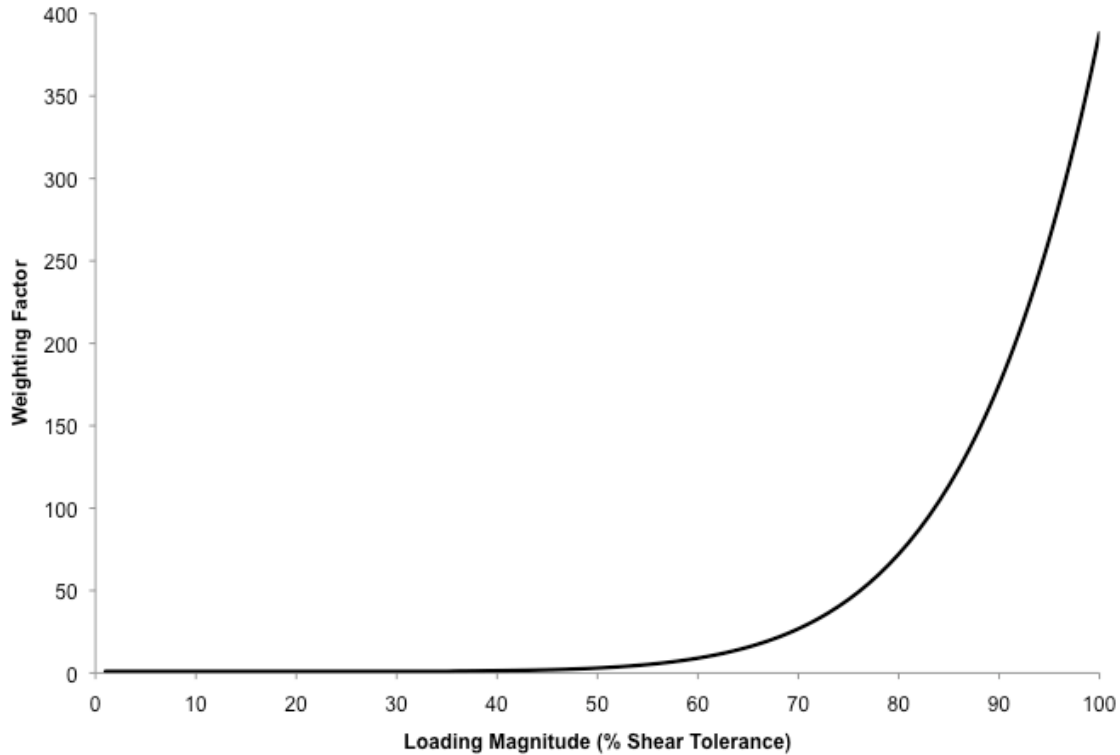


Figure 5.10 – Piecewise continuous weighting factor function of shear loading magnitude.

## 5.4 DISCUSSION

The current study clearly shows that load magnitude is a non-linear modifier of the fatigue life for the porcine vertebral joint exposed to repetitive submaximal shear loads. Results from this study imply that higher instantaneous shear load magnitudes should receive additional importance when determining cumulative shear loads in an occupational environment. A non-linear weighting method for instantaneous shear forces was also developed within this investigation based on cumulative shear load sustained

prior to failure with higher weighting factors being assigned to larger shear load magnitudes to compensate for the differing injury potential related to higher load magnitudes.

Isthmic spondylolytic fractures of the pars interarticularis are commonly associated with sub-maximal repetitive shear loading. Despite this association, limited research efforts have focused on biomechanical failure of the vertebral joint exposed to repetitive shear loading. Cyron and Hutton (1978) found that repetitive loading of the inferior facet in isolated human vertebrae caused bilateral fracture of the pars interarticularis. This is consistent with injuries observed for acute shear failure of isolated human vertebrae (Cyron et al., 1976) as well as porcine vertebral joints (Yingling and McGill, 1999; Gallagher et al., 2010; Chapters 3-4) and also consistent with the predominant injury of failed specimens from this investigation. However these authors (Cyron and Hutton, 1978) loaded specimens using a sinusoidal waveform with a peak-to-peak amplitude of 380 N and an average load of 570 N. This is approximately equivalent to a range from 19-38% of the acute failure tolerance determined by Cyron and colleagues in a prior study (Cyron et al., 1976). The findings from this investigation show that the load magnitude selected by Cyron and Hutton (1978) approached the threshold where this study has shown the injury potential associated with the applied shear loads increases non-linearly. Van Dieën and colleagues (2006) also found that posterior elements were compromised following repetitive shear loading between 20-80% of ultimate shear failure. Again only a single load magnitude was evaluated since their primary question focused on posterior element involvement in resisting repetitive shear loads. Lastly, Beadon and colleagues (2008) found that spondylolytic failure occurred only

after intermittent peak load magnitude had been increased to 1500 N (approx. 75% of shear failure tolerance) from 600 N (approx. 30% of shear failure tolerance). While the work of Beadon and colleagues (2008) demonstrated that load magnitude may influence the onset of shear failure under submaximal load magnitudes, their work was not motivated to determine a relationship between load magnitude and shear fatigue life of the vertebral joint. Similar to injuries observed in the current investigation, Beadon and colleagues (2008) also identified bilateral fracture of the cranial vertebra's pars interarticularis as the predominant injury from exposure to repetitive submaximal shear loads.

Injuries observed from specimens in this investigation varied as a result of different loading magnitudes. For this investigation, specimens assigned to higher shear loading magnitudes were also exposed to larger loading rates since the frequency of loading was controlled at 1 Hz. Specimens exposed to the 40% and 60% loading magnitude consistently showed bilateral failure of the cranial pars interarticularis with minimal occurrence of secondary injuries. Conversely, bilateral fracture of the cranial pars interarticularis was less common for specimens assigned to the 80% loading magnitude. Instead, combined injuries to the pars interarticularis, facets and endplates were observed at the highest loading magnitude. This may also be attributed to the increased facet tropism for specimens that were randomly assigned to the 80% loading magnitude. Similar to findings of this investigation, occurrence of endplate avulsions with higher shear loading rates has been previously documented by Yingling and McGill (1999). Similar investigations have also demonstrated that sub-maximal compressive load magnitude alters injury type and location (Parkinson and Callaghan, 2007b). However,

contrary to prior findings (Cripton et al., 1995; Yingling and McGill, 1999) for an acute failure protocol with higher shear load/displacement rates, the occurrence of bilateral cranial pars interarticularis fracture was less common at the highest loading magnitude for the current investigation. This difference is possibly attributed to the termination conditions for either the acute and repetitive loading protocols. Loading protocols for acute failure often use displacement limits (Gallagher et al., 2010) or decreases in force (Yingling and McGill, 1999; Gunning et al., 2001) to detect failure. Failure of the vertebral joint under either compressive or shear repetitive loading paradigms is more difficult to detect and has required manual detection following inspection of the collected data (van Dieën et al., 2006; Parkinson and Callaghan, 2007a; Parkinson and Callaghan, 2007b).

The algorithm that controlled the repetitive loading protocol used for this investigation matched displacement rates of the linear actuators using feedback from the load cells to targeted loading rates defined by the investigator. Prescribed displacement rates at the initiation of each loading cycle were dependent upon a function of the previous loading cycle's initial actuator displacement rate and the discrepancy between the achieved shear force and the targeted force (Appendix A.3). This allowed the initial displacement rate to stabilize throughout the repetitive loading protocol. However, rapid changes in specimen properties such as stiffness and hysteresis (as observed at the point of failure) would cause instability within the control algorithm leading to large fluctuations in actuator displacement and rate of displacement. This behavior was particularly evident at the 80% shear loading magnitude. As a protective measure for the instrumentation (load cells) and equipment (linear actuator, servomotors), the repetitive

loading protocol was terminated by the investigator upon detection of sudden increases in linear actuator displacement. Since unilateral pars interarticularis fractures were more common amongst specimens assigned to the 80% shear loading magnitude, investigator initiated termination of the repetitive loading protocol at the highest loading magnitude may have disrupted the injury process that eventually would have led to bilateral fractures of the pars interarticularis.

The current investigation is the first to directly quantify the relationship between shear load magnitude and cumulative shear load sustained prior to failure. Results from this investigation clearly indicate that the vertebral joint's fatigue life (both sustained cumulative load and the number of loading cycles sustained prior to failure) rapidly decays in a non-linearly fashion with increasing shear load magnitude. Previous research for compressive loading using both human and porcine specimens has also demonstrated that increasing load magnitude non-linearly decreases the number of compressive cycles (Brinckmann et al., 1987; Hansson et al., 1987) and cumulative compressive load (Parkinson and Callaghan, 2007b) sustained prior to failure. Findings from this investigation and the work of Parkinson and Callaghan (2007a) support the use of a tissue-based approach for determining appropriate weighting factors when calculating cumulative load exposure.

Different non-linear methods for weighting of compressive loads in estimates of cumulative exposure have been previously presented (Jager et al., 2000; Seidler et al., 2001; Parkinson and Callaghan, 2007a). Initial attempts of force weighting by raising instantaneous compressive load values by an arbitrarily chosen exponent to represent higher injury potential with higher compressive load were performed by Jager and



colleagues (2000) and Seidler and colleagues (2001). Parkinson and Callaghan (2007a) improved upon the methods for deriving weighting factors by relating their weighting factors directly to accumulated tissue damage from *in vitro* tests. The reciprocal of a power-law function was used to define a piecewise continuous weighting factor function in the current investigation. Parkinson and Callaghan (2007a) found that compressive loads below 37.5% of the failure tolerance did not require additional weighting when calculating cumulative compressive load. Congruently, the current investigation found that shear loads below 35.6% did not require additional weighting when determining cumulative shear load. Weighting factors derived from this investigation are directly related to sustained tissue damage that provides a biological basis for their development and implementation.

In order to enhance transference of the results from a porcine model to human vertebral joints, load magnitude for each group was scaled to a proportion of the calculated ultimate shear failure tolerance. Ultimate shear failure tolerance was calculated using a previously developed regression equation that used cranial pars interarticularis length and average facet angle as input (Chapter 4). The error associated with this equation was found to be  $\pm 232$  N (equivalent to approximately 10.9% of the ultimate shear failure tolerance). Since load magnitudes used in this investigation were separated by 20% intervals, error induced from the calculation of acute ultimate shear failure tolerance likely did not cause overlap in the relative loads experienced by specimens assigned to each group.

Using a deceased *in vitro* model eliminates the possibility of regenerative processes from influencing the onset of tissue damage (Cyron and Hutton, 1978). Periods

of rest can lead to tissue healing and regeneration of bone that may influence the vertebral joint's fatigue life (Cowin and Hegedus, 1976) and can also affect the cumulative load sustained prior to failure (Parkinson and Callaghan, 2007a). Initiation of bone fracture repair within the rat tibia has been shown to occur after a period of one week (Garavello-Freitas et al., 2003). However, stress fracture repair of the pars interarticularis, as observed in this investigation, is possibly limited by the presence of a synovial pseudoarthrosis in the pars interarticularis (Shipley and Beukes, 1998). Thus, the lack of regenerative processes when using a deceased *in vitro* model may have a minimal impact on the results of the current investigation. Cumulative shear load, the number of loading cycles sustained prior to failure and weighting factors derived in this investigation should be viewed as a conservative (i.e. worst case scenario) estimate of the increased tissue damage that may be inflicted by higher shear loads.

This investigation is the first to demonstrate the non-linear relationship between varying shear load magnitude and the fatigue life of the vertebral joint exposed to repetitive anterior shear loading. Both cumulative shear load and the number of loading cycles sustained prior to failure are non-linearly related to the magnitude of sub-maximal shear loading. This study demonstrates that shear loads that are higher than or equal to 60% (equivalent to approximately 1325 N from Chapter 3 and 4) of the ultimate shear failure tolerance carry greater injury potential. Injuries resulting from repetitive sub-maximal shear loading were to the cranial pars interarticularis, which is consistent with injuries observed for acute shear failure testing. Thus, the results from this investigation demonstrate that higher shear loads should receive additional importance when calculating cumulative shear exposure to evaluate injury risk. This enhances the

relationship between cumulative load estimates and low-back tissue injury. The piecewise continuous function presented here to derive appropriate weighting factors can be easily implemented within any assessment of occupational cumulative exposure to shear load. Similar to what has been done for compressive loading, future efforts should expand the weighting factor to a multivariate function of load magnitude and work to rest ratio.

## **CHAPTER 6**

### **USE OF FINITE ELEMENT ANALYSIS FOR QUANTITATIVELY INVESTIGATING THE MOMENT ARM HYPOTHESIS FOR ALTERED SHEAR FAILURE TOLERANCES UNDER COMBINED COMPRESSIVE LOADING AND FLEXION/EXTENSION POSTURES**

## 6.1 INTRODUCTION

Previous *in vitro* studies have clearly shown that the pars interarticularis is the primary site of failure under acute (Cyron et al., 1976; Crompton et al., 1995; Yingling and McGill, 1999; van Dieën et al., 2006; Gallagher et al., 2010; Chapters 3-4) as well as repetitive shear loading (Cyron and Hutton, 1978; Beadon et al., 2008; Chapter 5). The proposed mechanism for this fracture under shear loading is a bending moment generated about the pars interarticularis caused by contact between the articulating inferior and superior facets of the respective cranial and caudal vertebrae of a vertebral joint (Cyron et al., 1976; Yingling and McGill, 1999; Chapter 3). Evidence also exists that shows the vertebral joint's ultimate failure tolerance under acute shear failure is altered by both postural deviation (Yingling and McGill, 1999) and joint compression (Chapter 3). These studies (Yingling and McGill, 1999; Chapter 3) have both hypothesized that alterations in moment arm length between the force centroid on the articulating facet and the pars interarticularis play a role in modulating ultimate shear failure tolerance under different vertebral joint postural deviations and compressive loads. This investigation examines alterations in facet contact and the inherent changes in moment arm length that has been hypothesized to alter a vertebral joint's ultimate shear failure tolerance using a finite element model of the porcine C3-C4 functional spinal unit that has also been used in comparable *in vitro* testing (Chapters 3-5).

The finite element method is a useful tool for determining internal stress and strain distributions throughout a structure and can also allow for serial investigation of a large number of injury mechanisms (Brown, 2004). The finite element method has been used to demonstrate that the pars interarticularis of the human L4-L5 vertebral joint is the

weakest structure in the non-pathologic lumbar spine (Chosa et al., 2004). Moreover, finite element models have shown that increased stress is observed in the pars as a result of forces generated by facet contact (Schultz and Niethard, 1980; Chosa et al., 2004). Finite element models of the human lumbar spine have also demonstrated that complex loading that involves vertebral joint postural deviation and compressive force will influence the stress distributions within and contact locations on the articulating facets (Shirazi-Adl, 1991). Specifically, recent finite element results from a model of the L5-S1 joint have shown that contact pressures within the facet are higher with extension than flexion (El-Rich et al., 2009).

*In vitro* investigations have also demonstrated altered facet articulation with compressive force and postural deviation. Using pressure sensitive film placed in between articulating facets of an *in vitro* human lumbar functional spinal unit, Lorenz and colleagues (1983) showed that the magnitude of facet contact force increases both in extended postures and with higher compressive forces. Furthermore, this study also demonstrated that left facetectomy almost eliminated facet contact pressure of the intact right facet. In addition Dunlop and colleagues (1984) used pressure sensitive film in human lumbar cadaveric functional spinal units to illustrate that the location of contact pressure moved cranially on the facet surface with flexed postures and caudally with extended postures. Their study also showed that reducing disc height increased the area of facet contact. Other *in vitro* results have shown that the facets bear higher forces in extended postures than flexed postures (Adams and Hutton, 1980). Recently, Drake and colleagues (2008) demonstrated that interfacet spacing increased with flexed postures and decreased with extended postures. The combined implications from these *in vitro*

investigations demonstrate that facet articulation is modified by compressive force and postural deviation.

Results from Chapter 3 showed that ultimate shear failure tolerance of the porcine cervical spine increased with higher compressive forces and decreased from an extended to flexed posture. It was postulated that alterations in failure tolerances resulting from different compressive forces and/or flexion/extension postures are a function of changes in facet articulation. In particular the centroid of facet contact force that occurs during shear loading was hypothesized from Chapter 3 to change with compressive loading and postural deviation. Consequently, changes in facet contact location would also alter the moment arm length for the bending moment applied about the pars interarticularis which has been implicated as a primary factor that modulates shear failure tolerance (Cyron et al., 1976; Yingling and McGill, 1999; Chapter 3). Injury documentation from Chapter 3 also indicates that the caudal pars interarticularis is fractured more frequently when the vertebral joint is exposed to shear displacement in a flexed posture. This information suggests that alterations in facet interaction resulting from postural deviations may also alter the site of failure.

Alterations in facet contact resulting from postural deviation and compressive force have not been linked to changes in the magnitude of stresses developed within the pars interarticularis and the moment arm length from the force centroid of facet contact to the location of maximum stress within the pars interarticularis. The goal of this investigation was to employ the finite element method to quantify internal changes in stress through the pars interarticularis as a function of the compressive load and postural deviation and to link changes in stress concentration to alterations in the force centroid of

facet contact. Based on prior *in vitro* investigation, it was hypothesized that the moment arm length would increase for flexed postures and decrease for extended postures. With regards to compressive force, it was hypothesized that increased compression would lead to a reduction of the moment arm length. It was also hypothesized that compressive forces and extended postures would increase facet contact area while flexed postures would decrease facet contact area. Lastly, it was hypothesized that alterations in facet contact location and area would be reflected in congruent changes in stress through the pars interarticularis. Larger moment arm lengths were hypothesized to create a mechanical advantage that would result in a larger applied moment at the pars interarticularis. The increase in applied moment, as a result of increased moment arm length, would subsequently increase the stress observed at the pars interarticularis for two identical backward displacements of the inferior vertebra for a single vertebral joint.

## **6.2 METHODS**

### **6.2.1 Geometry generation**

#### *6.2.1.1 Individual vertebrae*

The exterior surface geometries for a C3 and C4 vertebra from the same porcine functional spinal unit (FSU) were independently created from point clouds generated by a pair of white light scanners (StarCam FW-3R 3D, VX Technologies Inc., Calgary, AB, Canada). Prior to scanning, each vertebra was coated with liquid developer (SKD-S2 Developer, Magnaflux, Glenview, IL, USA) to enhance contrast between the vertebra's exterior surface and its background. Each vertebra was posed on a black rotating tabletop



that contained a fixed set of white dots. These white dots were used as control points in subsequent steps for scan alignments within a single pose. Both scanners took a single scan of the specimen simultaneously by sequentially projecting light in coarse and fine patterns onto the specimen and table to construct independent point clouds from the reflective surfaces (sprayed bone or white dots) within each scanner's local coordinate system (Figure 6.1). The coarse pattern of dots was set with 20 by 20 pixel spacing between dots, dot radius of 3 pixels, and a resolution of 10 by 10 dots. Point clouds for each scanner and from a single scan were imported into a surface development software package (Geomagic Studio 9, Geomagic, Research Triangle Park, NC, USA). For a single scan, the point clouds (expressed in each scanner's respective local coordinate system) generated by each scanner were aligned to a set of points representing identical control points (white dots) that were present in both camera's point clouds (Figure 6.1). The end result from each scan was a merged point cloud from the two independent scanners. While ensuring that the specimen did not move relative to the table's surface, the table was carefully rotated approximately between 45-90 degrees in preparation for the next scan. Another scan was taken with the table in the rotated position and the same process of aligning the independent scans from each scanner was repeated. Each newly aligned scan was then added to the existing merged point cloud for that pose (Figure 6.1). Scans were taken with the specimen in a single pose until the table had been rotated by 360 degrees with the final result being a point cloud of the specimen in a single pose. The specimen's pose was then changed and the process of generating a single point cloud was repeated for the new pose. Each vertebra was scanned in four sequential poses (pose 1 = laying on inferior surface, pose 2 = laying on superior surface, pose 3 = laying on anterior

surface and pose 4 = laying on tip of spinous process that was embedded in black non-reflective molding clay).

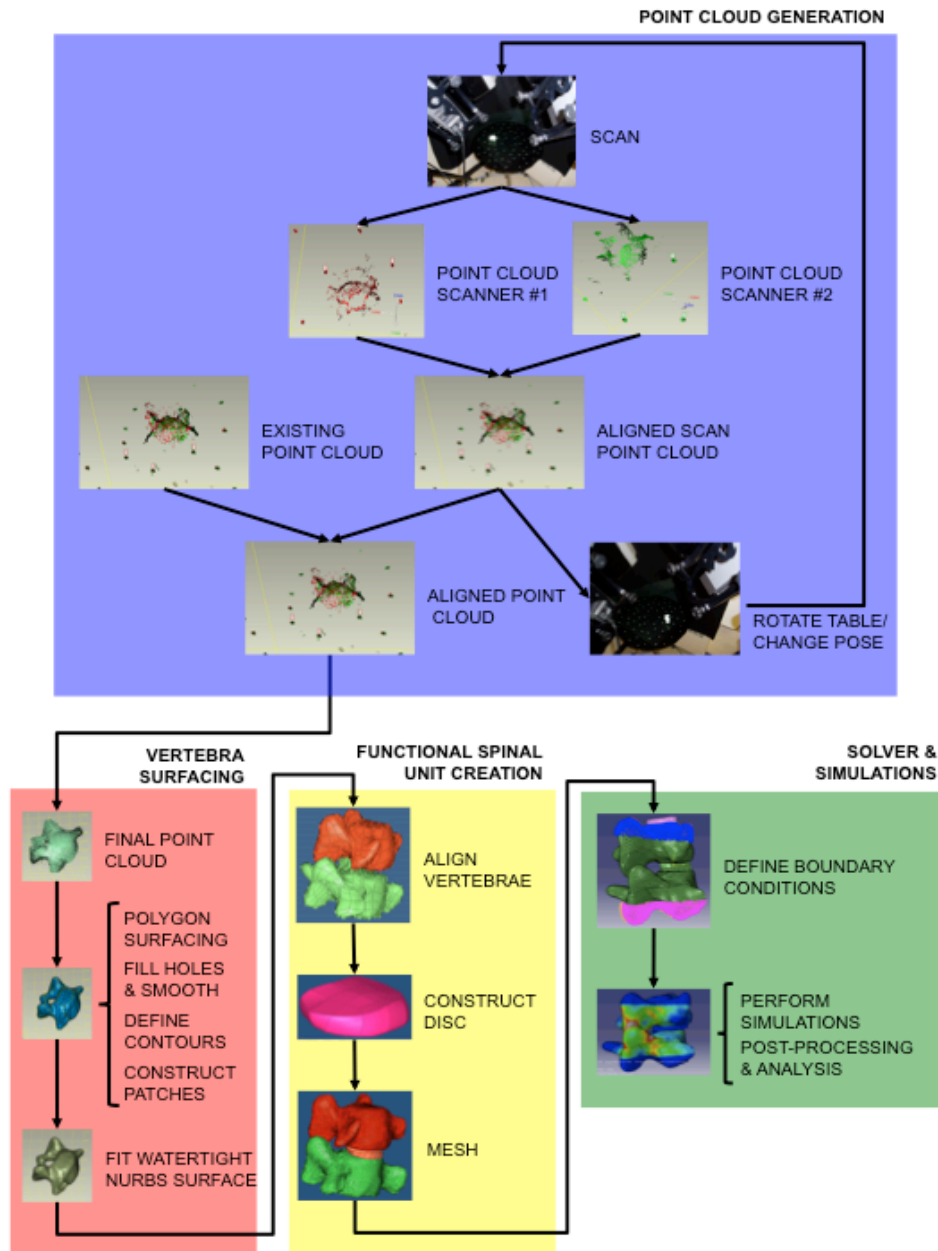


Figure 6.1 – Flowchart illustrating the step-by-step process of generating the vertebral geometry, meshing the functional spinal unit, defining simulation boundary conditions and analyzing results from the simulations.

For each vertebra, the final point clouds from each pose were sequentially aligned using identical anatomical landmarks. Point clouds from the first two poses (respectively laying on the inferior and superior surfaces) were aligned. This merged cloud was then aligned with the point cloud from the third pose (laying on the anterior surface) and the resulting merged cloud was then aligned with the point cloud from the fourth pose (laying on tip of spinous process that was embedded in black non-reflective molding clay). The final results were two point clouds representing each vertebra's exterior surface geometry (Figure 6.1).

Noise reduction using the built-in functions within Geomagic was performed on the vertebral point clouds prior to surfacing. The final C3 and C4 point clouds were then independently fit with a series of triangular polygons to create the exterior vertebral surfaces. Holes in each of the vertebral surfaces were patched using the built-in tools from the Geomagic software with the end results being watertight surface representations, consisting of triangular polygons, of the scanned C3 and C4 vertebrae. The polygons of the watertight surfaces for the C3 and C4 vertebra were smoothed and a non-uniform rational basis spline (NURBS) surface representation of the exterior was constructed from this surface (Figure 6.1). These NURBS surfaces were individually saved as initial graphics exchange specification (IGES) files that were used for meshing and disc geometry generation in Hypermesh (Hypermesh 10.0, Altair Engineering, Troy, MI, USA).

#### 6.2.1.2 Functional spinal unit (FSU)

The surface representations for the C3 and C4 vertebrae were imported into Hypermesh. The two vertebrae were manually aligned so that their relative orientations reflected the geometry of an intact porcine C3-C4 functional spinal unit (Figure 6.2).

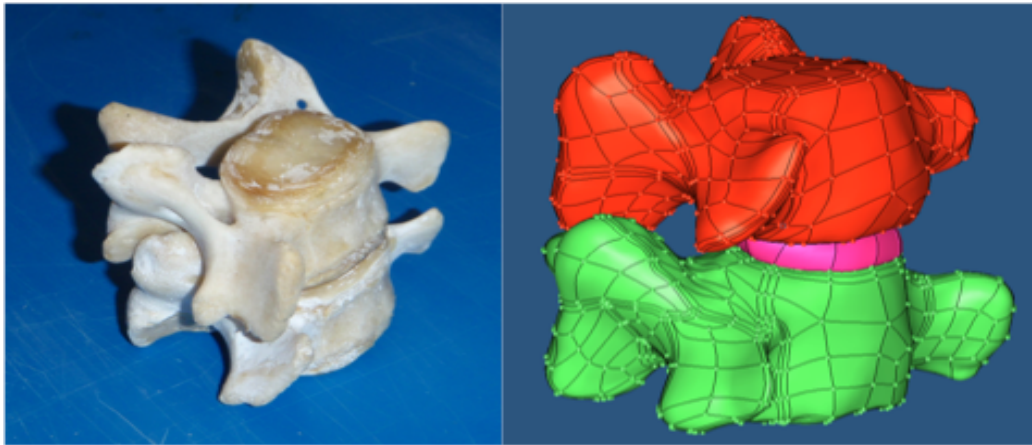


Figure 6.2 – Comparison of the stacked vertebrae (left) used to define the geometry of the modeled functional spinal unit (right).

Specifically, the C3 vertebra was adjusted so that the caudal surface of the vertebral body was directly above the cranial surface of the C4 vertebra. The caudal surface of the C3 vertebra and the cranial surface of the C4 vertebra were separated by an average vertical distance of  $4.69 \pm 0.08$  mm. This intervertebral disc space was chosen to mimic the intervertebral disc space ( $4.72 \pm 0.64$  mm), measured from sagittal plane x-rays of C3-C4 specimens taken in Chapter 4, at the midpoint between the anterior and posterior corners for each of the C3 and C4 vertebrae. Furthermore, the ratio of intervertebral disc space to average vertebral body height was similar between the model (21.3%) and the *in vitro* measurements ( $21.2 \pm 3.1\%$ ). The relative orientation between vertebrae also allowed for a space of approximately 1.01 mm between the articulating inferior facets of C3 and the

superior facets of C4. This gap was chosen to mimic previously used gaps between articulating facets in vertebral finite element models of human functional spinal units (Shirazi-Adl et al., 1986; Sharma et al., 1995), and were derived from *in vitro* measurements. Geometry for the intervertebral disc was constructed within Hypermesh to lie in between the caudal surface of the C3 vertebral body and the cranial surface of the C4 vertebral body. The surfaces for the caudal and cranial aspects of the intervertebral disc were taken directly from the C3 and C4 vertebrae respectively and contained a set of 14 smaller subsurfaces (Figure 6.1) arranged so that each subsurface on the cranial aspect of the intervertebral disc had a matching partner on the caudal aspect. Therefore, each intersection point between two or more subsurfaces for the cranial aspect of the disc had a matching partner on the caudal aspect of the disc. Furthermore, the intervertebral disc shared connection points with both the C3 and C4 vertebrae. Lines were constructed to connect the perimeters for the two surfaces as well as the matching pairs of interior intersection points. Using these lines, separate sets of surfaces were constructed for the disc's exterior surface and interior volume.

### **6.2.2 Element type, material properties and mesh refinement**

The modeled FSU consisted of cortical bone, trabecular bone, endplates and a disc material. Each of these materials was modeled as linear, isotropic and homogeneous.

### *6.2.2.1 Components*

#### *6.2.2.1.1 Cortical bone*

Geometry for the cortical shell on each vertebra's exterior was defined by the surface geometry generated from the white light scanning procedure that was previously described. The caudal surface of C3 and cranial surface of C4 were meshed with quadrilateral shell elements. Nodes for these elements were shared with the cranial and caudal portions of the intervertebral disc respectively. The remaining vertebral cortical shell was meshed with triangular shell elements. All shell elements were modeled with a constant thickness of 0.45 mm (Kato et al., 1998; Akahoshi et al., 2005), modulus of 19,400 MPa and Poisson's ratio of 0.34 (Kato et al., 1998).

#### *6.2.2.1.2 Trabecular bone*

The nodes comprising the shell elements of the cortical bone defined the exterior geometry for the trabecular bone. An automated meshing algorithm was executed within Hypermesh to generate a set of tetrahedral solid elements to represent the vertebral trabecular bone. Porcine trabecular bone was assigned a modulus of 229 MPa (Teo et al., 2006) and a Poisson's ratio of 0.3 (Kumaresan et al., 1999).

#### *6.2.2.1.3 Endplates*

The inferior endplate of C3 and the superior endplate of C4 were modeled with quadrilateral shell elements with a constant thickness of 0.45 mm. Endplate elements

were assigned a modulus of 50 MPa and a Poisson ratio of 0.4 (Kumaresan et al., 1999). Nodes defining these elements were also used to define connections between the vertebrae and the intervertebral disc.

#### 6.2.2.1.4 Intervertebral disc

Geometry for the intervertebral disc was defined by the quadrilateral shell elements on the caudal surface of the C3 vertebra and the cranial surface of the C4 vertebra. Hexahedral elements consisting of 8 nodes and a single integration point were created so that nodes were shared between the cranial aspect of the disc and the caudal surface of the C3 vertebra and likewise for the caudal disc surface with the cranial C4 surface.

The intervertebral disc is often modeled as a composite structure of the annulus fibers and nucleus pulposus (Stokes et al., 2010). A ground substance can also be included in the finite element representation of the intervertebral disc (Rao and Dumas, 1991). However, the intervertebral disc was modeled as a single uniform material for the current investigation with parameters that represented the combined influence of the three aforementioned materials. The intervertebral disc modulus was set to 25 MPa and a Poisson ratio of 0.49 was assigned (Aziz et al., 2008). The modulus used for the current model was similar to approximated moduli computed using measurements made from Chapter 3 (Table 6.1).

Table 6.1 – Estimates of the elastic modulus for the entire intervertebral disc using compressive forces, disc area, disc height changes from Chapter 3 (shown with a superscript ‘a’), and an average height for the unloaded porcine cervical intervertebral disc reported by Yates (2009) (shown with a superscript ‘b’).

<b>Compression (%)</b>	<b>Actual Compressive Force<sup>a</sup> (N)</b>	<b>Initial Disc Height<sup>b</sup> (mm)</b>	<b>Disc Height Change<sup>a</sup> (mm)</b>	<b>Disc Area<sup>a</sup> (mm<sup>2</sup>)</b>	<b>Stress at Max. Height Change (MPa)</b>	<b>Strain at Max. Height Change</b>	<b>Elastic Modulus (MPa)</b>
15%	1374	9	0.66	625	2.1984	0.073	29.978
30%	2897	9	1.77	661	4.3828	0.197	22.285
45%	4564	9	2.91	697	6.5481	0.323	20.252
60%	5720	9	3.9	652	8.7730	0.433	20.245



#### *6.2.2.2 Determining appropriate mesh size*

A convergence study was conducted in order to identify an appropriate number of elements that would improve computational efficiency while not degrading the consistency of solutions for the subsequently described simulations. Mesh convergence was identified by refining the triangular shell and vertebral tetrahedral meshes. Three meshes of each vertebra were constructed with increasing mesh refinement (Table 6.2). Each of these meshes was subjected to an identical simulation in order to determine convergence of mesh refinement. The conditions for the convergence simulations were backward shear displacement of the C4 vertebra at a constant velocity of 0.15 mm/s with no compressive force and no postural deviation for a period of 20 seconds. The C3 vertebral body was held in its initial position during these simulations. Maximum stress developed within the cortical shell on the right cranial pars interarticularis at the end of each simulation was used as the variable for determining convergence. Convergence was achieved if less than 1% difference in the peak stress occurred between two successively refined meshes (Kotha et al., 2004).

Table 6.2 – The number of nodes, elements, the magnitude of stress at the location of peak stress within the pars interarticularis and the percent change in stress between each of the three meshes constructed to identify convergence.

	Number of Nodes	Total Number of Elements	CORTICAL BONE	ENDPLATES	TRABECULAR BONE	DISC	Stress (MPa)	Percent Change (%)
			Number of Triangular Shell Elements	Number of Quadrilateral Shell Elements	Number of Tetrahedral Elements	Number of Hexahedral Brick Elements		
<b>Mesh 1</b>	5051	25293	6710	112	18359	112	109.98	
<b>Mesh 2</b>	16849	88952	18912	112	69816	112	134.64	22.42
<b>Mesh 3</b>	69546	377557	66359	112	310974	112	134.58	0.04

### 6.2.3 Simulation conditions

Each simulation was performed in a sequence of three phases (compression, rotation and shear displacement). The following is a description of the loads and boundary conditions required to perform each phase of the simulations. All simulations were conducted in ABAQUS CAE 6.9 (SIMULIA, Providence, RI, USA).

#### 6.2.3.1 Loads

Compressive forces were applied at 0%, 15%, 30%, 45% or 60% of the model specimen's predicted compressive strength. A linear regression equation relating average endplate area to compressive failure tolerance was used to predict compressive strength (Parkinson et al., 2005). The previously mentioned percentages translated into compressive force magnitudes of 0 N, 813.2 N, 1626.4 N, 2439.6 N and 3252.8 N for the model specimen. In order to appropriately mimic the boundary conditions of the *in vitro* tests, the compressive forces were transformed into constant pressures in the model. The pressure was applied to the outer surface of the shell elements defining the C3 vertebra's cranial surface. Compressive forces were transformed into pressures of 0 MPa, 2.776 MPa, 5.551 MPa, 8.327 MPa and 11.102 MPa using the cranial surface area (292.98 mm<sup>2</sup>) for the C3 vertebra.

#### 6.2.3.2 Boundary conditions

Prior to application of backward shear displacement of the C4 vertebra, the model was subjected to the compressive pressure and a postural deviation about the model's

flexion/extension (Z) axis. Since the modeled specimen was approximately 29% smaller than specimens tested in Chapter 3, and considering that larger flexion angles would not have allowed the facets of the modeled specimens to come into contact with each other during shear displacement, simulated flexed (5.67 degrees) and extended (3.15 degrees) postures were scaled to be 29% smaller than those reported in Chapter 3. These postural deviations fell within the respective range (flexion = 3.7 – 11.1 degrees; extension = 2.1 – 6.2 degrees) of neutral zone limits derived from the *in vitro* flexion/extension passive tests conducted for each specimen in Chapter 3. Nodes for shell elements covering approximately 25% of the C4 vertebral body and part of the exposed inferior facets were constrained from moving in all degrees of freedom during this step. From the compressed and rotated state, backward displacement of the C4 vertebra was performed at a constant displacement rate of 0.15 mm/s to mimic the *in vitro* test conditions during acute shear failure. This was performed for a simulated period of 20 seconds producing a total shear displacement of 3 mm for the C4 vertebra. Displacement of the C4 vertebral body was constrained to be entirely in the anterior-posterior direction in order to properly simulate the *in vitro* fixation and test conditions from Chapter 3 that physically constrained this axis of motion. The position of the C3 vertebral body was fixed during the backward displacement phase, again replicating the in-vitro testing configuration.

#### 6.2.3.3 Contact formulation

Contact between the adjacent vertebrae was modeled as frictionless and non-linear (Chosa et al., 2004; El-Rich et al., 2009), with node-to-surface contact defined between the cortical shell elements for both C3 and C4 (El-Rich et al., 2009).

#### 6.2.4 Post-processing

Output measurements extracted from the C3 vertebra for each simulation were the location of initial facet contact, the number of nodes in contact with the C4 vertebra, contact force, force centroid for facet contact, location of peak stress within the pars interarticularis and the magnitude of the stress at this location (Figure 6.3). The moment arm length between the force centroid for facet contact and the location of peak stress was also calculated. These output measurements were extracted for all iterations (i.e. time step) of the backward C4 displacement phase. Time points of interest during the displacement phase were the end of the shear displacement phase and a point at which identical strain was produced for each posture within a single compressive load. The moment arm lengths produced at the end of the shear displacement phase for all simulations with greater than 0% compressive force were also correlated with the ultimate shear failure tolerances quantified *in vitro* from Chapter 3 in order to determine the potential influence of moment arm length on ultimate shear failure.

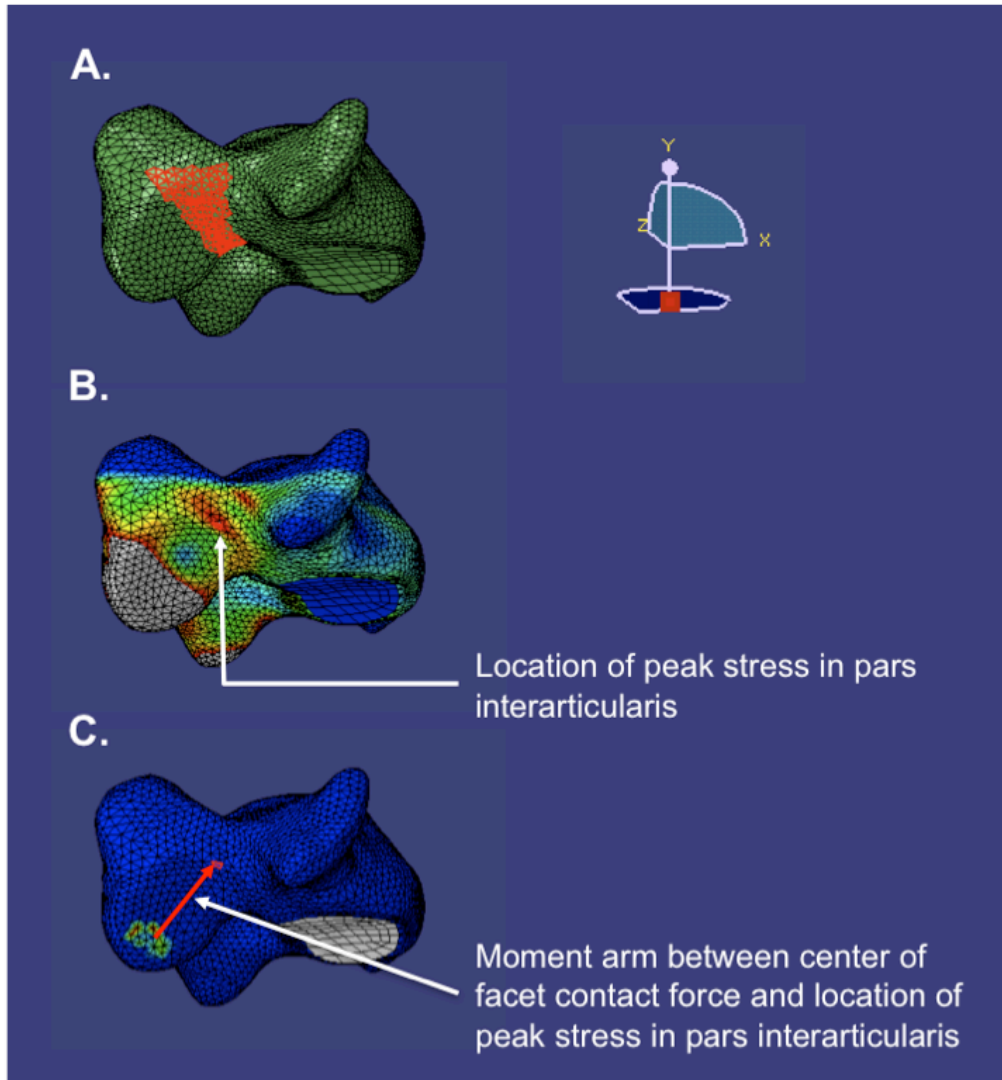


Figure 6.3 – The defined location for the pars interarticularis (A.), stress distribution following 3 mm of C4 backward shear displacement illustrating the location of peak stress within the pars interarticularis (B.), and the contacting node locations as well as the moment arm length between the force centroid of facet contact and the location of peak stress within the pars interarticularis (C.) for the C3 vertebra.

## 6.2.5 Model verification and validation

Verification of the meshing procedure, and the utility of tetrahedral elements was evaluated by comparing the finite element model results of a cantilevered beam meshed with tetrahedral elements to the beam's analytical solution. For the verification, a beam

of uniform thickness (10 mm), height (10 mm), and length (15 mm) was analyzed. An encastre boundary condition was applied to one end of the modeled beam along its length. This is equivalent to rigidly affixing the beam to a wall so that it cantilevers away from the wall. In both the analytical formulation, and the model's formulation, a 2000 N downward force was applied to the beam's opposite end. The three-dimensional structure of the beam in the finite element model was composed of 3519 tetrahedral elements. The beam was assigned the same linear, isotropic and homogeneous material properties as was used for trabecular bone in this study ( $E = 229 \text{ MPa}$ , Poisson's Ratio = 0.3). The maximum in-plane stress at the beam's top line affixed to the wall was analyzed between both analytical and modeled solutions.

The model's implementation (e.g. choice of material properties and/or boundary conditions) was validated by comparing calculated vertebral reaction forces from the modeled FSU in each simulated condition with data from comparable *in vitro* tests conducted in Chapter 3. The 95% confidence interval limits from the *in vitro* data were calculated after 3 mm of shear displacement for each of the 12 tested combinations of compressive force and postural deviation from Chapter 3. These limits were compared to the modeled reaction forces from the FSU in the current investigation under similar imposed conditions after 3 mm of shear displacement.

## **6.3 RESULTS**

### **6.3.1 Convergence study**

The location that was selected for testing convergence was similar between each of the three mesh densities and was chosen since this was the location of maximum stress within the pars interarticularis following the 3 mm of shear displacement with no compressive force and the vertebral joint in its neutral position. Stress at this location changed by 22.4% from the coarse mesh to the intermediate mesh, but only changed by 0.4% between the intermediate and fine meshes (Table 6.2). The intermediate mesh satisfied our convergence criterion of a 1% change in stress at the location of peak stress within the pars interarticularis and was used for all further simulations.

### **6.3.2 Model verification and validation**

The cantilevered beam's analytical solution produced a maximum in-plane stress of 180 MPa at the beam's constrained end (see Appendix D.1 for calculation). The modeled solution produced a maximum in-plane stress of 174.6 MPa at the same location for a discrepancy of 3.0% between the modeled and analytical solutions.

On average, reaction forces calculated from simulations conducted in the extended and neutral postures consistently exceeded the 95% confidence interval's upper limit (by respective averages of 49.7% and 38.5%), for shear force after 3 mm of displacement, calculated from the *in vitro* data collected in Chapter 3 (Table 6.3). The maximum discrepancy of 110.3% occurred for the extended posture with a compressive load equal to 15% of the calculated compressive tolerance. Reaction forces calculated



from simulations conducted in the flexed posture were consistently within the 95% confidence interval limits for shear force after 3 mm of displacement from comparable *in vitro* tests (Table 6.3).

Table 6.3 – Comparison of simulated reaction forces and the 95% confidence interval of measured shear forces, from comparable *in vitro* tests conducted in Chapter 3, following 3 mm of posterior shear displacement of an FSUs caudal vertebra.

Compression	Posture	Model Cranial Vertebra Reaction Force (N)	Force at 3 mm Displacement (N)	
			95% Confidence Interval	
			Lower	Upper
15%	Extended	3809.6	1543.1	1811.5
	Neutral	3012.2	1373.2	2242.5
	Flexed	1556.7	1195.8	1590.7
30%	Extended	3950.6	1894.0	2722.7
	Neutral	3289.8	1762.9	2101.4
	Flexed	1716.5	1256.3	1917.2
45%	Extended	4077.1	1257.7	3659.5
	Neutral	3509.7	2178.7	2815.8
	Flexed	1990.2	1234.7	2247.2
60%	Extended	4223.8	2294.4	3198.2
	Neutral	3699.7	1818.8	2670.8
	Flexed	2268.9	1832.2	2623.2

### **6.3.3 Simulation results following 3 mm of shear displacement**

#### *6.3.3.1 Compression*

Each 15% increment in compressive force generated a reduction in intervertebral disc height of 0.24 mm equivalent to 5.1% of the original disc height. Thus, a maximum intervertebral disc height reduction of 0.96 mm (or 20.4%) was evident at the 60% compressive force magnitude. Separation between the articulating inferior facets of C3 and superior facets of C4 decreased with increasing compressive force magnitude. In the neutral posture, compression that was greater than 45% of the predicted compressive tolerance brought the facets into contact prior to beginning the shear displacement (Table 6.4). Stress and strain at the location of peak stress within the pars after 3 mm of shear displacement both increased respectively by an average of  $21.2 \pm 2.0\%$  and  $23.6 \pm 1.9\%$  with each successive 15% increase in compressive force (Figures 6.4 & 6.5).

Table 6.4 – Shear displacement applied prior to initial facet contact for the left and right facets and for each simulation condition.

Compression (%)	Posture	Shear Displacement Until Facet Contact	
		Left (mm)	Right (mm)
0%	Extended	0	0
	Neutral	1.09	0.94
	Flexed		2.89
15%	Extended	0	0
	Neutral	0.64	0.64
	Flexed	3.00	2.44
30%	Extended	0	0
	Neutral	0	0.34
	Flexed	2.29	2.14
45%	Extended	0	0
	Neutral	0	0
	Flexed	1.69	1.84
60%	Extended	0	0
	Neutral	0	0
	Flexed	1.09	1.54

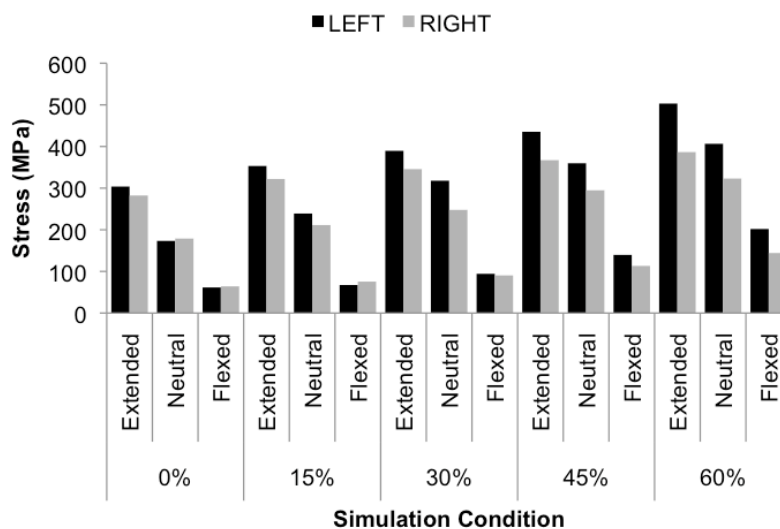


Figure 6.4 – Magnitude of stress at the location of peak stress within the C3 left and right pars interarticularis at the end of the 3 mm shear displacement phase for each simulation.

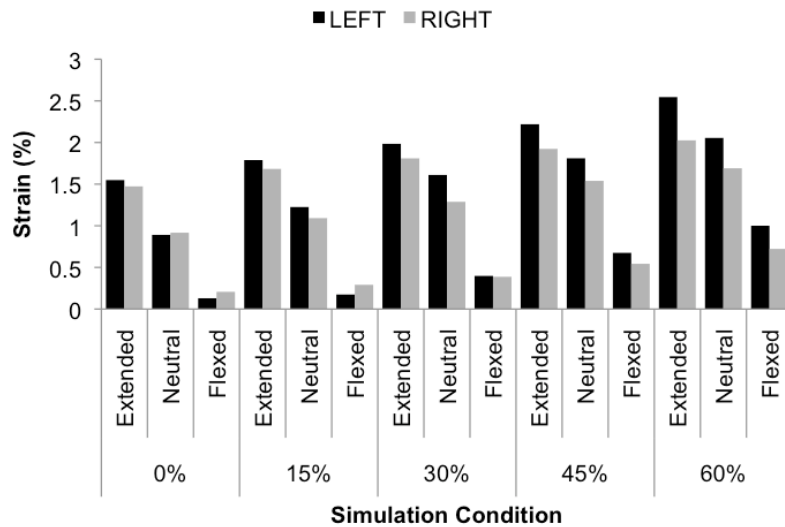


Figure 6.5 – Strain at the locations of peak stress within the C3 left and right pars interarticularis at the end of the 3 mm shear displacement phase for each simulation.

The number of nodes on the C3 inferior facets that came into contact with the C4 superior facets at the end of the 3 mm shear displacement increased by an average of  $18.5 \pm 2.8\%$  with each 15% increment in compressive force (Figure 6.6).

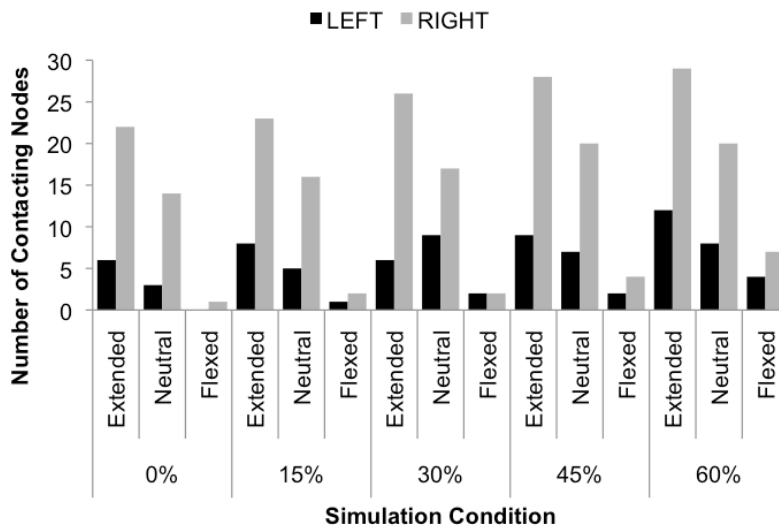


Figure 6.6 – The number of C3 cortical shell nodes, divided into left and right sides, in contact with the C4 cortical shell at the end of the 3 mm shear displacement phase for each simulation.

Increased compressive force lead to an upward and anterior translation for the force centroid of facet contact on the left inferior C3 facet surface by 0.24 mm and 0.12 mm respectively per 15% increment in compressive force (Table 6.5). The force centroid of facet contact on the right inferior facet only had an average superior and anterior migration of 0.05 mm and 0.06 mm for each 15% increment in compressive force (Table 6.5).

Table 6.5 – Center of facet contact force location at the end of each simulation for both left and right facets. The center of force location for the 0% compression and neutral posture served as the reference location for all other simulations. Values reported in this table are derived from the non-deformed nodal coordinates of nodes that were in contact at the end of each simulation. This ensures that the location for the center of facet contact force shown in this table is presented in the same context for each simulation. Anterior, upward, and medial migrations are given by positive values while posterior, downward and lateral migrations are given by negative values.

Compression (%)	Posture	LEFT (mm)			RIGHT (mm)		
		Anterior/Posterior	Vertical	Medial/Lateral	Anterior/Posterior	Vertical	Medial/Lateral
0%	Extended	0.64	0.62	0.13	0.11	0.40	-0.13
	Neutral	0	0	0	0	0	0
	Flexed				0.50	-0.96	1.15
15%	Extended	0.71	0.87	0.08	0.15	0.44	-0.09
	Neutral	0.16	0.15	0.04	0.02	0.07	-0.02
	Flexed	0.10	-0.53	0.36	0.18	-0.64	0.58
30%	Extended	0.83	1.12	0.07	0.22	0.47	-0.02
	Neutral	0.36	0.36	0.09	0.10	0.07	0.08
	Flexed	-0.03	-0.50	0.27	0.09	-0.54	0.40
45%	Extended	0.97	1.36	0.09	0.30	0.46	0.07
	Neutral	0.53	0.63	0.06	0.16	0.05	0.18
	Flexed	-0.44	-0.41	-0.04	0.20	-0.51	0.50
60%	Extended	1.04	1.69	0.06	0.39	0.40	0.22
	Neutral	0.52	0.92	-0.05	0.21	0.12	0.19
	Flexed	-0.40	-0.24	-0.11	0.19	-0.49	0.49

Superior and anterior migration, after 3 mm of shear displacement, for the force centroid of facet contact contributed to an average decrease of  $1.9 \pm 1.4\%$  in the moment arm length between the force centroid of facet contact and the location of peak stress within the pars interarticularis (Figure 6.7). The largest change in the moment arm length was 3.7% and occurred between the 15% and 30% compressive forces.

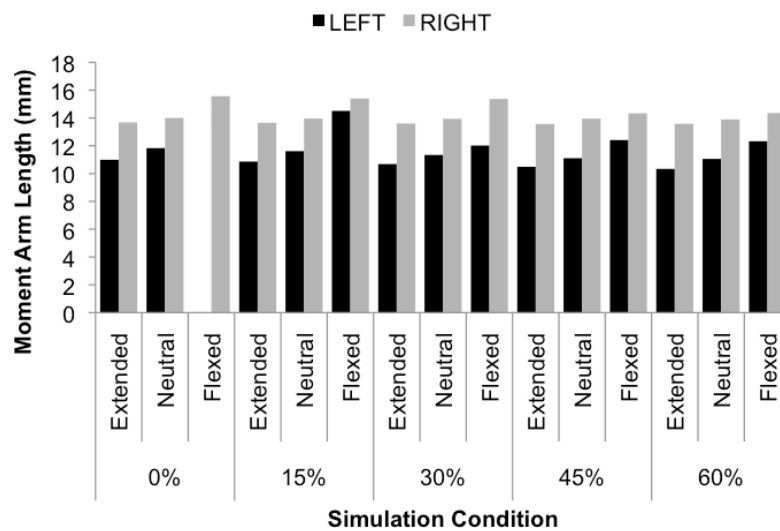


Figure 6.7 – Moment arm length between the center of facet contact force location on the left and right C3 facets and the locations of peak stress within the left and right pars interarticularis after the 3 mm shear displacement phase for each simulation.

### 6.3.3.2 Posture

Initial separation between the facets increased by an average of 1.82 mm with flexed postures compared to neutral (Table 6.4). There was no relationship between facet gap and extended postures since the extended posture immediately brought both the left and right facets into contact (Table 6.4). Compared to neutral postures, and after 3 mm of shear displacement, stress and strain for simulations performed in flexed postures were reduced by an average of  $62.8 \pm 2.8\%$  and  $70.4 \pm 5.2\%$  respectively (Figures 6.4 & 6.5).

Conversely, extended postures, compared to neutral postures, generated an average  $38.2 \pm 8.7\%$  and  $38.7 \pm 8.7\%$  increase in stress and strain respectively after 3 mm of shear displacement (Figures 6.4 & 6.5).

Flexed postures had an average decrease, compared to neutral postures, in the number of contacting nodes of  $80.6 \pm 6.8\%$  (Figure 6.6). Meanwhile, extended postures had an average increase, relative to neutral postures, in the number of contacting nodes by  $43.8 \pm 5.6\%$  (Figure 6.7). Flexed postures also generated an inferior and posterior shift in the force centroid of facet contact on the C3 inferior facets by an average of 0.66 mm and 0.18 mm respectively (Table 6.5). Extended postures produced a superior and anterior migration for the force centroid of facet contact by 0.46 mm and 0.27 mm (Table 6.5). Alterations in the force centroid of facet contact contributed to an  $11.9 \pm 2.9\%$  increase and a  $4.1 \pm 0.1\%$  decrease in the moment arm length to the location of peak stress within the pars interarticularis for flexed and extended postures respectively (Figure 6.7).

#### **6.3.4 Simulation results at consistent strain**

A separate analysis was conducted for the maximum stress, moment arm length and the number of facet surface nodes in contact at the identical strain level. The reference strain for the extended and neutral postures at a single compressive load was the strain produced at the location of maximum stress (Figure 6.5) for the flexed posture after 3mm of shear displacement. The flexed posture was chosen for the reference strain since this posture consistently had smaller strain values than either the neutral or extended postures. Furthermore, this analysis was performed only for cases where both



facets had come into contact when the target strain had been achieved. Simulations with no added compressive force were omitted from the analysis since both the left and right inferior facets of C3 had not come into contact with the superior facets of C4 for the flexed posture.

Maximum stress and the moment arm length were reduced while the number of contact nodes increased for both extended and neutral postures respectively (Figure 6.8). Furthermore, higher stresses were developed along an oblique line through the pars interarticularis as a result of facet interaction during the shear displacement phase (Figure 6.8). In order to achieve the same strain, maximum stress was reduced for both the extended (on average by  $19.0 \pm 7.1\%$ ) and neutral postures (on average by  $16.9 \pm 5.9\%$ ), relative to the flexed posture, at each compressive load (Table 6.6). The magnitude of reduction in maximum stress decreased with increasing compressive force with the largest (34.9%) and smallest (3.1%) reductions occurring at the 15% and 60% compressive force magnitudes respectively (Table 6.6).

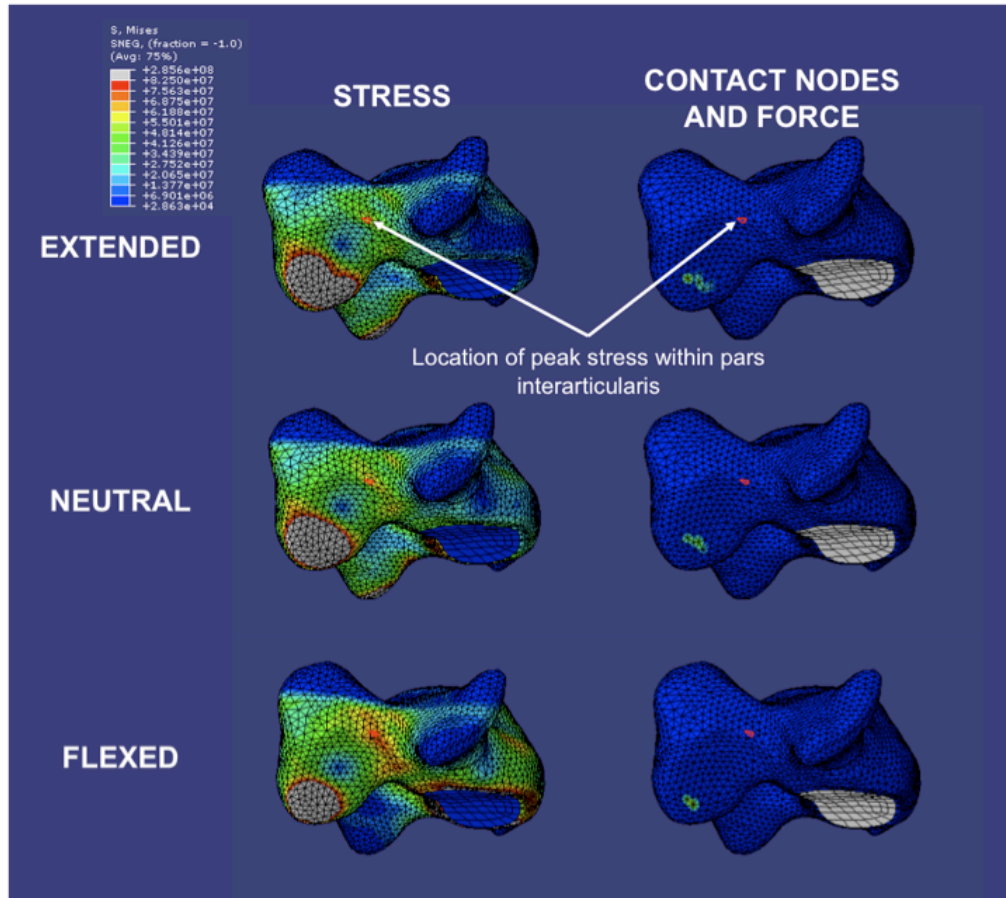


Figure 6.8 – Alterations in stress distribution and the number of facet nodes in contact with extended, neutral and flexed postures with 15% of compressive force applied to the superior surface of the C3 vertebra for identical strain. Note that the color of stress near the marked location of peak stress within the pars interarticularis changes from green to yellow to orange with extended, flexed, and neutral postures respectively. This indicates that stress within the pars interarticularis increases from an extended posture to a flexed posture for a given strain.

Table 6.6 – Magnitude of stress, moment arm length, and the number of contacting nodes for the identical strain of each posture within a single compressive load.

Target Strain (%)	Compression (%)	Posture	Stress (Mpa)		Moment Arm Length (mm)		Number of Contacting Nodes (#)	
			Left	Right	Left	Right	Left	Right
<b>0.17469</b>	<b>15%</b>	<b>Extended</b>	35.5	55.9	9.6	12.9	2	9
		<b>Neutral</b>	36.0	60.4	10.8	13.3	1	5
		<b>Flexed</b>	67.3	75.5	14.5	15.4	1	2
<b>0.39824</b>	<b>30%</b>	<b>Extended</b>	82.3	74.0	9.3	12.8	2	8
		<b>Neutral</b>	79.9	75.8	10.6	13.3	2	6
		<b>Flexed</b>	94.3	90.4	12.0	15.4	2	2
<b>0.67538</b>	<b>45%</b>	<b>Extended</b>	136.6	103.6	9.4	12.8	3	12
		<b>Neutral</b>	135.8	104.3	10.4	13.2	2	9
		<b>Flexed</b>	139.7	113.2	12.4	14.3	2	4
<b>1.0004</b>	<b>60%</b>	<b>Extended</b>	199.0	137.8	9.4	12.9	3	14
		<b>Neutral</b>	197.5	138.0	10.4	13.1	3	11
		<b>Flexed</b>	202.0	144.2	12.3	14.4	4	7

A similar trend was observed whereby the relative number of contact nodes at identical strain values increased with the extended ( $195.8 \pm 73.8\%$ ) and neutral ( $106.5 \pm 49.8\%$ ) postures when compared to the flexed posture (Table 6.6). Again, the largest (383.6%) and smallest (25.9%) increase in the number of contact nodes at the identical strain also occurred at the 15% and 60% compressive force magnitudes respectively (Table 6.6). Extended postures also had an average  $19.0 \pm 1.6\%$  reduction in the moment arm length, compared to flexed postures, in order to achieve the same strain (Table 6.6). Likewise, neutral postures had an average  $13.7 \pm 1.5\%$  reduction in moment arm length, compared to flexed postures, in order to achieve the same strain (Table 6.6). Reduction of moment arm length for extended (range = 16.8% - 24.9% reduction) and neutral (range = 12.0% - 19.7%) postures was not influenced by the magnitude of compressive force (Table 6.6).

### **6.3.5 Relationship of moment arm length changes with ultimate failure from *in vitro* testing**

Changes in moment arm lengths that were derived from the finite element model and produced by the varying simulation conditions (changing compressive forces and flexion/extension postures) were analyzed for their relationship to measured ultimate shear failure tolerances of the porcine cervical functional spinal unit exposed to similar boundary and loading conditions. Positive changes in moment arm length produced primarily by flexed postures and smaller compressive loads, and negative changes in moment arm length produced primarily by extended postures were negatively correlated ( $r = -0.71$ ) to smaller ultimate shear failure tolerances measured *in vitro* from vertebral functional spinal units exposed to similar boundary and loading conditions (Figure 6.9).

This implies that for the identical strain, increasing the moment arm length as a function of flexion/extension postural deviation leads to reductions in ultimate shear failure tolerance.

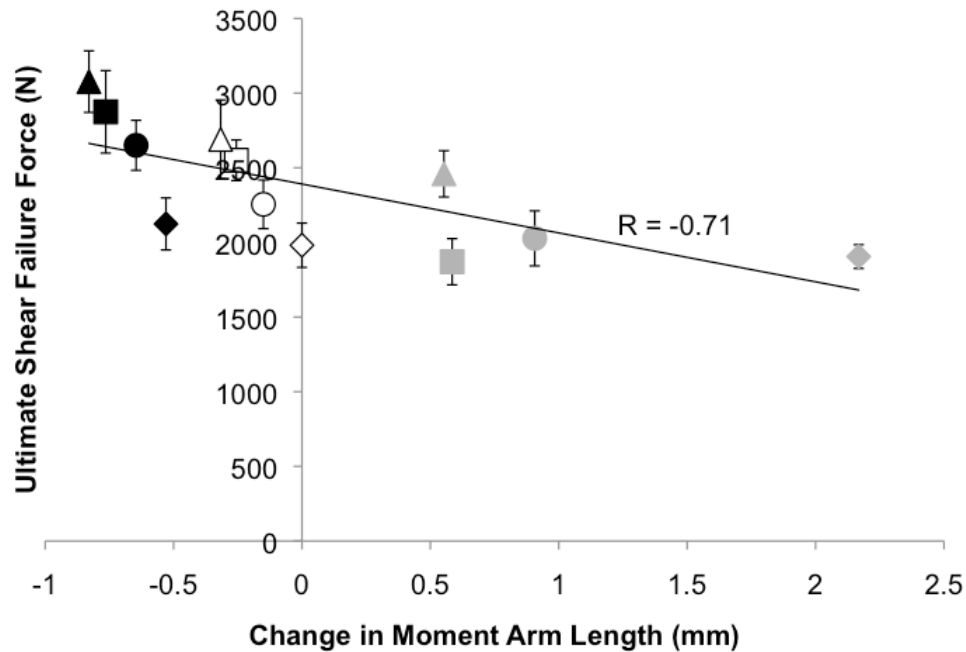


Figure 6.9 – The change in moment arm length, relative to the simulation with 15% compression and in the neutral posture, for each simulation versus the quantified ultimate shear failure tolerances for the identical test conditions in Chapter 3. Black, white, and gray symbols represent simulations/*in vitro* tests conducted in extended, neutral, and flexed postures respectively. Diamonds, circles, squares, and triangles represent simulations/*in vitro* tests conducted under 15%, 30%, 45%, and 60% compressive force respectively. Error bars represent the standard error of the mean ultimate shear failure tolerance calculated in Chapter 3.

## 6.4 DISCUSSION

The primary goal of this investigation was to use a finite element model of the porcine cervical functional spinal unit to investigate the hypothesis that ultimate shear failure of the vertebral joint under different compressive force and flexion/extension postures is modulated by the moment arm length between the force centroid of facet contact and the location of peak stress within the pars interarticularis. This study showed that vertebral flexion and extension respectively produced increased and decreased moment arm lengths and also created larger and smaller gaps between articulating facets. Although compressive loads lead to a small cranial migration of the force centroid of facet contact, the moment arm length between this location and the location of peak stress within the pars interarticularis was not substantially affected by compressive force. For an identical strain, results from this study indicate that stress within the pars interarticularis is smaller when the moment arm length is reduced by extension, and that stress is larger when the moment arm length is increased by flexion. These results provide quantitative evidence that the moment arm length between the force centroid of facet contact and the location of peak stress within the pars interarticularis is a critical factor that influences shear failure tolerance of the vertebral joint. Qualitatively, higher stresses were observed along an oblique line through the pars interarticularis during the shear displacement phase. Lastly, increased moment arm length, as a result of postural deviation and compressive force, explained 50% of the variance in ultimate shear failure load from the comparable *in vitro* tests conducted in Chapter 3. This indicates that the moment arm length between the force centroid of facet contact and the location of peak

stress within the pars interarticularis is a dominating factor that modulates anterior shear ultimate failure tolerances.

*In vitro* investigations using pressure sensitive films have shown that facet contact area and the location of facet contact is modulated by altered flexion/extension postures (Lorenz et al., 1983; Dunlop et al., 1984). In particular, extended postures were shown to increase the facet contact area (Lorenz et al., 1983) and lead to caudal migration for the area of facet contact while flexed postures reduced facet contact area and led to cranial migration for the area of facet contact (Dunlop et al., 1984). Findings regarding the effects of postural deviation on facet contact area and the location of facet contact as demonstrated by Dunlop and colleagues (1984) were congruent with the simulations performed for the current investigation. Simulations conducted in the current investigation showed that flexed postures caused the force centroid of facet contact to migrate cranially and also reduced the number of facet nodes that were in contact. Conversely, extended postures caused the force centroid of facet contact to migrate caudally and also increased the number of facet nodes that were in contact. These findings are also congruent with similar *in vitro* tests conducted using pressure sensitive film in between the articulating facets (Lorenz et al., 1983; Dunlop et al., 1984).

Disc height reduction produced by compression has also been shown to not substantially alter the location of facet contact (Dunlop et al., 1984), but did manage to increase the area of contact (Lorenz et al., 1983). The current investigation also demonstrated that the location of facet contact force did not change with additional compressive force. Previous *in vitro* research has shown that facet contact area increases by as much as 36% and 61% with disc height reductions of 1 mm and 4 mm

(approximately 11% and 44% of the total disc height) respectively (Dunlop et al., 1984). Disc height reductions reported for this investigation were equivalent to 0.24 mm (or 5.1% of initial disc height) for each 15% increment in compressive force applied in the simulations. Results from this investigation show that the number of nodes on the C3 facets that were in contact after 3 mm of shear displacement (a surrogate measure for contact area) increased by 18.5% with each successive 15% increment in applied compressive force. These findings indicate that the reported increased contact area reported by Dunlop and colleagues (1984) would have been achieved in this investigation at the 30% and 60% compressive force magnitudes. However, percentage of disc height change observed in this investigation does not mimic the estimated percentage of disc height (1 mm and 4 mm reductions that were approximately 11% and 44% of total disc height) change reported by Dunlop and colleagues (1984). This may be due to the use of a single material for the intervertebral disc.

Flexion/extension posture has also been shown to alter the gap between articulating facets. Drake and colleagues (2008) showed that flexion increases the gap between articulating facet while extension decreases the gap between articulating facets. These authors concluded that alterations in the gap between articulating facets create an injury mechanism that depends on postural deviation for scenarios where the facets are forced to come into contact with one another. The current study also demonstrated that the gap between articulating facets increases with flexion and decreases with extension. Furthermore, simulations performed in the current study showed that the gap between articulating facets is also decreased by additional compressive force. Relative changes in



the space between articulating facets with postural deviations reported in this investigation correspond to results from previous *in vitro* research (Drake et al., 2008).

Studies investigating the mechanism of vertebral joint failure under acute as well as repetitive shear loading have consistently identified a bilateral failure of the cranial pars interarticularis as the location of failure (Cripton et al., 1995; Yingling and McGill, 1999; van Dieën et al., 2006; Beadon et al., 2008; Gallagher et al., 2010; Chapters 3-5). Images produced by Yingling and McGill (1999) and failure patterns noted from sagittal plane x-rays and physical observation of specimens following acute as well as repetitive shear failure (Chapters 3-5) demonstrate that the line of fracture within the cranial vertebra's pars interarticularis, and for the functional spinal unit exposed to shear loading, travels obliquely from the superior and medial border of the inferior facet to the inferior and lateral border of the superior facet. Based on this observation within Chapter 3, the pars interarticularis length was defined within Chapter 4 as the distance between these two points as identified from an x-ray of a specimen taken in the sagittal plane.

Qualitative results presented in this investigation demonstrate that the inferior anterolateral portion of the pars interarticularis develops a high concentration of stress during facet interaction resulting from backward shear displacement of the caudal vertebra. This is consistent with reports that pars interarticularis fractures resulting from shear load initiate within the inferior anterolateral portion of the pars interarticularis (Cyron et al., 1978). Evidence of stress concentrations within the region defined by the superior and medial border of the inferior facet and the inferior and lateral border of the superior facet for the cranial vertebra are coincident with the line of fracture observed from *in vitro* testing that uses similar boundary conditions, indicating that fracture

patterns observed following acute and repetitive shear loading are most likely a result of stress concentrations developed along this oblique line. Furthermore, this fracture pattern is likely a result of a bending moment generated about the pars interarticularis by the interacting facet contact force.

Cyron and colleagues (1976) initially stated that failure of the pars interarticularis from direct facet loading is resultant from the moment generated by this contact force about the pars interarticularis. Finite element results have indicated that the stress distribution within the vertebral joint is influenced by postural deviations when studying complex loading scenarios (Shirazi-Adl, 1991). Yingling and McGill (1999) hypothesized that the moment arm length increases with flexed postures and is a modulator of ultimate shear failure tolerances for the vertebral joint. Yingling and McGill (1999) concluded that increased moment arm length contributed to higher ultimate shear failure forces when specimens were flexed. This conclusion does not correspond to the findings of Chapter 3 from this thesis or with the results presented within the current investigation. Results from Chapter 3 demonstrate that ultimate shear failure tolerance in a flexed posture was reduced, relative to failure tolerance in a neutral posture, by an average of 12.8% (or 303.5 N). Furthermore, results from the finite element model demonstrate that, in order to achieve the same strain, stress within the pars interarticularis and moment arm length are both increased with flexed postures. These findings indicate that the increased moment arm length produced by flexion is more likely to reduce the ultimate shear failure tolerance measured from *in vitro* studies. Conversely, results from Chapter 3 demonstrated that ultimate shear failure tolerance in extended postures was increased by 13.2% compared to failure tolerances in a neutral posture. Simulations from

the current investigation provide evidence that, in order to achieve the same strain, stress and the moment arm length are both decreased in extension. These findings indicate that decreased moment arm length produced by extension is more likely to increase ultimate shear failure tolerance of the vertebral joint as measured during the *in vitro* tests.

Changes in moment arm length produced primarily by altered flexion/extension posture in the current investigation demonstrated a negative correlation with the ultimate shear failure values from *in vitro* investigation under similar boundary conditions. Thus, results from the simulations conducted in this investigation provide quantitative support for the hypothesis that moment arm length between the center of facet contact force and the location of peak stress within the pars interarticularis is a modulator for the magnitude of stress developed within the pars interarticularis that can eventually lead to failure. The results from this investigation also indicate that increased ultimate shear failure tolerances quantified during *in vitro* testing with increased compressive forces may not be a direct result of reduced moment arm lengths as originally hypothesized. Instead a secondary mechanism whereby the increase in facet contact area with additional compression distributes the facet contact pressure over a larger area that ultimately requires a larger force, and consequently higher measured ultimate shear failure forces of the joint, in order to create failure of the pars interarticularis.

Finite element models of biological structures require the investigator to define a set of assumptions regarding the properties and behavior of materials, model geometry, as well as the loads and boundary conditions to be applied within the simulations. These assumptions provide a set of limitations for the finite element model. The geometry for the finite element model in the current investigation was constructed from the C3 and C4

vertebrae of a porcine C3-C4 functional spinal unit since the simulations performed in the current investigation were designed to mimic *in vitro* tests conducted using a porcine cervical model. The geometrical and functional similarities between the porcine cervical spine and the human lumbar spine have been documented (Yingling et al., 1999) and discussed in more detail within the previous three studies as a limitation. The approach used to develop the current model's geometry may create a more simplified representation of the real vertebral geometry than other studies that have developed geometries directly from computed tomography scans (Aziz et al., 2008; Pahr and Zysset, 2008; Young et al., 2008). Furthermore, the use of computed tomography scans might have allowed for a variable cortical thickness to be applied instead of the constant thickness used for the current investigation. However, the thickness of the cortical shell elements was taken from previously published finite element models (Kato et al., 1998; Akahoshi et al., 2005).

The current investigation presents the first iteration of this finite element model and was created to be a reasonable simplification of the porcine cervical functional spinal unit. In order to simplify the model, ligaments, surface cartilage covering the facets, and the facet joint capsule were not modeled for this initial investigation. Ligaments have been shown to provide negligible resistance to shear loading scenarios (Sharma et al., 1995) such as the ones imposed in the simulations for the current investigation. Inclusion and proper modeling of the facet cartilage may be able to improve the biofidelity of a vertebral finite element model (Womack et al., 2008). Since the model used for this investigation was the initial iteration, the cartilage surfaces were omitted. Further simulations that are performed with this model and involving facet contact should include

a material representation of the facet cartilage surface. Modeling the facet joint capsule and the synovial fluid within this capsule can add another level of biofidelity to this finite element model (Kumaresan et al., 1998). This level of detail can also be included in future iterations of this finite element model. These biological simplifications enhanced implementation while maintaining the biofidelity of the most critical structures (the vertebrae) and to provide a base on which future iterations of the model can build.

Thirdly, the material properties for all components within the model used for this investigation were linear, isotropic and homogenous. Material properties were literature-based values, with the exception of the lumped properties for the intervertebral disc, obtained from studies conducted on porcine vertebrae and functional spinal units. Elastic moduli used in this investigation for the cortical and trabecular bone were larger than values commonly used for modeling the same materials in finite element models of human vertebrae (Kumaresan et al., 1999; Fantigrossi et al., 2007). Differences in elastic moduli are primarily derived from the fact that porcine trabecular and cortical bone have a higher density than human trabecular and cortical bone (Inui et al., 2004). The intervertebral disc is often modeled with three separate components (annulus fibers, ground substance, and nucleus pulposus) (Natarajan et al., 2004; Stokes et al., 2010). The primary focus of the simulations performed in the current investigation was within the pars interarticularis and not the intervertebral disc. The intervertebral disc allowed for specimen height reduction with added compressive load and also provided resistance to flexion/extension postural deviations. Thus, the disc satisfied its primary purpose for the current investigation. However, future investigations should focus on developing an improved disc model.

Linear tetrahedral elements were chosen to model the trabecular bone due to the complexity of a vertebra's three-dimensional geometry. Hexahedral elements are typically favored in finite element modeling due to their ability to create 'good' quality elements and meshes (Cifuentes and Kalbag, 1992) that deform in a manner that maintains the mesh quality. Maintaining mesh quality is important for ensuring that the solution produced by the finite element model is computationally reliable. However, meshing of complex geometries with hexahedral elements can be a difficult and time-consuming process (Cifuentes and Kalbag, 1992). Ramos and colleagues (2006) demonstrated that linear tetrahedral elements performed equally as well as their hexahedral counterparts in a finite element model of the proximal femur. The loading conditions for their model were designed to mimic the most strenuous phase of walking and produced maximum strain values of 1693 microstrain (equivalent to 1.693%). This strain is comparable to strains observed at the element of peak stress within the pars interarticularis for simulations performed in this investigation and supports the use of tetrahedral elements within the current investigation. Furthermore, the utility of linear tetrahedral elements for the current model was verified by comparing the modeled and analytical solutions from a cantilevered beam with dimensions assigned to mimic the inferior facet and its connection with the pars interarticularis. The verification procedure found that the modeling procedure only underestimated the analytical solution by 3.0%, suggesting that the choice of tetrahedral elements for the FSU model was feasible.

The validation procedure found that reaction forces calculated from simulations conducted in extended and neutral postures consistently overestimated measured shear forces from comparable *in vitro* tests following 3 mm of shear displacement. Conversely,

the reaction forces calculated for simulations conducted in flexed postures were within the 95% confidence interval limits for measured shear forces from comparable *in vitro* tests. The two primary factors that could account for these discrepancies are the choice of material properties and/or boundary conditions (including choice of nodal sets) imposed upon the model. Material properties were obtained primarily from studies conducted on vertebrae of different races and/or species of pigs. While the race and species of pig may influence the measured material properties, it is more likely that choice of boundary conditions was the largest contributor to discrepancies between the modeled reaction forces and measured shear forces from comparable *in vitro* tests. The procedure for affixing the cranial and caudal vertebrae within the aluminum cups initially requires that their exposed superior and inferior facets be removed. This ensures the cup can be mounted flush with each vertebra's exposed endplate. However, the remaining vertebral posterior elements (e.g. lamina, pars interarticularis, articulating facets, spinous process) are not constrained by the potting procedure, allowing these elements to bend more readily with applied loads through the articulating facets. Conversely, the modeled boundary conditions may have been more similar to *in vivo* conditions where the exposed superior and inferior facets respectively from the FSUs cranial and caudal vertebra were not removed, but instead were constrained from movement. *In vivo*, each pair of superior facets for a single vertebra articulates with the inferior facets of the immediately cranial vertebra that may limit bending of the posterior elements during shear loading. This may increase stiffness *in vivo*, and subsequently measured shear forces for a given displacement. Thus, the choice of nodal sets for the imposed boundary conditions may not have not allowed the pars interarticularis of the modeled FSU to bend as easily as in

the comparable *in vitro* tests. Consequently, this may have led to the large discrepancy between measured shear forces from *in vitro* tests and simulated reaction forces calculated from the model. In particular, this is a plausible explanation for larger discrepancies observed during simulations conducted in extended and neutral postures where the facets would have been in contact over larger displacements. In order to achieve better representation of the *in vitro* testing conditions, the set of nodes that are constrained within the model likely need to be refined. This may improve correspondence between the measured and simulated forces for comparable sub-failure displacements.

In a recent review of spine biomechanics, Adams and Dolan (2005) stated that biomechanical testing and finite element modeling should compliment one another. The primary findings from this investigation compliment the results from Chapter 3 and support the hypothesis that altered flexion/extension postures and compressive forces applied to the vertebral joint can alter the moment arm length between the location for the force centroid of facet contact and the location of peak stress within the pars interarticularis during shear displacement. Specifically, flexion increased, while extension decreased, the moment arm length on average by 11.9% and 4.1% respectively. Increasing compressive force also produced a small average decrease of 1.4% in the moment arm length. Altered flexion/extension posture had a larger effect on the moment arm length compared to compressive force and may explain the more pronounced effect of flexion/extension posture on the ultimate shear failure tolerance observed in Chapter 3. Based on the results from this investigation, it is further hypothesized that compressive force acts in a secondary manner, perhaps by increasing facet contact area, to increase the shear failure tolerance of the vertebral joint.



# **CHAPTER 7**

## **THESIS SUMMARY AND CONTRIBUTIONS**

## 7.1 THESIS SUMMARY

The global purpose of the thesis was to develop a framework for understanding how failure properties of the functional spinal unit (FSU) under acute and repetitive shear loading are modulated. In particular, the studies of this thesis investigated the following four issues:

- i.) The combined influence that flexion/extension postural deviation and compressive load had on the ultimate shear failure tolerance of the vertebral joint
- ii.) The respective roles of bone density and vertebral morphology on ultimate shear failure tolerances
- iii.) The ability of sub-maximal shear load to modulate cumulative shear load and the number of loading cycles sustained prior to failure
- iv.) The influence of altered flexion/extension posture and compressive force on stress, strain, facet interaction and the length of the moment arm between the pars interarticularis and the force centroid of facet contact during anterior joint shear in a finite element model of a single vertebral joint.

Porcine cervical FSUs consisting of two vertebrae, the intervening intervertebral disc, and all surrounding ligaments were used for the three *in vitro* investigations in this thesis. Shear displacement in these investigations was imposed to the caudal vertebra of each FSU through a pair of linear actuators attached to brushless electrical servomotors. Compressive force was applied through a separate servo-hydraulic actuator while flexion/extension postural orientation was controlled via a separate electrical servomotor. A fourth investigation used a finite element model of the porcine C3-C4 vertebral joint to

study the influence of flexion/extension postural deviation and compressive force on facet contact and internal stress/strain distribution during anterior joint shear. The three *in vitro* studies contributed tissue-based insights into modulation of shear failure thresholds for the vertebral joint while the finite element model provided a way of explaining results observed in the first *in vitro* investigation.

The respective influence of flexion/extension postural deviation and compressive force was investigated in Chapter 3. Results showed that there was no statistically significant interaction between postural deviation and compressive force on ultimate shear failure tolerance. However, ultimate shear failure tolerance was significantly different with a reduction of 13.2% for flexed postures (compared to neutral), and increased (compared to neutral) by 12.8% with extended postures. This finding contrasted previous results showing that ultimate shear failure tolerance either increased (Yingling and McGill, 1999) or showed no change (van Dieën et al., 2006) with flexion. Shear stiffness also decreased significantly with flexed postures. Each 15% increment in compressive force was met with an average 11.1% increase in ultimate shear failure tolerance and while shear stiffness also increased with added compressive force. It was hypothesized that alterations in flexion/extension posture and/or compressive force altered the location for the force centroid of facet contact. These changes in the location of facet contact were hypothesized to produce subsequent changes in the bending moment at the pars interarticularis that altered the measured ultimate shear failure tolerance.

The roles of vertebral morphology and pars interarticularis bone density in modulating ultimate shear failure tolerance were studied in Chapter 4. Digital calipers

and x-rays were used to make measurements of vertebral morphology while measurements of bone density were made using peripheral quantitative computed tomography. The three leading factors for calculating ultimate shear failure tolerance were the pars interarticularis length for the cranial vertebra (44.3% explained variance), the average facet angle measured in the transverse plane (12.3% explained variance), and cortical bone area through the pars interarticularis (11.9% explained variance). Results from this investigation provide critical insight into the morphological characteristics that could influence vertebral failure under shear loading. Fractures observed in this investigation were similar to those reported for studies performed with human specimens (Cyron et al., 1976) and also similar to reported spondylolitic fractures resulting from shear loading in humans (Farfan et al., 1976). This provides additional evidence that the porcine cervical spine is a suitable surrogate *in vitro* model for studying human lumbar spine mechanics. Evidence from this study also showed that cranial pars interarticularis fractures are the dominant injury mechanism occurring in anterior joint shear. This fracture was linked to the shorter relative length of the cranial vertebra's pars interarticularis compared to those of the caudal vertebra. Furthermore, this was the first study that presented a mathematical model for determining ultimate shear failure tolerance. The regression model had similar errors (10.9% of shear failure tolerance) to a previously developed regression equation that predicts compressive failure tolerance (Parkinson et al., 2005). The mathematical model was used in the repetitive loading protocol to control sub-maximal load magnitude as a percentage of each specimen's calculated ultimate shear failure tolerance.

The relationship between sub-maximal shear load magnitude and vertebral joint fatigue life under repetitive shear loading was investigated in Chapter 5. Both the number of cycles and the cumulative shear load sustained prior to failure decreased in a non-linear manner with increasing sub-maximal shear load magnitude. These findings mirror results presented for similar investigations using repetitive compressive loading (Brinckmann et al., 1988; Parkinson and Callaghan, 2007b). Consequently, the findings of this study also suggested that estimates of cumulative shear load should assign greater importance to higher instantaneous shear loads. This was due to an increased injury potential at higher instantaneous shear loads. Cumulative load sustained prior to failure was used to develop a tissue-based weighting factor equation that would apply non-linearly increased weight to higher normalized shear load magnitudes in estimates of cumulative shear load. Specimens exposed to repetitive shear loading to 80% of their calculated ultimate failure tolerances demonstrated a higher likelihood of injury to a combination of structures such as unilateral fractures of either the cranial or caudal pars interarticularis, bilateral fracture of the caudal pars interarticularis and endplate avulsion. Injury patterns observed at the highest load magnitude (80% of the calculated ultimate shear failure tolerance) were less consistent than injuries observed at the two lower loading magnitudes (40% and 60%).

The final study in Chapter 6 investigated the hypothesis that the moment arm length between the force centroid of facet contact and the pars interarticularis was altered with flexed/extended postures and compressive force. Secondly, alterations in the moment arm length would be reflected in congruent changes in stress observed within the pars interarticularis. These hypotheses were derived from the *in vitro* results of the first

investigation (Chapters 3-5). A finite element model of the porcine C3-C4 functional spinal unit was created, and simulations were performed using similar boundary conditions as the comparable *in vitro* tests, to assess the plausibility of these hypotheses. Moment arm length was increased by 11.9% for flexed postures and decreased by 4.1% for extended postures. Alterations in moment arm length were larger for postural deviation than compressive force (average decrease of 1.4%) suggesting a secondary mechanism to explain the observed increase in shear failure tolerance with higher compressive loads from the first investigation (Chapter 3). One such possibility was the increase in the number of contacting nodes on the facet articular surfaces with higher compressive forces. Flexed postures also demonstrated higher stress in the pars interarticularis than either extended or neutral postures when the identical level of strain was considered. Lastly, alterations in moment arm length were able to explain 50% of the variance in measured ultimate shear failure tolerances from the first study (Chapter 3). Thus, the finite element model was successful in demonstrating the plausibility of moment arm length between the force centroid of facet contact and the pars interarticularis as a modulator of measured ultimate shear failure tolerance.

## **7.2 HYPOTHESES REVISITED**

As stated in Section 1.2, the general hypothesis for this thesis was that the mechanical response of the FSU under anterior shear loading will be influenced by a combination of flexion/extension postures, compressive loads, bone density, vertebral morphology, and the submaximal loading magnitude (for repetitive loading scenarios). The findings from this thesis clearly indicate that all of the aforementioned factors do

indeed modulate measured shear failure tolerances under both acute and repetitive loading paradigms. The following are the null-hypotheses that were listed in Section 1.2, and decisions regarding rejection of each null-hypothesis.

1. Ultimate failure load and displacement of the porcine FSU as well as shear stiffness and energy stored until failure under acute external shear load will not be influenced by varying compressive loads or flexion/extension postures.

DECISION: Null hypothesis rejected for ultimate failure tolerance, shear stiffness, and energy stored until failure. Null hypothesis retained for ultimate displacement. Extension and flexion respectively increased and reduced measured ultimate shear failure tolerances, shear stiffness, and energy stored until failure. Increasing magnitude of compressive force also increased measured ultimate shear failure tolerances, shear stiffness, and energy stored until failure. Ultimate shear displacement was not influenced by either flexion/extension postural deviation or compressive force.

2. Combinations of bone mineral density and morphological factors of the posterior elements will not provide appropriate estimates of the ultimate failure load under shear loading.

DECISION – Null hypothesis retained. Bone mineral density had a smaller contribution to mathematical models for non-destructively calculating ultimate

shear failure tolerance than other morphological factors. However, facet angles measured in the transverse plane and the pars interarticularis length were identified as predictors of ultimate shear failure tolerance.

3. The magnitude of external shear loading will not influence the cumulative shear load experienced by the porcine cervical FSU prior to failure.

DECISION – Null hypothesis is rejected. Larger magnitudes of repetitively applied sub-maximal shear load reduced the cumulative shear load sustained prior to failure in a non-linear manner.

4. Flexion/extension postures as well as compressive loads will not influence the internal stress developed at the pars interarticularis under shear loading.

DECISION – Null hypothesis is rejected. Although not statistically evaluated, for a similar strain, extended postures reduced stress developed at the pars interarticularis compared to neutral and flexed postures under shear loading. Increasing compressive force also increased stress developed within the pars interarticularis under shear loading.

5. Model results will not be related to any hypotheses derived from the comparable *in vitro* work performed in Study 1.



DECISION – Null hypothesis rejected. Model derived moment arm lengths between the force centroid of facet contact and the location of peak stress within the pars interarticularis were able to explain 50% of the variance and were negatively correlated with ultimate shear failure tolerances measured from comparable *in vitro* testing performed in Study 1.

### **7.3 CONCEPTUAL MODEL FOR MODULATION OF ANTERIOR JOINT SHEAR FAILURE**

Potvin (2008) stated in a recent review of occupational spine biomechanics that while spine injury mechanisms from compressive loading have been studied extensively, there is a need for further basic research into vertebral tissue tolerances under shear as well as complex loading scenarios. Norman and colleagues (1998) also determined that peak shear load was a strong predictor for the incidence of low-back pain reporting. Results presented within this thesis address both of these statements and can be used to lay the groundwork for a basic conceptual model of vertebral shear injury potential.

As illustrated in this thesis, the primary mechanism for injury as a result of shear loading is a bending moment applied about the pars interarticularis by facet contact forces derived from interaction between the inferior facets of a cranial vertebra and the superior facets of the adjacent caudal vertebra. Thus, changes in facet interaction are the most likely mechanical means for altering injury potential of the vertebral joint under shear loading. Modulation of facet interaction and subsequent vertebral injury potential resulting from shear loading can be understood using an approach that is similar to the principal factors (force, repetition, and posture) for determining injury potential within

occupational biomechanics (Figure 7.1). In addition to these three factors, the conceptual model includes vertebral morphology as a fourth factor that modulates facet interaction and possible injury under shear loading. Each of the four primary factors has the potential to interact with the other three primary factors in order to change facet interaction and subsequent injury potential. Each of these factors has been addressed within the thesis, however considerable work remains to uncover potential interactions between each of the factors as they relate to vertebral injury during shear loading exposures.

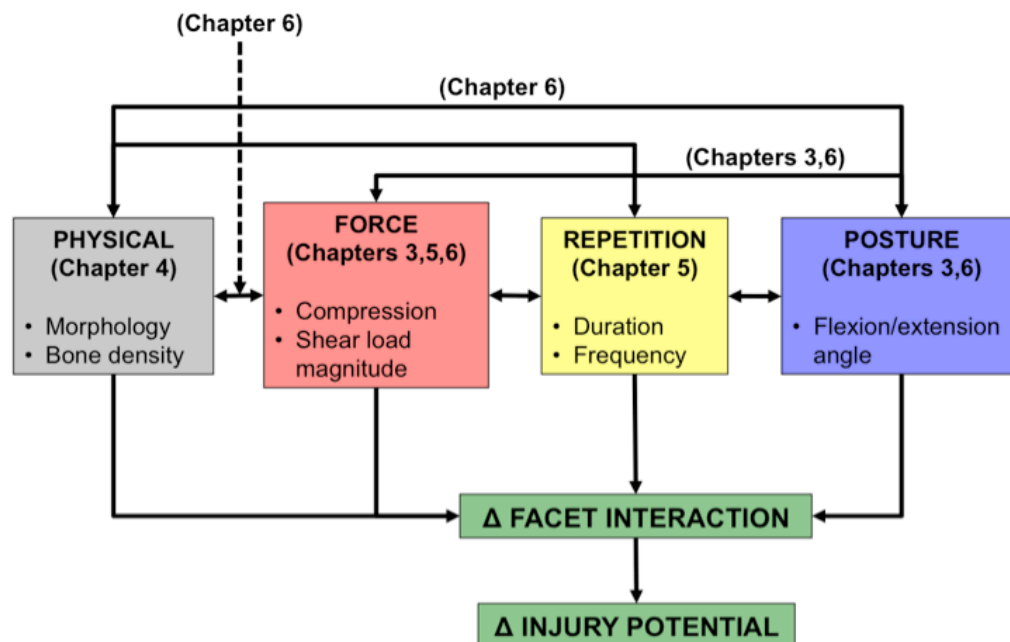


Figure 7.1 – Conceptual model for modulation of vertebral injury potential as a result of shear loading. The model consists of four primary factors that were addressed by the respectively shown chapters. Each of the primary factors has the potential to interact with any or all of the other three primary factors. The possibilities for some of these interactions were investigated within this thesis and are shown here. The dashed arrow indicates that Chapter 6 addressed the interaction between physical characteristics of the vertebra and the influence of compressive force on facet interaction.

Flexion and extension respectively decreased and increased while compressive force increased the measured ultimate shear failure tolerances (Chapter 3). Based on

previously offered hypotheses (Cyron et al., 1976; Yingling and McGill, 1999), these alterations in shear failure tolerance were hypothesized to be linked to changes in the moment arm length between the force centroid of facet contact on the inferior facet and the location of peak stress within the pars interarticularis for the cranial vertebra. Increased measured ultimate shear failure forces were the consequence of decreased moment arm lengths. Conversely, decreased measured ultimate shear failure forces were the consequence of increased moment arm lengths. Plausibility for the moment arm hypothesis for postural deviation was presented from finite element model results that showed the force centroid of facet contact on the inferior facet of the cranial vertebra shifted caudally while the force centroid of facet contact shifted cranially as a result of changes in facet interaction (Chapter 6). Consequently, the moment arm length was reduced for extended postures and increased for flexed postures lending support for the moment arm hypothesis of altered shear injury potential resulting from postural deviation. The combined results from the *in vitro* testing and the finite element modeling also demonstrate how the interaction between physical characteristics of the vertebrae and postural deviation were investigated within this thesis.

Conversely, compressive force did not ascribe to the same moment arm hypothesis as postural deviation. Increased compressive forces did not demonstrate reductions in moment arm lengths as determined from finite element simulations (Chapter 6). Instead a second mechanism whereby measured ultimate shear failure tolerances are increased as a result of increased facet contact area with higher compressive forces was proposed from the finite element model simulations (Chapter 6). Increases in contact area with higher compressive forces were similar to *in vitro* findings

using pressure sensitive film (Dunlop et al., 1984). The new hypothesis proposes that distributing facet contact forces over a larger area with higher compressive loads modulates facet interaction that subsequently reduces stress within the pars and increases measured ultimate shear failure tolerances. It is also possible that increases in measured ultimate shear failure tolerance with higher compressive forces may be a result of changes in load sharing between the articulating facets and the intervertebral disc.

Interestingly, there was no statistically significant interaction between postural deviation and compressive force on the measure ultimate shear failure forces. Postural deviation to the flexion and extension limits of the neutral zone's linear region also demonstrated similar changes in measured ultimate shear failure tolerances as a 15% increase in applied compressive force.

Morphological characteristics of the facets can also play a role in modulating measured ultimate shear failure tolerances (Chapter 4). The primary morphological characteristic used for predicting measured ultimate shear failure tolerance was the length of cranial vertebra's pars interarticularis. However, facets that were oriented closer to the sagittal plane also demonstrated higher ultimate shear failure tolerances. Forces transmitted to the pars interarticularis as a result of facet contact are likely to be smaller when the facets are oriented closer to the sagittal plane with direct shear loading. This implies that more direct shear force would be required to generate the critical force required to create fracture of the pars interarticularis when the facets are oriented closer to the sagittal plane.

Lastly, increasing magnitude of sub-maximal shear load generates a non-linear decrease in the shear fatigue life of the vertebral joint (Chapter 5). *In vitro* results of

specimens tested in the neutral posture (Chapters 3 & 4) indicate that the shear yield force is approximately 72% of the measured ultimate shear failure tolerance with a range of 35% – 97%. Higher sub-maximal shear loads that approach or exceed the shear yield force may generate residual deformation and microdamage that could influence facet interaction that subsequently contributes to the non-linear decay in shear fatigue life.

## **7.4 GLOBAL LIMITATION**

Individual limitations that are specific to each of the studies presented within this thesis are discussed within their respective chapters. One common limitation with each of the studies in this thesis is the use of the porcine cervical spine as a surrogate model for the human lumbar spine.

Appropriate selection of an animal model is very important for linking results to human tissues (Alini et al., 2008; Busscher et al., 2010). The porcine cervical spine is smaller, but morphologically similar to the human lumbar spine (Yingling et al., 1999). In particular, the porcine cervical vertebrae have smaller pars interarticularis compared to the human lumbar vertebrae (Yingling et al., 1999). Despite this, ultimate shear failure loads have been previously shown to be similar between porcine cervical and human lumbar FSUs (Yingling et al., 1999). Facet orientation of the porcine cervical spine is similar to the human lumbar spine (Oxland et al., 1991).

Using the porcine model allowed for control of confounding factors such as age and load exposure prior to death as well as the means by which death occurs in an attempt to improve inter-specimen homogeneity (Smit, 2002; Schmidt et al., 2005). Moreover, the porcine cervical spine was used to develop the finite element model

geometry in order to allow for a direct comparison between *in vitro* testing results and the model simulations. Fractures observed from the *in vitro* studies in this thesis are similar to observed *in vivo* shear related injuries. This finding adds further support for using the porcine cervical spine as a surrogate model for the human lumbar spine. Data from this thesis also showed that facet and spinal canal dimensions of the porcine cervical spine are congruent with similar measurements made on the human lumbar spine (Table 7.1). In particular, facet angle in the horizontal plane, spinal canal depth and width, interfacet distances, and ratios between facet width and length were found to be congruent between porcine cervical and human lumbar specimens. Larger measured shear stiffness and smaller measured ultimate failure displacements may be attributed to differences in displacement measuring protocols between studies.

Table 7.1 – Comparison of morphology and structural properties between human lumbar and porcine cervical specimens from previous studies as well as this thesis. The asterisk indicates that all ranges of motion are based on pure moment loading with  $\pm 2 - 2.5$  Nm applied to the specimen.

Measurement	Human Lumbar	Previous Porcine Cervical	Current Thesis		
			Study 1	Study 2	Study 3
Upper Endplate Depth (mm)	32.7 – 34.7 <sup>1</sup>	22.28 <sup>1</sup>	24.2	24.6	24.4
Lower Endplate Depth (mm)	33.9 – 34.9 <sup>1</sup>	22.53 <sup>1</sup>	26.0	26.1	25.7
Pedicle Width (mm)	6.9 – 16.2 <sup>1-3</sup>	8.67 – 8.91 <sup>1</sup>		9.5	
Pars Interarticularis Height (mm)	44.8 – 49.1 <sup>1</sup>	28.81 – 29.34 <sup>1</sup>			
Pars Interarticularis Width (mm)	N/A	8.35 – 8.48 <sup>1</sup>			
Sagittal Facet Angle (degrees)	40.88 – 62.3 <sup>1,4,5</sup>	44.5 – 48.5 <sup>1,11</sup>	45.9	45.6	45.0
Sagittal Facet Tropism (degrees)			3.6	3.0	3.2

Table 7.1 continued

Measurement	Human Lumbar	Previous Porcine Cervical	Current Thesis		
			Study 1	Study 2	Study 3
Transverse Facet Angle (degrees)	87.2 – 90 <sup>1</sup>	81.2 – 81.7 <sup>1</sup>			
Spinal Canal Depth (mm)	12.1 – 18.1 <sup>1,2</sup>	9.78 <sup>1</sup>		13.3	
Spinal Canal Width (mm)	16.1 – 17.1 <sup>1,2</sup>	17.92 <sup>1</sup>		18.7	
Superior Facet Length (mm)	12.27 – 15.30 <sup>15</sup>		13.0	13.6	13.1
Superior Facet Width (mm)	10.36 – 15.45 <sup>15</sup>		12.5	13.0	12.7
Inferior Facet Length (mm)	13.27 – 17.79 <sup>15</sup>		11.2	12.0	10.8
Inferior Facet Width (mm)	10.05 – 14.56 <sup>15</sup>		11.9	12.4	12.1
Inside Superior Interfacet Distance (mm)			23.4	23.7	23.9
Outside Superior Interfacet Distance (mm)	26.84 – 35.27 <sup>15</sup>		42.6	43.5	42.4
Inside Inferior Interfacet Distance (mm)			23.6	23.4	24.6
Outside Inferior Interfacet Distance (mm)	24.99 – 43.82 <sup>15</sup>		41.0	41.4	41.7
Superior Facet Width to Length Ratio	0.76 – 1.01 <sup>15,16</sup>		0.96	0.95	0.97
Inferior Facet Width to Length Ratio	0.68 – 0.94 <sup>15,16</sup>		1.06	1.03	1.12
Flexion/Extension Range of Motion* (degrees)	3 – 8 <sup>6-9</sup>	22.4 – 23.9 <sup>12,13</sup>			
Lateral Bend Range of Motion* (degrees)	4.5 – 6.9 <sup>6-9</sup>	27 – 35.2 <sup>12,13</sup>			
Axial Rotation Range of Motion* (degrees)	1 – 2 <sup>6-9</sup>	4.5 – 8.5 <sup>12,13</sup>			

Table 7.1 continued

Measurement	Human Lumbar	Previous Porcine Cervical	Current Thesis		
			Study 1	Study 2	Study 3
Anterior Shear Stiffness (N/mm)	155 <sup>10</sup>	139 – 212 <sup>1,11</sup>	1051	842	
Ultimate Anterior Shear Force (N)	1710 – 2894 <sup>10</sup>	1980 – 3538 <sup>1,11</sup>	2372	2203	
Ultimate Anterior Shear Displacement (mm)	13 <sup>10</sup>	10 – 18 <sup>11,14</sup>	6.0	6.6	

1. Yingling et al., 1999.

2. Zhou et al., 2000.

3. McLain et al., 2004.

4. Masharawi et al., 2004.

5. Panjabi et al., 1993

6. Kettler et al., 2007.

7. Oxland and Panjabi, 1992.

8. Panjabi et al., 1994.

9. Busscher et al., 2010.

10. Crompton et al., 1995.

11. Gallagher et al., 2010.

12. Schmidt et al., 2005.

13. Goertzen et al., 2004.

14. Yingling and McGill, 1999.

15. Masharawi et al., 2005

16. Panjabi et al., 1992.

## 7.5 FUTURE RESEARCH DIRECTIONS

As indicated in the literature review (Section 2.3.2.2), the facet joint capsule (consisting of two articulating facets, articular cartilage, capsular ligaments, synovial fluid and meniscus) has been implicated as a source of low-back pain signaling (Mooney and Robertson, 1976; Yang and King 1984; Cavanaugh et al., 2006) and involved with proprioception (Cavanaugh et al., 1996). Yang and King (1984) presented a mechanical theory for low-back pain signaling as a result of facet joint capsule compression while recent evidence has documented the neuromuscular response following facet joint capsule stretching (Azar et al., 2009). Future work should focus on the neuromuscular consequences as well as the nociceptive neural discharge resulting from scenarios such as vertebral shear loading that result in facet compression.



A direct extension of work presented in this thesis and parallel to the direction of force-weighted estimates of cumulative compressive load (Parkinson and Callaghan, 2008) would be to investigate the role that variable rest to work ratios have on the cumulative tolerance of the vertebral joint exposed to sub-maximal shear loading. This would make weighting factors derived from a bivariate mathematical model of sub-maximal shear load magnitude and the rest to work ratio. Given the relationship between altered measured ultimate shear force and flexion/extension postural deviation that was presented in Chapter 3, it would be a logical subsequent step to determine the effect of flexion/extension postural deviation on the vertebral joint's cumulative shear tolerance.

Limitations of the finite element model presented in Chapter 6 should also be addressed in future studies. Most importantly, the intervertebral disc should consider the orientation and mechanical response of the annular fibers and nucleus pulposus. Findings from research recently presented on the relative importance of connections between the inter-lamellar and intra-lamellar matrices (Schollum et al., 2009; Schroeder et al., 2010; Gregory et al., in press) should be incorporated to future iterations of the intervertebral disc used in the finite element model presented in this thesis. These improvements are imperative for any investigations, such as herniation studies, where the site of injury or area of interest is within or surrounding the intervertebral disc. Other areas of improvement for the finite element model include the addition of ligaments surrounding the vertebral joint, improved facet joint capsule modeling by including capsular ligaments, articular cartilage covering the facet surfaces, and variable cortical bone thickness throughout each vertebra derived from computed tomography scans of each vertebra.

## 7.6 CONTRIBUTIONS OF THE THESIS

The following are the novel or supporting contributions from the work presented in this thesis. *In vitro* protocols used for this thesis employed a novel 6 degree of freedom material testing system for testing anterior vertebral joint shear (Chapters 3-5).

Chapter 3 discovered that compression and flexion/extension postural deviation do not interact to modulate injury potential of the vertebral joint under acute shear failure. This chapter also was the first investigation to show that measured ultimate shear failure tolerance by 11.1% for each 15% increment in compressive force. Meanwhile, measured ultimate shear failure tolerance decreased by 13.2% for flexed postures, a finding that was in direct opposition to findings presented by Yingling and McGill (1999) and van Dieen and colleagues (2006), and increased by 12.8% for extended postures. Chapter 3 also confirmed findings from previous investigations (Cripton et al., 1995; Yingling and McGill 1999; Beadon et al., 2008; Gallagher et al., 2010) that the cranial vertebra's pars interarticularis as the dominant site of failure following acute and repetitive shear loading. This thesis also observed for the first time that caudal vertebra's pars interarticularis fractured more frequently if vertebral joint is flexed (Chapter 3).

Chapter 4 was the first study to systematically identify vertebral morphological characteristics that govern shear injury potential (cranial vertebra's pars interarticularis length – 44.3% explained variance, average facet angle measured in the transverse plane – 12.3% explained variance, cortical bone area through pars interarticularis – 11.9% explained variance). This investigation was also the first to develop an equation for non-destructively calculating ultimate vertebral shear failure tolerance (Chapter 4).

Furthermore, this investigation presented a novel measurement protocol for performing peripheral quantitative computed tomography scans of the pars interarticularis (Chapter 4).

A servomotor control algorithm for performing studies of repetitive anterior joint shear was developed for Chapter 5. This investigation was the first to quantify the non-linear injury potential generated by larger sub-maximal shear forces (Chapter 5). The higher likelihood for multiple vertebral injury sites including unilateral fractures of either the cranial or caudal pars interarticularis, bilateral fracture of the caudal pars interarticularis and endplate avulsion at larger sub-maximal shear load magnitudes was also a novel observation. Similar methods to those used by Parkinson and Callaghan (2007a) for compressive loading, helped to develop the first tissue-based equation for determining appropriate weighting factors to be applied to sub-maximal shear loads in calculations of cumulative shear load (Chapter 5).

A finite element model for the porcine C3-C4 vertebral joint was also completely developed within this thesis (Chapter 6). The methodology outlined a technique for using white light scanning to develop biological finite element model geometry (Chapter 6). Results from the finite element model confirmed the original hypothesis presented by Yingling and McGill (1999) that the moment arm length between the force centroid of facet contact and the cranial pars interarticularis increases (by 11.9%) for flexed postures and decreases (by 4.1%) for extended postures (Chapter 6). This investigation also confirmed that in order to achieve the same strain, increased stress and decreased contact area is observed with flexed postures compared to neutral and extended postures (Chapter 6). The finite element model also demonstrated that compression reduced moment arm

length by an average of 1.4% (Chapter 6). Similar to *in vitro* findings (Dunlop et al., 1984), this study demonstrated that compression increased facet contact area during anterior joint shear and that the location of contact force moved cranially with flexed postures and caudally with extended postures (Chapter 6). The finite element model also confirmed the original hypothesis generated by Cyron and colleagues (1976), and also suggested by results within Chapter 3, by demonstrating that alterations in the moment arm length were able to explain 50% of the variance in measured ultimate shear failure tolerance under similar *in vitro* testing conditions (Chapter 6).

The final contribution of this thesis is the development of a novel framework, presented in Chapter 7, for understanding modulation of vertebral shear injury potential from the combined results of Chapters 3-6.

## REFERENCES

- Adams, M.A., Bogduk, N., Burton, K., and Dolan, P. (2002). *The Biomechanics of Back Pain*. Churchill Livingstone, London, England.
- Adams, M.A., and Dolan, P. (2005). Spine biomechanics. *Journal of Biomechanics*, 38: 1972-1983.
- Adams, M.A., and Hutton, W.C. (1980). The effect of posture on the role of the apophysial joints in resisting intervertebral compressive forces. *The Journal of Bone and Joint Surgery (Br)*, 62: 358-362.
- Akahoshi, S., Sakai, A., Arita, S., Ikeda, S., Morishita, Y., Tsutsumi, H., Ito, M., Shiraishi, A., and Nakamura, T. (2005). Modulation of bone turnover by alfacalcidol and/or alendronate does not prevent glucocorticoid-induced osteoporosis in growing minipigs. *Journal of Bone and Mineral Metabolism*, 23: 341-350.
- Alini, M., Eisenstein, S.M., Ito, K., Little, C., Kettler, A.A., Masuda, K., Melrose, J., Ralphs, J., Stokes, I., and Wilke, H.J. (2008). Are animal models useful for studying human disc disorders/degeneration? *European Spine Journal*, 17: 2-19.
- Argoubi, M., and Shirazi-Adl, A. (1996). Poroelastic creep response analysis of a lumbar motion segment in compression. *Journal of Biomechanics*, 29: 1331-1339.
- Ashe, M.C., Khan, K.M., Kontulainen, S.A., Guy, P., Liu, D., Beck, T.J., and McKay, H.A. (2006). Accuracy of pQCT for evaluating the aged human radius: an ashing, histomorphometry and failure load investigation. *Osteoporosis International*, 17: 1241-1251.
- Azar, N.R., Kallakuri, S., Chen, C., Lu, Y., and Cavanaugh, J.M. (2009). Strain and load thresholds for cervical muscle recruitment in response to quasi-static tensile stretch of the caprine C5-C6 facet joint capsule. *Journal of Electromyography and Kinesiology*, 19: E387-E394.
- Aziz, H.N., Galbusera, F., Bellini, C.M., Mineo, G.V., Addis, A., Pietrabissa, R., and Brayda-Bruno, M. (2008). Porcine models in spinal research: calibration and comparative finite element analysis of various configurations during flexion-extension. *Comparative Medicine*, 58: 174-179.
- Bass, C.R., Planchak, C.J., Salzar, R.S., Lucas, S.R., Rafaels, K.A., Shender, B.S., and Paskoff, G. (2007). The temperature-dependent viscoelasticity of porcine lumbar spine ligaments. *Spine*, 32: E436-E442.
- Beadon, K., Johnston, J.D., Siggers, K., Itshayek, E., and Cripton, P.A. (2008). A repeatable ex vivo model of spondylolysis and spondylolisthesis. *Spine*, 33: 2387-2393.

- Belytschko, T., Kulak, R.F., Schultz, A.B., and Galante, J.O. (1974). Finite element stress analysis of an intervertebral disc. *Journal of Biomechanics*, 7: 277-285.
- Biggemann, M., Hilweg, D., and Brinckmann, P. (1988). Prediction of the compressive strength of vertebral bodies of the lumbar spine by quantitative computed tomography. *Skeletal Radiology*, 17: 264-269.
- Boden, S.D., Riew, K.D., Yamaguchi, K., Branch, T.P., Schellinger, D., and Wiesel, S.W. (1996). Orientation of the lumbar facet joints: association with degenerative disc disease. *The Journal of Bone and Joint Surgery (Am)*, 78: 403-411.
- Bogduk, N., and Engel, R. (1984). The menisci of the lumbar zygapophyseal joints. A review of their anatomy and clinical significance. *Spine*, 9: 454-460.
- Bogduk, N., and Twomey, L.T. (1991). Clinical anatomy of the lumbar spine. Churchill Livingstone, London, England.
- Bogduk, N., Tynan, W., and Wilson, A.S. (1981). The nerve supply to the human lumbar intervertebral discs. *Journal of Anatomy*, 132: 39-56.
- Breau, C., Shirazi-Adl, A., and de Guise, J. (1991). Reconstruction of a human ligamentous lumbar spine using CT images--a three-dimensional finite element mesh generation. *Annals of Biomedical Engineering*, 19: 291-302.
- Brinckmann, P., Biggemann, M., and Hilweg, D. (1988). Fatigue fracture of human lumbar vertebrae. *Clinical Biomechanics*, 2-Suppl: S1-S23.
- Brown, T.D. (2004). Finite element modeling in musculoskeletal biomechanics. *Journal of Applied Biomechanics*, 20: 336-366.
- Busscher, I., van der Veen, A.J., van Dieën, J.H., Kingma, I., Verkerke, G.J., and Veldhuizen, A.G. (2010). *In vitro* biomechanical characteristics of the spine: a comparison between human and porcine spinal segments. *Spine*, 35: E35-E42.
- Callaghan, J.P., and McGill, S.M. (1995). Frozen storage increases the ultimate compressive load of porcine vertebrae. *Journal of Orthopaedic Research*, 13: 809-812.
- Callaghan, J.P., and McGill, S.M. (2001). Intervertebral disc herniation: studies on a porcine model exposed to highly repetitive flexion/extension motion with compressive force. *Clinical Biomechanics*, 16: 28-37.
- Cao, K.D., Grimm, M.J., and Yang, K.H. (2001). Load sharing within a human lumbar vertebral body using the finite element method. *Spine*, 26: E253-E260.

- Cavanaugh, J.M., Lu, Y., Chen, C., and Kallakuri, S. (2006). Pain generation in lumbar and cervical facet joints. *The Journal of Bone and Joint Surgery (Am)*, 88-Suppl: 263-267.
- Cavanaugh, J.M., Ozaktay, A.C., Yamashita, H.T., Avramov, A., Getchell, T.V., and King, A.I. (1997). Mechanisms of low back pain: a neurophysiologic and neuroanatomic study. *Clinical Orthopaedics and Related Research*, 335: 166-180.
- Cavanaugh, J.M., Ozaktay, A.C., Yamashita, H.T., and King, A.I. (1996). Lumbar facet pain: biomechanics, neuroanatomy and neurophysiology. *Journal of Biomechanics*, 29: 1117-1129.
- Cholewicki, J., and McGill, S.M. (1996). Mechanical stability of the in vivo lumbar spine: implications for injury and chronic low back pain. *Clinical Biomechanics*, 11: 1-15.
- Chosa, E., Totoribe, K., and Tajima, N. (2004). A biomechanical study of lumbar spondylolysis based on a three-dimensional finite element method. *Journal of Orthopaedic Research*, 22: 158-163.
- Cifuentes, A.O., and Kalbag, A. (1992). A performance study of tetrahedral and hexahedral elements in 3-D finite element structural analysis. *Finite Elements in Analysis and Design*, 12: 313-318.
- Cohen, S.P., and Raja, S.N. (2007). Pathogenesis, diagnosis, and treatment of lumbar zygapophysial (facet) joint pain. *Anesthesiology*, 106: 591-614.
- Cowin, S.C., and Hegedus, D.H. (1976). Bone remodeling I: theory of adaptive elasticity. *Journal of Elasticity*, 6: 313-326.
- Cramer, G.D., and Darby, S.A. (1995). Basic and clinical anatomy of the spine, spinal cord, and ANS. Mosby, St. Louis, MO, USA.
- Crawford, R.P., Rosenberg, W.S., and Keaveny, T.M. (2003). Quantitative computed tomography-based finite element models of the human lumbar vertebral body: effect of element size on stiffness, damage, and fracture strength predictions. *Journal of Biomechanical Engineering*, 125: 434-438.
- Cripton, P.A., Berleman, U., Visarius, H., Begeman, P.C., Nolte, L.P., and Prasad, P. (1995). Response of the lumbar spine due to shear loading. *Proceeding of the Centers for Disease Control on Injury Prevention through Biomechanics*, Detroit: Wayne State University: 111-126.
- Cyron, B.M., and Hutton, W.C. (1978). The fatigue strength of the lumbar neural arch in spondylolysis. *The Journal of Bone and Joint Surgery (Br)*, 60: 234-238.



- Cyron, B.M., Hutton, W.C., and Troup, J.D. (1976). Spondylolytic fractures. *The Journal of Bone and Joint Surgery (Br)*, 58: 462-466.
- Dath, R., Ebinesan, A.D., Porter, K.M., and Miles, A.W. (2007). Anatomical measurements of porcine lumbar vertebrae. *Clinical Biomechanics*, 22: 607-613.
- Dhillon, N., Bass, E.C., and Lotz, J.C. (2001). Effect of frozen storage on the creep behavior of human intervertebral discs. *Spine*, 26: 883-888.
- Dickerson, C.R., Saha, S., and Hotchkiss, C.E. (2008). Relationships between densitometric and morphological parameters as measured by peripheral computed tomography and the compressive behavior of lumbar vertebral bodies from macaques (*Macaca fascicularis*). *Spine*, 33: 366-372.
- Don, A.S., and Robertson, P.A. (2008). Facet joint orientation in spondylolysis and isthmic spondylolisthesis. *Journal of Spinal Disorders and Techniques*, 21: 112-115.
- Drake, J.D., Aultman, C.D., McGill, S.M., and Callaghan, J.P. (2005). The influence of static axial torque in combined loading on intervertebral joint failure mechanics using a porcine model. *Clinical Biomechanics*, 20: 1038-1045.
- Drake, J.D., and Callaghan, J.P. (2008). Do flexion/extension postures affect the in vivo passive lumbar spine response to applied axial twist moments? *Clinical Biomechanics*, 23: 510-519.
- Drake, J.D., and Callaghan, J.P. (in press). The effect of physiological axial twist rotational displacement rates on the porcine cervical spine's acute failure limit. *Journal of Biomechanics*.
- Drake, J.D., Dobson, H., and Callaghan, J.P. (2008). The influence of posture and loading on interfacet spacing: an investigation using magnetic resonance imaging on porcine spinal units. *Spine*, 33: E728-E734.
- Drews, S., Matsuura, M., and Putz, R. (2008). The trabecular architecture of the superior articular process of the lumbar spine (L2-S1). *Surgical and Radiologic Anatomy*, 30: 209-213.
- Dunlop, R.B., Adams, M.A., and Hutton, W.C. (1984). Disc space narrowing and the lumbar facet joints. *The Journal of Bone and Joint Surgery (Br)*, 66: 706-710.
- Ebbesen, E.N., Thomsen, J.S., Beck-Nielsen, H., Nepper-Rasmussen, H.J., and Mosekilde, L. (1999). Lumbar vertebral body compressive strength evaluated by dual-energy X-ray absorptiometry, quantitative computed tomography, and ashing. *Bone*, 25: 713-724.

- Eberlein, R., Holzapfel, G.A., and Frolich, M. (2004). Multi-segment FEA of the human lumbar spine including the heterogeneity of the annulus fibrosus. *Computational Mechanics*, 34: 147-163.
- Eberlein, R., Holzapfel, G.A., and Schulze-Bauer, C.A.J. (2001). An Anisotropic Model for Annulus Tissue and Enhanced Finite Element Analyses of Intact Lumbar Disc Bodies. *Computer Methods in Biomechanics and Biomedical Engineering*, 4: 209-229.
- Edmondston, S.J., Singer, K.P., Day, R.E., Breidahl, P.D., and Price, R.I. (1994). In-vitro relationships between vertebral body density, size, and compressive strength in the elderly thoracolumbar spine. *Clinical Biomechanics*, 9: 180-186.
- Edmondston, S.J., Singer, K.P., Day, R.E., Price, R.I., and Breidahl, P.D. (1997). Ex vivo estimation of thoracolumbar vertebral body compressive strength: the relative contributions of bone densitometry and vertebral morphometry. *Osteoporosis International*, 7: 142-148.
- El-Rich, M., Villemure, I., Labelle, H., and Aubin, C.E. (2009). Mechanical loading effects on isthmic spondylolytic lumbar segment: finite element modeling using a personalised geometry. *Computer Methods in Biomechanics and Biomedical Engineering*, 12: 13-23.
- Eriksson, S.A., Isberg, B.O., and Lindgren, J.U. (1989). Prediction of vertebral strength by dual photon absorptiometry and quantitative computed tomography. *Calcified Tissue International*, 44: 243-250.
- Fagan, M.J., Julian, S., and Mohsen, A.M. (2002a). Finite element analysis in spine research. *Proceedings of the Institution of Mechanical Engineers. Part H, Journal of Engineering in Medicine*, 216: 281-298.
- Fagan, M.J., Julian, S., Siddall, D.J., and Mohsen, A.M. (2002b). Patient-specific spine models. Part 1: Finite element analysis of the lumbar intervertebral disc--a material sensitivity study. *Proceedings of the Institution of Mechanical Engineers. Part H, Journal of Engineering in Medicine*, 216: 299-314.
- Fantigrossi, A., Galbusera, F., Raimondi, M.T., Sassi, M., and Fornari, M. (2007). Biomechanical analysis of cages for posterior lumbar interbody fusion. *Medical Engineering & Physics*, 29: 101-109.
- Farfan, H.F., Osteria, V., and Lamy, C. (1976). The mechanical etiology of spondylolysis and spondylolisthesis. *Clinical Orthopaedics and Related Research*, 117: 40-55.
- Galante, J.O. (1967). Tensile properties of the human lumbar annulus fibrosus. *Acta orthopaedica Scandinavica*, Suppl. 100: 1-91.

- Gallagher, K.M., Howarth, S.J., and Callaghan, J.P. (2010). Effects of anterior shear displacement rate on the structural properties of the porcine cervical spine. *Journal of Biomechanical Engineering*, 132: 1149-1154.
- Gallagher, R.H., Simon, B.R., Johnson, P.C., and Gross, J.F. (1982). Finite elements in biomechanics. John Wiley & Sons Ltd, Toronto, ON, Canada.
- Garavello-Freitas, I., Baranauskas, V., Joazeiro, P.P., Padovani, C.R., Dal Pai-Silva, M., and da Cruz-Höfling, M.A. (2003). Low-power laser irradiation improves histomorphometrical parameters and bone matrix organization during tibia wound healing in rats. *J Photochemistry and Photobiology. Biology, B*, 70: 81-89.
- Gardner-Morse, M.G., and Stokes, I.A. (2003). Physiological axial compressive preloads increase motion segment stiffness, linearity and hysteresis in all six degrees of freedom for small displacements about the neutral posture. *Journal of Orthopaedic Research*, 21: 547-552.
- Goel, V.K., and Gilbertson, L.G. (1995). Applications of the finite element method to thoracolumbar spinal research--past, present, and future. *Spine*, 20: 1719-1727.
- Goertzen, D.J., Lane, C., and Oxland, T.R. (2004). Neutral zone and range of motion in the spine are greater with stepwise loading than with a continuous loading protocol. An in vitro porcine investigation. *Journal of biomechanics*, 37: 257-261.
- Gracovetsky, S., Farfan, H.F., and Lamy, C. (1981). The mechanism of the lumbar spine. *Spine*, 6: 249-262.
- Graham, R.S., Oberlander, E.K., Stewart, J.E., and Griffiths, D.J. (2000). Validation and use of a finite element model of C-2 for determination of stress and fracture patterns of anterior odontoid loads. *Journal of Neurosurgery*, 93-Suppl: 117-125.
- Gregory, D.E., Milosavljevic, S., and Callaghan, J.P. (2006). Quantifying low back peak and cumulative loads in open and senior sheep shearers in New Zealand: examining the effects of a trunk harness. *Ergonomics*, 49: 968-981.
- Gregory, D.E., Veldhuis, J.H., Horst, C., Wayne Brodland, G., and Callaghan, J.P. (in press). Novel lap test determines the mechanics of delamination between annular lamellae of the intervertebral disc. *Journal of Biomechanics*.
- Gunning, J.L., Callaghan, J.P., and McGill, S.M. (2001). Spinal posture and prior loading history modulate compressive strength and type of failure in the spine: a biomechanical study using a porcine cervical spine model. *Clinical Biomechanics*, 16: 471-480.

- Hansson, T.H., Keller, T.S., and Spengler, D.M. (1987). Mechanical behavior of the human lumbar spine. II. Fatigue strength during dynamic compressive loading. *Journal of Orthopaedic Research*, 5: 479-487.
- Hansson, T., Roos, B., and Nachemson, A. (1980). The bone mineral content and ultimate compressive strength of lumbar vertebrae. *Spine*, 5: 46-55.
- Hirsch, C., and Galante, J. (1967). Laboratory conditions for tensile tests in annulus fibrosus from human intervertebral discs. *Acta Orthopaedica Scandinavica*, 38: 148-162.
- Hirsch, C., and Nachemson, A. (1954). New observations on the mechanical behavior of lumbar discs. *Acta Orthopaedica Scandinavica*, 23: 254-283.
- Howarth, S.J., Beach, T.A., Pearson, A.J., and Callaghan, J.P. (2009). Using sitting as a component of job rotation strategies: Are lifting/lowering kinetics and kinematics altered following prolonged sitting. *Applied Ergonomics*, 40: 433-439.
- Hukins, D.W.L., and Meakin, J.R. (2000). Relationship between structure and mechanical function of the tissues of the intervertebral joint. *Integrative and Comparative Biology*, 40: 42-52.
- Hutton, W.C., Cyron, B.M., and Stott, J.R. (1979). The compressive strength of lumbar vertebrae. *Journal of Anatomy*, 129: 753-758.
- Inoue, H., Ohmori, K., Ishida, Y., Suzuki, K., Tanaka, E., and Murakami, S. (1998). Finite element analysis of the lower lumbar neural arch under facet loading. *Journal of Spinal Disorders*, 11: 241-247.
- Inui, A., Itamoto, K., Takuma, T., Tsutsumi, H., Tanigawa, M., Hayasaki, M., Taura, Y., and Mamba, K. (2004). Age-related changes of bone mineral density and microarchitecture in miniature pigs. *The Journal of Veterinary Medical Science*, 66: 599-609.
- Jackson, H.C., Winkelmann, R.K., and Bickel, W.H. (1966). Nerve endings in the human lumbar spinal column and related structures. *The Journal of Bone and Joint Surgery (Am)*, 48: 1272-1281.
- Jager, M., Jordan, C., Luttmann, A., Laurig, W., and Dolly Group (2000). Evaluation and assessment of lumbar load during total shifts for occupational manual materials handling jobs within the Dortmund Lumbar Load Study – DOLLY. *International Journal of Industrial Ergonomics*, 25: 553-571.
- Janevic, J., Ashton-Miller, J.A., and Schultz, A.B. (1991). Large compressive preloads decrease lumbar motion segment flexibility. *Journal of Orthopaedic Research*, 9: 228-236.

- Jones, A.C., and Wilcox, R.K. (2007). Assessment of factors influencing finite element vertebral model predictions. *Journal of Biomechanical Engineering*, 129: 898-903.
- Kalichman, L., and Hunter, D.J. (2007). Lumbar facet joint osteoarthritis: a review. *Seminars in Arthritis and Rheumatism*, 37: 69-80.
- Kaminsky, J., Rodt, T., Gharabaghi, A., Forster, J., Brand, G., and Samii, M. (2005). A universal algorithm for an improved finite element mesh generation Mesh quality assessment in comparison to former automated mesh-generators and an analytic model. *Medical Engineering & Physics*, 27: 383-394.
- Kato, N., Koshino, T., Saito, T., and Takeuchi, R. (1998). Estimation of Young's modulus in swine cortical bone using quantitative computed tomography. *Bulletin (Hospitals for Joint Diseases (New York, NY))*, 57: 183-186.
- Kemper, A.R., McNally, C., and Duma, S.M. (2007). The influence of strain rate on the compressive stiffness properties of human lumbar intervertebral discs. *Biomedical Sciences Instrumentation*, 43: 176-181.
- Kettler, A., Liakos, L., Haegerle, B., and Wilke, H.J.. (2007). Are the spines of calf, pig and sheep suitable models for pre-clinical implant tests? *European Spine Journal*, 16: 2186-2192.
- Kotha, S.P., Hsieh, Y.F., Strigel, R.M., Müller, R., and Silva, M.J. (2004). Experimental and finite element analysis of the rat ulnar loading model-correlations between strain and bone formation following fatigue loading. *Journal of Biomechanics*, 37: 541-548.
- Kumaresan, S., Yoganandan, N., and Pintar, F.A. (1998). Finite element modeling approaches of human cervical spine facet joint capsule. *Journal of Biomechanics*, 31: 371-376.
- Kumaresan, S., Yoganandan, N., and Pintar, F.A. (1999). Finite element analysis of the cervical spine: a material property sensitivity study. *Clinical Biomechanics*, 14: 41-53.
- Lee, R.Y., and Evans, J.H. (2000). The role of spinal tissues in resisting posteroanterior forces applied to the lumbar spine. *Journal of Manipulative and Physiological Therapeutics*, 23: 551-556.
- Liebschner, M.A., Kopperdahl, D.L., Rosenberg, W.S., and Keaveny, T.M. (2003). Finite element modeling of the human thoracolumbar spine. *Spine*, 28: 559-565.
- Lin, H.S., Liu, Y.K., and Adams, K.H. (1978). Mechanical response of the lumbar intervertebral joint under physiological (complex) loading. *The Journal of Bone and Joint Surgery (Am)*, 60: 41-55.

- Liu, J., Ebraheim, N.A., Haman, S.P., Shafiq, Q., Karkare, N., Biyani, A., Goel, V.K., and Woldenberg, L. (2006). Effect of the increase in the height of lumbar disc space on facet joint articulation area in sagittal plane. *Spine*, 31: E198-E202.
- Lorenz, M., Patwardhan, A., and Vanderby, R. (1983). Load-bearing characteristics of lumbar facets in normal and surgically altered spinal segments. *Spine*, 8: 122-130.
- Lu, W.W., Luk, K.D., Holmes, A.D., Cheung, K.M., and Leong, J.C. (2005). Pure shear properties of lumbar spinal joints and the effect of tissue sectioning on load sharing. *Spine*, 30: E204-E209.
- Lu, Y.M., Hutton, W.C., and Gharpuray, V.M. (1996). Do bending, twisting, and diurnal fluid changes in the disc affect the propensity to prolapse? A viscoelastic finite element model. *Spine*, 21: 2570-2579.
- Markolf, K.L. (1972). Deformation of the thoracolumbar intervertebral joints in response to external loads: a biomechanical study using autopsy material. *The Journal of Bone and Joint Surgery (Am)*, 54: 511-533.
- Masharawi, Y., Dar, G., Peleg, S., Steinberg, N., Alperovitch-Najenson, D., Salame, K., and HersHKovitz, I. (2007). Lumbar facet anatomy changes in spondylolysis: a comparative skeletal study. *European Spine Journal*, 16: 993-999.
- Masharawi, Y., Rothschild, B., Dar, G., Peleg, S., Robinson, D., Been, E., and HersHKovitz, I. (2004). Facet orientation in the thoracolumbar spine. *Spine*, 29: 1755-1763.
- Masharawi, Y., Rothschild, B., Salama, K., Dar, G., Peleg, S., and HersHKovitz, I. (2005). Facet tropism and interfacet shape in the thoracolumbar vertebrae. Characterization and biomechanical interpretation. *Spine*, 30: E281-E292.
- McElhaney, J.H. (1966). Dynamic response of bone and muscle tissue. *Journal of Applied Physiology*, 21: 1231-1236.
- McLain, R.F., Yerby, S.A., and Moseley, T.A. (2002). Comparative morphometry of L4 vertebrae: comparison of large animal models for the human lumbar spine. *Spine*, 27: E200-E206.
- McGill, S. (2007). *Low Back Disorders: Evidenced-based Prevention and Rehabilitation*. Human Kinetics, Champaign, IL, USA.
- McGill, S.M., Hughson, R.L., and Parks, K. (2000). Changes in lumbar lordosis modify the role of the extensor muscles. *Clinical Biomechanics*, 15: 777-780.

- McGill, S., Norman, R., Yingling, V., Wells, R., and Neumann, P. (1998). Shear happens! Suggested guidelines for ergonomists to reduce the risk of low back injury from shear loading. *30th Annual Conference of the Human Factors Association of Canada*, Mississauga, ON, Canada.
- Mooney, V., and Robertson, J. (1976). The facet syndrome. *Clinical Orthopaedics and Related Research*, 115: 149-156.
- Mosekilde, L., and Danielsen, C.C. (1987). Biomechanical competence of vertebral trabecular bone in relation to ash density and age in normal individuals. *Bone*, 8: 79-85.
- Myklebust, J.B., Pinar, F., Yoganandan, N., Cusick, J.F., Maiman, D., Myers, T.J., and Sances, A. (1988). Tensile strength of spinal ligaments. *Spine*, 13: 526-531.
- Natarajan, R.N., Williams, J.R., and Andersson, G.B. (2004). Recent advances in analytical modeling of lumbar disc degeneration. *Spine*, 29: 2733-2741.
- Nordin, M., and Frankel, V.H. (2001). Basic biomechanics of the musculoskeletal system. Lippincott Williams & Wilkins, Philadelphia, PA, USA.
- Norman, R., Wells, R., Neumann, P., Frank, J., Shannon, H., and Kerr, M. (1998). A comparison of peak vs cumulative physical work exposure risk factors for the reporting of low back pain in the automotive industry. *Clinical Biomechanics*, 13: 561-573.
- Ochia, R.S., Tencer, A.F., and Ching, R.P. (2003). Effect of loading rate on endplate and vertebral body strength in human lumbar vertebrae. *Journal of Biomechanics*, 36: 1875-1881.
- Overaker, D.W., Langrana, N.A., and Cuitiño, A.M. (1999). Finite element analysis of vertebral body mechanics with a nonlinear microstructural model for the trabecular core. *Journal of Biomechanical Engineering*, 121: 542-550.
- Oxland, T.R., and Panjabi, M.M. (1992). The onset and progression of spinal injury: a demonstration of neutral zone sensitivity. *Journal of Biomechanics*, 25: 1165-1172.
- Oxland, T.R., Panjabi, M.M., Southern, E.P., and Duranceau, J.S. (1991). An anatomic basis for spinal instability: a porcine trauma model. *Journal of Orthopaedic Research*, 9: 452-462.
- Pahr, D.H., and Zysset, P.K. (2008). From high-resolution CT data to finite element models: development of an integrated modular framework. *Computer Methods in Biomechanics and Biomedical Engineering*, 12: 45-57.

- Panjabi, M.M. (1992). The stabilizing system of the spine. Part II. Neutral zone and instability hypothesis. *Journal of Spinal Disorders*, 5: 390-396.
- Panjabi, M.M., Krag, M., Summers, D., and Videman, T. (1985). Biomechanical time-tolerance of fresh cadaveric human spine specimens. *Journal of Orthopaedic Research*, 3: 292-300.
- Panjabi, M.M., Oxland, T., Takata, K., Goel, V., Duranceau, J., and Krag, M. (1993). Articular facets of the human spine. Quantitative three-dimensional anatomy. *Spine*, 18: 1298-1310.
- Panjabi, M.M., Goel, V., Oxland, T., Takata, K., Duranceau, J., Krag, M., and Price, M. (1992). Human lumbar vertebrae. Quantitative three-dimensional anatomy. *Spine*, 17: 299-306.
- Panjabi, M.M., Oxland, T.R., Yamamoto, I., and Crisco, J.J. (1994). Mechanical behavior of the human lumbar and lumbosacral spine as shown by three-dimensional load-displacement curves. *The Journal of Bone and Joint Surgery*, 76-A: 413-424.
- Parkinson, R.J., and Callaghan, J.P. (2007a). The role of load magnitude as a modifier of the cumulative load tolerance of porcine cervical spinal units: progress towards a force weighting approach. *Theoretical Issues in Ergonomics Science*, 8: 171-184.
- Parkinson, R.J., and Callaghan, J.P. (2007b). Can periods of static loading be used to enhance the resistance of the spine to cumulative compression? *Journal of Biomechanics*, 40: 2944-2952.
- Parkinson, R., and Callaghan, J.P. (2008). Quantification of the relationship between load magnitude, rest duration and cumulative compressive tolerance of the spine: development of a weighting system for adjustment to a common injury exposure level. *Theoretical Issues in Ergonomics Science*, 9: 255-268.
- Parkinson, R.J., Durkin, J.L., and Callaghan, J.P. (2005). Estimating the compressive strength of the porcine cervical spine: an examination of the utility of DXA. *Spine*, 30: E492-E498.
- Pitzen, T., Geisler, M., Muller-Storz, H., Barbier, D., Steudel, W., and Feldges, A. (2002). A finite element model for predicting the biomechanical behaviour of the human lumbar spine. *Control Engineering Practice*, 10: 83-90.
- Potvin, J.R. (2008). Occupational spine biomechanics: A journey to the spinal frontier. *Journal of Electromyography and Kinesiology*, 18: 891-899.
- Potvin, J.R., Norman, R.W., and McGill, S.M. (1991). Reduction in anterior shear forces on the L4/L5 disc by the lumbar musculature. *Clinical Biomechanics*, 6: 88-96.



- Ramos, A., and Simões, J.A. (2006). Tetrahedral versus hexahedral finite elements in numerical modelling of the proximal femur. *Medical Engineering & Physics*, 28: 916-924.
- Rao, A.A., and Dumas, G.A. (1991). Influence of material properties on the mechanical behaviour of the L5-S1 intervertebral disc in compression: a nonlinear finite element study. *Journal of Biomedical Engineering*, 13: 139-151.
- Reinbold, W.D., Genant, H.K., Reiser, U.J., Harris, S.T., and Ettinger, B. (1986). Bone mineral content in early-postmenopausal and postmenopausal osteoporotic women: comparison of measurement methods. *Radiology*, 160: 469-478.
- Schmidt, R., Richter, M., Claes, L., Puhl, W., and Wilke, H.J. (2005). Limitations of the cervical porcine spine in evaluating spinal implants in comparison with human cervical spinal segments: a biomechanical in vitro comparison of porcine and human cervical spine specimens with different instrumentation techniques. *Spine*, 30: 1275-1282.
- Schollum, M.L., Robertson, P.A., and Broom, N.D. (2009). A microstructural investigation of intervertebral disc lamellar connectivity: detailed analysis of the translamellar bridges. *Journal of Anatomy*, 214: 805-816.
- Schroeder, Y., Huyghe, J.M., van Donkelaar, C.C., and Ito, K. (2010). A biochemical/biophysical 3D FE intervertebral disc model. *Biomechanical Modeling and Mechanobiology*, 9: 641-650.
- Schultz, K.P., and Niethard, F.U. (1980). Strain on the interarticular stress distribution. measurements regarding the development of spondylolysis. *Archives of Orthopaedic and Trauma Surgery*, 96: 197-202.
- Sedlin, E.D., and Hirsch, C. (1966). Factors affecting the determination of the physical properties of femoral cortical bone. *Acta Orthopaedica Scandinavica*, 37: 29-48.
- Seidler, A., Bolm-Audorff, U., Heiskel, H., Henkel, N., Roth-Küver, B., Kaiser, U., Bickeböller, R., Willingstorfer, W.J., Beck, W., and Elsner, G. (2001). The role of cumulative physical work load in lumbar spine disease: risk factors for lumbar osteochondrosis and spondylosis associated with chronic complaints. *Occupational and Environmental Medicine*, 58: 735-746.
- Seidler, A., Bolm-Audorff, U., Siol, T., Henkel, N., Fuchs, C., Schug, H., Leheta, F., Marquardt, G., Schmitt, E., Ulrich, P.T., Beck, W., Missalla, A., and Elsner, G. (2003). Occupational risk factors for symptomatic lumbar disc herniation; a case-control study. *Occupational and Environmental Medicine*, 60: 821-830.

- Serhan, H.A., Varnavas, G., Dooris, A.P., Patwadhan, A., and Tzermiadianos, M. (2007). Biomechanics of the posterior lumbar articulating elements. *Neurosurgical Focus*, 22: E1-E6.
- Sharma, M., Langrana, N.A., and Rodriguez, J. (1995). Role of ligaments and facets in lumbar spinal stability. *Spine*, 20: 887-900.
- Sharma, M., Langrana, N.A., and Rodriguez, J. (1998). Modeling of facet articulation as a nonlinear moving contact problem: sensitivity study on lumbar facet response. *Journal of Biomechanical Engineering*, 120: 118-125.
- Shipley, J.A., and Beukes, C.A. (1998). The nature of the spondylolytic defect. Demonstration of a communicating synovial pseudarthrosis in the pars interarticularis. *The Journal of Bone and Joint Surgery (Br)*, 80: 662-664.
- Shirazi-Adl, A. (1989). On the fibre composite material models of disc annulus--comparison of predicted stresses. *Journal of Biomechanics*, 22: 357-365.
- Shirazi-Adl, A. (1991). Finite-element evaluation of contact loads on facets of an L2-L3 lumbar segment in complex loads. *Spine*, 16: 533-541.
- Shirazi-Adl, A. (1994). Nonlinear stress analysis of the whole lumbar spine in torsion--mechanics of facet articulation. *Journal of Biomechanics*, 27: 289-299.
- Shirazi-Adl, A., Ahmed, A.M., and Shrivastava, S.C. (1986). A finite element study of a lumbar motion segment subjected to pure sagittal plane moments. *Journal of Biomechanics*, 19: 331-350.
- Silva, M.J., Keaveny, T.M., and Hayes, W.C. (1997). Load sharing between the shell and centrum in the lumbar vertebral body. *Spine*, 22: 140-150.
- Silva, M.J., Keaveny, T.M., and Hayes, W.C. (1998). Computed tomography-based finite element analysis predicts failure loads and fracture patterns for vertebral sections. *Journal of Orthopaedic Research*, 16: 300-308.
- Simon, B.R., Wu, J.S., Carlton, M.W., Kazarian, L.E., France, E.P., Evans, J.H., and Zienkiewicz, O.C. (1985). Poroelastic dynamic structural models of rhesus spinal motion segments. *Spine*, 10: 494-507.
- Smeathers, J.E., and Joanes, D.N. (1988). Dynamic compressive properties of human lumbar intervertebral joints: a comparison between fresh and thawed specimens. *Journal of Biomechanics*, 21: 425-433.
- Smit, T.H. (2002). The use of a quadruped as an in vivo model for the study of the spine - biomechanical considerations. *European Spine Journal*, 11: 137-144.

- Spoor, C.F., Zonneveld, F.W., and Macho, G.A. (1993). Linear measurements of cortical bone and dental enamel by computed tomography: applications and problems. *American journal of Physical Anthropology*, 91: 469-484.
- Stokes, I.A., and Gardner-Morse, M. (2003). Spinal stiffness increases with axial load: another stabilizing consequence of muscle action. *Journal of Electromyography and Kinesiology*, 13: 397-402.
- Stokes, I.A., Laible, J.P., Gardner-Morse, M.G., Costi, J.J., and Iatridis, J.C. (in press). Refinement of Elastic, Poroelastic, and Osmotic Tissue Properties of Intervertebral Disks to Analyze Behavior in Compression. *Annals of Biomedical Engineering*.
- Sullivan, A., and McGill, S.M. (1990). Changes in spine length during and after seated whole-body vibration. *Spine*, 15: 1257-1260.
- Suwito, W., Keller, T.S., Basu, P.K., Weisberger, A.M., Strauss, A.M., and Spengler, D.M. (1992). Geometric and material property study of the human lumbar spine using the finite element method. *Journal of Spinal Disorders*, 5: 50-59.
- Tampier, C. (2006). Progressive disc herniation: An investigation of the mechanism using histochemical and microscopic techniques. *M.Sc. Thesis*, University of Waterloo: Waterloo, Ontario.
- Tencer, A.F., and Mayer, T.G. (1983). Soft tissue strain and facet face interaction in the lumbar intervertebral joint--Part II: Calculated results and comparison with experimental data. *Journal of Biomechanical Engineering*, 105: 210-215.
- Teo, J.C., Si-Hoe, K.M., Keh, J.E., and Teoh, S.H. (2006). Relationship between CT intensity, micro-architecture and mechanical properties of porcine vertebral cancellous bone. *Clinical Biomechanics*, 21: 235-244.
- van Dieën, J.H., van der Veen, A., van Royen, B.J., and Kingma, I. (2006). Fatigue failure in shear loading of porcine lumbar spine segments. *Spine*, 31: E494-E498.
- van der Veen, A.J., van Dieën, J.H., Nadort, A., Stam, B., and Smit, T.H. (2007). Intervertebral disc recovery after dynamic or static loading in vitro: is there a role for the endplate? *Journal of Biomechanics*, 40: 2230-2235.
- Wilcox, R.K. (2007). The influence of material property and morphological parameters on specimen-specific finite element models of porcine vertebral bodies. *Journal of Biomechanics*, 40: 669-673.
- Womack, W., Woldtvedt, D., and Puttlitz, C.M. (2008). Lower cervical spine facet cartilage thickness mapping. *Osteoarthritis and Cartilage*, 16: 1018-1023.

- Wong, C., Gehrchen, P.M., Darvann, T., and Kiaer, T. (2003). Nonlinear finite-element analysis and biomechanical evaluation of the lumbar spine. *IEEE Transactions of Medical Imaging*, 22: 742-746.
- Woo, S.L., Debski, R.E., Zeminski, J., Abramowitch, S.D., Saw, S.S., and Fenwick, J.A. (2000). Injury and repair of ligaments and tendons. *Annual Review of Biomedical Engineering*, 2: 83-118.
- Yahia, H., Drouin, G., and Newman, N. (1990). Structure-function relationship of human spinal ligaments. *Zeitschrift für mikroskopisch-anatomische Forschung*, 104: 33-45.
- Yang, K.H., and King, A.I. (1984). Mechanism of facet load transmission as a hypothesis for low-back pain. *Spine*, 9: 557-565.
- Yates, J. (2009). Establishing the effect of vibration and postural constraint loading on the progression of intervertebral disc herniation. *M.Sc. Thesis*, University of Waterloo: Waterloo, Ontario.
- Yingling, V.R., Callaghan, J.P., and McGill, S.M. (1997). Dynamic loading affects the mechanical properties and failure site of porcine spines. *Clinical Biomechanics*, 12: 301-305.
- Yingling, V.R., Callaghan, J.P., and McGill, S.M. (1999). The porcine cervical spine as a model of the human lumbar spine: an anatomical, geometric, and functional comparison. *Journal of Spinal Disorders*, 12: 415-423.
- Yingling, V.R., and McGill, S.M. (1999). Anterior shear of spinal motion segments. Kinematics, kinetics, and resultant injuries observed in a porcine model. *Spine*, 24: 1882-1889.
- Young, P.G., Beresford-West, T.B., Coward, S.R., Notarberardino, B., Walker, B., and Abdul-Aziz, A. (2008). An efficient approach to converting three-dimensional image data into highly accurate computational models. *Philosophical Transactions. Series A, Mathematical, Physical, and Engineering Sciences*, 366: 3155-3173.
- Zhou, S.H., McCarthy, I.D., McGregor, A.H., Coombs, R.R.H., and Hughes, S.P.F. (2000). Geometrical dimensions of the lower lumbar vertebrae - analysis of data from digitized CT images. *European Spine Journal*, 9: 242-248.

## **APPENDICES**

## A. GALIL CODE

### A.1 Shear precondition

```
CYCLE= 0
FORCE= 0
JOGSPEED= 39
JG ,,0,0
IPOSW= _TPW
IPOSZ= _TPZ
INITPOSN= IPOSW + IPOSZ
BGWZ
#INITPSH
TARGET= 400
CYCLE= CYCLE+1
JP #ENDPROG,CYCLE=6
JG ,, -JOGSPEED, -JOGSPEED
#PUSH
FORCEW= @AN[4]
FORCEZ= @AN[5]
FORCEW= (FORCEW + 0.0300929)*205.21
FORCEZ= (FORCEZ - 0.00365714)*206.72
FORCE= FORCEW + FORCEZ
JP #INITPLL,TARGET<FORCE
JP #PUSH
#INITPLL
TARGET= -400
JG ,,JOGSPEED,JOGSPEED
#PULL
FORCEW= @AN[4]
FORCEZ= @AN[5]
FORCEW= (FORCEW + 0.0300929)*205.21
FORCEZ= (FORCEZ - 0.00365714)*206.72
FORCE= FORCEW + FORCEZ
JP #INITPSH,TARGET>FORCE
JP #PULL
#ENDPROG
```

## A.2 Acute shear failure

```
VFLEX=-1
#angflex
JP#angflex,VFLEX=-1
rate=444
#shrrate
JP#shrrate,rate=444
zrate=-118
wrate=zrate
XQ #ASAMP,1
v1=-1556
#FLEX
SETPOINT=v1
SPX= 1000
PAX= SETPOINT
BGX
WT 30720
TARGET= 0
JG ,,0,0
BGWZ
#S
BEGIN= TIME
#MOVING
ANALOGW=@AN[4]
ANALOGZ=@AN[5]
TOTFORCE= ANALOGW + ANALOGZ
JOGSPEED= 500*TOTFORCE
JG ,,JOGSPEED,JOGSPEED
CURRENT= TIME
ELAPSE= CURRENT-BEGIN
JP #MOVING,ELAPSE<10240
#SHEAR
JG ,,zrate,wrate
BGWZ
WT 190000
#FINISH2
```

### A.3 Repetitive shear failure

```
TARGPCT=0.2
FULLRATE=3192
TRATE=@INT[TARGPCT*FULLRATE]
IPUSH=(-9307.9*TARGPCT)+607.49
IPULL=(7236.3*TARGPCT)-390.68
CYCLE=0
DUR=0
FORCE=0
CURSTF=0
PREVSTF=0
RATERR=0
XQ #ASAMP,1
JG,,0,0
BGWZ
WT1000
#INITPSH
JOGSPEED=@INT[IPUSH]
PREVJOG=0
CYCLE=CYCLE+1
JP #FINISH2,CYCLE>21600
FORCEW=(@AN[4] + 0.0300929)*205.21
FORCEZ=(@AN[5] - 0.00365714)*206.21
INITF=FORCEW + FORCEZ
DISPW=_TPW*25.4/20000
DISPZ=_TPZ*25.4/20000
INITDISP=(DISPW+DISPZ)/2
START=TIME
#SPUSH
JG,,JOGSPEED,JOGSPEED
FORCEW=(@AN[4] + 0.0300929)*205.21
FORCEZ=(@AN[5] - 0.00365714)*206.21
FORCE=FORCEW+FORCEZ
JP #CHKSTF,FORCE>.5*.95*TRATE
CURRENT=TIME
DUR=(CURRENT-START)/1000
JP #CHKSTF,DUR>.475
ERROR=FORCE-(TRATE*DUR)
PREVJOG=JOGSPEED
A=DUR/.475
JOGSPEED=@INT[JOGSPEED + (.75*(1-A)*ERROR)]
JP #ADJPUSH,ERROR>0
JP #SPUSH
#ADJPUSH
JOGSPEED=PREVJOG
```



```

JP #SPUSH
#CHKSTF
DISPW=_TPW
DISPZ=_TPZ
DISP=(DISPW+DISPZ)/2*25.4/20000
CURSTF=-((FORCE - INITF)/(DISP - INITDISP))
PREVSTF=CURSTF
RATERR=(TRATE - ((FORCE - INITF)/DUR))/TRATE
JP #INITPUL,@ABS[RATERR]<0.05
IPUSH=IPUSH*(1+(0.5*RATERR))
#INITPUL
JOGSPEED=@INT[IPULL]
PREVJOG=0
FORCEW=(@AN[4] + 0.0300929)*205.21
FORCEZ=(@AN[5] - 0.00365714)*206.21
INITF=FORCEW + FORCEZ
DISPW=_TPW*25.4/20000
DISPZ=_TPZ*25.4/20000
INITDISP=(DISPW+DISPZ)/2
START=TIME
#SPULL
JG,,JOGSPEED,JOGSPEED
FORCEW=(@AN[4] + 0.0300929)*205.21
FORCEZ=(@AN[5] - 0.00365714)*206.21
FORCE=FORCEW+FORCEZ
JP #ENDPULL,FORCE<0
CURRENT=TIME
DUR=(CURRENT-START)/1000
JP #ENDPULL,DUR>.48
ERROR=FORCE-(TRATE*(.48-DUR))
PREVJOG=JOGSPEED
A=DUR/.48
JOGSPEED=@INT[JOGSPEED + (2*ERROR)]
JP #ADJPULL,ERROR<0
JP #SPULL
#ADJPULL
JOGSPEED=PREVJOG
JP #SPULL
#ENDPULL
RATERR=(TRATE - ((INITF - FORCE)/DUR))/TRATE
JP #INITPSH,@ABS[RATERR]<0.05
IPULL=IPULL*(1+(0.5*RATERR))
JP #INITPSH
#FINISH2

```

## B. DATA PROCESSING CUTOFF DETERMINATION

### B.1 Digital filter cutoffs for Chapters 3-5

Test	Load Cell	Optotrak Kinematics	Linear Potentiometer	Test	Load Cell	Optotrak Kinematics	Linear Potentiometer
1	5.04	3.04	4.36	21	2.25	1.99	4.50
2	3.33	3.37	4.04	22	3.36	2.03	4.45
3	4.18	3.13	4.31	23	2.52	1.82	4.20
4	4.55	3.84	4.27	24	5.24	3.40	4.14
5	5.08	3.21	4.22	25	2.79	2.11	4.21
6	2.39	2.70	4.19	26	2.03	2.16	4.46
7	3.31	2.09	4.12	27	3.82	2.43	4.14
8	1.68	1.97	4.11	28	1.67	2.08	4.40
9	2.96	2.09	4.14	29	4.59	4.00	4.43
10	2.63	2.35	4.14	30	4.12	2.76	4.35
11	2.64	1.98	4.21	31	3.31	4.56	4.16
12	3.33	2.39	4.23	32	3.70	2.73	4.17
13	2.96	2.13	4.01	33	4.20	3.17	4.17
14	4.53	3.55	4.19	34	3.63	2.65	4.21
15	5.96	4.02	4.22	35	4.57	3.52	4.20
16	3.04	2.41	4.47	36	4.23	3.25	4.26
17	4.07	3.79	4.20	37	4.11	3.80	
18	5.01	2.39	4.45	38	1.68	2.16	
19	1.83	1.99	4.54	39	2.16	1.95	
20	4.16	2.12	4.54	40	3.30	3.13	
<b>Average</b>					3.50	2.76	4.26
<b>Standard Error</b>					0.17	0.12	0.02

**B.2 Inter-rater reliability of measurements made from peripheral quantitative computed tomography**

	<b>Inferior</b>			<b>Superior</b>		
	<b>Rater 1</b>	<b>Rater 2</b>	<b>R<sup>2</sup></b>	<b>Rater 1</b>	<b>Rater 2</b>	<b>R<sup>2</sup></b>
<b>Total Density (mg/cm<sup>3</sup>)</b>	504.1 (11.8)	504.8 (11.6)	0.984	552.9 (13.7)	553.5 (13.6)	0.983
<b>Trabecular Density (mg/cm<sup>3</sup>)</b>	432.2 (10.1)	435.8 (9.9)	0.979	462.0 (10.7)	463.2 (10.6)	0.994
<b>Cortical + Subcortical Density (mg/cm<sup>3</sup>)</b>	691.5 (12.2)	684.1 (12.3)	0.931	735.2 (11.3)	731.6 (11.7)	0.974
<b>Total Area (mm<sup>2</sup>)</b>	121.7 (4.0)	112.9 (3.7)	0.686	118.5 (4.0)	114.7 (3.7)	0.800
<b>Trabecular Area (mm<sup>2</sup>)</b>	89.8 (3.6)	83.3 (3.3)	0.762	79.3 (3.3)	76.8 (3.2)	0.855
<b>Cortical + Subcortical Area (mm<sup>2</sup>)</b>	31.8 (1.6)	29.5 (1.5)	0.818	39.2 (2.4)	37.9 (2.0)	0.887

### B.3 Half maximum height (HMH) cutoff determination and inter-rater reliability

	<b>Rater 1</b>	<b>Rater 2</b>	<b>R<sup>2</sup></b>	<b>Cutoffs</b>
<b>Cortical Density (mg/cm<sup>3</sup>)</b>	1081.2 (14.8)	1091.2 (14.0)	0.041	
<b>Trabecular Density (mg/cm<sup>3</sup>)</b>	416.3 (17.5)	420.8 (12.2)	0.245	
<b>Soft Tissue Density (mg/cm<sup>3</sup>)</b>	117.4 (7.9)	91.9 (6.7)	0.081	
<b>Cortical Cutoff Density (mg/cm<sup>3</sup>)</b>	748.7 (13.0)	756.0 (10.4)	0.233	754
<b>Trabecular Cutoff Density (mg/cm<sup>3</sup>)</b>	266.9 (8.4)	256.3 (6.5)	0.483	260

## C. CONTROL ALGORITHM PERFORMANCE

### C.1 Repetitive shear control algorithm performance

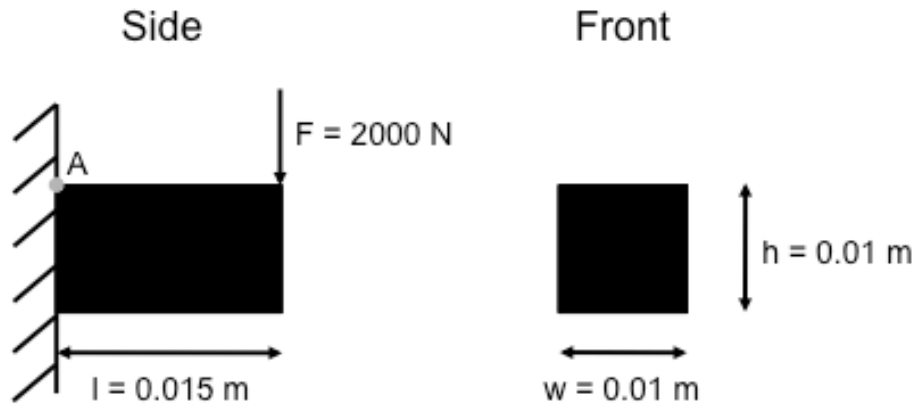
		Target Loading Magnitude			
		20%	40%	60%	80%
<b>Duration (sec.)</b> <b>Target = 0.5 sec.</b>	<b>Loading</b>	0.457 (0.004)	0.467 (0.004)	0.483 (0.001)	0.493 (0.003)
	<b>Unloading</b>	0.396 (0.012)	0.473 (0.004)	0.481 (0.002)	0.474 (0.004)
<b>Percent Load Error (%)</b>	<b>Loading</b>	6.07 (1.07)	2.97 (0.34)	3.59 (0.96)	6.44 (1.20)
	<b>Unloading</b>	3.56 (0.41)	2.92 (0.88)	1.90 (0.15)	6.90 (1.50)
<b>Percent Load Rate Error (%)</b>	<b>Loading</b>	8.37 (1.70)	5.83 (1.03)	5.25 (1.39)	8.61 (1.89)
	<b>Unloading</b>	25.35 (5.41)	5.37 (1.25)	5.99 (1.44)	12.07 (1.99)

## D. CALCULATIONS

### D.1 Analytical solution for a cantilevered beam

Beam dimensions (in meters):  $l = 0.015$ ,  $w = h = 0.01$

Applied force is 2000 N downward.



Stress at point A.

$$\sigma = \frac{My}{I}$$

Where  $M = Fl$ ,  $y = \frac{h}{2}$ , and  $I = \frac{wh^3}{12}$ . Substitute these expressions into the previous equation.

$$\sigma = \frac{6Fl}{wh^2}$$

Substitute values for  $F$ ,  $l$ ,  $w$ , and  $h$ .

$$\sigma = \frac{6(2000)(0.015)}{(0.01)^3}$$

$$\sigma = 180 \text{ MPa}$$